Universidade de Aveiro
Ano 2021

Daniela Filipa da Silva Fonseca

Desenvolvimento de microagulhas biopoliméricas para aplicação na administração de fármacos e extração de fluido intersticial

Development of biopolymeric-based microneedles for application in drug administration and interstitial fluid extraction

Universidade de Aveiro
Ano 2021

Daniela Filipa da Silva Fonseca

Desenvolvimento de microagulhas biopoliméricas para aplicação na administração de fármacos e extração de fluido intersticial

Development of biopolymeric-based microneedles for application in drug administration and interstitial fluid extraction

Tese apresentada à Universidade de Aveiro para cumprimento dos requisitos necessários à obtenção do grau de Doutor em Química Sustentável, realizada sob a orientação científica da Doutora Carmen Sofia Rocha Freire, Investigadora Principal do Departamento de Química da Universidade de Aveiro, e co-orientação do Doutor Armando Jorge Domingues Silvestre, Professor Catedrático do Departamento de Química da Universidade de Aveiro.

Apoio financeiro do POCTI no âmbito do III Quadro Comunitário de Apoio.

O doutorando agradece o apoio financeiro da FCT e do FSE no âmbito do III Quadro Comunitário de Apoio (PD/BD/115621/2016).

Dedico esta tese aos meus pais, por tudo.

“Passion is energy.
Feel the power that comes from focusing
on what excites you.”

-Oprah Winfrey

o júri

Presidente

Prof. Doutor Rui Luís Andrade Aguiar
Professor catedrático da Departamento de Eletrónica, Telecomunicações e Informática da Universidade de Aveiro

Vogais

Prof.ª Doutora Maria Helena Mendes Gil
Professora catedrática do Departamento de Engenharia Química da Universidade de Coimbra

Prof.ª Doutora Catarina Batista Fialho Rosado
Professora auxiliar da Escola de Ciências e Tecnologias da Saúde da Universidade Lusófona de Lisboa

Prof.ª Doutora Isabel Filipa Martins de Almeida
Professora auxiliar da Faculdade de Farmácia da Universidade do Porto

Doutora Carla Andreia Cunha Vilela
Investigadora auxiliar da Universidade de Aveiro

Doutora Carmen Sofia da Rocha Freire Barros (orientadora)
Investigadora principal da Universidade de Aveiro

agradecimentos

A realização desta tese de doutoramento contou com o apoio imprescindível de professores, família e amigos, que ao contribuírem de formas muito diversas, transformaram esta etapa numa incrível viagem.

Em primeiro lugar, manifesto o agradecimento à FCT, ao CICECO e ao Departamento de Química, que tornaram possíveis a concretização desta tese.

Expresso os meus sinceros agradecimentos aos meus orientadores. À Doutora Carmen e ao Professor Armando agradeço pela competência científica, acompanhamento, disponibilidade, críticas e sugestões, bem como pela amizade. Ao Professor Armando, o meu desde sempre co-orientador, agradeço em particular a amizade e generosidade ao longo da minha formação.

À Carla Vilela agradeço o acompanhamento, a disponibilidade e dedicação. À Professora Helena e à Verónica, um carinhoso agradecimento. Obrigado pelo apoio na parte prática e pelos valiosos ensinamentos. À Professora Isabel Almeida, ao Professor Paulo Costa, à Professora Patrícia Pereira, à Doutora Inês Sá, à Professora Manuela, à Professora Margarida um obrigado especial pela dedicação, disponibilidade e apoio na elaboração dos artigos. Um agradecimento especial à Fátima e à Xana, que muito carinhosamente me acolheram no laboratório de histopatologia e me permitiram acompanhar o trabalho prático. À Professora Catarina Rosado, ao Professor Pedro e todas as meninas dos laboratórios da Lusófona, um obrigado muito especial, pela dedicação e pela orientação. Trabalhar ao vosso lado foi uma dádiva!

A minha vida na Universidade de Aveiro foi enriquecida por muitas pessoas à minha volta. Agradeço aos meus colegas de laboratório, sempre encorajadores e divertidos. Partilhar o dia-a-dia convosco foi uma experiência e um privilégio. Em especial agradeço à Cátia, à Catarina e ao Ângelo, pelo carinho, companheirismo e amizade. Ao Fábio agradeço o encorajamento, e em especial, o riso. Obrigado pelos jantares, cafés, gelados, filmes, viagens e tantas outras coisas que nos transportam para o nosso mundinho de disparates e diversão! À Filipa, quero agradecer por tudo! Não há palavras que descrevam a gratidão que eu tenho em ter-te na minha vida, pelo suporte emocional, pelo companheirismo, pelo riso. Estes anos contigo foram só o início de uma amizade que é para a vida toda.

Quero expressar a minha mais profunda gratidão à minha família! Pai e mãe, o vosso suporte, afeto e presença constante foram o meu amuleto da sorte. À minha irmã e à minha afilhada, obrigada pelas performances musicais e dose de brincadeira. Aos avós e ao conjunto extenso de tios e tias, primos e primas, sempre prontos a oferecer motivação e apoio. Ao meu querido Riquinho, obrigado por me mostrares que o carinho de um patudo peludo é das melhores coisas que a vida tem para oferecer.

Por fim, um obrigado muito ternurento a ti Diogo, que preenches a minha vida com um brilho especial. Partilhar esta fase contigo tornou esta jornada ainda mais incrível!

palavras-chave

Microagulhas, biopolímeros, administração transdérmica, compostos bioativos, fluido intersticial, cosmética, diagnóstico.

resumo

As microagulhas são sistemas constituídos por pequenas projeções em forma de agulhas, com dimensões na ordem dos micrómetros. As microagulhas foram conceptualizadas com o objetivo de administrar fármacos através da via transdérmica e combinar os benefícios das injeções subcutâneas com a simplicidade dos pensos transdérmicos. Estas microestruturas perfuram o estrato córneo e criam microporos transitórios que facilitam o transporte de compostos bioativos através da pele, de forma minimamente invasiva e indolor. Além disso, ao contactar com a região superior da derme, as microagulhas permitem recolher fluido intersticial para análise de diversos metabolitos. Em particular, nas últimas décadas, o estudo destes sistemas está muito direcionado para o desenvolvimento de microagulhas com polímeros naturais devido à sua biocompatibilidade e características biomiméticas. A utilização de biopolímeros assenta também no seu carácter biodegradável e na necessidade de implementar práticas sustentáveis neste domínio. Assim, este trabalho tem como objetivo o desenvolvimento, caracterização e aplicação de sistemas de microagulhas inovadoras fabricadas a partir de biopolímeros, nomeadamente polissacarídeos e proteínas, de forma a responder à necessidade de desenvolver materiais de elevado desempenho e com um impacto ambiental reduzido.

O primeiro capítulo apresenta as características e propriedades das microagulhas, seguida pela introdução e descrição das microagulhas biopoliméricas, com foco nas suas propriedades e aplicações. O segundo capítulo desta tese foca-se no desenvolvimento de microagulhas de gelatina metacrilatada (10% (m/v)) para utilização como ferramenta de diagnóstico. Estas microagulhas têm uma elevada capacidade de intumescimento e permitem a absorção de fluido intersticial, que é posteriormente extraído e utilizado para análise de metabolitos. A avaliação do potencial de extração destas microagulhas foi testado com um sistema modelo *in vitro* de agarose e utilizando a ureia como metabolito modelo. Foram testadas duas concentrações de ureia de forma a mimetizar condições normais e de doença (renal), e foi possível recuperar >98% do analito. A citocompatibilidade deste material, associada à sua capacidade de absorção de fluido suporta a utilização das microagulhas de gelatina metacrilatada como ferramenta de diagnóstico, oferecendo uma alternativa promissora na era de diagnóstico “point of care”.

Com o intuito de desenvolver novas plataformas de administração de fármacos, o terceiro capítulo desta tese descreve a preparação e caracterização de microagulhas de pululano, utilizando soluções de 6, 9, 12, 15, 18 e 24% (m/v) de polímero. De uma forma geral, foram produzidas microagulhas de geometria regular e uniforme, tendo sido selecionadas as microagulhas de pululano com 24% (m/v) para a avaliação do potencial funcional deste sistema, através da incorporação de insulina.

resumo (cont.)

As microagulhas de pululano contendo insulina apresentam uma morfologia regular com microagulhas de 500 μm de altura e com resistência mecânica para perfurar pele humana *ex vivo*, atingindo até 381 μm de profundidade. A estabilidade da insulina no patch de microagulhas foi confirmada por dicroísmo circular, ao longo de um mês de armazenamento a 4, 20 e 40 ºC, tendo sido possível evidenciar a capacidade das microagulhas de pululano para armazenar e transportar este agente terapêutico sem recurso a climatização.

No quarto capítulo, foi estudado o potencial de membranas de nanocelulose bacteriana como reforço mecânico e suporte macromolecular para a incorporação de compostos bioativos (rutina) em microagulhas fabricadas com ácido hialurónico (5% (m/v)) para aplicação na área da cosmética. A atividade antioxidante deste composto fenólico é mantida durante seis meses de armazenamento das microagulhas à temperatura ambiente e na ausência de luz solar. A permeação da rutina foi avaliada em células de Franz utilizando pele de porco e a segurança do sistema modelo, incorporando apenas ácido hialurónico e celulose bacteriana, foi testada em 13 voluntários humanos. A avaliação da vermelhidão, eritema e perda transepidérmica de água na pele dos voluntários não apresenta diferenças estatisticamente diferentes na região de aplicação e controlo, confirmando a segurança do sistema.

Numa perspetiva diferente, o quinto capítulo foca-se num estudo preliminar de preparação e caracterização de microagulhas de gelatina e pectina com incorporação de curcumina para possível aplicação no tratamento do melanoma. A produção de microagulhas com gelatina e pectina iniciou-se com a avaliação do impacto de diferentes composições poliméricas na morfologia e nas propriedades mecânicas das microagulhas, tendo-se selecionado as microagulhas produzidas com 75% gelatina e 25% pectina para incorporar curcumina. A viabilidade celular de três linhas celulares de melanoma foi estudada para diferentes concentrações de curcumina, de forma a obter uma curva de dose-reposta. Nesta fase definiu-se o IC_{50} para as diferentes linhas celulares e a quantidade de curcumina (10 μg) a incorporar nos sistemas de microagulhas. Os resultados preliminares evidenciam o potencial da incorporação de curcumina em microagulhas biopoliméricas e a sua aplicabilidade como candidatas no tratamento de melanoma.

Em conclusão, com este trabalho de doutoramento foram reportados sistemas de microagulhas biopoliméricos inovadores e funcionais. A elevada versatilidade das microagulhas constituídas por biopolímeros permitiu desenvolver sistemas direcionados para administração de compostos bioativos, nomeadamente insulina, rutina e curcumina. Estes sistemas demonstraram reter a atividade biológica dos compostos bioativos e a estabilidade mecânica das microagulhas. O carácter intumescente da gelatina metacrilatada revelou o seu potencial como ferramenta para extração de fluido intersticial, o que representa um avanço significativo no diagnóstico e monitorização do estado de saúde, especialmente para doenças emergentes e crónicas.

keywords

Microneedles, biopolymers, transdermal adminstration, bioactive compounds, interstitial fluid, cosmetics, diagnostics.

abstract

Microneedles are arrays comprised of small needle-like projections, of micron-sized dimensions. Microneedles were first conceptualized aiming to enable the transdermal administration of drugs and combining the advantages of subcutaneous injections with the simplicity of transdermal patches. These micron-sized structures disrupt the *stratum corneum*, creating transitory pores which facilitate drug permeation through skin, in a minimally invasive and painless way. Furthermore, by contacting with the upper dermis, the microneedles enable interstitial fluid absorption for analysis of metabolites. In particular, in the last few decades, the use of biopolymers to fabricate microneedles has gained much interest due to their biocompatibility, biodegradability and biomimetic features. Proper consideration needs to be placed onto the sustainable character of these biomaterials and the need to pursue environmentally sustainable practices. Hence, this work aims at studying the preparation, evaluation and application of innovative microneedles systems using biopolymers, namely polysaccharides and proteins, to answer to the need for developing biomaterials of high performance with reduced environmental impact.

The first chapter gives a general introduction to the characteristics and properties of microneedles, followed by an overview of biopolymeric microneedles, focusing on their properties and applications. The second chapter of this thesis is focused on the development of microneedles for point-of-care diagnostics, using methacryloyl gelatin (10% (w/v)). These microneedles have high swelling ability, which allows interstitial skin fluid absorption that is afterwards extracted and used for analysis of metabolites. To infer about the diagnostic potential, an agarose *in vitro* system was employed for urea extraction as a model analyte. Two different concentrations were tested, to mimic a health and (renal) disease state, and it was concluded that >98% analyte was recovered. In this sense, the cytocompatibility of this material coupled with the fluid uptake ability supports the application of methacryloyl gelatin microneedles as a diagnostic tool, offering a promising alternative in this era of point of care diagnostics.

Aiming at developing new platforms for drug administration, the third chapter of this thesis describes the preparation and characterization of pullulan microneedles, using 6, 9, 12, 15, 18 e 24% (w/v) of polymer solutions. These presented a regular and uniform geometry and the microneedles prepared with 24% (w/v) pullulan were selected for insulin incorporation and evaluation of the functional properties. The insulin-loaded pullulan microneedles presented a regular morphology and 500 μm in length, mechanically strong to insert human skin *ex vivo*, creating pores up to 381 μm depth. The conformational stability of insulin into the pullulan system was confirmed through circular dichroism, during one month of storage at 4, 20 and 40 ºC.

abstract (cont.)

Therefore, it was possible to highlight the ability of pullulan microneedles to store and deliver this therapeutic agent with no need of cold chain monitoring. In the fourth chapter, the potential of bacterial nanocellulose as a mechanical reinforcement and macromolecular support for the incorporation of bioactive compounds (rutin) was studied using hyaluronic acid (5% (w/v)) microneedles for cosmetics. The antioxidant activity of this phenolic was kept for six months storage of microneedles at room temperature in the dark. Rutin permeation was evaluated using Franz cells and pig skin samples. In addition, the safety of the model system incorporating only bacterial cellulose and hyaluronic acid was evaluated by 13 human volunteers. Redness, erythema and transepidermal water loss in volunteer's skin were evaluated and no statistical differences were found between the control and the application site, confirming the safety of the system.

In a different perspective, the fifth chapter focuses on the preliminary evaluation of gelatin and pectin microneedles for curcumin incorporation, envisioning their potential application in melanoma treatment. The preparation of gelatin-pectin microneedles is described, aiming to evaluate the impact of the polymeric composition on the morphology and mechanical performance. Microneedles prepared with 75% gelatin and 25% pectin were selected for the incorporation of curcumin. Cell viability of three melanoma cell lines was evaluated for different curcumin concentrations, to study the dose-response curve. At this stage, it was defined an IC_{50} for each cell line and defined the amount of 10 µg curcumin to incorporate into the microneedles systems. Preliminary evaluation highlights the potential for curcumin incorporation into these biopolymeric microneedles and its application as candidates for melanoma treatment.

In conclusion, this PhD thesis reported the development of several innovative and functional biopolymeric microneedles systems. The outstanding versatility of biopolymeric microneedles, enabled the development of systems guided for the administration of bioactive compounds, namely insulin, rutin and curcumin. These systems proved to retain the bioactives' biological activity and the microneedles mechanical stability. The intumescent character of methacryloyl gelatin revealed their potential as a diagnostic tool, which represents a significant step in diagnostics and monitoring of healthcare state, especially for emergent and chronic diseases.

TABLE OF CONTENTS

PUBLICATIONS AND COMMUNICATIONS

Papers in peer reviewed journals (4)

Daniela F. S. Fonseca, Carla Vilela, Armando J. D. Silvestre, Carmen S. R. Freire, A compendium of current developments on polysaccharide and protein-based microneedles, International Journal of Biological Macromolecules, 2019, 136, 704-728.

Daniela F. S. Fonseca, Paulo C. Costa, Isabel F. Almeida, Patrícia Dias-Pereira, Inês Correia-Sá, Verónica Bastos, Helena Oliveira, Margarida Duarte-Araújo, Manuela Morato, Carla Vilela, Armando J. D. Silvestre, Carmen S. R. Freire, Pullulan microneedle patches for the efficient transdermal administration of insulin envisioning diabetes treatment, Carbohydrate Polymers, 2020, 241, 116314.

Daniela F. S. Fonseca, Carla Vilela, Ricardo J. B. Pinto, Verónica Bastos, Helena Oliveira, José Catarino, Pedro Faísca, Catarina Rosado, Armando J. D. Silvestre, Carmen S. R. Freire, Bacterial nanocellulose-hyaluronic acid microneedles for skin applications: *In vitro* and *in vivo* evaluation, Materials Science and Engineering: C, (118) 2021.

Daniela F. S. Fonseca, Paulo C. Costa, Isabel F. Almeida, Patrícia Dias-Pereira, Inês Correia-Sá, Verónica Bastos, Helena Oliveira, Carla Vilela, Armando J. D. Silvestre, Carmen S. R. Freire, Swellable gelatin methacryloyl microneedles for extraction of interstitial skin fluid towards minimally invasive monitoring of urea, Macromolecular Biosciences, 2020, 2000195.

Oral communications (8)

Flash communication (FT10): Bacterial cellulose based functional nanomaterials for dermal drug delivery and skin treatment. **Daniela F. S. Fonseca,** Nuno H. C. S. Silva, Carla Vilela, Armando J. D. Silvestre, Carmen S. R. Freire, presented at the International Symposium on Bioinspired Macromolecular Systems, held on 6th-8th November 2017, University of Aveiro, Portugal.

Freire, Carmen, Vilela, Carla, Rodrigues, Catia, **Fonseca, Daniela**, Silvestre, Armando, Novel multilayered drug delivery systems based on bacterial nanocellulose for skin

treatment, presented at 255th National Meeting and Exposition of the American-Chemical-Society (ACS) - Nexus of Food, Energy, and Water, held on 18th-22nd March 2018 in New Orleans, Los Angeles, USA.

Daniela F. S. Fonseca, C. Vilela, Armando J. D. Silvestre, Carmen S. R. Freire, Pullulan-based microneedles for transdermal delivery of pharmaceutical ingredients, presented at the 3rd International EPNOE Junior Scientists Meeting held on 14th-15th of May 2018 in Maribor, Slovenia.

Daniela F. S. Fonseca, C. Vilela, Armando J. D. Silvestre, Carmen S. R. Freire, Microneedles: rising stars in drug delivery. Rising science communicators, Jornadas CICECO, 2018, University of Aveiro, Portugal. **Honorable mention.**

Daniela F. S. Fonseca, Carla Vilela, Armando J. D. Silvestre, Carmen S. R. Freire, Microneedles: holding the key to pain-free injections, presented at the Research Summit 2018, held on 28th-29th December 2018, University of Aveiro. **Best pitch award.**

Daniela F. S. Fonseca, Carla Vilela, Armando J. D. Silvestre, Carmen S. R. Freire, Nanocellulose-hyaluronic acid microneedles for cosmetic applications, presented at the 10th International Conference on Skin Challenges held on 25th-27th February 2019, in Porto, Portugal.

Daniela F. S. Fonseca, Carla Vilela, Armando J. D. Silvestre, Carmen S. R. Freire, Biopolymeric microneedles: new frontiers in drug administration, presented at the Research Summit 2019, held on 3rd-5th July 2019, University of Aveiro.

Daniela F. S. Fonseca, Armando J. D. Silvestre, Carmen S. R. Freire, Biopolymeric microneedles: shaping the future of transdermal delivery and diagnostics, presented at the Research Summit 2020, held on 24th-26th June 2020, University of Aveiro. **Honorable mention.**

Poster communications (2)

Daniela F. S. Fonseca, Nuno H. C. S. Silva, Carla Vilela, Armando J. D. Silvestre, Carmen S. R. Freire, Bacterial cellulose based functional nanomaterials for dermal drug delivery and skin treatment, presented at the International Symposium on Bioinspired Macromolecular Systems, held on 6th-8th November 2017, University of Aveiro, Portugal.

Daniela F. S. Fonseca, Carla Vilela, Paulo Costa, Isabel F. Almeida, Armando J. D. Silvestre, Carmen S. R. Freire. Pullulan-based microneedles for transdermal delivery of insulin. Poster presented at Encontro de Ciência, held on 2nd-4th July 2018, Centro de Congressos de Lisboa, Portugal.

Additional work (1)

Daniela F. S. Fonseca, João P. F. Carvalho, Verónica Bastos, Helena Oliveira, Catarina Moreirinha, Adelaide Almeida, Armando J. D. Silvestre, Carla Vilela, Carmen S. R. Freire, Antibacterial Multi-Layered Nanocellulose-Based Patches Loaded with Dexpanthenol for Wound Healing Applications. Nanomaterials 2020, 10, 2469.

LIST OF TABLES

LIST OF FIGURES

GENERAL ABBREVIATIONS

BC	Bacterial nanocellulose
BSA	Bovine serum albumin
c-GelMA	Crosslinked gelatin methacryloyl
CMC	Carboxymethyl cellulose
CS	Chitosan
Cur	Curcumin
DD	Drug delivery
DDS	Drug delivery systems
FDA	US Food and Drug Administration
FITC	Fluorescein isothiocyanate
Gel	Gelatin
GRAS	Generally recognized as safe
HA	Hyaluronic acid
HIV	Human immunodeficiency virus
Ig	Immunoglobulin
ISF	Interstitial skin fluid
LbL	Layer-by-layer
MNs	Microneedles
MEMs	Micro-electromechanical systems
MTT	3-(4,5-dimethyl-2-thiazolyl)-2,5-diphenyl tetrazolium bromide
MW	Molecular weight
P	Partition coefficient
PBS	Phosphate buffered saline
PDMS	Poly(dimethylsiloxane)
Pec	Pectin
PL	Pullulan
PVA	Poly(vinyl alcohol)
PVP	Poly(vinylpyrrolidone)
RH	Relative humidity
SC	*Stratum Corneum*
TEWL	Transepidermal water loss
TDD	Transdermal drug delivery
WHO	World Health Organization

AIM AND OUTLINE OF THIS THESIS

CONTEXT

In its ever-growing scope, the pharmaceutical industry is shaped by the continuous challenges and expectations of the healthcare system, in the pursuit of more efficient drugs, drug delivery systems (DDS) and diagnostic strategies [1,2]. Globally, the transdermal route is considered a friendly approach and a desirable alternative to other forms of drug delivery (DD), being one of the most successful and innovative focus of research in the area [3,4]. This field has been particularly boosted by the growing exploitation of microneedles (MNs), due to their minimal invasiveness, painless skin penetration, therapeutic efficacy and relative safety [5–7].

Conceptualized as micron-sized needles placed on the underside of a patch, MNs were created to combine the advantages of conventional injections and transdermal patches. These miniaturized systems have been shaped into different forms using different materials with the utmost purpose of increasing drugs' skin permeability [5]. With versatility to incorporate a panoply of active ingredients - from small molecules to biotherapeutics - MNs technology has found applications that cross scientific boundaries and range from cosmetics to vaccination, sensing and diagnostics [5–7].

During the past few decades, noteworthy advancements have been made by taking advantage of biopolymers, as polysaccharides and proteins, for the fabrication of MNs [8,9], due to their biocompatibility, availability, biodegradability and renewability. Some biopolymers are naturally found in human tissues and the chemical composition and structure of natural polymers are very similar to the macromolecules of the native extracellular environment, matching specific structural and functional elements. Hence, they are easily recognised and accepted by the human body while contrasting the onset of adverse events [10,11]. In addition, biopolymers can undergo chemical modification to meet varying technological needs and provide cutting edge solutions [12–14]. Some of these sophisticated MNs are characterized by their responsive nature, tailored mechanical properties, sensing ability or controlled degradation rate [5–7].

Nowadays, biopolymers are extensively exploited to meet the demand of environmentally sustainable technologies, including applications in the healthcare domain. This urgent challenge is reflected by the 17 Sustainable Development Goals adopted by the United Nations Member States. Within this framework, it is recognized the need to ensure healthy lives and sustainable consumption and production, preserving the environment [15]. Therefore, by combining the knowledge over MNs and the principles and practices of green chemistry, we may hold the key to build an environmentally sustainable society. In order to capitalize on this, practices involving the

use of natural resources, non-hazardous solvents, no harmful by-products, and energy-efficient processes in the preparation of MNs need to be applied.

OBJECTIVES AND OUTLINE OF THIS THESIS

As aforementioned, the development of biopolymeric MNs taking advantage of simple technologies and greener solvents is of utmost importance. Therefore, this PhD project is aimed at developing MNs systems, for DD and fluid uptake using biopolymers through sustainable fabrication processes and evaluate their properties and biological performance. This thesis contributes with a perspective on the characteristics and potential of different biopolymeric MNs, nurturing and accelerating the knowledge in the MNs field. In this context, the specific objectives of this research are thereby outlined as the following:

- ✓ Develop MNs based on polysaccharides (pullulan (PL), hyaluronic acid (HA), bacterial nanocellulose (BC) and pectin (Pec)) and proteins (crosslinked gelatin methacryloyl (c-GelMA) and gelatin (Gel)) using benign solvents through solvent casting and evaluate their potential for DD or interstitial skin fluid extraction (ISF);
- ✓ Carry out the mechanical characterization of the biopolymeric MNs and evaluate their skin insertion ability;
- ✓ Characterize the MNs in terms of their thermal and functional properties, such as water uptake, cytocompatibility and ability to stabilize bioactive ingredients;
- ✓ Determine the extent of DD;
- ✓ Assess the safety and efficacy of the biopolymeric MNs *in vitro* and when possible, by *in vivo* tests.

The present PhD thesis is organized in 6 chapters as illustrated in Figure 0.1. **Chapter 1** introduces the most relevant state of the art of this field. It includes a general overview about transdermal drug delivery (TDD), focusing on the advantages and challenges of this DD route. Then, a revision of MNs is provided, with particular emphasis on their characteristics, preparation methodologies and applications. Finally, a detailed description of polysaccharide and protein-based MNs described in literature is given. **Chapters 2 to 5** present the main results of the research conducted on this thesis and describe the progresses beyond the state of the art. Different biopolymeric-based MNs were fabricated, characterized according to their mechanical, structural and thermal properties. Cytocompatibility assessments were also performed as well as the

assessment of pharmacokinetic parameters, and when applicable, safety and efficacy *in vitro* and *in vivo*.

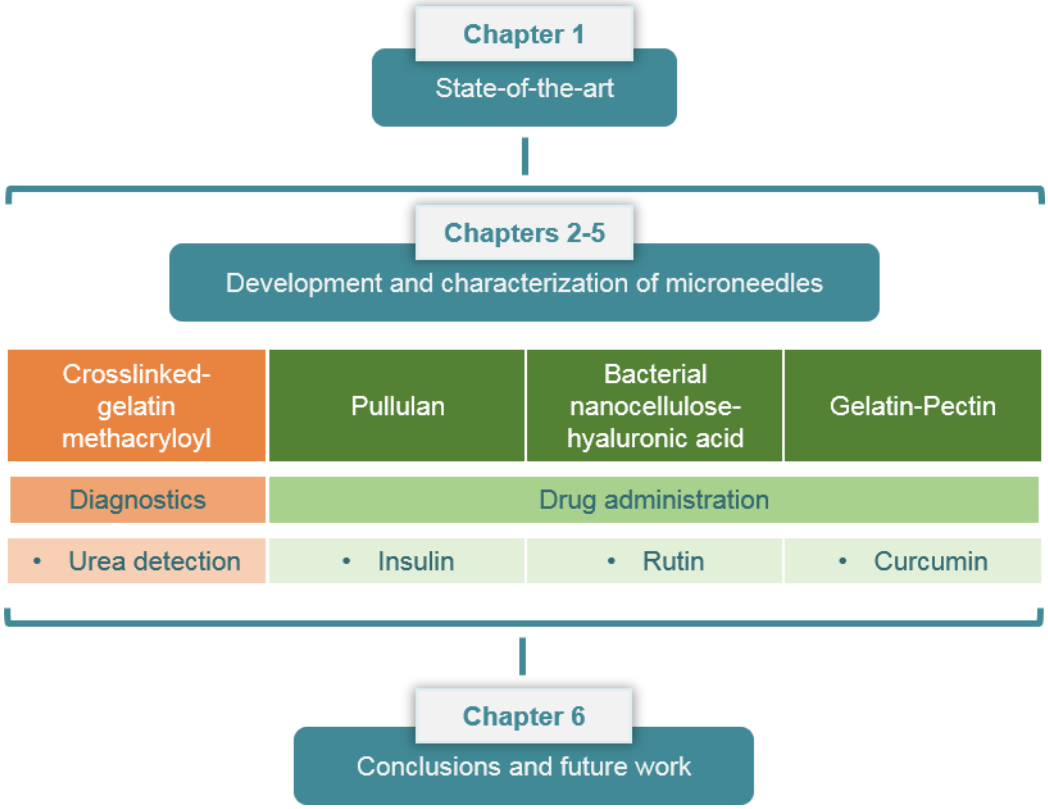

Figure 0. 1. PhD thesis workflow: from the state-of-the-art to the development and characterization of biopolymeric MNs and the target applications.

In particular, **Chapter 2** focuses on the preparation of c-GelMA MNs and their evaluation as diagnostic devices for transdermal biological fluid extraction and subsequent monitoring of urea. GelMA, which consists of Gel derivatized with methacrylate groups, was chosen as a biopolymeric matrix due to its excellent swellable capacity. Furthermore, this material retains Gel cytocompatibility, provides shape fidelity upon micromolding and photo-crosslinking enables stability at physiological temperature.

Chapter 3 is dedicated to the development of MNs using PL as starting biopolymeric matrix for insulin administration. In this study, the film-forming ability of this polysaccharide coupled with a sustainable character, biocompatibility and low hygroscopic nature, prompted the fabrication of these delivery systems. **Chapter 4** describes the development of a functional MN system for cosmetic purposes, incorporating HA and BC. BC is employed as a macromolecular support for the incorporation of rutin as active ingredient, whereas HA has been well recognized for its role in the cosmetic area and was used to produce the MNs. Herein, the safety and efficacy of this system is supported by *in vivo* tests performed using human volunteers.

In **Chapter 5**, preliminary results about the formulation of Gel-Pec MNs incorporating curcumin (Cur) are described. Gel and Pec were selected as biopolymers that produce reversible physical hydrogels creating improved materials. In this study, Cur was introduced into the MNs as a free compound or as part of a nanogel system, and the cytotoxicity of this phenolic compound was evaluated using three melanoma cell lines.

Finally, **Chapter 6** highlights the final remarks of this thesis and gives an overview of the future potential trends in this domain. Lastly, proposals of the future work arising from these studies are provided, aiming to bring more emphasis on the future of this research area.

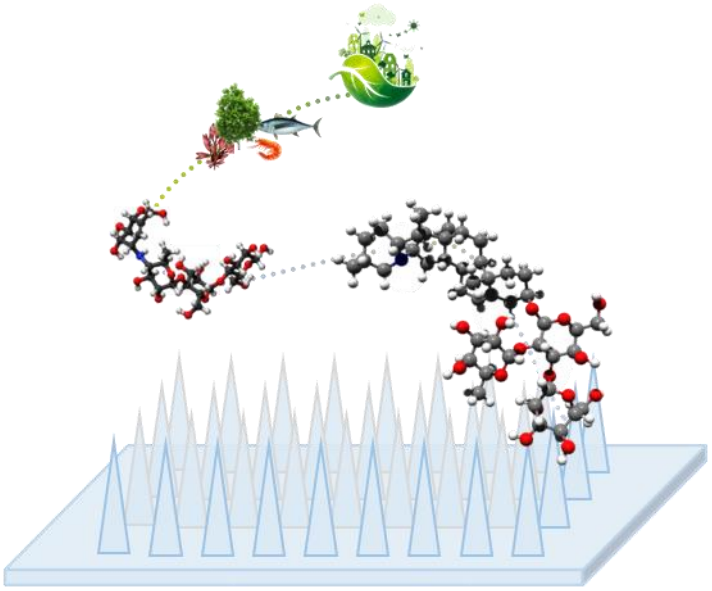

CHAPTER 1. BIBLIOGRAPHIC REVISION

This chapter is adapted from the published manuscript:
Daniela F. S. Fonseca, Carla Vilela, Armando J. D. Silvestre, Carmen S. R. Freire, A compendium of current developments on polysaccharide and protein-based microneedles, International Journal of Biological Macromolecules, 2019, 136, 704-728.

1.1. General considerations about transdermal drug delivery

During the past few decades, we have witnessed an enormous progress in the research, development and improvement of DDS [1,16,17]. The technological advances of this burgeoning field emerged as optimized formulations or delivery devices, aiming to enhance the therapeutic efficacy of the different pharmacological agents, either biotherapeutics (*e.g.*, insulin and vaccines) or drugs (*e.g.*, diclofenac and ibuprofen) [17,18]. Notably, considering that the therapeutic efficiency strongly relies on the administration route, the focus is to overcome the challenges of conventional DD. The most common limitations are the pharmaceutical's degradation in the gastrointestinal tract in oral administration, and the poor patient compliance of parenteral injections [1,16,19]. Therefore, the field of DD is driving research towards the development of easy-to-use systems, with good patient compliance, a reduced frequency of dosing and self-administration at the point-of-care, with lower therapy costs and reduced environmental impact [20–24].

Among the different DDS, TDD aiming at delivering pharmaceuticals through skin, has attracted a lot of attention. From a global perspective, the transdermal route offers key benefits, such as targeted delivery and lower systemic exposure and toxicity, because drugs avoid first-pass metabolism, gastrointestinal degradation and food-drug interactions, thus improving their bioavailability [3,4,25]. Furthermore, the simple and painless self-application of TDD systems, coupled with their easy storage and transportation, makes them particularly relevant for health care in developing countries [20,22,26]. Regardless of these features, TDD success is hindered by the barrier function provided by skin, which due to its complex and multi-layered cellular architecture, limits DD efficiency [27]. In general, suitable candidates for TDD are molecules with potent pharmacological activity, low molecular weight ((MW) <400 Da, ideally), balanced lipophilicity (log *P*(octanol-water partition coefficient) ideally around 2 to 3) and a measurable solubility both in oil and water [28]. Hence, TDD is restricted to a narrow range of pharmaceuticals, as a result of the difficulty of finding formulations with appropriate physicochemical properties to passively permeate through skin [4,20].

To address these limitations and enable successful transdermal delivery of different pharmaceuticals, a rather-novel strategy involves using MNs [6,8,29]. These DDS are three-dimensional micron-sized needles placed on the underside of a patch, designed to combine the advantages of both hypodermic needles and transdermal patches as illustrated in Figure 1.1 [5]. This field is experiencing outstanding developments, which is supported by the several excellent general reviews on the subject of DD using MNs [5,8,30–34].

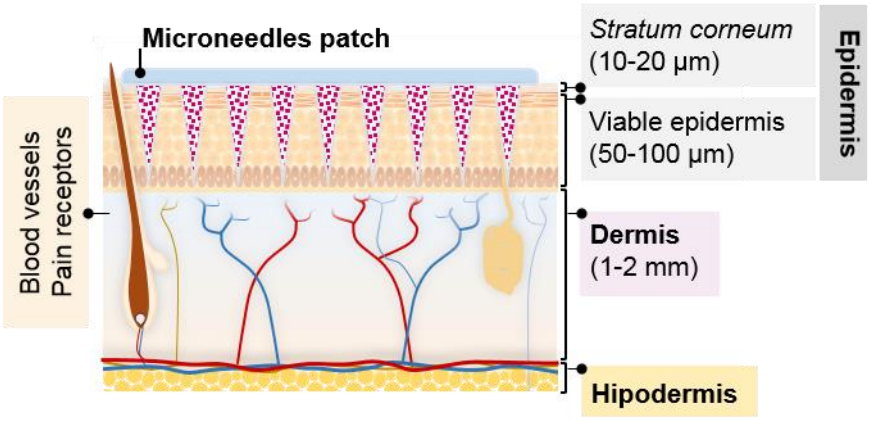

Figure 1. 1. Schematic representation of the side view of MNs inserted into the skin [5].

Throughout the history of MNs fabrication, the use of a wide range of materials has been reported. The first MNs were fabricated using silicon [35–37], metals (*e.g.*, titanium [38] and stainless steel [39]), ceramics [40] and glass [41]. Nevertheless, polymers are nowadays playing a central role in the preparation of MNs [8]. This large and versatile class of materials can be tailored with a great variety of structures and hence, physical and biological functions to meet specific needs [12–14]. In this vein, polymers are considered one of the cornerstones for biomedical applications [14,42,43]. Currently, as a result of the general concern for sustainability, biopolymers, in particular polysaccharides and proteins, are receiving unprecedented attention over the synthetic polymers in the fabrication of MNs. This is due to their biocompatibility and low immunogenicity, biomimetic features, ability to enhance drug pharmacokinetics, abundance and renewable character [8,14,17,44,45]. The panoply of biopolymers available in nature has allowed the fabrication of MNs with unique characteristics [8], and from this perspective, the infinite opportunities of fabricating sophisticated biopolymer-based MNs are only limited by our imagination.

This chapter aims at providing a brief overview of the general characteristics and DD strategies of MNs, covering aspects that range from their advantages, geometry and fabrication technology to their mechanical features. This chapter also presents the potential and challenges of using polysaccharide and protein-based MNs to deliver drugs, vaccines and other molecules. The final section looks into the main findings regarding the mechanical properties of the biopolymeric MNs.

1.2. Fundamentals of MNs

1.2.1. Definition and characteristics

MNs, first conceptualized in 1976 [46], take the form of transdermal patches with microscale protrusions designed to disrupt the *stratum corneum (SC*) of the skin and

other epithelial tissues, creating microconduits through which external molecules can passively diffuse (Figure 1.1) [47–49]. Typically, MNs have from 25 to 2000 μm in length [50], small enough to avoid stimulation of peripheral nerve fibers or puncture the blood vessels. Upon application of MNs, DD efficiency can be dramatically enhanced, and the types of pharmaceuticals transported *via* transdermal route can be significantly diversified [5,8,32]. In 1998, Henry *et al*. [47] reported the successful fabrication of solid silicon MNs for TDD of calcein (hydrophilic drug of 622.5 Da), showing for the first time that the *in vitro* permeability of human skin could be increased by up to 4 orders of magnitude, after pierced by 150 μm long needles.

Conceptually, the success of MNs results from combining the advantages of traditional TDD systems with the targeting of conventional hypodermic needles. Some key drivers for this enduring success are minimal invasiveness, low pain, self-administration, easy disposal and the ability to increase transcutaneous flux of pharmaceuticals [5,8,32,34]. In contrast, the creation of microscopic pores that lead to hypersensitivity reactions, delayed onset, reliable dosing and the potential for misuse, are some of the concerns regarding these DD devices [51]. In general, MNs can be classified accordingly to their structure (Figure 1.2 (A)), body shape (Figure 1.2 (B)) and tip shape (Figure 1.2 (C)) [5,52].

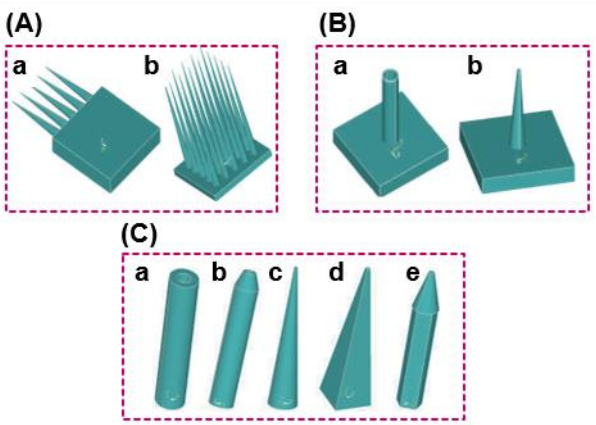

Figure 1. 2. Schematic illustration of MNs. (A) Microneedle structure defined as (a) in-plane and (b) out-of-plane. (B) Shape defined as (a) hollow and (b) solid shape. (C) Geometry of needles defined as (a) cylindrical, (b) tapered tip, (c) conical, (d) pyramidal and (e) pentagonal-base canonical tip [52].

MNs are fabricated into two basic designs, *viz.* in-plane (Figure 1.2 (A)a) and out-of-plane (Figure 1.2 (A)b) [5,52]. The needles of in-plane MNs are parallel to the fabrication surface, whereas the out-of-plane MNs arise perpendicular to the baseplate. In addition, the out-of-plane MNs can be classified as hollow (Figure 1.2 (B)a) or solid (Figure 1.2 (B)b) shape MNs, and have different geometries, such as cylindrical (Figure

1.2 (C)a), tapered tip (Figure 1.2 (C)b), conical (Figure 1.2 (C)c), square base or pyramidal (Figure 1.2 (C)d) and pentagonal-base conical tip (Figure 1.2 (C)e) [52].

1.2.2. DD strategies

The delivery of therapeutic agents using MNs is typically described according to five types of systems and the associated patterns of DD. Specifically, MNs can be classified as solid (Figure 1.3 (a)), coated (Figure 1.3 (b)), dissolving (Figure 1.3 (c)), hollow (Figure 1.3 (d)) and hydrogel-forming MNs (Figure 1.3 (e)) [5].

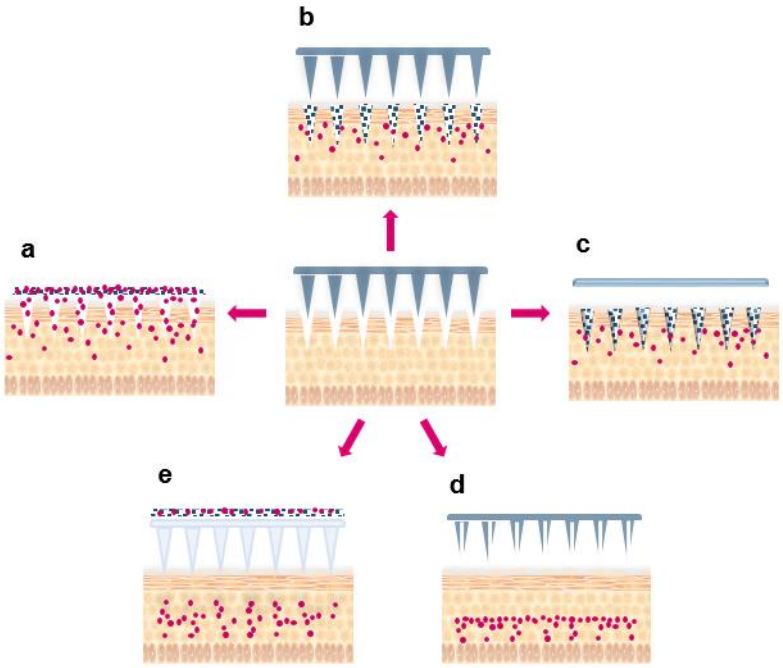

Figure 1. 3. Classification of MNs accordingly to patterns of DD. (a) Solid, (b) coated, (c) dissolving, (d) hollow, (e) hydrogel-forming MNs [5].

Solid, coated and hollow MNs can be fabricated using silicon [35–37], metals and alloys (*e.g.,* titanium [38], stainless steel [39], palladium, palladium-cobalt alloys and nickel [53,54]), ceramics (*e.g.,* ceramic oxides such as alumina, zirconia and fused silica [40]), glass [41,55] and polymers (*e.g.,* polyvinylpyrrolidone (PVP) [56], poly(vinyl alcohol) (PVA) [57], poly(γ-glutamic acid) [58], HA [59], chitosan (CS) [60], among others [61–66]). Dissolving MNs can be fabricated using sugars (*e.g.*, maltose, trehalose and sucrose [67–69]) or water-soluble polymers [57,61,70], whereas hydrogel-forming MNs are prepared using polymers [5,8,29,32].

Solid MNs (Figure 1.3 (a)), employed in the so-called ‘poke with patch’ approach, were developed as a 1st generation transcutaneous system [71,72]. First, MNs are

applied to skin to create transient pores in the *SC*. Then, conventional drug formulations like transdermal patches, ointments, creams, gels or lotions are applied, and the permeation occurs *via* passive diffusion [71–73].

Coated MNs (Figure 1.3 (b)) rely on the 'coat and poke' strategy which consists in coating the arrays with therapeutic formulations that are released after skin insertion [74]. The pharmaceutical formulations are applied alone or combined in polymeric matrices, usually by dip coating [74,75]. More recently, scientists have explored additive manufacturing, namely by layer-by-layer (LbL) approaches to deposit therapeutic agents in different layers, using polyelectrolyte solutions or polymeric nanocapsules [76,77]. Coated MNs may be an alternative for vaccination purposes or the delivery of potent drugs, but are not suitable for applications requiring high drug doses due to the restricted amounts that can be coated onto the finite surface area of the MNs [74].

Dissolving MNs (Figure 1.3 (c)) is an umbrella term used to describe dissolving or degradable matrices. The DD strategy is based upon the 'poke and release' approach. In brief, the array is inserted into the skin, the needle structure dissolves and releases its cargo [25,71]. The pharmaceutical agents can be introduced in the tip of the needle, in the whole needle structure as part of matrix and also encapsulated in particles [32,78]. The main limitation of using dissolvable MNs is the deposition of material into skin if they are used on a regular basis, which possibly can make these devices undesirable [79].

Hollow MNs (Figure 1.3 (d)) are characterized by having a conduit structure through which the fluid drug formulation is delivered, by "poke and flow" approach [80,81]. These devices can deliver larger amounts of substances, when compared with the former types of MNs [41,82,83]. However, it is important to highlight that the clogging of needle openings with skin tissue during insertion raises some concerns [84]. To overcome this limitation, alternative designs suggest the bore-opening at the side of the needle [85]. Furthermore, the dense tissue around the needles causes flow resistance [86], which can be overcome by partial needle retraction after skin insertion [41]. A disadvantage of using hollow MNs is that liquid formulations require suitable and complex reservoirs [87].

Lastly, hydrogel-forming MNs (Figure 1.3 (e)) are prepared from crosslinked polymeric materials. The first systems were designed with a patch drug reservoir attached [88,89]. After insertion, the hydrogel needles take up ISF and swollen, allowing drugs from the back patch to diffuse through the structure into the skin. This device enables the intact removal of MNs array after use, leaving no polymer residues behind. Another strategy involves the introduction of the drug formulation inside the array rather than in an external patch [90].

1.2.3. Manufacturing of MNs

MNs of a diversity of sizes and shapes can be fabricated using a plethora of methodologies (Figure 1.4) [5].

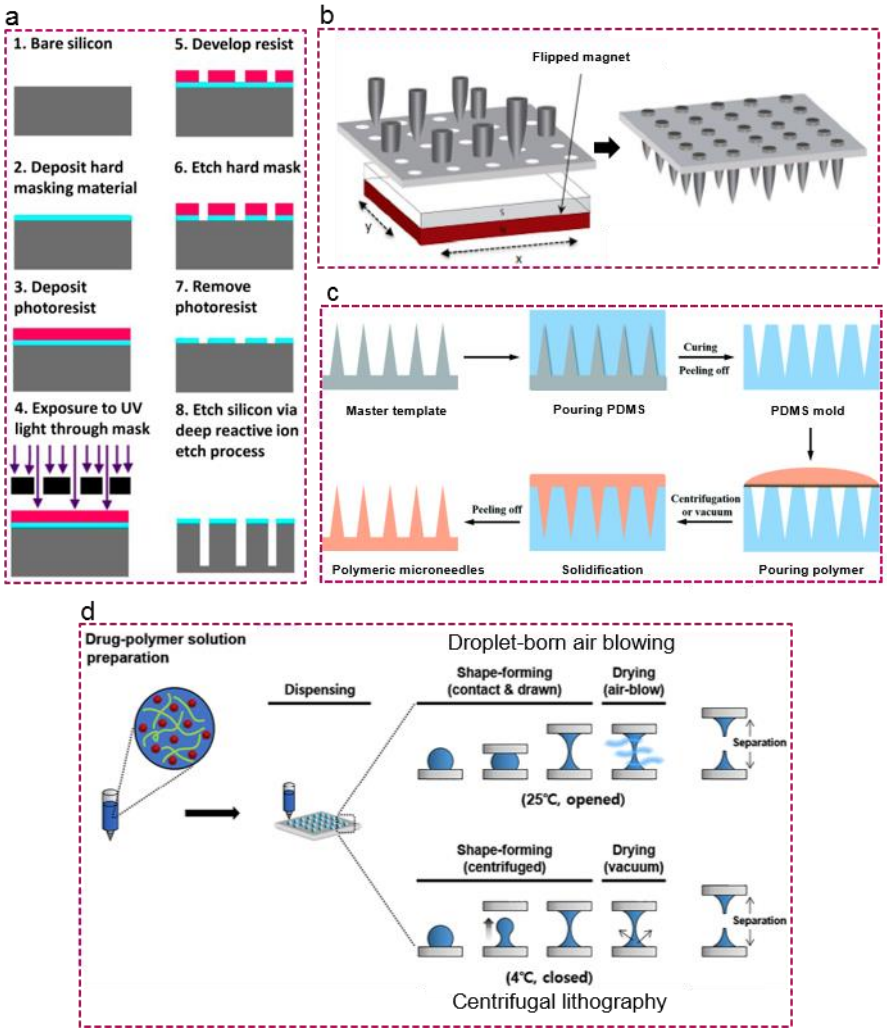

Figure 1. 4. Representative illustration of (a) conventional microfabrication technology [91], (b) magnetic assembly process [92], (c) general micromolding process [8] and (d) droplet-based methods, namely droplet-born air blowing and centrifugal lithography [93].

In the extensive body of information related to the preparation of MNs, the term microfabrication is usually reported. In fact, microfabrication refers to one precision field responsible for the development of small three-dimensional micron-sized structures by coupling serial direct-write technologies with precision machining methods [94]. The first MNs made of silicon were fabricated based on the conventional microfabrication technology, *i.e.* micro-electromechanical systems (MEMS) technology (Figure 1.4 (a)). It involves three basic techniques, namely deposition, patterning and etching [91,95].

The initial step consists in the deposition of thin films with varying thickness, from a few nm to about 100 µm. Then, patterning involves the transfer of a geometric pattern

into the film. Lithography is used to transfer a pattern into a photosensitive material by selectively exposing it to a radiation source. Photolithography is the most commonly adopted process, but this step can also be performed using ion beam lithography, electron beam lithography, X-ray lithography and diamond patterning. The next phase involves etching (either wet or dry), which consists in cutting the unprotected parts of the material to generate the chosen design, either by using strong acid or mordant [50]. MEMS technology offers the advantage of allowing the fabrication of both solid and hollow MNs. However, this complex process involves multiple steps, requiring long fabrication time and clean room processing, becoming relatively expensive [95,96].

The fabrication of solid or hollow metal MNs can be performed by MEMS technology, electroplating or electrodeposition, photochemical etching and laser cutting [5]. The most simple method involves the manual assembly of conventional hypodermic needles [97]. Metallic MNs can also be integrated into a base substrate by magnetic assembly (Figure 1.4 (b)) [92]. As an alternative, to this technology, infrared laser can be used. In this case, infrared laser cuts the metal structures that are then bend at 90 °C, creating an out-of-plane array [98]. Besides laser cutting and manual assembly, metal MNs can also be produced using drawing lithography that allows the creation of relatively ultra-high-aspect-ratio MNs. It consists in using a thin layer of a thermosetting polymer which then follows controlled drawing by using pillars of defined patterns. This method enables the creation of three-dimensional solid long polymeric needles that can be employed as a mold to finally create hollow metallic MNs [99].

Glass MNs are prepared by pulling fire-polished glass pipettes using a micropipette puller. Then, the blunt-tip can be beveled at an angle of 35-38°. Usually, these MNs are attached to syringes [41]. On the other hand, ceramic MNs are generally fabricated using micromolding techniques, either by sintering processes or photo-polymerization [5,100].

Micromolding is a set of fabrication methods which involves replicating microstructures using molds as master structures (Figure 1.4 (c)). It starts with the fabrication of the master MN templates, a structure containing a negative or inverse of the desired pattern geometry, followed by the preparation of the female molds. Then, the ceramic material is introduced onto female molds, followed by sintering or photo-crosslinking [101].

Polymeric MN arrays have been fabricated by using different manufacturing methods, namely micromolding techniques [56,102,103], which includes hot embossing [104], injection [94] and investment molding [105] and solvent casting [106]. Other processes include drawing lithography [69], electro-drawing [107,108], droplet-borne air blowing [109], photolithography [110,111] and continuous liquid interface production [112]. More recently, additive manufacturing by 3D printing has been also studied

[113,114]. These technologies take advantage of the versatility of this class of materials, in terms of viscosity, dissolution properties and post-modification. Micromolding is the most widely used method due to its cost efficiency, good reproducibility and scalability [101]. In this case, the polymeric material is introduced onto the female molds, and then the material is dried or photo-crosslinked, depending on the nature of the polymer. Finally, the MNs are peeled off from the female molds, which transcribe completely the microstructures of the master template. The use of master templates made of ceramics [90], PVA [115], or polydimethylsiloxane (PDMS) [116] has been reported. Among these, PDMS has been chosen as the most interesting material for small-scale micromolding due to its good transcription ability, excellent thermo-stability, and poor adhesion, which is beneficial for the separation of the polymeric MNs arrays from the mold [117].

Some of the most common micromolding techniques are injection molding, hot embossing, and casting [101]. Injection molding requires the use of thermoplastic materials which are melted in the injection molding machine. Then, they are injected into the molds, where they cool and solidify into the final parts. The successful development of MNs depends upon a variety of factors, namely injection speed, mold cavity temperature, accuracy in design and manufacture of the master template [94]. In the hot embossing process, the mold and polymer are heated and pressed. Then, the mold is cooled to room temperature and the MNs arrays are demoulded [104,118,119].

By polymer investment molding, two processes are combined, namely the traditional injection molding with investment casting, enabling the creation of hollow parts [105]. Another example involves the preparation of hollow MNs by casting, using a sacrificial template produced through a double deep X-ray lithography process [104]. This fabrication process does not require a clean room environment and uses little instrumentation. However, among the most common micromolding techniques, solvent casting is the most adopted [101]. Here, the material is placed into the female molds, followed by centrifugation or vacuum to fill the empty spaces and then drying or photo-crosslinking [90,120,121]. Despite the many advantages of micromolding, there are still some concerns for biomedical applications. First, the complex multiple fabrication steps are time consuming. Also, if heat or UV-light are involved in the fabrication process, the use of sensitive drugs, peptides, proteins and vaccines is rather limited [122]. To simplify the fabrication of MNs and preserve the biological activity of the active ingredients, a one-step fabrication procedure combining both shape-forming and solidification steps was reported [123]. This technique, called centrifugal lithography (Figure 1.4 (d)), takes advantage of polymer solutions [123], and involves placing drops of polymer into a base (inner plate) of two parallel fixed plates, followed by centrifugation. The centrifugation step allows the drop to shape into an hour-glass structure, which will contact the outer-

plate and solidifies the MNs. Finally, the plates are pulled in different directions, allowing the separation of two MNs from one-polymer drop.

A different strategy, the droplet air-blowing technique (Figure 1.4 (d)), uses forced air-blowing to shape the viscous polymer solution into MNs and involves six steps [109]. First, polymer droplets are dispersed over a flat substrate, used to support the MNs base. Then, in the second step, the drug droplet is dispensed over the baseplate and then, the upper plate follows a downward movement to enable contact with the dispensed droplets. On the fourth step, the upward movement of the upper plate controls the length and then air-blowing is applied to solidify and shape the droplets. Finally, the two plates are separated to create two MN arrays on both upper and lower plates [109]. During fabrication, the thickness of the baseplate is determined by the volume of the polymer droplet dispensed in the first step. Drug loading can be easily controlled by the pressure and time of droplet dispensing. Compared to micromolding methods, the conditions of droplet-borne air blowing method are more moderate since neither heat nor UV irradiation is involved. The effect of two droplet-based fabrication methods, namely centrifugal lithography and droplet-born air blowing was compared, by analyzing the change in activity of the encapsulated drugs, namely epidermal growth factor, which is known as an unstable peptide, and ascorbic acid, an easily oxidized low-molecular-weight chemical compound. The results showed that centrifugal lithography exerts less stress during the fabrication process, which involves low temperatures and vacuum-drying conditions, minimizing activity loss of the incorporated drugs. Furthermore, the morphological features and physical properties of the fabricated MNs, such as fracture force and morphology, were similar [93].

3D printing, also called additive manufacturing, was used as a method to fabricate MNs by adding materials LbL, by using a virtual Computer Aided Design model to create a physical object, in this case micron-sized needles [124]. 3D printing technology can use photopolymerization, in which UV-sensitive polymers are used and are layer-wise cured, allowing the construction of needles. 3D printers commonly used for printing thermoplastic materials include fused deposition modelling, as reported for the fabrication of poly(lactic acid) MNs [125]. It was also reported the 3D printing by stereolithography using a biocompatible resin [113,114].

Scaling up the manufacturing processes of MNs remains one of the biggest challenges of the pharmaceutical industry and process design is crucial to achieve standardization and cost-effectiveness. The aforementioned technologies display several advantages and constraints. If, in one hand, lithographic processes enable the preparation of highly complex shaped structures, the fact that is only applied to photo-curable polymers, is time-consuming and involves panoply of steps, can make it

unattractive for industrial application. On the other hand, centrifugal lithography or droplet air-blowing enable both shape forming and solidification at the same time under mild conditions, reducing the preparation time and technology needed. Nevertheless, post-processing might be required, and this approach only works with polymers within a certain viscosity range. Indeed, with the advent of 3D printing, characterized by an inherent flexibility in fabricating complex structures, it is expected a more rapid development of these microstructures. In brief, the successful translation of methodologies to manufacture MNs at an industrial level will depend on several factors, mainly on the nature of the material, stability of the active compounds, and the facilities required. In general, these core technologies have potential to ensure commercial-scale application, but their scale-up will always demand an adjustment and optimization of variables.

1.2.4. Mechanical properties

For MNs technology to become a reality, it is imperative to investigate the influence of a variety of factors related with their properties [126–128]. In general, the main factors affecting skin insertion ability of MNs are needle geometry such as shape, aspect ratio, and tip radius. During skin insertion, MNs suffer the influence of compressive, buckling, free bending and shear forces, as well as skin resistive forces [128]. Therefore, since MNs experience a wide range of stress, particularly during insertion and removal, they must possess inherent strength to avoid failure, namely by bending, buckling and fracturing [36,129].

In this vein, mechanical evaluation of MNs is performed in order to infer about their efficiency and safety prior to use. The first mechanical characterization of MN arrays was described by Zahn *et al*. [129], through the evaluation of the breaking strength of a single needle. In brief, this test consisted of a single, hollow silicon MN and a mechanical force gauge that gradually increased the vertical force applied at the tip (0-20 g) until it fractured. Since then, several tests have been employed to characterize the mechanical properties of MNs.

To infer about the mechanical properties of MNs, three tests can be performed, namely the axial and transverse fracture force tests and the three-point bending test. The evaluation of the axial force involves applying a force perpendicular to the baseplate. This test records both displacement and force while the MNs are pushed against a hard surface at a defined rate (Figure 1.5 (a)) [130–132]. When MNs fracture, a sudden decrease in the force *vs* displacement curve is observed. Needle failure force is determined by the maximum force detected immediately before this drop [130,131].

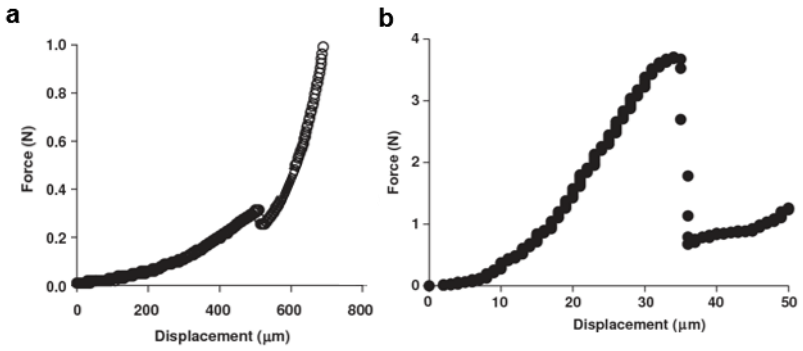

Figure 1. 5. Force (N) versus displacement curves of MNs regarding (a) axial force test and (b) transverse force test [130].

This test should be regarded with caution as some of the reports only use a single MN [128,129] and the failure force of a MN array cannot be strictly correlated with that of a single structure. Furthermore, this test does not fully simulate the forces experienced by the needles when inserted into the skin. Instead, they are compressed against a hard surface, which results in a concentration of the forces at the tip of the needles, whereas during the penetration into a soft tissue the forces are distributed over a larger area [132]. The transverse fracture force test evaluates the behavior of MNs during insertion. Because of skin surface irregularities and its natural elasticity, the MNs arrays are not completely inserted and the transverse bending of the needles can be detected [130,131]. A mechanical test station is used, and a force is applied to the MN *y*-axis at a defined point of the needle shaft. As aforementioned, a sudden drop in the force-displacement curve defines the MNs failure [130,133] (Figure 1.5 (b)). The main limitation of this test is the need to manually align the metal probe with a defined length [133]. Even when this task is performed with the aid of a microscope camera, it still leads to experimental inaccuracies [130].

In addition to the mechanical testing of the MNs themselves, evaluating the baseplate is also important as the fracture of this component during patient application is not acceptable. Thus, this structure needs to be flexible enough to conform to the topography of the skin without fracturing. To evaluate the baseplate strength and flexibility, a three-points bending test has been employed. The texture analyzer uses a metal probe to apply forces to the baseplates placed between two aluminium blocks. In this case, a maximum peak observed in the force-distance curve represents the force required to break the baseplate. The baseplate bending upon fracture is also determined to evaluate the flexibility of this structure [133].

Prediction of the mechanical failure is analogous to the theoretical approaches for columns, and predicting the force load that causes a column to buckle is traditionally performed by numerical or finite element analysis [134]. After skin penetration MNs can

undergo failure through buckling and yield failure and the developed theory applies to any column whose cross-sectional variation can be written as a function of the axial coordinate [379]. MNs critical buckling load can be simulated during an axial force load, accordingly to previously reported analytical methods of Smith [134,135]. Considering the fixed-free case, where the MN base is fixed in position and the tip can freely move, the MNs can be modelled using the following equations for a square-base pyramidal (P_{cr1}) and conical geometry (P_{cr2}):

$$P_{cr1} = E[120\{H_2(H_2^2(H_2 - 2H_1) + 2H_1^3) - H_1^4\} + \pi^2\{20(H_2(H_2^2(-H_2 + H_1) - H_1^3) + H_1^4) + \pi^2(H_2(H_2(H_2(H_2 + H_1) + H_1^3) + H_1^4)\}]/(240\pi^2L^2)$$

$$P_{cr2} = E[120\{R_2(R_2^2(R_2 - 2R_1) + 2R_1^3) - R_1^4\} + \pi^2\{20(R_2(R_2^2(-R_2 + R_1) - R_1^3) + R_1^4) + \pi^2(R_2(R_2(R_2(R_2 + R_1) + R_1^3) + R_1^4)\}]/(80\pi^2L^2)$$

Where *E* is the Young's modulus, *L* is the needle length, H_1 and H_2 are MN widths at the base and tip, respectively, and R_1 and R_2 are MN radii at the base and tip, respectively.

The critical load for these structures needs to be superior than the penetration force required for the MN to penetrate skin without undergoing mechanical failure The significance of this simulation values can be used to determine the safety factor. Defined as the ratio of failure force to insertion force, this parameter should be well above unity to ensure mechanical strength to insert skin without breaking [128].

Apart from the assessment of the mechanical properties of MNs, it is important to study the force required for MNs skin insertion. In this vein, Davis *et al.* [128] determined that about 0.058-0.34 N.needle^{-1} were needed to ensure skin insertion of metal MNs in human volunteers. This data confirms the feasibility of manual insertion. Using hollow silicon MNs, the insertion forces were estimated to range between 0.10 N for the sharpest needle to 4.15 N for MNs with a blunt tip [36]. Furthermore, using ultra-sharp MNs, the insertion force can be reduced to below 10 mN [136]. On the other hand, Lhernould *et al*. [137] fabricated polymeric-based MNs using polycarbonate and confirmed that to ensure successful skin insertion, a maximum force of ~0.15 N.needle^{-1} is required. Regarding MNs application, their success is determined by the ability to penetrate through skin.

To evaluate skin penetration, transepidermal water loss measurements (TEWL) can be performed [138]. Microscopic techniques are also useful, either by application of a dye (Figure 1.6 (a)) over the perforated skin surface [131] or by cross-sectioning and histological examination (Figure 1.6 (b)) [41].

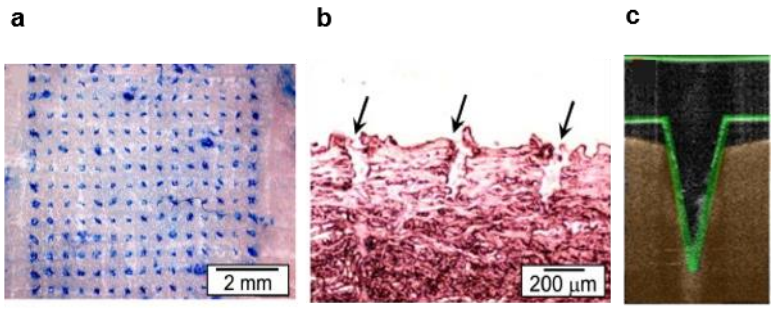

Figure 1. 6. Skin penetration visualization using (a) dyes, (b) hematoxylin eosin staining [139] and (c) optic coherence tomography [140].

Concerning the histological procedure, the preparation of samples might change the aspect of micropore structure. As a non-invasive methodology, optic coherence tomography (Figure 1.6 (c)) is useful, enabling the determination of pore diameter and depth [140]. The insertion studies are usually performed using biological tissues, either from humans or other animals like pigs or mice [141,142]. Notwithstanding the value of using biological materials, there are some constraints associated with the fact that the skin is usually heterogeneous, unstable, can be difficult to collect and its use must strictly comply with regulations for the use of human or animal tissues [143]. Therefore, Larrañeta *et al*. [144] reported the use of Parafilm® as a model membrane to simulate skin insertion. These authors folded the polymeric membrane into an eight-layer film to approximate skin thickness. Then, when comparing the insertion using neonatal porcine skin, the insertion depths were lower for Parafilm® but proved to be useful as an alternative to biological tissue for MNs insertion studies.

In sum, to ascertain the mechanical properties of MNs, a variety of tests can be performed. At the same time, the diversity of needle geometry and size coupled with the assortment of tests makes the comparison between MNs quite difficult. In this case, MNs technology and development would benefit from standardization of procedures to evaluate their mechanical performance.

1.3. Biopolymer-based MNs

A wide range of polymers derived from biological systems, *i.e.* biopolymers, such as polysaccharides (*e.g*., HA [59,78,123,145–177], sodium chondroitin sulphate [178–183], cellulose [62,184–198], chitin and CS [199–208], starch [139], dextran [209] and PL [210]), proteins (*e.g*., Gel [61,64,211–217], silk [116,218–225], collagen [226,227], suckerins [66] and zeins [65,228]) and DNA [229], have been employed in the fabrication of MNs. These have been directly used in their native form, after chemical modification

(*e.g.*, methacrylated hyaluronic acid [230] or c-GelMA [217], carboxymethyl cellulose (CMC) [61,159]), alone, as blends or composites.

Polysaccharides and proteins play a paramount role in the development of MNs and these two classes of biopolymers share some chemical similarities with the components of extracellular matrix and are easily recognized and accepted by the human body [10]. After absorption, they follow elimination by metabolism or excretion through the renal system, considering that they are below the glomerular threshold, avoiding tissue accumulation [11]. In this sense, polysaccharides and proteins used in MNs development are either approved by the FDA (US Food and Drug Administration) or classified as GRAS (generally recognized as safe) [231,232]. Polysaccharides and proteins exhibit a great structural diversity and many inherent properties, which influence the mechanical properties and penetration ability of MNs and determine the bioactivity and stability of the pharmaceutical ingredients [135,233,234]. Specific properties such as polymer MW, swelling behavior, and possible interactions between the biopolymer and the drug will influence and tailor drug release rate [11,17,235]. Naturally, these myriad features influence their behavior and polysaccharide and protein-based MNs can be grouped into dissolvable, biodegradable and swellable devices, as summarized in Table 1.1 and discussed in the following paragraphs.

Table 1. 1. Advantages and disadvantages of dissolvable, biodegradable and swellable polymeric MNs [8].

MNs	Advantages	Disadvantages
Dissolvable	Dissolves within short periods allowing a fast drug release Increased drug loading by encapsulation or coating Precise drug loading	Patients need to wait for complete dissolution before removing the patch
Biodegradable	Usually employed for sustained drug release Increased drug loading by encapsulation or coating Precise drug loading	Polymer residues can be detected in skin after few days
Swellable	Allows attachment of drug reservoir Intact removal from skin Softness precludes reinsertion after removal Leaves no measurable polymer residue behind Treatment can be stopped if necessary	Limited drug loading into the polymeric matrix Crosslinking conditions may affect bioactivity of drugs

Dissolvable biopolymeric MNs are fabricated using water-soluble macromolecules which dissolve after skin insertion [8], namely dextran [234,236], HA [59,78,93,116,123,130,145–177], sodium chondroitin sulphate [178–182], Gel [61,64,211,213–216], a collagen-enriched extract from fish scales [226,237,238] or dissolved silk fibroin [61,64,211–217]. In general, the array dissolves within several seconds or minutes upon skin insertion.

The fast dissolution is accompanied by the quick release of the pharmaceutical agents, which makes them suitable for instant drug release [135,233,234]. Considering different molecular weights of the same polymer or other components can tailor the dissolution profile. Hence, dissolution matrices amenable for prolonged DD can also be fabricated [176]. Dissolvable MNs are poised to provide a beneficial route to the administration of biopharmaceuticals in the lower-microgram range, in smaller doses than those administered using injections, reducing not only the systemic effects but also the treatment costs [175]. Additionally, because the drug formulation is incorporated as part of the dissolving matrix, drug loading and release is precise. Owing to this, the patch is only removable after full needle dissolution.

Biodegradable MNs are fabricated using polysaccharides and proteins that degrade after skin insertion [225,239]. The term biodegradation refers to the degradation process that takes place in a biological environment, in this case, inside the body under the influence of enzymes [240]. Usually, mechanisms of biodegradation may require a gradual breakdown of the material which is a longer process when compared with that of dissolvable MNs. Therefore, biodegradable MNs are very attractive for sustained DD. One of the major features that convey significant impact on the capacity of these biopolymers to be used in biomedical devices is their relative degradation rate, that can be modulated to provide flexibility in drug release [225,239].

Non-water soluble polysaccharides and proteins such as chitin [199], CS [200–202,207,208,241], starch [139,183] and silk [21,116,199,208,218,219,225] are the most used. More recently, suckerins, proteins extracted from squids, were also studied in the fabrication of biodegradable MNs [66]. Regarding the biodegradation ability of MNs, Yin *et al*. [224] evaluated the enzymatic degradation of modified silk MNs *in vitro*. To mimic the ISF, collagenase I and protease XIV were added to phosphate buffered saline (PBS). After incubation using protease XIV for 10 days, silk MNs modified using 2-ethoxyethanol displayed more than 65% mass loss.

Regarding swellable polysaccharide and protein MNs, these are fabricated using crosslinkable hydrogels which due to their crosslinked structure, swell in the skin without dissolving [224,230]. On behalf of this feature, these biopolymers allow not only the release of preloaded drugs but also the extraction of ISF [242]. To create swellable MNs it is reported the use of methacrylated HA [230] and c-GelMA [217,243] and modified silk [224]. Compared to the aforementioned types of MNs, these deposit no tip materials in the skin and have flexibility to stop the treatment if adverse drug reactions or overdose occur [244]. Typically, the swelling ability of these biopolymers is controlled by their crosslinking degree, which in turn tailor the drug release rate [245]. It is important to highlight that these MNs should have sufficient mechanical strength in the dry state to

allow penetration into the *SC* and partially retain this toughness in the hydrated state, in order to enable the intact removal from the skin.

According to their performance *in vivo*, polysaccharide and protein MNs are employed in the TDD of small molecules, nanomedicines (*e.g.* nanocapsules) and biotherapeutics (*e.g.,* proteins, peptides or vaccines). Polysaccharide and protein-based MNs are designed to meet the properties of their cargos enabling DD through bolus or sustained administration. The pharmaceutical ingredients can be incorporated into the MN matrix, namely the tips, base or backing adhesive layer, or coated onto the surface of the structure. To control drug release, drugs can also be preloaded into nanoparticles which are then encapsulated in the matrix [7,8,31,32]. Besides drug administration, biopolymeric MNs have also been studied in ISF extraction for diagnosis and lastly, for cosmetic purposes [8]. The next sections will give an overview of the main polysaccharide and protein-based MNs described in literature (Table 1.2 and 1.3), with focus on their applications usefulness and challenges for potential clinical application.

1.3.1. Polysaccharides-based MNs

The recent trend of using polysaccharides in the preparation of biobased materials has naturally been extended to the fabrication of MNs [246]. In fact, polysaccharides like HA [59,78,93,116,123,130,145–177], CS [60,200–202,207,208], and dextran [234,236], among others [181,182] have been used alone or combined with other biopolymers [62,135,159,176] to engineer MNs for the delivery of drugs, such as doxorubicin [155] and lidocaine [247], biopharmaceuticals, such as insulin [139,160,213] or vaccines [166], and also natural extracts [166]. The next sections give an overview of polysaccharides used in MNs. Table 1.2 highlights some of the most recent examples of polysaccharide-based MNs reported in literature in terms of basic components, pharmaceutical ingredients and outcomes of their application.

Table 1. 2. Overview of polysaccharide-based MNs for the delivery of active pharmaceutical ingredients

Biopolymer(s)	Other components	Pharmaceutical ingredient	Outcome	Reference
Hyaluronic acid		All-*trans* retinoic acid, ovalbumin, tetanus toxoid- and diphtheria toxoid	Good stability of MNs; storage for 12 months induced immunological responses.	[59]
		Tuberculin purified derivatives	Induced an immune response; useful in tuberculosis diagnosis.	[123]
		5-Aminolevulinic acid (5-ALA)	5-ALA MNs displayed superior tumor inhibiting effects at a lower dose in a shorter application time than 5-ALA solution.	[165]
	Carboxymethylcellulose as baseplate	Caffeine	Lipolysis improved significantly after 6 weeks; weight loss of about 12.8 ± 0.75% in high-fat diet-induced obese mice; significant anti-obesity activity of MNs.	[172]
		Enterovirus 71 virus-like particles	Immunization induced high levels of antibody responses, comparable to intramuscular injection; enterovirus conferred protection against hand-foot-and-mouth disease.	[173]
	Nanostructured lipid carriers using compritol, labrafil	Nile red	Successful delivery system for lipophilic compounds.	[174]
		IgG (Immunoglobulin G)	Protein tertiary structure was preserved; more than protein was 80% recovered.	[175]
	Amylopectin	Niacinamide and ascorbic acid	Potential to be used in cosmetics due to its anti-oxidant activity.	[176]
		Adenosine	Displayed better or comparable results relative to cream application.	[177]
		Adenosine	Improved facial wrinkles when combined with cream.	[145]
		Glutathione	Glutathione was released without being oxidized; MNs were safe for skin whitening purposes.	[146]
		Mesoporous silica-coated nanoparticles incorporating small interfering RNA (siRNA)	Monitoring of gene expression and efficient gene silencing of target mRNA in the 3D cell model of abnormal scar.	[147]

Table 1.2. (cont.)

Biopolymer(s)	Other components	Pharmaceutical ingredient	Outcome	Reference
Hyaluronic acid		Rhodamine B	Ultrasonication and iontophoresis increases permeation, shortening the initial delivery time.	[148]
	Au nanocages loaded with drug	Doxorubicin	Photothermal effect of nanocages coupled with drug allowed tumor destruction.	[149]
		Doxorubicin-loaded transferosomes	Drug distribution in lymph nodes was enhanced, compared to epidermal diffusion; increased its bioavailability in plasma.	[150]
		Dermatophagoids farinae extract	Useful as allergen-specific immunotherapy method.	[151]
		Live attenuated *Bacille Calmette-Guerin* bacillus	Vaccination effects comparable to conventional injections; technology allows delivery of vaccine powders.	[152]
		Arginine/lysine polypeptide, acetyl octapeptide-3, palmitoyl tripeptide-5, adenosine, and seaweed extracts	25.8% decrease of fine wrinkles; 15.4% improvement of skin hydration; skin density and dermis thickness increased 14.2% and 12.9%.	[153]
		β- 3 -adrenoceptor agonist and thyroid hormone	White adipose tissue browning; suppression gain of body fat and weight in obese mouse models.	[154]
		PEGylated gold nanorod and doxorubicin	Good cell inhibition in epidermoid cancer; photothermal effect destroyed A431 cells.	[155]
		Ascorbic acid 2-glucoside	Sterility using e-beam irradiation maintained the dose and activity of the drug.	[156]
		Methotrexate	Attenuation of epidermal hyperplasia, reduction of IL-23 and IL-17; amelioration of psoriasis-like skin inflammation in mice; therapeutic effect at a reduced dosage compared with oral administration.	[157]
		Bleomycin	Inhibition of proliferation of human hypertrophic scar fibroblasts; TGF-b1 was significantly lower than that of the bleomycin solution group.	[158]

Table 1.2. (cont.)

Biopolymer(s)	Other components	Pharmaceutical ingredient	Outcome	Reference
Hyaluronic acid	Carboxymethyl cellulose and Amylopectin	Rhodamine B Niacinamide	Increased rhodamine permeability.	[159]
Hyaluronic acid	3-aminophenylboronic acid-modified alginate	Insulin	Insulin induced a sustained hypoglycemic effect in diabetic mice.	[160]
Hyaluronic acid crosslinked with *N*,*N*'-methylenebis(acrylamide)	Nanoparticles of dextran loaded with glucose oxidase and anti-PD1 antibodies	Anti-PD1 immunotherapy	Robust immune response in a single-administration using a mouse model; higher inhibition of tumor growth when compared to intratumor injection.	[78]
Methacrylated hyaluronic acid		Fluorescein, FITC-Dextran (3–5 kDa), and Doxorubicin hydrochloride	swelling ability was tuned by controlling the UV crosslinking duration; >80% of fluorescein, FITC-Dextran and >50% of doxorubicin were released within 30 min.	[161]
Hyaluronic acid crosslinked with 1,4-Butanediol diglycidyl ether		FITC-dextran	Delayed dissolution of MNs compared with pure HA MNs; slow diffusion of FITC-dextran release (60% against 100% at the end of 2 h.	[162]
Hyaluronic acid nanoparticles crosslinked with 2,2′ (ethylenedioxy) bis (ethylamine) (X-linked HA-NPs)		Rhodamine B isothiocyanate-dextran (RITC)-dextran	Slow release of RITC-dextran from X-linked HA-NPs; at 2 days (48 h), the intensity of the X-linked HA-NP-MNs was about two times stronger than the intensity of the free HA MNs.	[163]
Hyaluronic acid	Quercetin-dithiodipropionic acid-oligomeric hyaluronic acid (Que-DA-oHA) copolymers micelles	Curcumin	42.3 ± 3.2% and 70.8 ± 3.9% was released after 60 and 360 min of curcumin was delivered *in vitro*.	[164]
Hyaluronic acid		Green tea extract	Reduction of bacterial growth (95%) on wound infected sites, for both gram (-) and (+) bacteria.	[166]
Hyaluronic acid	Hyaluronic acid crosslinked with 1,4-butanediol diglycidyl ether	Hyaluronic acid	Delayed degradation of H to obtain a sustained drug release.	[162]

Table 1.2. (cont.)

Biopolymer(s)	Other components	Pharmaceutical ingredient	Outcome	Reference
Hyaluronic acid	Hyaluronic acid crosslinked with 1,4-butanediol diglycidyl ether	Hyaluronic acid	The ratio of crosslinked HA increased in HA, decreased the degradation rate; might be used as derma filler in cosmetic or anti-ageing treatment.	[167]
Hyaluronic acid		Ovalbumin and adenovirus vector	Immunization comparable to the conventional vaccination; improved responses to every soluble antigen like toxoids.	[168]
		Fluorescein isothiocyanate - dextran	Increased permeation of high molecular weight drugs.	[169]
		Insulin	Dose-dependent hypoglycemic effect; similar to subcutaneous injection.	[170]
		Magnesium ascorbyl phosphate (MAP)	Increased MAP delivery (96.8±3.9 $\mu g.cm^{-2}$) compared with the passive (44.9±16.3 $\mu g.cm^{-2}$).	[171]
Sodium chondroitin sulphate	Poly(vinyl pyrrolidone), lyotropic liquid crystal systems	Sinomenine hydrochloride	Sustained release for potential application on adjuvant arthritis.	[178]
	Poly(vinyl pyrrolidone)	Neurotoxin	Anti-inflammatory activity *ex-vitro*; cumulative release of neurotoxin of 96% in 4 h.	[179]
	Trehalose	Recombinant Staphylococcal enterotoxin B protein (rSEB)	High levels of specific antibody in mice; 100% protection against a lethal SEB toxin challenge; half-dose MNs provided only 60% protection.	[180]
		Capsaicin	Pharmacological activity comparable tp topical administration; Rapid local analgesic action.	[181]
		Insulin	Good dose-dependency response; maximum hypoglycemic effect observed at 1.7 ± 0.2 h for the fully-loaded tip and 1.5 ± 0.2 h for the partially loaded tip.	[182]
	Hydroxyethyl starch (tips)	Hepatitis B surface antigen (tips)	Same level of immunogenicity as a commercial vaccine; antigenicity was retained at 37 and 45 °C; 10% loss was observed after 6 months at 50 °C.	[183]

Table 1.2. (cont.)

Biopolymer(s)	Other components	Pharmaceutical ingredient	Outcome	Reference
Carboxymethyl cellulose		Recombinant human adenovirus type 5 vector encoding HIV-1 gag	Induces generation of long-lived antigen - specific cells at the mucosal surfaces.	[184]
		Valproic acid	Induces hair regrowth with higher accuracy when compared with topical formulations.	[191]
		(Anti-TNF-alpha-Ab)-HA conjugates	Applicable release profiles, to locally treat a broad range of inflammatory skin diseases.	[192]
		Insulin	Enhanced long-term stability and prolonged release kinetics.	[193]
	Dextran	BSA	Mechanical properties improved by the addition of dextran; better release from the CMC mixture than pure CMC.	[194]
	Amylopectin	Rhodamine B Ascorbic acid	Improvement of 3-fold permeability of rhodamine B and six-fold increase of ascorbic acid, when compared to topical administration.	[62]
		SARS-CoV-2 vaccines	2 weeks after immunization, significant responses were detected; stability of vaccine after gamma irradiation.	[190]
Hydroxypropyl methyl cellulose	Double hydroxides nanoparticles	Ovalbumin	Significantly strong antibody response; higher than with subcutaneous injection.	[195]
		Lactobacillus	Fast dissolution with no local tissue irritation; *Lactobacillus* were functionally bioactive *in vivo*.	[196]
	Carboxymethyl cellulose	Donepezil hydrochloride	More effective drug administration than via oral route; could replace the current treatment of Alzheimer's disease.	[197]
	Poly(vinyl alcohol) as back layer	Etonogestrel microcrystal particles	Steadier plasma levels when compared with intradermal injection.	[198]
	Poly(methylvinylether co-maleic anhydride)	Lidocaine hydrochloride	Fast onset time (<5 min) when compared with cream (100 min) but lower efficacy; stable for 3 months under 40 ± 2 °C and a humidity of 75 ± 5%.	[185]

Table 1.2. (cont.)

Biopolymer(s)	Other components	Pharmaceutical ingredient	Outcome	Reference
Hydroxypropyl methyl cellulose	Carboxymethyl cellulose, hyaluronic acid, poly (vinyl alcohol), poly(vinylpyrrolidone)	Polydatin	Improvement of *in vitro* permeation; polydatin complexes showed significant inhibitory effects on swelling of the ankle in the arthritic mice.	[187]
	Trehalose, maltose and poly (vinyl alcohol)	*Neisseria gonorrhoeae* vaccine antigen encapsulated into crosslinked albumin matrix	Significant increase in antigen-specific IgG antibody titers and antigen-specific lymphocytes in mice; all immunogenic epitopes are covered and preserved from degradation.	[188]
	Carbopol 971P NF	Triamcinolone acetonide	Oral patch increased the triamcinolone acetonide delivery by 42%; as attachment time increased, the amount of compound delivered was significantly greater when compared with conventional mucosal patches.	[189]
	Polyvinylpyrrolidone	α-arbutin	Comparing with the gel formulation, the MNs increase the delivery of α-arbutin about 4.7 times; MNs were able to keep the active substance at the application site.	[186]
Chitin		Purified protein derivative, mixture of antigens	Positive tests as a diagnostic tool.	[199]
Chitosan	Trehalose, poly(vinyl pyrrolidone)/poly(vinyl alcohol) as supporting system	Luteinizing hormone releasing hormone analogs, goserelin	Castration level was maintained for 2 weeks.	[200]
	β-sodium glycerophosphate and hydroxypropyl β-cyclodextrin	Levonorgestrel	Similar pharmacokinetic profile compared to oral administration.	[201]
	Poly(vinyl alcohol) + Polyvinylpyrrolidone (supporting array)	Ovalbumin	Low-dose ovalbumin (200 μg) induced higher immunization in rats than intramuscular injection of full dose (500 μg); high antibody levels were observed for 18 days.	[202]

Table 1.2. (cont.)

Biopolymer(s)	Other components	Pharmaceutical ingredient	Outcome	Reference
Chitosan	Poly(vinyl alcohol) + Polyvinylpyrrolidone (supporting array)	Influenza vaccine	Higher influenza virus-specific antibody levels induced by MNs than those elicited by influenza vaccine; MNs induced a immune-enhancing effect for 4 weeks and lasted for at least 16 weeks.	[203]
		Rhodamine B	Acid-Treated water-Soluble chitosan MNs enabled sustained rhodamine B release, in the course of dissolution for more than 72 h.	[204]
	Rhodamine + poly(N-isopropylacrylamide)	Vascular endothelial growth factor (VEGF)	MNs promote inflammatory inhibition, collagen deposition, angiogenesis, and tissue regeneration during wound closure.	[205]
	Sodium hyaluronate (tips)	Ovalbumin	Rapid release of antigens by dissolution of HA tips, priming the immune system; prolonged antigen release due to biodegradability of chitosan for 4 weeks; considerably higher immune responses in rats than a traditional two or double-dose subcutaneous vaccination.	[206]
	Magnetic graphene quantum dots + Polyethylene glycol	Lidocaine hydrochloride	Increased drug release from 25.7% to 96.4% using electrical stimulation.	[207]
		Bovine serum albumin	Sustained release for at least 8 days.	[208]
Starch	gelatin	Insulin	Delivery of the entire payload within 5 min.	[139]
Dextran		Poly-L-arginine	Dose-dependent immunoreaction; proposed as an alternative skin allergy device.	[209]
Pullulan		FITC-BSA Fluorescein sodium	Good protein stability; after 28 h, 1479 ± 364 $\mu g.cm^{-2}$ of fluorescein sodium and 1105 ± 123 $\mu g.cm^{-2}$ of FITC-BSA permeated through porcine skin.	[210]

Table 1. 3. Overview of protein-based MNs for the delivery of active pharmaceutical ingredients

Biopolymer(s)	Other components	Pharmaceutical ingredient	Outcome	Reference
Gelatin	Carboxymethyl cellulose	Insulin	Relative pharmacologic availability and relative bioavailability of insulin was 95.6 and 85.7%, satisfactory when compared with traditional injection.	[61]
			Reduction of subcutaneous fat at the site of MNs application; promotion of lipolysis and inhibiting lipogenesis.	[64]
	Calcium sulphate	Insulin	More sustained hypoglycemic effect when compared with subcutaneous injection.	[211]
	Carboxymethyl cellulose	Lidocaine	Increased lidocaine permeability, up to 4.8-fold, by combining MN and ultrasound pre-treatment studies.	[212]
	Carboxymethyl cellulose as back layer	Insulin	Gradual and moderate decrease of blood glucose levels.	[213]
	Sucrose	Inactivated polio vaccine	Vaccination of rhesus macaques induced a weaker serological response when compared to IM but with potential do eradicate poliomyelitis.	[214]
	α-calcium hemihydrate	Clonidine hydrochloride	Released of 55% of drug at a constant rate during the first 4h.	[215]
Gelatin crosslinked using genipin	Poly(vinyl alcohol)-coated poly(lactic acid) (supporting pedestal)	Insulin	Controlled insulin release; degree of crosslinking enhances the mechanical strength as well as humidity resistance.	[216]
Gelatin methacryloyl		Doxorubicin	Mechanical properties and drug release adjusted by the degree of crosslinking; sustained drug release up to 24 h.	[217]
Silk fibroin	Poly(vinyl alcohol) (supporting pedestal)	Insulin	Hypoglycemic effect with a maximum decrease in blood glucose levels of 64%, against the 54% achieved by injection.	[116]
		Rhodamine B	Prolonged drug release up to 8 days.	[218]
		Vaccines against influenza, *Clostridium difficile*, and *Shigella*	Provided evidence for dose sparing since the actual dose was lower than the coated dose.	[219]

Table 1.3. (cont.)

Biopolymer(s)	Other components	Pharmaceutical ingredient	Outcome	Reference
	Proline	Insulin	Insulin release is maintained up to 60 h.	[220]
	Phenylboronic acid/acrylamide	Insulin	Glucose-responsive MNs corresponded to the glucose change pattern; MNs retained its shape after 1 week.	[221]
	Poly(ethylene glycol) diacrylate and sucrose	Rhodamine B, indocyanine green and doxorubicin	Controllable release of therapeutic molecules by regulation of sucrose content.	[222]
	Poly(lactic-co-glycolic acid)		Mechanically adjusted and highly stretchable MNs; secure perivascular DD.	[223]
	2-Ethoxyethanol	Fluorescein isothiocyanate - dextran	Swellable system displaying 2-10 times higher transdermal delivery than films with identical drug loading.	[224]
		Tetracycline	Antibiotic-loaded MNs decreased the growth of bacteria (10-fold).	[225]
Fish scale biopolymer (mainly collagen)	cellulose nanocrystals	Lidocaine hydrochloride	Successful transdermal administration with drug permeation rate increasing from 2.5 to 7.5% after 36 h.	[226]
Collagen		Trypan blue	Loading capacity and the release rate depends on the size of the needle; the more heighted, the longer the time release.	[227]
Suckerins		Kanamycin	Efficient anti-bacterial activity, due to intrinsic antibiotic activity of suckerins coupled with kanamycin.	[66]
Zein		Ovalbumin	Lower bacterial penetration compared with hypodermic injection; coated ovalbumin was stable under storage at ambient and refrigerator conditions.	[65]
		Tamoxifen Gemcitabine	Coating of MNs results in greater deposition for tamoxifen; the poke-and-patch approach provided greater permeation for gemcitabine.	[228]

1.3.1.1. Hyaluronic acid MNs

HA is a major component of the extracellular matrix and cartilage with mucoadhesive properties [17]. This polysaccharide has negative charge and the salt form is highly soluble in water. In this vein, HA is mainly used in the fabrication of dissolvable MNs, as reported by Matsuo *et al*. [168]. Using MNs of 200, 300 and 800 μm in height these authors found that after insertion into mice and rats skin, the needle tips dissolved within 5 min and the body structure fully dissolved in 1 h (Figure 1.7) [59].

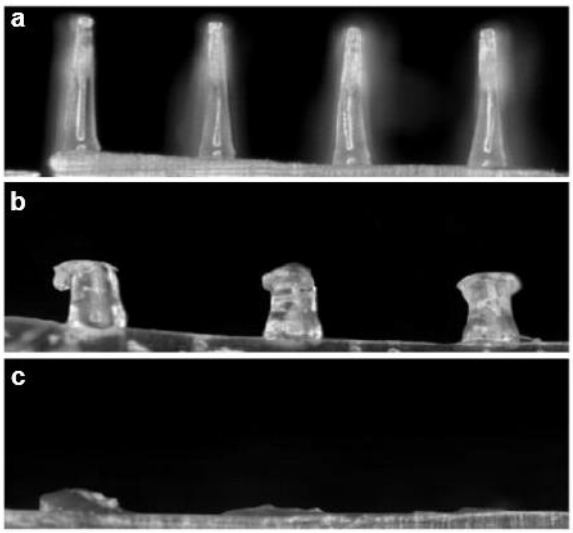

Figure 1. 7. Bright field micrograph of 800 μm hyaluronic acid microneedle arrays (a) before skin insertion and after (b) 5 and (c) 60 minutes [59].

Kang *et al.* [177] fabricated adenosine-loaded HA MNs for cosmetic purposes and found that 15 min after insertion into porcine skin the needles were fully dissolved, with a penetration depth of 92% the needle height. During a 10-week clinical test, the use of HA MNs improved skin wrinkling, density, elasticity and hydration when compared with the topical cream application.

Instead of incorporating the pharmaceutical ingredients into all the needle matrix, Liu *et al*. [248] studied the fabrication of tip-loaded HA MNs which dissolved within 30 seconds. In this work, the transdermal delivery of exendin-4, a glucagon-like protein-1 receptor agonist, which mimics the activity of mammalian hormone glucagon-like peptide 1, was studied and fluorescein isothiocyanate (FITC) labelled dextran was used for the permeability tests. *In vitro* studies showed an initial burst release during the first 30 sec and most labelled dextran was dissolved within 5 min. When comparing with subcutaneous injection of exendin-4 in type 2 diabetic rats, the MNs produced similar plasma concentration profiles and had comparable effects on glucose tolerance and insulin

secretion, indicating that exendin-4 loaded HA MNs can be used as an alternative for treatment of type 2 diabetes.

On a different perspective, Chen *et al.* [152] fabricated HA MNs that dissolved within 10-15 min. These needles were designed with a deep cave to pack directly live attenuated Bacille *Calmette–Guerin* bacillus (Figure 1.8 (a)), the only licensed vaccine for tuberculosis prevention. With this strategy, the vaccine powder was exposed to skin ISF (Figure 1.8 (b-c)), dissolved and diffused into skin. After 6 h it was spread into the epidermis and after 19 h most vaccine had diffused through skin (Figure 1.8 (d)).

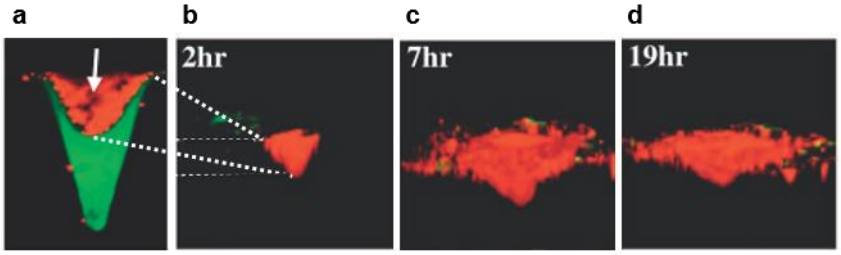

Figure 1. 8. Three-dimensional images of side view of MNs obtained by two photon confocal microscopy. (a) Integral microneedle with vaccine represented by the white arrow and (b) two, (c) 7 and (d) 19h after insertion into skin [152].

Overall, this study confirmed the successful delivery without inducing over inflammation. Additionally, vaccine's viability and the penetration ability of MNs was almost not altered during 60 days of storage at room temperature [152]. Accordingly to the World Health Organization (WHO), Bacille *Calmette–Guerin* vaccine is stable for at least two years when stored at 2-8 °C [249]. Despite the short-time stability of Bacille *Calmette–Guerin* into MNs, when compared with the conventional method, this study shows the usefulness of these devices in non-developed areas where cold chain storage is not possible, and the fast administration is the purpose. The authors opened new perspectives in this area of vaccine technology, showing that MNs are also useful for vaccine storage, with a universal methodology that simplifies fabrication and preparation [152].

Regarding the delivery of nanomedicines, Wang *et al*. [78] fabricated HA MNs with pH-sensitive dextran nanoparticles incorporating anti-PD-1 (aPD-1, antibodies that block the programmed death-1 pathway) and glucose oxidase (Figure 1.9).

The MNs matrix was fabricated using crosslinked HA by *in situ* photopolymerization of *N,N'*-methylenebis(acrylamide). The nanoparticles are composed of an acid-degradable polymeric matrix, fabricated by modified dextran (conjugated with ethoxypropene enabling substitution of hydroxyl to acetal group), alginate (a polyelectrolyte surfactant), glucose oxidase/catalase system and anti-PD-1. Hence, this system was applied towards a melanoma site with a simple administration. Dextran nanoparticles convert glucose into

gluconic acid, creating an acidic environment which then promotes nanoparticle dissociation and release of the antibodies (Figure 1.9 (a)).

These authors found that a single administration induces robust immune responses in B16F10 mouse melanoma (Figure 1.9 (b)). The release of anti-PD-1 was pH-dependent and glucose-mediated and the bioactivity of the antibodies remained at over 90% after one-month storage at 4 °C. This system did not induce any significant decrease in cell viability and skin recovered quickly, with no significant inflammation detected 2 days after administration.

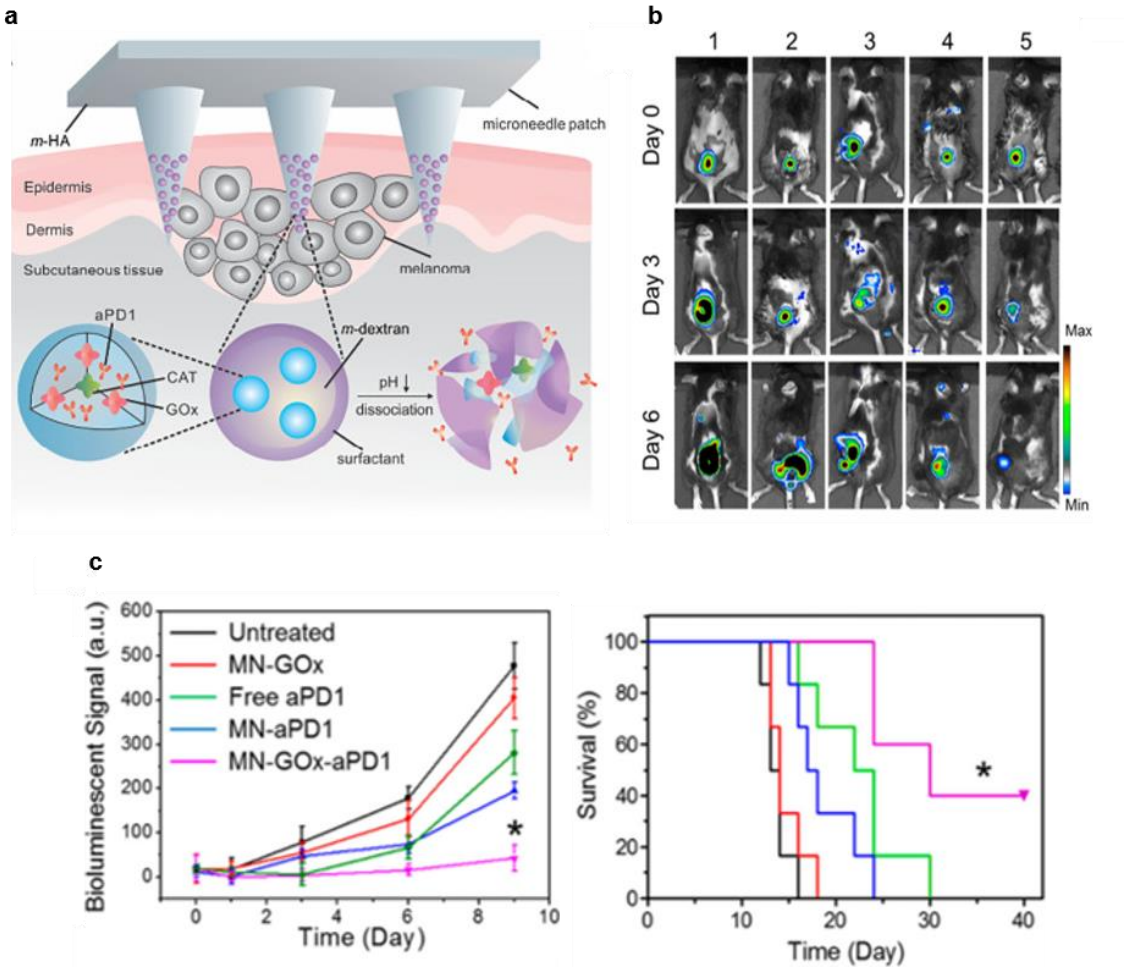

Figure 1. 9. (a) Schematic representation of MNs for skin tumor treatment. (b) *In vivo* bioluminescence imaging of the tumors of different groups indicated (1, untreated; 2, MN-GOx; 3, free aPD1; 4, MN-aPD1; 5, MN-GOx-aPD1). (c) Quantified tumor signals according to Kaplan - Meier survival curves for the treated and the control mice. Shown are eight mice per treatment group [78].

This work allows concluding that the antitumor ability of the MN patch is due to the sustained release of anti-PD-1 and the enhanced retention in a tumor microenvironment. Despite the incorporation of small molecules or biomacromolecules into HA MNs, the loading of cells was also studied. For instance, HA MNs loaded with adipose-derived stromal vascular fraction cells was evaluated on diabetic wound healing. Cell incorporation

resulted into an accelerated wound healing in porcine models when compared with HA MNs or the use of cells fraction alone. Therefore, the local administration of HA and derived cells using MNs may be an alternative method for treatment of wounds in diabetic patients [250]. From a different angle, to decrease the dissolution rate and increase the mechanical strength of HA MNs, Park *et al*. [176] introduced amylopectin into a MNs system designed to deliver model cosmetic ingredients, namely niacin and ascorbic acid. In this study, the mechanical strength of the MNs increased with increasing amounts of amylopectin added up to a ratio of 1:2.3 (HA:amylopectin). However, higher amylopectin contents led to stiffer and brittle structures, too difficult to peel off the mold without breaking. Dong *et al*. [149] fabricated HA MNs loaded with Au nanocages and doxorubicin. These Au nanoparticles were incorporated to reinforce the mechanical properties of the dissolving MNs and to make use of their excellent photothermal effect. Hence, this system initiates a photothermal effect after irradiation using near-infrared light, which coupled with the chemotherapeutic effect of doxorubicin, is able to synergistically destroy superficial skin tumors. Besides, to tailor drug release, Kim *et al.* [156] added trehalose and PVP to HA MNs and found that both additives could facilitate the release of peptides. It was also found that PVP may prevent peptide aggregation and enzymatic degradation, resulting in a more efficient diffusion of the drug into the systemic circulation.

Monkärë *et al*. [175] fabricated Immunoglobulin G (IgG)-loaded HA MNs, avoiding elevated temperatures or high pH. As a result, they found that about 82% of the protein was recovered and fluorescence microscopy unveiled that its tertiary structure was not changed after MNs fabrication. Liu *et al.* [170] found that storage of insulin-loaded HA MNs at −40, 4, 20, and 40 °C during a month did not altered the stability of the peptide, with more than 90% of insulin detected in the MN patches. Furthermore, the authors also found that insulin is rapidly released from MNs after storage. The complete dissolution and delivery of insulin-loaded MNs within 1 h and that MNs containing from 0.13-0.44 U of insulin promoted a decrease in glycemia levels from 43% to 88%, tuning the hypoglycemic response. In a different study, HA MNs incorporating *all-trans* retinoic acid (used as model compound due to its poor water solubility), dissolved almost completely in 2 h, delivering up to 90% of its content. During the first hour, only 76% of the *all-trans* retinoic acid was delivered and the structure was not completely dissolved. Then, to establish the stability of *all-trans* retinoic acid and tetanus toxoid/diphtheria toxoid divalent vaccine into HA MNs they were stored at different temperatures. Retinoic acid content was reduced to 78% after 1 week at room temperature (25 °C) and after 24 weeks the reduction reached 45%. On the other hand, during 24 weeks under refrigerated conditions (4 °C) a decrease of 13% was observed. Regarding the tetanus toxoid/diphtheria toxoid vaccine, the MN arrays were stored during 6 and 12 months at 4, 25 and 40 °C in heat-sealed aluminium laminated sachets. After

vaccination of rats, both anti-tetanus toxoid and anti-diphtheria toxoid titers were induced, showing that storage temperature did not affected the loaded tetanus toxoid and diphtheria toxoid and hence, the immune response [59].

In addition, HA MNs inhibited ascorbic acid 2-glucoside degradation after e-beam sterilization (40 kGy). HA MNs maintained their morphological features and fracture force after sterilization and did not affect the dissolution rate and drug release of HA MNs. Furthermore, sterilization could effectively reduce microorganism and endotoxin contamination levels. This work shows the potential in using HA as a biopolymeric matrix which offers the advantage of allowing the sterilization requirements without activity loss of encapsulated pharmaceuticals [156].

Besides the incorporation of other polymers or particles, the functionalization ability of biopolymers is evidenced by a study reported by Wang *et al.* [8]. In literature, the development of swellable MNs using methacrylated HA for timely metabolic analysis (Figure 1.10 (a)) is reported [78].

This chemically modified biopolymer was prepared by reaction of HA with methacrylic anhydride followed by crosslinking of the methacrylated moieties by radical polymerization under UV light at different times, from 3, 5, 10 to 15 min. Methacrylated HA MNs showed full skin insertion after being pressed with 1.5 N into porcine skin. The patch was removed intact from skin and only a slight deformation of MNs was detected, as a result of swelling. The swelling speed of these MNs is similar (Figure 1.10 (b)). They swell visibly within the first 5 sec and reach a plateau within 1 min, regardless of the previous UV exposure time. Nevertheless, the swelling ratio provided different results and the lower the crosslinking degree, less liquid is extracted by the patch. For example, MNs prepared with 3 and 15 min of UV exposure were able to extract liquid as nine and two times its own mass, respectively as a reflex of the increasing network density. In addition, a lower network density is related with an easy recovery of the extracted fluids from the MNs. After insertion into mouse skin *in vivo*, the patches were able to extract 1.4 mg of ISF after 1 min and about 2.3 mg after 10 min. Furthermore, 30 min after removal, the skin spots were recovered indicating decreased potential of infection. Still, despite deformation by liquid absorption, all MN arrays were able to retain shape and left no residual waste in the skin. Hence, this study was an important contribution to demonstrate the possibility of ISF extraction using MNs since this fluid makes up to 45% of the volume fraction of human skin (Figure 1.10 (c) and (d)).

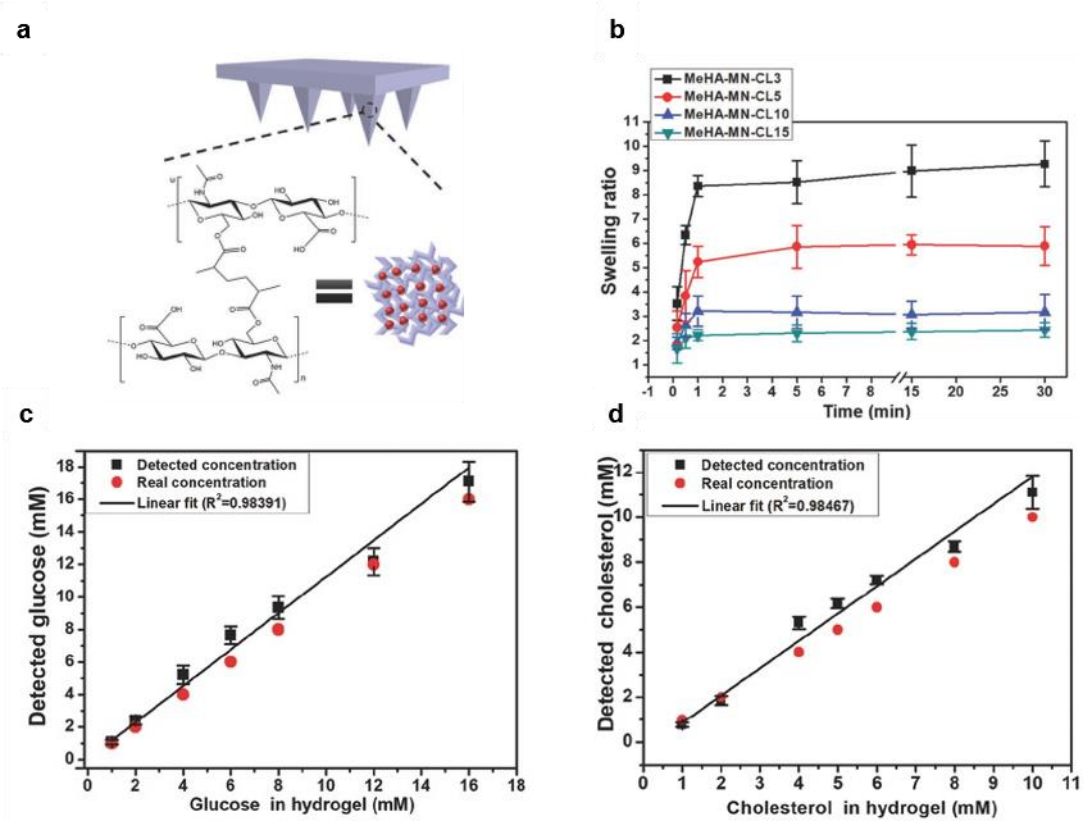

Figure 1. 10. Swellable MNs fabricated using methacrylated hyaluronic acid. (a) Schematic representation of the crosslinked network. (b) Swelling behaviour of methacrylated MNs with time. (c) Correlation of the real glucose concentrations in hydrogel with the calculated values based on extraction and the recovery using 10 krpm centrifugation for 5 min. The dots were fitted as line with R^2 = 0.98391. (d) Correlation of the real cholesterol concentrations in hydrogel with the calculated values based on the extraction and the recovery using 10 000 rpm centrifugation for 5 min. The dots were fitted as line with R^2= 0.98467. *P < 0.05 [230].

Crosslinking HA using 1,4-butanediol diglycidyl ether tailors the degradation and swelling ability of HA MNs, modifying drug release [162,167]. MNs formulated with crosslinked HA are proposed to delay drug release. HA solutions are highly viscous solutions and MNs display no permanent swelling behavior due to its water-soluble character whereas crosslinked HA forms an hydrogel in water that lasts longer after swelling due to retarded enzymatic degradation [162]. Zhang *et al*. [167] formulated HA MNs with HA particles crosslinked using 1,4-butanediol diglycidyl ether. The incorporation of HA particles improved the MNs mechanical strength and decreased the degradation of the matrix by enhancing the *in situ* swelling ability. A different methodology was described by Larrañeta *et al*. [251] who prepared hydrogels using HA and Gantrez S97, a copolymer of methyl vinyl ether and maleic acid. The multiple acid groups of Gantrez, enable the establishment of ester bonds with HA hydroxyl groups. Hence, using methylene blue as a model molecule, these authors found that crosslinked HA MNs can sustain the release up to 2 days. Due to the antimicrobial ability of these hydrogels, these MNs are proposed to mitigate device-associated infections.

1.3.1.2. Chondroitin sulphate MNs

Sodium chondroitin sulphate is widely used in the fabrication of distinct biomaterials, and similarly to HA, is a component of the extracellular matrix and cartilage [17] and its salt form is highly soluble in water [61]. Regarding MNs fabrication, Fukushima *et al*. [61] studied the transdermal delivery of human growth hormone and desmopressin in rats using MNs fabricated with sodium chondroitin sulphate and dextran. In this study, the MNs performed similarly and the pharmacokinetic profile was characterized by a fast attainment of peak concentration at the first 15 min. Then, it was followed by a gradual decrease in human growth hormone plasma levels, with a terminal half-life of around 25 min. Upon application of both sodium chondroitin sulphate and dextran-MNs, these authors found a direct relationship between dose and concentration. Furthermore, drug bioavailability was about 95% in sodium chondroitin sulphate MNs and 73% in dextran MNs. When compared with the intravenous injection, human growth hormone displayed much shorter elimination half-life, of about 4 mins. Therefore, the increased terminal half-life of 25 mins upon MNs application is attributed to the absorption rather than to the elimination phase. Regarding desmopressin (1.07 kDa) delivery, sodium chondroitin sulphate needles showed an absorption phase half-life of 14 mins and the pharmacokinetic profiles were characterized by a peak concentration within the first 30 min. Also, a terminal half-life of approximately 2 h was determined. Regarding storage, these devices proved to be stable for at least 1 month under refrigeration or freezing conditions. Yukako *et al*. [60] studied the administration of leuprolide acetate (1.2 kDa) using sodium chondroitin sulphate MNs and reported a low bioavailability of the peptide. *In vitro* tests showed that the peptide was released within 3 min. Then, after application into rat skin, plasma concentration reached its maximum within 15 min. Nevertheless, the degradation rate of leuprolide acetate was very fast leading to only 32% of drug being bioavailable.

1.3.1.3. Cellulose-based MNs

CMC and (hydroxypropyl)methyl cellulose are cellulose derivatives widely used for biomedical purposes. These water-soluble polymers are mainly employed due to their ability as thickening, binding and stabilizing agents, and also due to their film-forming ability [252,253].

Kim *et al.* [197] reported the development of (hydroxypropyl)methyl cellulose MNs incorporating donepezil hydrochloride (an acetylcholinesterase inhibitor used in the treatment of Alzheimer's disease) in the needle tips. In this work, over 95% of the drug was delivered within 5 min of insertion and all MNs were fully dissolved in skin within 15 min.

Zaric *et al*. [184] prepared MNs using CMC and used sucrose as protein stabilizer. A recombinant human adenovirus type 5 vector encoding human immunodeficiency virus-1 gag, to generate robust antigen-specific $CD8^+$ T cells in the tissue, was also added. The MNs patch was able to dissolve about two-thirds in length within 3 min of application, which was appropriate for effective delivery of the virus onto the dorsal skin of mice. In this study it was shown that this type of vaccination leads to the production of antigen-specific $CD8^+$ T cells, validating the delivery efficiency of the MNs patch. In this case, the major problem in vaccine administration using MNs is overcome, since it is possible to maintain the immunogenicity of live vaccines after lyophilization or drying. These are retained at the mucosal sites and can quickly expand in response to locally released antigenic challenge. If these advantages are combined with the benefits of using MNs, namely easy storage and transportation, with no cold-chain requirements, increased safety as no sharp wastes generated, easy self-administration and patient compliance, these MNs can easily be translated into clinic applications. Using CMC MNs, the administration of probiotics was also evaluated using *Lactobacillus*. The effectiveness was supported by the production of lactic acid *ex vivo* in pig skin and *in vivo* in rats. This work demonstrates that the probiotics delivered by MNs were bioactive and functional in a pain-free manner and may improve local skin health and immune functions [196]. In a total different vein, Lahiji *et al*. [191] reported the fabrication of CMC MNs incorporating valproic acid to induce hair regrowth (Figure 1.11 (a)).

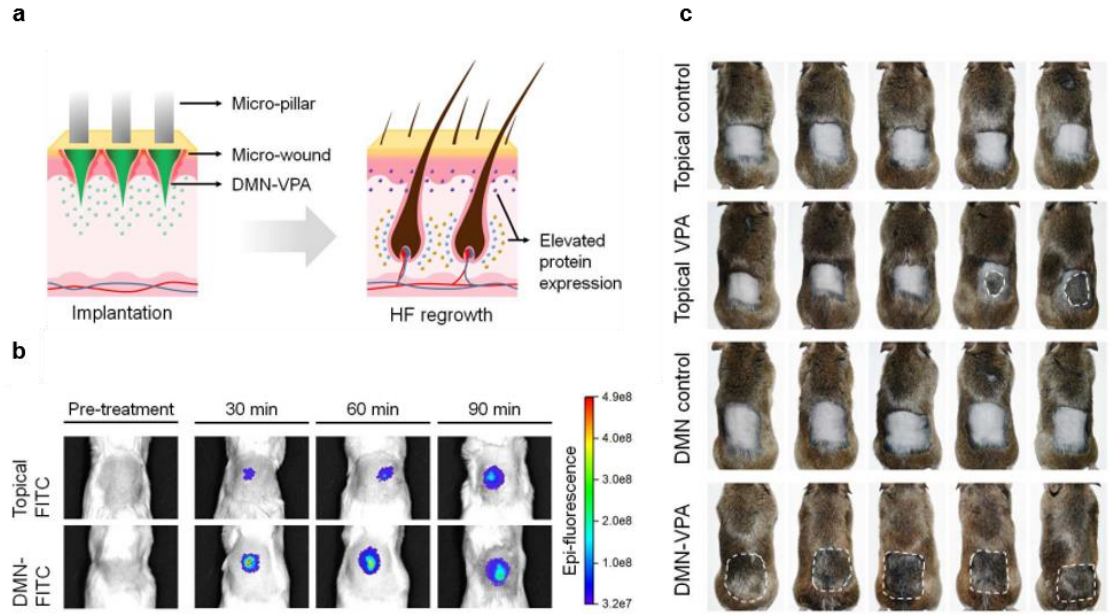

Figure 1. 11. (a) Schematic representation of MNs delivering valproic acid. (b) Fluorescence images of valproic acid delivery in mice. (c) Photograph of hair regrowth in mice [191].

After incorporation into MNs, the active ingredient showed no activity loss, proving to activate Wnt receptor cells, which are involved in initiating hair follicle growth. The cumulative release of valproic acid using MNs was higher and faster than using a topical formulation. About 120 min after application, 87% and 21 % of valproic acid was delivered using MNs and topical formulation respectively, showing the higher efficiency of valproic acid delivery using MNs. Finally, to evaluate hair- regrowth, valproic acid was administered into mice skin at telogen phase, once a day, for 28 days.

The results showed that at the last day of treatment, mice treated with valproic acid-loaded MNs and two (out of seven) treated with topical valproic acid evidenced hair regrowth (Figure 1.11 (b)). Using topical valproic acid, the hair regrowth mostly in the center of the shaved area, whereas the use of MNs led to a uniformly covered area, with high accuracy over the affected area. Consequently, more hair follicles were found on skin of valproic acid-loaded MNs (Figure 1.11 (c)). Overall, valproic acid-loaded MNs elevates hair follicles regrowth, accelerating telogen-to anagen transition, with clear evidence of not damaging the hair shafts or the epidermis layer.

The outstanding potential of CMC MNs is reflected by a very recent technological advancement in which the SARS-CoV-2 S1 sequence was incorporated, aiming to respond to the current coronavirus pandemic [190]. Dissolvable MNs were used to vaccinate mice with SARS-CoV-2 S1 subunit vaccines and 2 weeks after immunization, significant antigen-specific antibody responses were detected when compared to control. Furthermore, the immunogenicity of gamma irradiation sterilized vaccines was comparable to the non-sterile MNs, which supports the feasibility of CMC to deliver these vaccines.

1.3.1.4. Chitin and chitosan MNs

Chitin is the second most abundant natural polysaccharide, after cellulose, and by deacetylation originates CS, a polysaccharide widely studied for biomedical applications [199,208,241]. At slightly acidic aqueous conditions, CS possesses a high density of positive charges which enables tissue adhesion and mucoadhesion [254]. CS is degraded by hydrolysis of the acetylated residues and its degradation rate is correlated with the MW and its deacetylation degree [11]. Then, hydrolysis of sugar moieties by lysozyme, avoids CS accumulation in tissues [255]. In addition, FDA recognizes CS as GRAS and is approved for use in wound dressings and cartilage repair [232,256,257]. Furthermore, some CS-based formulations for DD are being studied in clinical trials [257]. Chitin and CS have also been used for the preparation of MNs for sustained DD. Jin *et al.* [199] prepared biodegradable coated chitin MNs arrays, for tuberculosis skin diagnostic test. Chitin MNs are mechanically robust and physiologically inert, water-insoluble and did not showed

significant swelling. Upon application to guinea pig skin, these MNs ensured the delivery of a mixture of tuberculosis antigens that gave a true-positive test, confirming the potential of using these MNs as a convenient diagnostic tool [199].

Chen *et al.* [208] fabricated biodegradable CS MNs for sustained delivery of bovine serum albumin (BSA). Using a homemade applicator these CS MNs were easily inserted into porcine skin and after 30 min a burst release of 20% BSA was detected. Then, in the following 8 days, a slower and sustained release was observed, with 95% of BSA released during this time. However, this study showed that CS MNs soften and break after insertion, leaving behind some polymeric residues that were detected in skin, in the 4 days after insertion. Regarding protein stability, circular dichroism revealed that both the fabrication procedure and storage were gentle enough to avoid denaturation of the model protein, which unveils the usefulness of using CS MNs to incorporate a myriad of biopharmaceuticals [208].

In a distinct study, Chen *et al.* [202] reported the fabrication of CS MNs to allow a sustained release of the model antigen ovalbumin (Figure 1.12 (a)).

This implantable system comprises a back layer of a synthetic polymer, poly(L-lactide-co-*D,L*-lactide), to overcome skin indentation during insertion and provide a more effective skin penetration. The needle tips are composed by ovalbumin-loaded CS. After insertion, the back-layer dissolves and the CS tips release ovalbumin (Figure 1.12 (b)). The micropores produced due to skin disruption were not detected after 6 h. Histological section of rat skin showed that the implanted MN tips became smaller with time and at the 28th day, there was still fluorescence of the Alexa-ovalbumin in the small MN tips. Considering the biodegradability of CS within 3-4 weeks, this study suggests that these devices can release antigens within a timeline of 4 weeks (Figure 1.12 (c)).

Regarding the *in vivo* release behavior, about 50% of the antigen was released from the MNs within the first two days and after 3 weeks little fluorescence was detected (Figure 1.12 (d)). In addition, CS MNs enabled immunization with a lower dose of antigen, decreased from 500 to 200 µg, a 2.5-fold reduction, when compared with conventional injection. These MNs induced a stronger immune response probably by prolonging antigen retention in skin. Overall, this system offers the benefit of guaranteeing the delivery of the intended dose into skin avoiding waste, providing useful option for long-term delivery of vaccines into skin. Interestingly, this study demonstrated immunization with one administration of non-living antigen, which is usually difficult with a single injection, as it usually fails to elicit robust and durable immunity.

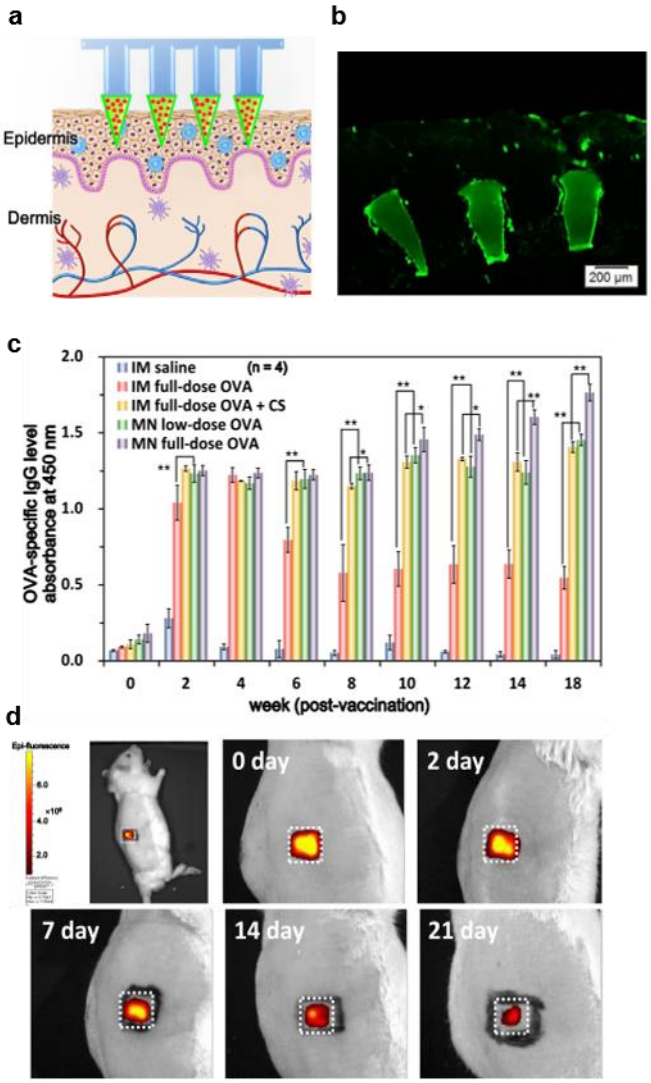

Figure 1. 12. Chitosan MNs with a dissolvable pedestal for ovalbumin delivery. (a) Schematic representation. (b) Fluorescence micrograph of the FITC-MNs after insertion. (c) Ovalbumin-specific levels of IgG after administration of MNs. (d) *In vivo* skin retention profile of ovalbumin [202].

On the other hand, using the same system, Chen *et al.* [200] delivered luteinizing hormone analogs, which is the current androgen-deprivation therapy used in the management of prostate cancer. After MNs application in mice, these authors detected an increase in serum luteinizing hormone levels which declined at day 7. Testosterone increased up to day 14 and then declined to at day 21, producing a castration state and proving the usefulness of these CS MNs into an androgen-deprivation state.

1.3.1.5. Starch-based MNs

Starch is a natural polysaccharide with a long tradition in the pharmaceutical industry [258]. Its ease of processing and filmogenic ability when gelatinized, make it attractive for the development of materials for biomedical applications [259]. In the development of MNs,

it was blended with other biopolymers due to its brittle behavior. Ling *et al.* [139] physically blended starch with gelatin to deliver insulin and found that MNs penetrated to approximately 200-250 μm, about one third of the needle length. In addition, they delivered the entire payload in the first 5 minutes and efficiently lowered blood glucose levels. Interestingly, it was found that more than 90% of the insulin was stable after storage 25 or 37 °C for one month. This indicates the convenience of using these starch MNs while reducing the cost of cold chain storage and transportation.

1.3.1.6. Dextran MNs

Dextran is a bacterial exopolysaccharide, mainly consisting of α-(1→6) D-glucose residues, with a few α-(1→2), α-(1→3) or α-(1→4) linkages. This highly water-soluble polymer is easily functionalized, allowing the easy tailoring of its properties. Dextran finds a wide range of applications in medical and pharmaceutical fields due to its biocompatibility and enzymatic degradability [260]. The fabrication of MNs by taking advantage of dextran as the main polymeric component is described in the preparation of a skin allergy test device (Table 1.2) [209]. For this purpose, poly-L-arginine, used as a model allergen, was incorporated into the dextran MNs and the proof of concept was performed in rats. After administration, a higher immunoreactivity was obtained when compared with the intradermal injection and the prick test. Immunogenicity was attained using lower antigen doses in MNs, which makes them economically superior when compared with prick test.

1.3.1.7. Pullulan MNs

PL is a non-ionic polysaccharide consisting of maltotriose units consisting of a unique linkage pattern with two α-(1→4) and one α-(1→6) glycosidic bonds. This hydrophilic linear polymer is commercially obtained by fermentation from *Aureobasidium pullulans* [261]. PL has an excellent film forming ability, coupled with a non-hygroscopic nature and good mechanical properties. Furthermore, the biocompatible nature and competitive economic value makes it an advantageous source of polymeric materials for biomedical applications, competing with the natural gums obtained from other plants and marine algae [262].

Very recently, Vora *et al*.[210] evaluated the preparation of MNs using PL and demonstrates their suitability in the transdermal delivery of model drugs (Figure 1.13).

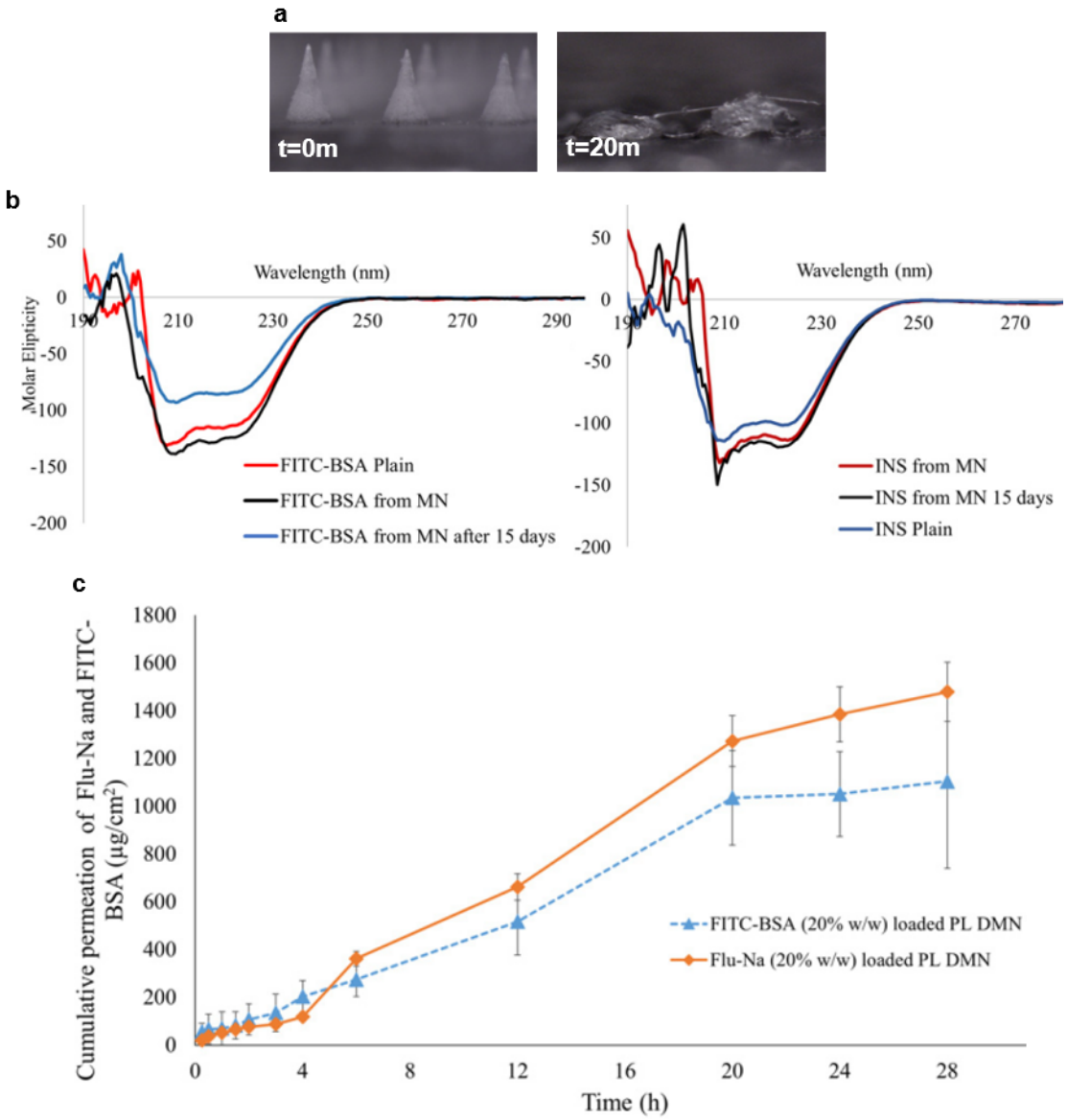

Figure 1. 13. (a) Digital micrographs of PL MNs dissolution at t=0 and t= 20 min following insertion into neonatal porcine skin. (b) Stability of secondary structure of FITC-BSA and insulin by circular dichroism. (c) *Ex vivo* cumulative permeation of FITC-BSA and fluorescein sodium across porcine skin (means ± S. D., n≥3) [210].

The incorporation of methylene blue, fluorescein sodium and fluorescein isothiocyanate (FITC)-BSA, produced MNs with sharp tips, which dissolved within 20 min (Figure 1.13 (a)). The polymeric matrix contributed to enhance storage ability of FITC-BSA and insulin, by preserving the structural integrity of both proteins, as shown in (Figure 1.13 (b)). Regarding the transdermal delivery of model compounds from the PL MNs, the superior molecular weight of FITC-BSA contributed to a lower release when compared to fluorescein sodium. By using a Franz diffusion cell apparatus, PL MNs were inserted into porcine skin for 28h and the authors concluded that 1479 ± 364 µg.cm^{-2} of fluorescein sodium and 1105 ± 123 µg.cm^{-2} of FITC-BSA were permeated (Figure 1.13 (c)). Owing to the biocompatible nature

of the polymeric matrix, this study demonstrates that PL may be used as a promising tool for the preparation of MNs.

1.3.2. Proteins-based MNs

Regarding protein-based MNs, these have been fabricated mainly with Gel [61,64,213] and silk [116,218,219,224] for the delivery of small drugs, namely lidocaine [226] and tamoxifen [65], and biopharmaceuticals such as insulin [211,213] and vaccines against influenza, *Clostridium difficile*, and *Shigella* [219]. Other proteins from animal source, particularly suckerins [66] and collagen extracts [238], are seldomly employed. A general overview of the proteins used in the fabrication of MNs is given in Table 1.3.

1.3.2.1. Gelatin MNs

Gel is a water-soluble biopolymer which results from the partial hydrolysis of collagen from skin, bones and connective tissue. Due to its highly conserved domains, Gel promotes cell adhesion with a non-immunogenic response, with relevance for biomedical purposes [263]. Regarding the fabrication of Gel MNs, An *et al*. [64] reported its use as the structural material and the component for biological activity. The intracutaneous delivery of Gel proved to locally reduce the adipose tissue. MNs were inserted into skin for 2 days and Franz diffusion tests showed that 70% of the dissolving polymer diffused through the skin layer. *In vivo* tests using rats showed that after application of Gel MNs the adipose tissue weight was reduced by 20% when compared with the control. In addition, the fat area was reduced by 60%, with clear evidence of adipocyte size reduction with subsequent shriveling. In particular, Gel administration is correlated with repressed transcription of lipogenic enzymes and an ability to reduce fat accumulation. Overall, this biopolymer was used not only as structural element of the MNs but also as the active agent which can regulate fat metabolism and have an active role in local reduction of fatty tissue. These MNs open new perspectives regarding the incorporation of other pharmaceutical ingredients such as anti-obesity active principles.

In another vein, Gel and sucrose based MNs were studied for the delivery of inactivated polio vaccine [214]. Gel MNs were able to penetrate pig and monkey skin and dissolved almost completely after 15 minutes leaving no residual sharp wastes (Figure 1.14 (a)).

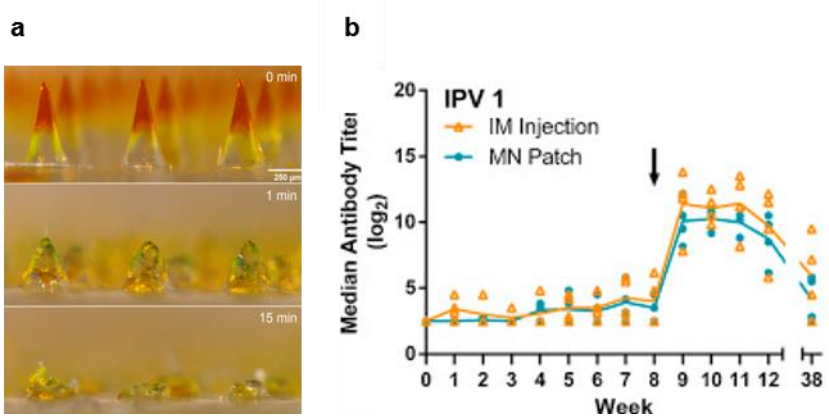

Figure 1. 14. (a) Gelatin MNs before and after insertion into pig skin. (b) Serologic response and neutralizing antibody titers to poliovirus following vaccination. Rhesus macaques were vaccinated at week 0 and week 8 with IPV given either by microneedle (MN) patch or intramuscular (IM) injection. Serum was collected weekly and analysed using a serotype-specific micro-neutralization assay. Each data point represents a single animal while the lines represent the median of each group. [214].

Inactivated polio vaccine administration showed that after the first week the neutralizing titers were weak. However, 100% seroconversion was achieved as reflected by the dramatically increase in the antibody titers (Figure 1.14 (b)). Therefore, using gelatin MNs for polio vaccination displayed immunogenic ability in rhesus macaques and may offer a simpler method for mass vaccination to facilitate polio eradication. As water dissolving matrices, Gel MNs dissolve quickly and different strategies have been studied aiming to control drug release. Yu *et al*. [63] prepared bio-ceramic MNs by adding hydroxyapatite to Gel in the formulation of the DD devices. These MNs exhibited low cytotoxicity against RAW 246.7 cells (murine macrophage cell line) and excellent cytocompatibility for maintaining biological activity of insulin. In the administration of insulin using these MNs the results showed that insulin concentration increases quickly and then declines slowly. On the other hand, the subcutaneous injection of insulin leads to a sharp increase of the plasma insulin concentration and then decreased. Hence, owing to the fact that plasma insulin level can be maintained for longer periods of time, insulin delivery is sustained. Using genipin as crosslinking agent in Gel MNs with a separable tip, Chen *et al*. [216] found that insulin delivery could be tailored (Figure 1.15).

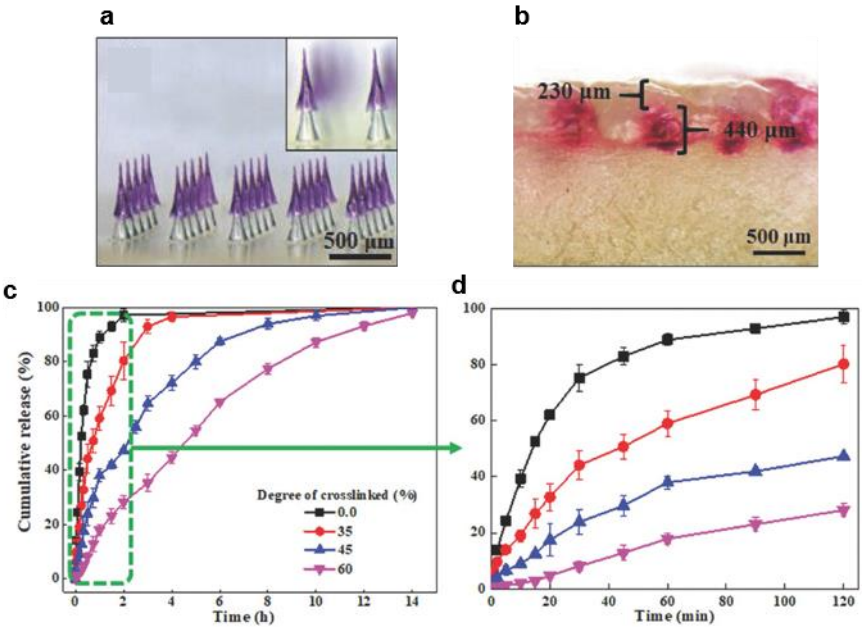

Figure 1. 15. Rapidly-separating gelatin MNs (a) before and (b) after skin insertion. (c) *In vitro* release of FITC-insulin and (d) cumulative release at the first 120 minutes [216].

The incorporation of PVA as a back layer allows the proper insertion and dissolution of Gel tips into skin (Figure 1.15 (a-b)). The increasing of the degree of crosslinking enhances the mechanical strength and the resistance to humidity. Furthermore, the *in vitro* (Figure 1.15 (c-d)) and *in vivo* insulin release tests showed significant changes in the release rates in MNs with different crosslinking degrees. The hypoglycemic effect in diabetic mice demonstrated that the higher crosslinking resulted in controlled insulin release compared with other treatments and prolonged effectiveness in virtue of genipin as a crosslinking agent for producing biocompatible MNs.

1.3.2.2. Silk fibroin MNs

Silk consists mainly of two proteins, *i.e.*, silk fibroin which constitutes the core of silk fibers, and sericin, hydrophilic proteins that coat these fibers. Silk fibroin is a protein approved by FDA for biomedical purposes, insoluble in water and characterized by *β*-sheet structure with high tensile strength and toughness [264]. Silk degradation occurs due to the action of proteolytic enzymes such as chymotrypsin, actinase and carboxylase. First, the protein is adsorbed by different enzymes through binding domains on the protein's surface. Then, after digestion, the amino acids are easily absorbed [265,266]. The interest in using dissolved silk fibroin, relies on the fact that this protein generates non-inflammatory products, which can be metabolized by cells [266]. In addition, this matrix possesses adjustable mechanical properties owing to its crystalline domains responsible for improving rigidity and therefore, the mechanical strength of MNs [267].

Regarding the preparation of MNs from silk fibroin, Raja *et al*. [21] studied the fabrication of a series of arrays with various shapes and sizes. Different strategies of drug loading demonstrated the ability of using silk fibroin to tailor DD. Loading BSA directly in the MN array enabled a sustained delivery of the compound, with only 0.4% being released after 16h of insertion. The maximum drug released was achieved using MNs loaded and coated with drug leading to more than 5 μg of BSA delivered in 3 h. After 16 h, almost 10 μg of drug was delivered from the MNs loaded and coated with drug. This study unveils the successful use of silk fibroin in tuning drug release and can be useful in providing a sustained administration of macromolecules.

On the other hand, Stinson *et al*. [219] reported the fabrication of silk fibroin MNs for vaccination purposes. These needles were coated with *influenza*, *Clostridium difficile*, and *Shigella* vaccine antigens, and silk fibroin to provide thermostability during drying and storage. After application into mice skin, humoral responses were generated confirming the successful delivery of antigens. Owing to the incomplete elution of the antigens from the patch, the specific IgG and IgA were lower than those obtained after injection with the same dose. Furthermore, these MNs combine the product stability and mechanical strength of coated insoluble microneedles. In this vein, silk MNs are well-suited for use as delivery system and may offer long-term potential for vaccination purposes.

Yin *et al*. [224] reported the fabrication of a swellable MN system based on modified silk fibroin. Herein, the authors prepared swellable MNs by blending silk with different low molecular agents (urea, glycine, dimethylformamide and 2-ethoxyethanol). The modified resulting silk fibroin MNs exhibited decreased dissolution abilities and an extraordinary swelling property. The 2-ethoxyethanol-silk fibroin MNs were the most promising ones, showing minimal dissolution, less than 10%, and a great swelling ability (500%) at a mixing ratio of 1:10 (w/w). These MNs successfully penetrated skin and after introduction into PBS it is possible to verify that there is a correlation between pore dimension and swelling ability. For instance, a swelling ratio of 650% can be achieved using a ratio of 0.5:10 (2-ethoxyethanol: silk fibroin) and using a ratio of 3.0:10, a swelling ratio of 250% can be achieved. To access the *in vivo* enzymatic degradation, these authors used protease XIV and collagenase I and found that there is a negative correlation between degradation and blending ratio. For instance, MNs fabricated with 0.5:10 (2-ethoxyethanol: silk fibroin) exhibited more than 65% mass loss within 10 days using protease XIV. This assay also shows that these swellable systems do not cause irritation or skin sensitization. Using these swellable silk MNs, the release of FITC-dextran was about 2-10 times larger than the corresponding control. In this process of drug administration, the porous dimensions play a critical role. Also, the release profile unveils that there is a direct relationship between releasing kinetics and swelling ability. Higher swelling MNs incorporating 40 kDa FITC-

dextran exhibited higher releasing kinetics than MNs with lower swelling degrees (250%) and incorporating 20 kDa FITC-dextran. Therefore, this type of system holds a huge potential in controlled delivery systems.

On a different perspective, DeMuth *et al*. [268] fabricated silk MNs for enhanced immunogenicity by loading a polyinosinic:polycytidylic acid vaccine into the silk tips. These silk tips were implanted into a MNs system with a dissolvable base. After dissolution the silk material remained in skin releasing the immunogenic agent, during two weeks. MNs loaded with a fraction of vaccine dose induced stronger $CD8^+$T cell proliferation, increasing percent $tetramer^+$ $CD8^+$ T cell proliferation. Furthermore, silk loaded tips led to increased induced 10-fold higher T-cell and humoral responses when compared with the intravenous injection.

1.3.2.3. Other protein-based MNs

Suckerins, are a group of proteins extracted from jumbo squid and characterized by containing a high content of *β*-sheets as building blocks which in turn, self-assemble into a supramolecular network. These proteins are reported to be useful due to their thermoplastic properties and solubility in weak acidic solvents [121,269,270]. Ding *et al*. [66] prepared MNs based on suckerins with good penetration ability (Figure 1.16 (a)).

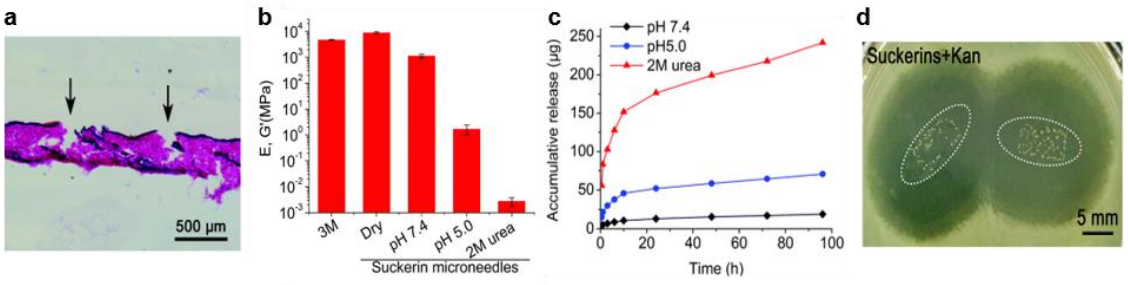

Figure 1. 16. Efficiency of suckerin MNs in DD. (a) Haematoxylin-eosin staining of rat skin showing skin breakage (arrows) after penetration. (b) Mechanical properties of suckerin MNs in different conditions obtained. (c) Accumulative release profiles of rhodamine B from suckerin MNs under different conditions. (d) Photograph of inhibition of *E. coli* exposed to kanamycin-loaded suckerin MNs [66].

Their mechanical strength can be tuned by a variation of pH or by the addition of a hydrogen bond disruptor, which tailor the secondary structure of these proteins and hence, their drug release ability (Figure 1.16 (b)). These authors were able to tailor the Young's modulus of suckerins-based MNs over nearly 6 orders of magnitude simply by incubation in different pH solutions or urea. This data suggests a direct relationship between Young's modulus and *β*-sheet content which is consistent with the load bearing functionality of nanoscale *β*-sheets. The authors took advantage of exploiting the easy of processing,

biocompatibility and *β*-sheet induced supramolecular self-assembly. A decrease in elastic modulus in MNs is associated with increased swelling and hence, chain mobility, inducing an increase in the mesh size of the polymeric network, which is then expected to increase the permeability for drug diffusion [66]. Using rhodamine, a fast drug release was observed in the first 10 h and after that a continuous sustained release was observed over time. With 2 M urea, up to 28% rhodamine was released after 100 h (Figure 1.16 (c)). After the incorporation of an antibiotic agent, kanamycin, a decrease in bacterial density was detected after MNs insertion (Figure 1.16 (d)). Regarding the biocompatibility, human dermal fibroblasts were selected for this study and upon contact they started to spread and continued to proliferate up to day 7 with almost no dead cells observed.

Fish scale biopolymer, a collagen enriched extract obtained from tilapia (*Oreochromis spp*.) has good film forming ability and a has shown to be a good candidate for preparation of MNs by micromolding. Olatunji *et al*. [238] reported the preparation of fish scale-based MNs showing that they can successfully penetrate porcine skin and dissolve over time. By mixing with cellulose nanocrystals, the dissolution of the needles was prevented and these were able to absorb up to 300% its own weight in water [237]. The incorporation of lidocaine into these composite MNs was successfully demonstrated in permeation studies. An increased drug permeation was observed for all four loading concentrations (2.5–10% w/w) and a pseudo steady state profile was observed for 5.0–10.0% w/w lidocaine MN loading after 30 h with an apparent flux shows increasing trends for 2.5–7.5% w/w after 36 h.

The fabrication of MNs using zein was recently reported. Zein is a plant-sourced protein which enables the preparation of glossy, tough, and greaseproof films with low water vapor permeability and resistance to microbial attack [271]. Zein enables the preparation of structures with good mechanical performance and therefore, good penetration ability. Using ovalbumin as a model antigen, Bhatnagar *et al*. [65] showed that microbial penetration was lower when administering zein MNs, when compared with hypodermic needles. Using ovalbumin coated or entrapped into the zein matrix, these MNs displayed efficient DD. Nevertheless, a higher dose of ovalbumin needs to be deposited into the needles to elicit a similar antibody response comparable with that of intradermal administration. Overall, these results support the convenient use and safety of zein MNs for transcutaneous immunization.

1.4. Mechanical properties of polysaccharide and protein MNs

Polysaccharide and protein MNs are frequently evaluated by the axial force test. Usually these MNs exhibit force-displacement curves with no discontinuity, which indicates no distinct transition point with indication of buckling failure. An overview of the failure force of polysaccharide and protein MNs is summarized in Table 1.4.

Table 1. 4. Failure force after an axial force load of polysaccharide and protein-based MNs.

Microneedle composition	Failure force (N.needle^{-1}) or maximum withstanding force	Reference
Hyaluronic acid	> 0.05	[154]
Hyaluronic acid	0.4-0.6	[109]
Hyaluronic acid	≈0.28	[59]
Sodium alginate	0.18 Transverse force failure 0.04	[130]
Cy5-loaded Hyaluronic acid	> 0.05	[154]
Epidermal growth factor-loaded-hyaluronic acid	0.63-0.78	[93]
Enterovirus particles loaded-sodium hyaluronate	>0.08	[173]
Ascorbic acid loaded-hyaluronic acid	0.059-0.161	[93]
Glutathione loaded-hyaluronic acid	0.25-0.40	[146]
Lysozyme loaded-hyaluronic acid	0.20	[272]
Hyaluronic acid crosslinked with *N,N*'-methylenebis(acrylamide) loaded with dextran nanoparticles	0.38	[78]
3-aminophenylboronic acid-modified alginate and hyaluronate crosslinked with calcium and loaded with insulin	0.37	[160]
Hyaluronic acid loaded with silica-coated nanoparticles incorporating small interfering RNA	0.08	[147]
Methacrylated hyaluronic acid	>0.15	[230]
Gelatin and calcium sulphate	0.4	[211]
Bullet shaped-gelatin	≈0.3	[64]
Conical shaped-gelatin	≈0.15	[64]
Chitosan	>0.2	[208]
Chitosan	≈0.25	[204]
Chitosan–magnetic graphene quantum dot	>0.16	[207]
Dextran with chitosan and beta-sodium glycerophosphate	Bearing pressure 60N	[201]
Dextran	Bearing pressure 90N	[201]
Carboxymethyl cellulose	0.032-0.048	[193]
Carboxymethyl cellulose	0.5-0.8	[109]
Fish scale biopolymer	≈0.12	[238]
Silk	24-54 g/needle	[218]
Silk before treatment After water vapor treatment	0.225 0.175	[21]
Zein Albumin-coated zein	0.45 0.53	[65]

The failure force, in this case, the axial fracture force, should be above the force needed for skin insertion to ensure proper skin insertion. Polysaccharide and protein MNs can have failure forces between 0.12 N.needle^{-1} for MNs fabricated with fish scale, a collagen-enriched extract, to 0.8 N.needle^{-1} for CMC MNs. As summarized in Table 1.4, most polysaccharide and protein MNs display a fracture force higher than 0.15 N.needle^{-1}. Considering that ~0.15 N.needle^{-1} are required for skin insertion, most biopolymeric MNs insert skin successfully. To determine skin insertion, the parameter of margin of safety is

usually determined to guarantee skin insertion MNs should be designed in order to increase this parameter [5,128]. However, when comparing biopolymeric-based MNs with the other materials, namely silicon, metals and ceramics, these display lower strength. In general, polymers have better toughness than glass and ceramics [5].

Apart from the materials choice, the geometry, aspect ratio and humidity also affect the MNs mechanical properties. In general, the polysaccharide and protein MNs prepared hitherto present two typical shapes: pyramidal and conical. In 2008, Lee *et al*. [135] found that CMC polymeric MNs with pyramidal shapes exhibited better mechanical strength than those with conical shapes, probably due to their larger cross- sectional area at the same base width/diameter. In addition, Gel MNs were fabricated into two different shapes, namely conical and bullet shape and after an axial force load, it was found that bullet-type MNs have higher mechanical strength. These microstructures preserve structural integrity with higher force loading and proved to be more suitable for insertion as they increase deliver of Gel when compared with the conical ones [64].

Also, the mechanical strength of MNs with the same shape could be further improved by increasing the base width/diameter, *i.e*. decreasing the aspect ratio [131]. Notwithstanding the important achievements reported by Lee *et al*. [135] and Park *et al*. [131] it should be noted that widening the MNs base to decrease the aspect ratio may result in inefficient skin insertion. In this vein, Chen *et al*. [208] reported that increasing tip sharpness facilitates skin insertion. Using pyramidal CS MNs with a tip radius of 5 μm these authors observed an insertion depth twice than that obtained with MNs with a tip radius of 10 μm. Also, MNs with the smallest aspect ratio exhibited the highest mechanical strength and the deepest insertion depth. Furthermore, these authors reported that there is no significant difference in mechanical strength for MNs with the same aspect ratio and different dimensions and that both shapes and aspect ratios are crucial in influencing the mechanical properties of the arrays.

Owing to the fact that the exposure of MNs to air humidity can influence their mechanical properties, Wang *et al*. [127] simulated the exposure of MNs to different relative humidity (RH) conditions with the temperature fixed at 25 °C and studied the effect on the mechanical strength and insertion ability of dissolving MNs fabricated with HA, CS and Gel. The authors found that when analyzing the mechanical properties, the force-displacement curves showed that when the displacement went from 0 to 0.25 mm, the compression forces were of 0.40, 0.38 and 0.39 N for HA, CS and Gel respectively. In addition, all these MNs showed 100% insertion rate.

Then, to understand the effect of RH the samples were conditioned at 20, 40, 60 and 80% RH for 30 min. For the HA MNs, compared with dried MNs, when the RH increased at 20%, the mechanical strength remained unaltered (displacement of 0.2 mm with force of

almost 0.4 N) but after storage at 40 and 60% RH, a slight reduction was observed, with MNs presenting values closer to 0.2 N.needle^{-1} with a displacement of 0.2 mm. Nevertheless, the insertion ratio was always close to 100%. However, with 80% RH the mechanical strength reduced drastically to <0.1 N.needle^{-1} at 0.2 mm displacement. Regarding CS and Gel MNs, the mechanical strength and insertion ability showed little change after storage at 20% RH. Similarly, to HA MNs mentioned above, there is a slight decrease in the mechanical strength at 40 and 60% RH with successful insertion kept almost at 100%. In this case, at 80% RH MNs tips disappeared, so, the force-displacement values were not determined.

In fact, when compared with CS and Gel, HA MNs were able to keep the needle-like shape. After storage at 80% RH, the structure loses strength and MNs can no longer be inserted in skin. In summary, dissolving MNs showed different changes in response to varying RH storage conditions. When conditioning samples at 20% RH the samples showed no water absorption. However, at 40, 60% and 80% RH for HA MNs, the water absorption rate increased from 0.5 to 4.9% and to 11.8%, respectively. Regarding CS and Gel the water absorption increased slightly when the samples were conditioned at 40 and 60% RH, but at 80% the absorption rates were of 8.0 and 9.6%. Overall, all these MNs can be used within 30 min after opening the packaging, which is supported by their good insertion rates.

One of the drawbacks of some dissolvable biopolymers relies on their hygroscopic nature which will negatively impact the mechanical strength of these patches or drug stability after exposure to environment humidity. Hiraishi *et al*. [59] studied the performance of HA MNs incorporating HA, dextran and PVP. These devices were conditioned in a desiccator with 75% RH and after 1 week, the mechanical strength decreased 50% in relation to the dried patch, to 0.14 N.needle^{-1}. The incorporation of different pharmaceutical ingredients, namely all-*trans* retinoic acid and ovalbumin also had a significant impact on the mechanical strength of MNs. Loading MNs with all-*trans* retinoic acid decreased the mechanical strength in about 50%, with the failure forces ranging between 0.04-0.056 N.needle^{-1} for needles of 300 μm in height and 0.073-0.1 N.needle^{-1} for MNs of 800 μm. The same tendency was observed for MNs incorporated with ovalbumin, which presented lower mechanical strength regardless the protein concentration.

Different mechanical failure forces are recorded for the wide diversity of biopolymers reported in literature, and the incorporation of active ingredients, as well as the composition of the matrix, influence this parameter. It is shown that different biopolymeric matrices have potential for clinical application, as long as these systems present skin disruption capability and ability to keep the active ingredients integrity.

Remarkably, the use of polysaccharides and proteins offers a wide range of advantages due to their low toxicity, inherent biocompatibility, degradability and renewable

character, which are essential to address the needs of a sustainable society. However, polysaccharides and proteins-based MNs face some limitations as well. The intrinsic variability of biopolymers, associated specially with animal and plant sourcing, coupled with their lack of standardization and changes in aesthetics during storage or processing, are some of the factors that should be considered when these enter into large scale production.

The future of the development of polysaccharides and proteins-based MNs depends largely on the development of smart devices for DD, ISF and diagnosis using nanocarriers and nanostructured polymers, which will certainly be boosted by the advent of nanotechnology.

This field holds huge potential and it should be very successful. It is imperative to highlight that these MN devices are poised to provide an alternative to conventional administration of pharmaceuticals via oral route. Regarding the limitations of the oral route, the portability and well-known acceptability by patients, should be considered. Elegant structures and remarkable combinations of polysaccharides and proteins have worked towards the successful delivery of different pharmacological agents using MNs, with a range of applications in several areas of human endeavor. As such, it is expected that biopolymer based MNs will play an essential role in modern healthcare.

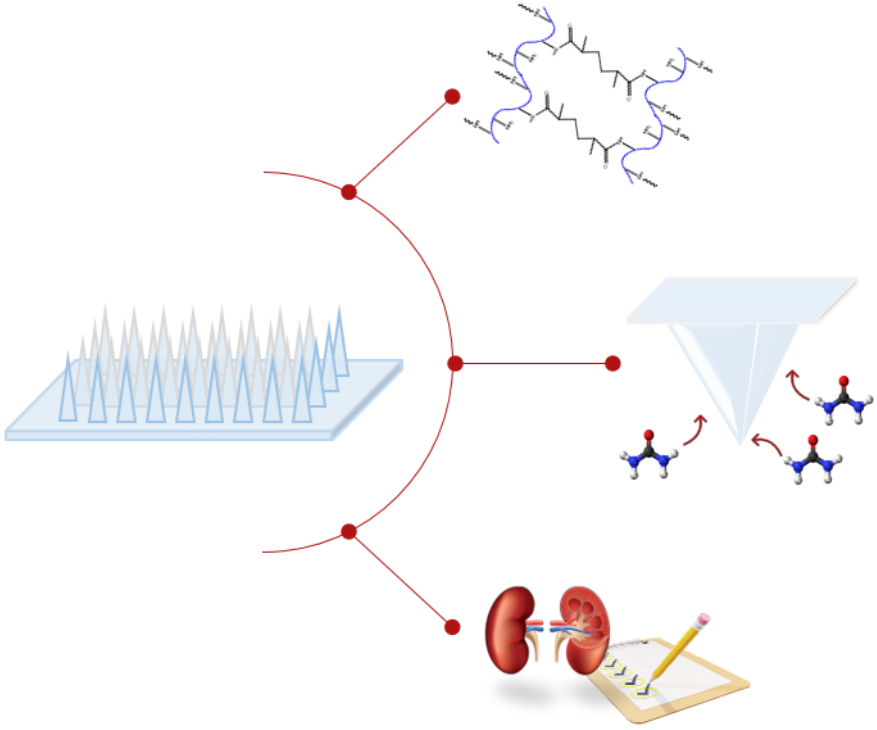

CHAPTER 2. SWELLABLE GELATIN METHACRYLOYL MICRONEEDLES FOR EXTRACTION OF INTERSTITIAL SKIN FLUID TOWARDS MINIMALLY INVASIVE MONITORING OF UREA

This chapter is adapted from the published manuscript:
Daniela F. S. Fonseca, Paulo C. Costa, Isabel F. Almeida, Patrícia Dias-Pereira, Inês Correia-Sá, Verónica Bastos, Helena Oliveira, Carla Vilela, Armando J. D. Silvestre, Carmen S. R. Freire, Swellable gelatin methacryloyl microneedles for extraction of interstitial skin fluid towards minimally invasive monitoring of urea, Macromolecular Biosciences, 2020, 2000195.

2.1. Abstract

Urea, the main nitrogenous waste product of protein metabolism, is eliminated almost exclusively by the kidney, and hence, displays considerable clinical significance in the assessment of kidney disorders. The aim of this study is to prepare and investigate the potential of swellable c-GelMA MNs as a platform for minimally invasive extraction of ISF towards straightforward point-of-care healthcare monitoring of renal complaints, by quantification of urea. c-GelMA MNs are successfully prepared by photo-crosslinking and micromolding, faithfully replicating the master molds (387 ± 16 µm height, 200 µm base and 500 µm tip-to-tip distance). These MNs patches display good mechanical properties, withstanding more than 0.15 N per needle without breaking. *Ex vivo* skin insertion assays reveal that the MNs penetrate up to 237 µm depth, reaching the dermis, where they should extract ISF considering a real application. In an *in vitro* application using an agarose skin model system, the c-GelMA MNs are able to efficiently recover urea (> 98%). Additionally, these MNs exhibit non-cytotoxic effects towards human keratinocytes. These findings suggest that c-GelMA MNs are promising devices for sampling ISF and offline analysis of urea, opening new avenues for simple point-of-care healthcare monitoring.

2.2. Introduction

Kidney ailments, as chronic kidney disease, kidney stones and polycystic kidney disease, recognized as a comorbidity of diabetes and hypertension, are strongly linked to higher risk of cardiovascular diseases, infection and cancer. Therefore, they are considered a global public health problem, contributing to the global major burden of noncommunicable diseases, and having a direct impact on high global mortality and morbidity [273,274]. It is estimated that the prevalence and associated burden of kidney disease is responsible for 5-10 million deaths per year worldwide [274]. The quantification of biomarkers present in various body fluids represents a versatile tool for diagnosis, prognosis, monitoring, therapy and disease management [275]. Currently, the most common body fluids used for biomarkers detection are blood, urine and saliva [275]. However, ISF, which is formed by blood transcapillary filtration is gaining increasing relevance in this realm [276]. Surrounding the capillary beds in the connective tissue, the ISF contains systemic biomarkers and its composition varies along with physiological changes [277,278]. Therefore, the ISF constitutes an informative proxy of serum and plasma, and appears as a promising alternative for blood, the gold standard in health monitoring [276,279]. Nevertheless, ISF is still relatively unexplored, mainly due to the lack of simple and reliable technologies for its extraction [280].

In an era of decentralized healthcare systems, the need to provide appropriate and timely care to patients shaped the development of easy to use miniaturized devices [281]. Among the different technologies developed to collect the ISF, MNs arise as minimally invasive devices that are painless, well-tolerated, easy-to-use and have the ability of self-application [230,280,282–288]. The first MNs designed for ISF extraction were fabricated into solid or hollow structures, using silicon, glass or metal [289]. However, the brittle nature of glass poses safety risks to the patients and may cause environmental hazards. In addition, they require extra devices such as external pumps to acquire sufficient ISF for analysis [9,29]. To circumvent these issues, swellable MNs were prepared using hydrogel-forming polymers [242,283]. These swellable polymeric systems consist of a crosslinked polymer network that swells upon contact with an aqueous solution keeping their structural integrity [290]. These are able to extract ISF in one step, without the need of assisting devices, while keeping minimal tissue damage. The first hydrogel-forming MNs for ISF sampling and analysis were produced with poly(methylvinylether-*co*-maleic anhydride), crosslinked with polyethylene glycol [242,283], and exploited for lithium monitoring [242] and extraction and quantification of model drugs (theophylline and caffeine) and glucose [283]. These MNs systems were applied for 1 hour to extract the adequate amounts of ISF (*ca.* 0.84 mg) for analysis but

no direct relationship was found between the detected metabolites and their real concentration in ISF [242,283].

Nowadays, biopolymers, namely polysaccharides and proteins, have received significant attention on the materials science field because of their abundance, renewable nature, biocompatibility, biodegradability and possibility of functionalization [9]. However, only a few biopolymer-based MNs systems for ISF sampling have been reported so far [230,291–293]. For instance, one study described the preparation of poly(L-lactide) MNs coated with an alginate-peptide nucleic acids hybrid material. These MNs patches, with 77 needles of 550 μm height, were tested to sample and detect nucleic acid biomarkers from ISF, being able to extract up to 6.5 μL of fluid in 2 min when immersed in PBS [291]. In a different perspective, swellable MNs fabricated with HA modified with methacrylic anhydride [230], displayed high water uptake and were able to extract 2.3 ± 0.4 mg ISF in 10 min *in vivo* (100 needles of *ca.* 800 μm). These HA swellable MNs were investigated for the minimally invasive sampling of metabolites, such as glucose and cholesterol, and after 30 min of application on mice, the results showed the same trend as the those obtained with traditional glucometer and cholesterol meter. Gel is a widely available and used protein in the biomedical field that can be also functionalized with polymerizable moieties, as methacrylic groups [294]. GelMA is a commercially available Gel derivative, prepared by reacting Gel with methacrylic anhydride, which can be crosslinked upon exposure to UV irradiation (c-GelMA), and is able to retain high water quantities. Moreover, this polymeric matrix combines reproducibility, stability and modularity of synthetic biomaterials, and therefore has been widely used in the biomedical field [294–298]. Very recently, GelMA was investigated to prepare swellable MNs systems [243]. These MNs (121 needles array of 600 μm height) were investigated for ISF extraction and detection of glucose and an antibiotic (vancomycin). However, to the best of our knowledge, no reports about the design of biopolymeric MNs for fluid extraction and monitoring of urea, targeting the burden of kidney diseases have been reported so far.

In this sense, the present work describes the preparation and characterization of swellable hydrogel MNs based on c-GelMA (70-90% degree of substitution) towards simple platforms to sample urea using an *in vitro* system. The obtained MNs were prepared by photo-crosslinking and micromolding and evaluated in terms of their morphology, mechanical properties, thermal stability and swelling ability. In order to confirm their safety for skin applications, the biocompatibility of c-GelMA MNs was tested *in vitro* in human keratinocytes. Skin insertion ability was assessed using human abdominal skin *ex vivo*. Finally, as a proof of concept, the use of c-GelMA MNs for the recovery urea was explored, using an *in vitro* agarose system, that is currently used as

a reproducible skin physical model for different *in vitro* testing purposes [299], including biomarkers extraction [230,243] using MNs. Two concentrations, 5 and 20 mM, to mimic physiological levels in normal and kidney disease states were investigated.

2.3. Materials and methods

2.3.1. Chemicals and materials

GelMA (bloom 300, 70-90% degree of substitution), Irgacure 2959 (2-hydroxy-4′-(2-hydroxyethoxy)-2-methylpropiophenone, 98% purity), sodium phosphate dibasic (≥99.0% purity), sodium phosphate monobasic (≥99.0% purity), 3-(4,5-dimethyl-2-thiazolyl)-2,5-diphenyl tetrazolium bromide (MTT, 98%), dimethyl sulfoxide (DMSO, ≥99.7%) urea (≥99% purity), urea assay kit was purchased from Sigma-Aldrich (St Louis, MO). Sodium chloride (≥99% purity) was purchased from Fluka (Sigma-Aldrich Chemie GmbH, Steinheim, Germany), and agarose (for molecular biology) was purchased from Panreac (AppliChem GmbH, Darmstadt, Germany). Ultrapure water was obtained using a Milli-Q® Integral Water Purification System. The HaCaT cell line was purchased from Cell Line Services (Eppelheim, Germany) and Dulbecco's modified Eagle's medium, fetal bovine serum (FBS), L-glutamine, penicillin-streptomycin (10,000 $U.mL^{-1}$), and fungizone (250 $U.mL^{-1}$) were purchased from Gibco®, Life Technologies (Grand Island, NY, USA).

2.3.2. Fabrication of c-GelMA MNs patches

To prepare pyramidal-shape MNs, female molds of PDMS (Micropoint Technologies Pte Ltd., Singapore), size 8 mm × 8 mm, arrays of 15 × 15 needles with 550 μm height, 200 μm base and needle pitch 500 μm, were used. The methodology used for the preparation of the c-GelMA MNs was adapted from procedures previously reported for other crosslinked MNs [217,230]. Briefly, 10 and 20% (w/v) GelMA solution was prepared by dissolving the polymer in Mili-Q water under constant stirring at 40 °C. Then, approximately 5% (w/w in relation to GelMA) of photoinitiator (Irgacure 2959) was added. 60 mg of solution was added to the PDMS mold and centrifuged (Hettich® Rotofix 32A) at 6000 rpm (4025 *g*) during 10 min to guarantee that the GelMA solution filled the pyramidal holes. Afterwards, the MN molds were exposed to UV light (300-430 nm, 7W, 230 V, 50 Hz) for one minute. The crosslinked MNs were left to dry at 30 °C overnight and then removed from the master mold.

2.3.3. Characterization of c-GelMA MNs patches

2.3.3.1. Fourier transform infrared- Attenuated total reflection spectroscopy

Fourier transform Infrared-attenuated total reflection (FTIR-ATR) spectra of GelMA and c-GelMA were obtained on a Perkin Elmer FT-IR System Spectrum BX spectrophotometer (Perkin-Elmer Inc., USA) equipped with a single horizontal Golden Gate ATR cell. To obtain each spectrum, 64 scans were acquired in the 4000–500 cm^{-1} range, with a resolution of 4 cm^{-1}.

2.3.3.2. Morphological characterization

The obtained c-GelMA-based MNs were characterized using a stereomicroscope (Nikon SMZ18, Tokyo, Japan) and images were captured with a camera (SRH Plan Apo 2, Tokyo, Japan). Magnification power of the ocular lens was 5× and magnification of the objective lens was 1.5, 5 and 8×, corresponding to a total magnification of 7.5, 25 or 40×, respectively. Image acquisition was performed using NIS Elements Imaging Software (4.50.00 (Built 1117), 2017).

Morphological analysis of the as-prepared MNs was complemented by scanning electron microscopy (SEM). Micrographs were obtained using a high voltage microscope (HITACHI SU 70) operated at 15.0 kV. Samples were previously coated with carbon using an EMITECH K950 coating system.

2.3.3.3. Mechanical characterization and preliminary insertion tests

Mechanical axial compressive tests were performed on the c-GelMA MNs, using a TA.XT2 Texture Analyser (Stable Micro Systems Ltd., Haslemere, UK). The MN patches were placed on the flat rigid surface of a stainless-steel base plate. An axial force was applied perpendicular to the axis of the MN array, at a constant speed of 0.01 $mm.s^{-1}$. The force was measured when the moving sensor touched the uppermost point of the needles. Then, the texture analyser recorded the force required to move the mount as a function of needle displacement [131].

For preliminary insertion studies, a simple method previously described [144] was performed. First, Parafilm M® (Bemis Company Inc., Soignies, Belgium) was folded into eight layers to simulate the thickness of excised skin, and the MN arrays were then inserted into the Parafilm M® using the texture analyser and applying a force of 40 N for 30 seconds. Then, to measure the insertion ratio and depth, each layer of Parafilm M® was examined under the microscope and the number of holes in each layer was counted.

2.3.3.4. Thermogravimetric analysis

Thermogravimetric analysis (TGA) of GelMA and c-GelMA was carried out with a SETSYS Setaram TGA analyzer (SETARAM Instrumentation, Lyon, France) equipped with a platinum cell. Samples were heated from room temperature up to 800 ºC at a constant rate of 10 ºC.min^{-1} under a nitrogen flow.

2.3.3.5. Water uptake of c-GelMA MNs patches

Firstly, MNs were directly immersed in PBS for 60 min and at specific time intervals (5, 10, 30, 30 and 60 min), the excess of PBS present on the surface was removed and their weight measured. The water uptake was determined as outlined in Equation (1):

$$\text{Water uptake (\%)} = ((W_n - W_i)/W_i) \times 100 \quad (1)$$

where W_i is the initial weight, and W_n is the weight of the MN arrays after water uptake at t=*n*.

The water uptake by the MNs over time can be fitted by the Voight-based model, commonly employed for describing swelling kinetics of hydrogels [300]. Data were processed to determine the degree of swelling (S_t) (Equation 2), at any moment and then the rate parameter (*r* in min, *r*=-1/slope), which stands for the time required to reach 63% of the maximum swelling capacity:

$$S_t = S_e(1-e^{t/r}). \quad (2)$$

S_e represents the equilibrium water holding capacity and *t* represents the swelling time in min. The slope of the straight line, obtained by rearranging the previous equation and plotting $\ln(1-S_t/S_e)$ against time, gives the rate parameter.

To predict the fluid uptake *in vivo*, the c-GelMA MNs were inserted for 30 min into a simple skin model, prepared with an agarose hydrogel (1.4% (w/v)) coated with a Parafilm® layer [230]. The water uptake was determined by gravimetry, and the swelling ability was determined by the needle's volume increase. Needle's volume was determined by stereomicroscopy by measuring the needle's sizes.

2.3.3.6. In vitro cell viability assays

The manipulation and growth of the HaCaT cell line, a nontumorigenic immortalized human keratinocyte cell line, were performed and adapted to meet Cell Line Services (CLS) recommendations. HaCaT cells were aseptically grown in Dulbecco's modified Eagle's medium, supplemented with 10% fetal bovine serum (FBS), 2 mM L-glutamine, 1% penicillin-streptomycin (10,000 U.mL^{-1}), and 1% fungizone (250 U.mL^{-1}), at 37 °C in

a humidified atmosphere with 5% CO_2, as previously described [301]. Cells were daily observed for confluence and morphology using an inverted phase-contrast Eclipse TS100 microscope (Nikon, Tokyo, Japan).

Cell viability was determined by the colorimetric MTT assay [302]. Cells were seeded in 96 wells plates at 6,000 cells.well^{-1} for 24 h exposure. First, extracts of GelMA, c-GelMA and the photoinitiator (Irgacure 2959) were prepared by placing each material (one GelMA MNs patch, one c-GelMA MNs patch, and *ca.* 1 mg Irgacure 2959) into 1 mL of culture medium for 24h. Then, cells were exposed to these extracts and further incubated for 24 h. HaCaT cells exposed to culture medium were used as a negative control. At the end of the incubation time, 50 µL of MTT (at a concentration of 1 g.L^{-1}) were added to each well and incubated for 4 h at 37 ºC in 5% CO_2 humidified atmosphere. After that, culture medium with MTT was removed and replaced by 150 µL of DMSO and the plate was placed in a shaker for 2 h in the dark to completely dissolve the formazan crystals. The absorbance of the samples was measured with a BioTek Synergy HT plate reader (Synergy HT Multi-Mode, BioTeK, Winooski, VT) at 570 nm with blank corrections.

2.3.4. Ex vivo skin insertion

Human abdominal skin tissue was obtained from female donors submitted to an abdominoplasty at *Centro Hospitalar de São João*-CHSJ (Porto, Portugal), after signing the respective informed consent. Skin collection was granted approval from the Ethics Committee of CHSJ. After cosmetic surgery, skin samples were transported under refrigerated conditions and submitted to adipose tissue removal by blunt dissection using a scalpel (blade nº 24). Then, the skin surface was cleaned, dried, wrapped in aluminium foil and stored in a freezer at -20 °C until further use.

Prior to the insertion experiments, the skin sample was defrosted and cut into 25 mm diameter circles using a biopsy punch. Skin samples were then placed in a sealed Petri dish, on top of a cotton pad embedded in phosphate buffered saline for 1 h to prevent dehydration. Then they were fixed into a rigid support, and the MNs arrays placed on their surface. The MNs were pressed against skin with a force of 40 N for 30 seconds using the TA.XT2 Texture Analyser (Stable Micro Syetems, Ltd., Haslemere, UK) [144]. Afterwards, the MN arrays were peeled off and skin was exposed to China ink for 1 min for identification of the perforation sites. Residual ink was wiped from skin samples. To prepare histological specimens, skin samples were embedded in Bouin's solution, fixed in 10% formalin, dehydrated and embedded in paraffin wax. Serial 7-µm thick sections were cut from each block using a pfm Rotary 3006 EM automated

microtome. The skin sections were stained with haematoxylin and eosin and analysed using a Nikon Eclipse E600 microscope to confirm MNs skin penetration and determine its full depth [208].

2.3.5. Recovery and detection of urea from c-GelMA MNs

Urea, 5 and 20 mM, was used as model analyte and incorporated into an agarose (1.4% (w/v)) hydrogel, in order to mimic physiological levels in normal and kidney disease states [303]. The dry mass of MNs (n=3) was recorded and then, these were inserted into the hydrogel through the Parafilm M® layer. After 30 min, the mass was recorded, and the arrays were transferred into Eppendorf tubes supplemented with 200 µL of Mili-Q Water. These were centrifuged for 5 min at 10000 rpm [230] Urea was determined using an urea assay kit. It reacts as a substrate with compounds in the presence of enzymes and forms a product that reacts with a probe, which results quantitatively in the generation of a colored product, determined at 570 nm by UV-Vis spectroscopy [304].

2.3.6. Statistical analysis

Statistical analyses were performed using GraphPad Prism Software (GraphPad Software Inc., San Diego, CA, USA). Data is presented as the mean values ± standard error. A Student's paired *t*-test was used for comparisons between data points and multiple data sets between groups were analysed with a one-way analysis of variance (ANOVA) followed by a Tukey's post hoc test, when necessary. For all comparisons, a difference of $p < 0.05$ was regarded as statistically significant. For the *in vitro* cell viability assays, data was analysed by a one-way ANOVA followed by a Holm-Šídák test to evaluate the significance between the different MNs and cell viability was calculated with respect to control cells.

2.4. Results and discussion

The main objective of this study was the preparation (Figure 2.1 (a)) and characterization of swellable c-GelMA MNs, and to explore their potential as non-invasive micron-sized devices for ISF extraction (Figure 2.1 (b)) envisioning real-time urea monitoring. First, the fabrication of c-GelMA MNs was optimized by testing GelMA solutions with distinct concentrations, specifically 10 and 20% (w/v), and evaluating the morphology and appearance of the MNs arrays obtained. The c-GelMA MNs were fabricated via simple micromolding followed by photo-crosslinking.

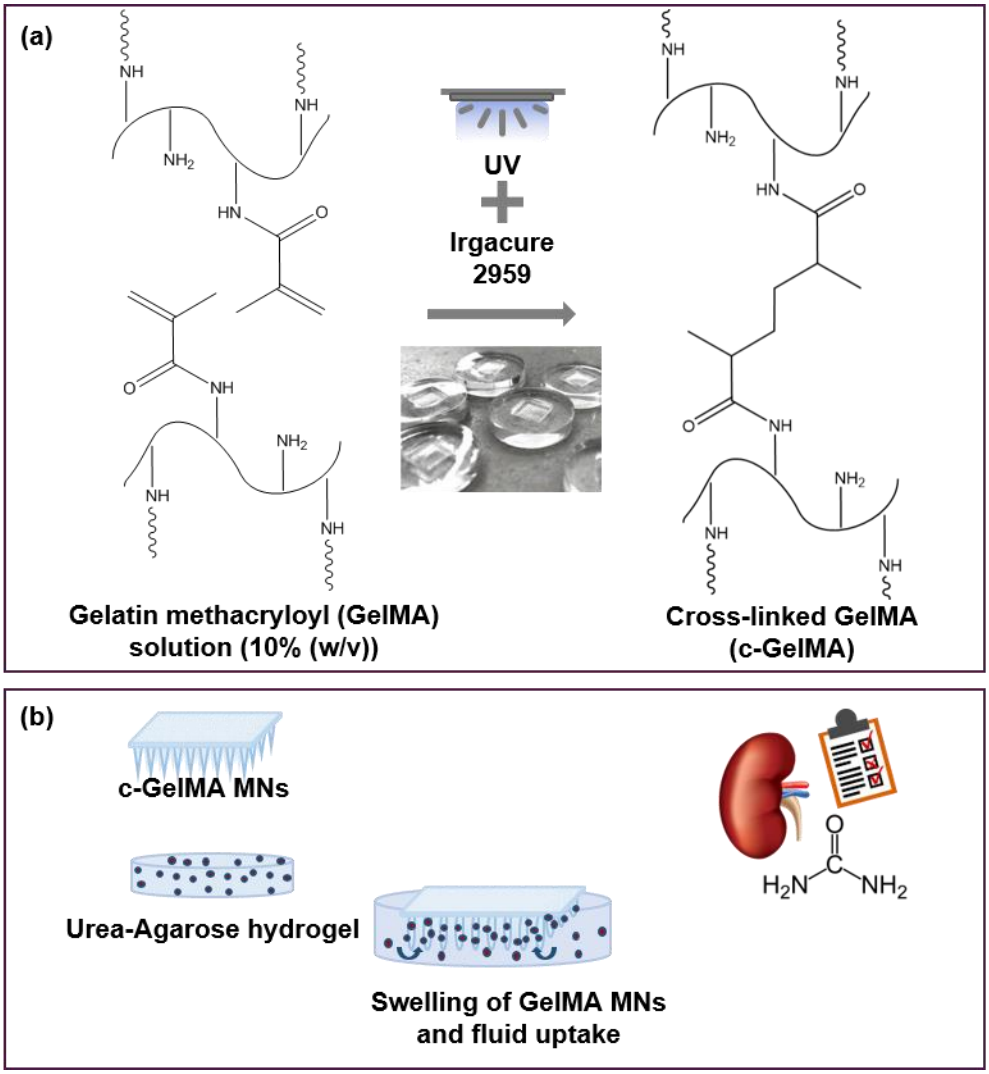

Figure 2. 1. Schematic representation of (a) crosslinking of GelMA and (b) *in vitro* swelling and fluid uptake by the obtained MNs using an agarose model system.

The MNs prepared with the 10% (w/v) solution were homogeneous and presented full arrays, with crack-free and regular needles. Using higher GelMA amounts, namely 20% (w/v), the polymer solution is very viscous, with reduced fluidity, which led to difficult mold perfusion, thereby forming irregular MN structures. Moreover, the presence of bubbles was also observed, along the needles and over the base, which is not acceptable in terms of shape quality. Therefore, 10% (w/v) GelMA MNs were selected for the subsequent characterization studies. First of all, the success of the crosslinking was confirmed by FTIR-ATR spectroscopy and the morphological features of the MNs were assessed, in particular their size and shape, as well as the mechanical performance. Then, to determine the practicality of using c-GelMA MNs as swellable devices, water absorption studies were conducted. The safety of the material was evaluated using an immortalized human keratinocyte cell line, and *ex vivo* human skin

was used for *in vitro* insertion tests. Finally, the recovery of urea (*i.e.* model analyte) was performed using a physical skin model system based on an agarose hydrogel covered by Parafilm®, to evaluate the potentialities of the MNs patches to extract biomarkers.

2.4.1. Characterization of c-GelMA MNs patches

2.4.1.1. Fourier transform infrared- Attenuated total reflection spectroscopy

FTIR-ATR spectroscopy was used to confirm the success of the crosslinking and the structure of the MNs. The FTIR-ATR spectra of GelMA and c-GelMA are displayed in Figure 2.2.

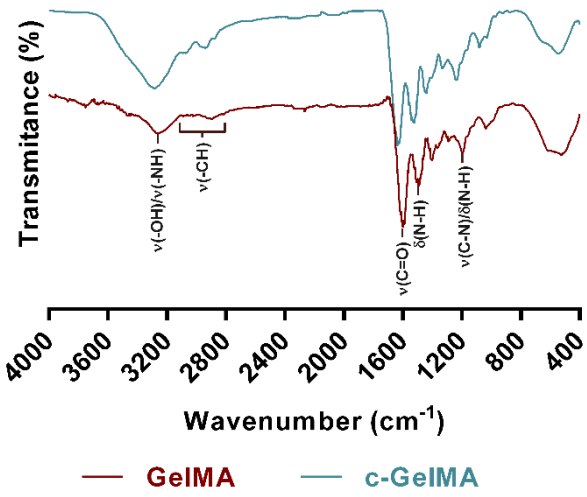

Figure 2. 2. FTIR-ATR spectra of GelMA and c-GelMA.

The spectrum of GelMA and c-GelMA display the characteristic peaks of Gel polymer. The typical absorption band around 3346 cm^{-1} is attributed to the O–H and N–H stretching vibrations. The peaks in the region 2800-3100 cm^{-1} are ascribed to the stretching vibration of C–H groups. The backbone structure of Gel is associated with the absorption bands at 1651 cm^{-1} (C=O stretching, amide I), 1544 cm^{-1} (N–H bending coupled to C–H stretching, amide II), and 1253 cm^{-1} (C–N stretching and N–H bending, amide III) [305]. It is noteworthy that the typical peak at around 1640 cm^{-1}in the spectrum of GelMA, that corresponds to the C=C stretching of the methacrylate groups, is too close to the amide I C=O stretching peak, and therefore it is difficult to detect and to verify its disappearance after crosslinking, *i.e.* its absence in the spectrum of c-GelMA. Evidence of this characteristic region would clearly confirm the success of the crosslinking reaction. Nevertheless, this was possible by the evidence of the increase/emergence of the typical peaks in the region 2800-3100 cm^{-1}, attributed to the C–H stretching of $-CH_2$ and tertiary -CH groups formed during the crosslinking reaction.

2.4.1.2. Morphological characterization

The as-prepared c-GelMA MNs successfully replicated the master mold shape, as shown in Figure 2.3 (a-c).

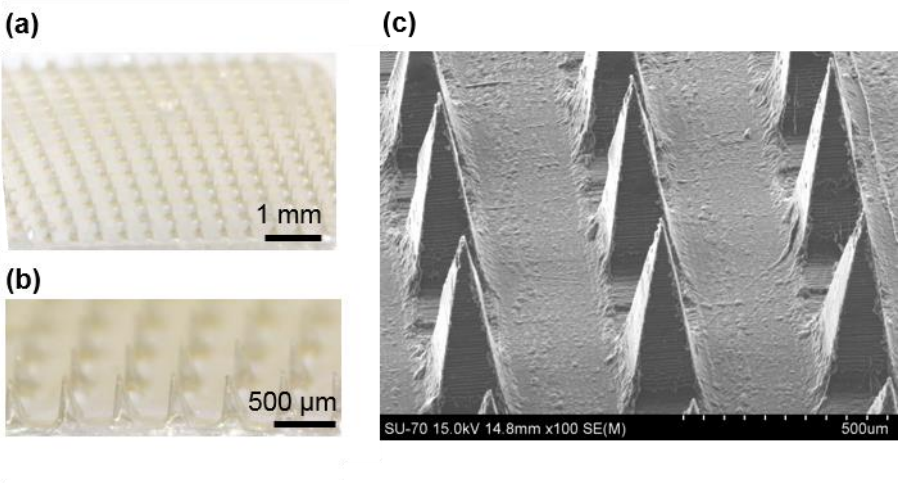

Figure 2. 3. c-GelMA MNs arrays. (a) and (b) Optic and (c) scanning electron micrographs.

Arrays of 15 × 15 needles with a square base and sharp tips were obtained over a square array of 0.8 cm side (Figure 2.3 (a-b)). SEM analysis confirmed the uniform and regular morphology of the needles (Figure 2.3 (c)), as previously reported for conical-shaped c-GelMA MNs [217]. Furthermore, the resulting MNs displayed no agglomerates or air bubbles along the structure, which is imperative for good insertion ability. On average, the as-prepared MNs measured 387 ± 16 µm in height, 200 ± 1 µm in the base and 496 ± 5 µm between the needle's tips. The decrease (*ca.* 27-33%) in MNs height, when compared with the depth of the master mold, is related with the solvent evaporation as described in literature for other biopolymeric MNs prepared by solvent casting [160,306]. These height values permit these MNs to be capable to disrupt the *SC* but not reach the nervous on skin and hit the blood vessels, endorsing their non-invasive character.

2.4.1.3. Mechanical characterization and preliminary insertion studies

To assure successful performance of c-GelMA MNs, these devices need to insert into the skin without breakage, allowing the material to reach the dermis and absorb enough ISF for biomarkers quantification. Herein, to evaluate the mechanical failure

force of c-GelMA MNs, the axial force load *vs* displacement was obtained using a texture analyzer. Figure 2.4 (a) unveils the displacement of MNs recorded by compression.

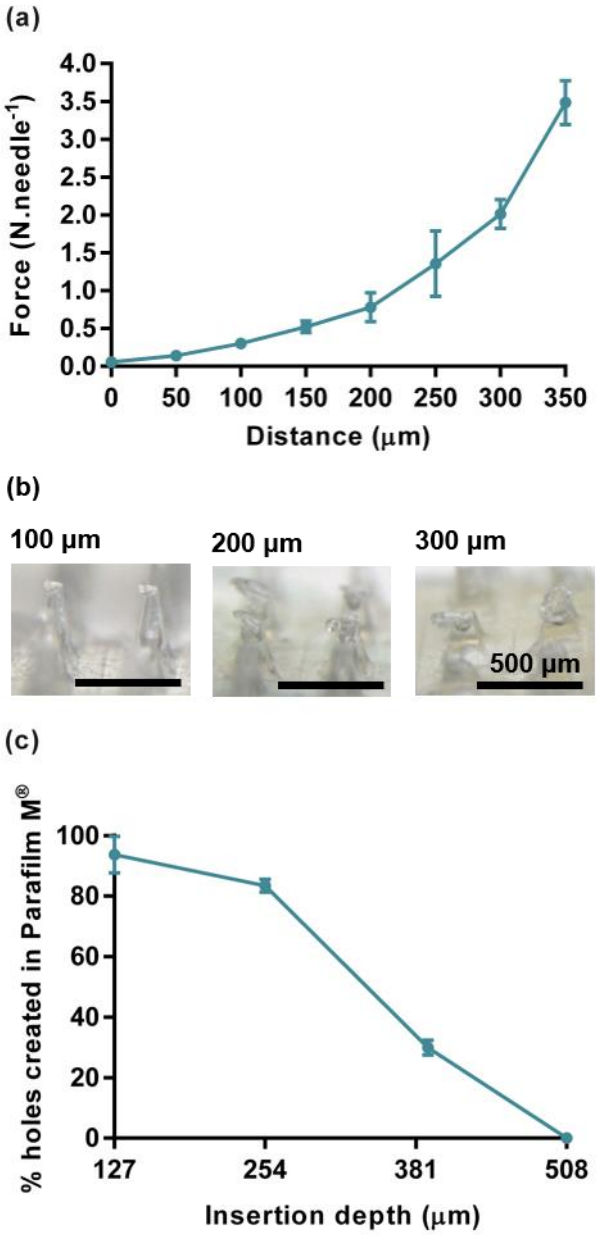

Figure 2. 4. (a) Force-displacement curve of c-GelMA MNs under an axial force load (*n*=9, measurements performed on 9 different regions of 5 arrays). (b) Optic micrographs of c-GelMA MNs at 100, 200 and 300 µm of displacement. (c) Insertion of c-GelMA MNs into a polymeric model membrane for skin insertion using Parafilm M® (*n*=3).

The present data indicates that there is no discontinuity in the applied force along with the displacement (Figure 2.4 (a)), which suggests that these c-GelMA needles did not fractured, but instead bended. This progressive deformation, without breaking, is visible on the micrographs presented in Figure 2.4 (b), at 100, 200 and 300 µm displacements. At 100 µm displacement, the MNs withstand 0.30 ± 0.03 N.needle^{-1},

which overcome the threshold value of 0.15 N.needle^{-1} reported for skin insertion using MNs [128] and notably confirm the suitability of c-GelMA MNs for skin insertion. These results demonstrate that the MNs patches under study present considerably higher mechanical strength than those reported in literature [217], which estimated that c-GelMA MNs crosslinked for 60 seconds and having 600 µm in height withstand *ca.* 0.12 N.needle^{-1}. This difference in the mechanical strength is in agreement with the study of Jung-Hwan *et al*. [126], showing that longer poly(lactic-co-glycolic acid) MNs present smaller fracture forces when compared with shorter needles of the same polymer.

Afterwards, to have a first insight into the skin insertion ability of these c-GelMA MNs, a skin model system, consisting of eight layers of Parafilm®, was used and an average force of 40 N was exerted for 30 seconds to apply the MNs patches. It was observed that the MNs were able to penetrate through the first (89 ± 3 % insertion), second (84 ± 1 % insertion) and third Parafilm® layers (30 ± 2 % insertion) (Figure 2.4 (b)). The third layer corresponds to a penetration depth of 381 µm, where about 30 % of needles perforated. At this penetration depth, the MNs would certainly reach the skin dermis and contact with the ISF. This is in line with previous results in which crosslinked hyaluronic acid MNs perforated up to 300 µm in depth, suggesting the successful penetration through the epidermis and dermis where there is a high amount of ISF [230].

2.4.1.4. Thermogravimetric analysis

The thermal stability of the samples GelMA and c-GelMA was assessed by TGA under a nitrogen atmosphere, as shown in Figure 2.5, to have an insight into their stability under sterilization conditions, typically required for biomedical devices and products.

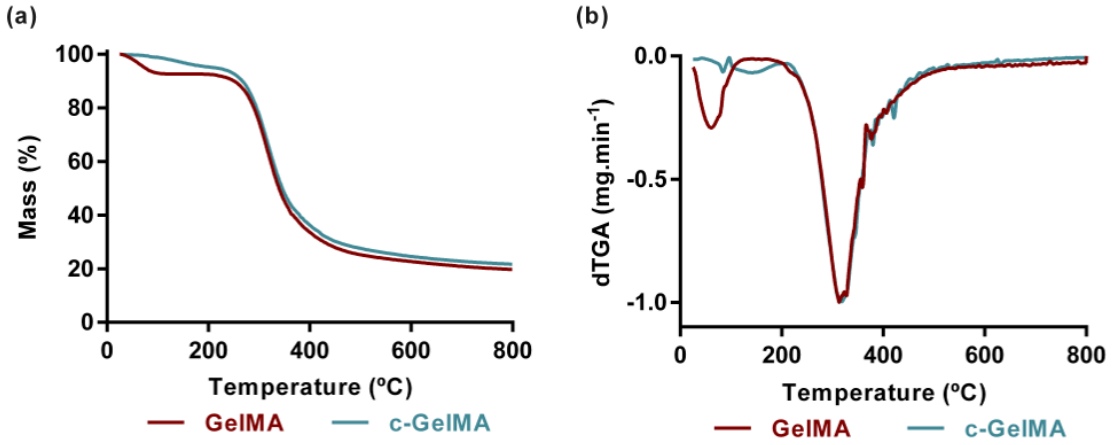

Figure 2. 5. (a) Thermograms and (b) corresponding derivative plot of GelMA and c-GelMA.

The thermal degradation profile of GelMA exhibits two weight-loss steps. A first weight loss of about 10 %, attributed to moisture loss, is observed between 25 and 120 °C, while a second and main decomposition stage, with maximum decomposition temperature around 309 °C, is associated with the protein degradation [307], with a weight loss of >75 %. The remaining residue at 800 ºC was around 20 %. The TGA curve of c-GelMA unveils a similar pattern, with a two-step weight-loss feature. The first decomposition stage, at about 77 ºC corresponds to a weight loss of 5% and is associated with the typical loss of absorbed water. Moreover, the broad low-intensity degradation peak at 125 ºC is assigned to the evaporation of water molecules entrapped within the cross–linked polymeric network, as previously proposed for other natural and synthetic based cross-linked polymeric networks [308,309]. The second stage event, with a maximum temperature around 310 ºC, is associated with the crosslinked protein degradation, leaving a residue of < 25%. These results suggested that the crosslinking process does not affect the thermal stability of gelatin. The high degradation temperatures observed ensure high thermal stability of the material at elevated temperatures (>121 ºC), suggesting their suitability, for example, for autoclaving sterilization.

2.4.1.5. Water uptake of c-GelMA MNs patches in PBS and agarose hydrogel

The water uptake ability of swellable MNs is one of the most important properties when envisioning the extraction of biomarkers, as it reflects their ability to absorb the ISF. To understand the water uptake ability, the weight gain of the c-GelMA MNs patches when placed into PBS is displayed in Figure 2.6 (a).

In general, the weight gain of c-GelMA MNs increased with time to a certain point, and then reached the equilibrium, where the polymeric network is fully saturated. After one minute of immersion in PBS, weight gain is about 39 ± 3 % and increases to 201 ± 4 % after 20 min, where it reaches a plateau. This value is close to that previously reported for c-GelMA MNs used for DD on cancer treatment, which display a weight gain up to 250 % [217]. Other c-GelMA presented superior values, *ca.* 400% [243], nonetheless, different reticulation degrees may explain these differences, however no information about this parameter was indicated in these previous studies.

A decrease in weight gain with an extended duration of soaking was not detected, indicating that there is no dissolution of polymer and hence, reinforcing the successful crosslinking of GelMA and safety of the device as far as this could be connected with leaving GelMA residues on skin. The data was further fitted by the Voight-based model usually employed for describing swelling kinetics of hydrogels [300].

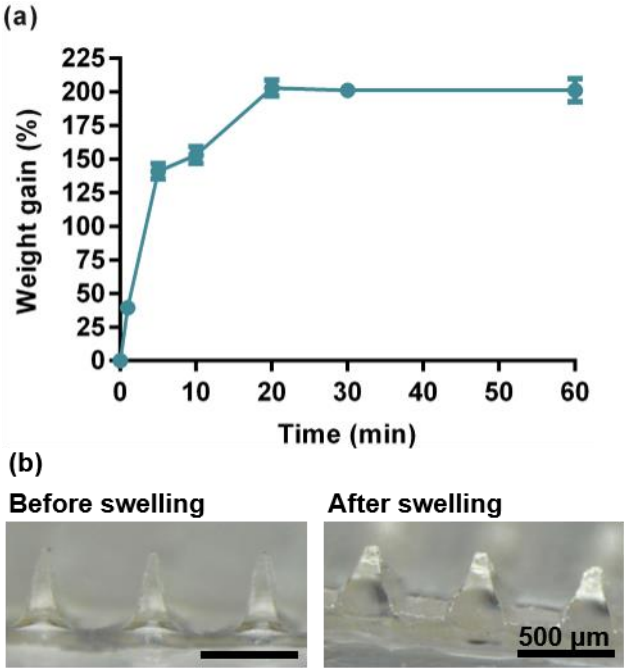

Figure 2. 6. (a) Weight gain (%) of c-GelMA MNs after immersion into PBS for 1, 10, 20, 30 and 60 min (*n*=5) and (b) Morphological traits of c-GelMA MNs before and after placing into an agarose hydrogel for 30 min.

Pursuant to the Voight-based model, the c-GelMA MNs display a sampling rate constant of 3.85, meaning that 63% of the full swelling capacity is achieved in less than 4 min. This is important considering the applicability of these systems, which aim to be employed for short time periods. To have the closest insight into the *in vivo* performance of these systems, c-GelMA MNs patches were placed in contact with an agarose hydrogel system for a timeframe of 30 min, resembling a clinical application [230]. In this case, it was possible to observe a weight gain of 146 ± 2 %, that correspond to a decrease of about 30 % in weight gain, when compared with the results obtained in PBS for 30 min. This behavior might be explained by the fact that the whole system absorbs water when immersed in the PBS solution, and when using the agarose hydrogel system, only the tips are immersed in the hydrogel and contact directly with water.

After removal of the patches from the agarose hydrogel, the c-GelMA MNs kept their shape, which indicates that these patches are crosslinked and can maintain their morphological integrity (Figure 2.6 (b)). The swelling ability of c-GelMA MNs after insertion into an agarose hydrogel system for 30 min was also determined by Optic microscopy (Figure 2.6 (b)) by measuring the increment in their dimensions. In fact, the volume of these MNs increases from $5 \pm 0.2 \times 10^{-3}$ mm^3 in native MNs to $9.3 \pm 0.2 \times 10^{-3}$ mm^3 in the swelled systems, which correspond to about 1.8 times their initial volume. This swelling effect may stabilize the needles into the insertion point and has the potential

to facilitate afterwards the release of the payload [217], *i.e.* biomarkers in the ISF. In this study, the c-GelMA MNs were able to extract 3.5 ± 0.1 mg of fluid per patch from the agarose system during 30 min of insertion.

2.4.1.6. In vitro cell viability assays

To assess the cytocompatibility, it could be relevant to perform the screening using keratinocytes and human skin fibroblasts. However, considering that the material is mainly contacting the epidermis and only reaches the top of dermis, the keratinocytes are greatly exposed and hence, were chosen for the assay.

In this vein, to evaluate the cytocompatibility of the c-GelMA MNs and investigate their suitability for dermal application, HaCaT cells were exposed to the c-GelMA MNs, to GelMA and the initiator for comparison. The cell viability after exposure to each tested system was determined and is shown in Figure 2.7.

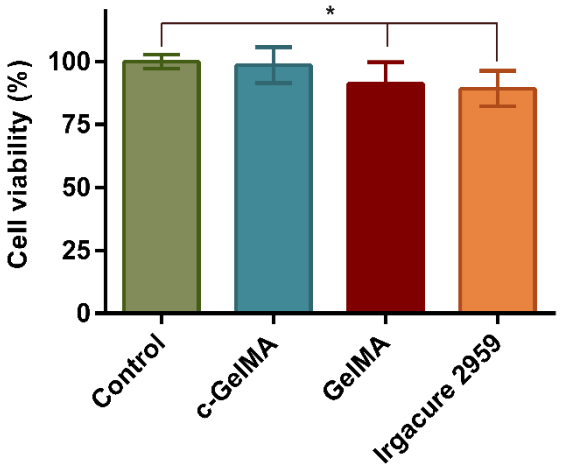

Figure 2. 7. Cell viability of HaCaT cells upon exposure to GelMA MNs, c-GelMA MNs and the initiator, Irgacure 2959 for 24 h (n=12, two independent experiments, * statistically significant differences (p<0.05) relative to control).

According to ISO 10993-5:2009(E), all tested samples are considered non-cytotoxic because cell viability is maintained above 70%, confirming the innocuous nature of the raw materials and of the ensuing crosslinked polymeric MNs. These results are comparable to those reported by Zhao *et al*. [310], which investigated the effect of c-GelMA hydrogels on HaCaT cells and found that there were no significant differences in cell elongation, migration or aggregation, and hence, no cytotoxicity. In sum, it was ascertained that the metabolic function of HaCaT cells is not impaired after exposure to

these c-GelMA MNs or the individual components, which confirm their safety for clinical use.

2.4.2. Ex vitro skin insertion

To assess the ability of the as-prepared c-GelMA to penetrate skin, an *ex vivo* insertion test was performed, using human abdominal skin (Figure 2.8).

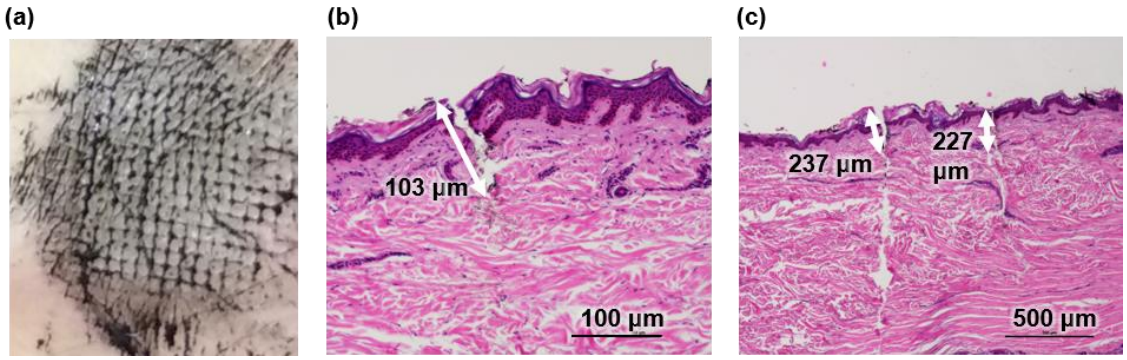

Figure 2. 8. (a) Photograph of top view of human abdominal skin after being pierced by c-GelMA MNs and stained using China Ink. (b-c) Histological cross-section of human abdominal skin after being pierced by c-GelMA, hematoxylin and eosin staining.

A small probe was used exerting a force of 40 N for 30 seconds, followed by the application of a dye, aiming to stain the insertion points and unveil the full depth of the needle insertion. The skin surface exhibited an array of black spots, which corresponded to the insertion sites (Figure 2.8 (a)), confirming the successful skin perforation. According to the histological section analysis (Figure 2.8 (b-c)), MNs insertion depths ranged from 103 to 237 µm, corresponding to 26-61% of the needles' height. Luo et al. [217] reported the preparation of c-GelMA MNs and concluded that 600 µm needles create microcavities with an insertion depth corresponding to 67-100% of their height. These differences in skin insertion may be related to natural skin elasticity and shape [311]. However, for the purpose of this work, these results confirm the ability of c-GelMA MNs to perforate skin and reach the dermis, where they should absorb ISF due to their high swelling ability. Along with the skin insertion ability test, the c-GelMA MNs were left in the skin for 30 min, and the weight difference was determined.

Using human abdominal skin *ex vivo*, the c-GelMA MNs were able to extract 3.0 ± 0.7 mg of fluid, which is comparable to the amount absorbed in the assays with the model agarose system. Interestingly, this value is higher than that reported for other swellable MNs, namely poly(methylvinylether-*co*-maleic anhydride) MNs and methacrylated HA MNs that can extract *ca.* 0.84 and 1.4 mg of ISF respectively, following an *in vivo* application [230,242,283], which can improve their potential for the detection and

quantification of target metabolites. These differences in the extraction rate of fluid are certainly associated with the different chemical natures of the polymers used and the degree of crosslinking that strongly influences the swelling ability of the MNs. Therefore, these results confirm the suitability of the system for skin fluid applications and that the as-prepared c-GelMA MNs may be considered promising candidates for fast and precise ISF extraction.

2.4.3. Extraction of urea from a skin model system using the c-GelMA MNs patches

ISF is a source of panoply of metabolites, which can be of utmost importance for clinical diagnostics. Considering that these c-GelMA MNs patches swell upon skin insertion, an efficient extraction and recovery of metabolites are expected. In this work, urea was used as model metabolite because of its relevance on the monitoring of renal disorders [273]. The extraction of urea from the skin model system (agarose hydrogel) was investigated by targeting the blood concentration of normal and chronic kidney disease, 5 and 20 mM, respectively [303], and successfully quantified with a commercial assay kit. The detected concentrations are in agreement with those of the agarose hydrogels as displayed in Figure 2.9.

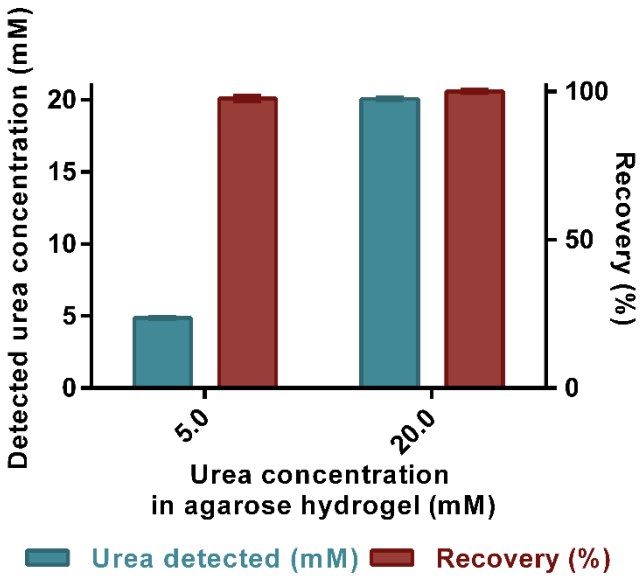

Figure 2. 9. Correlation of urea concentrations and recovery from c-GelMA MNs after insertion into a model agarose hydrogel system (*n*=5).

Recovery efficiency of 97.6 ± 1.0 % and 100.4 ± 0.5 % for the 5 mM and 20 mM urea-loaded agarose hydrogels was obtained respectively. The amount of urea

recovered from the c-GelMA MNs corresponds to 4.9 ± 0.1 and 20.1 ± 0.1 mM for the normal and disease model respectively, reflecting the suitability of detecting and quantifying different urea amounts to establish proper healthcare monitoring. Since changes of blood metabolites are reflected in ISF, the application of c-GelMA MNs is favored and the present work reflects the usefulness of employing c-GelMA MNs to correlate urea levels with specific health conditions. Literature reports the use of gold-coated MNs for urea sensing by urea hydrolysis, but the lower response of this system remains an issue [312]. On the other hand, iontophoresis and microdialysis have been explored as alternatives for the minimally invasive monitoring of urea, however they lack for practicality when compared with MNs [303,313,314]. This indicates that c-GelMA MNs are a potentially powerful platform for urea diagnosis and can be further explored for the concomitant extraction of multiple metabolites which will enable the follow-up of different health conditions and of the major noncommunicable diseases.

2.5. Conclusions

The present study demonstrates for the first time the potential of c-GelMA MNs as a platform for ISF sampling and urea analysis. Herein, we demonstrate the successful development of swellable c-GelMA MNs by the fabrication of uniform arrays with pyramidal needles and sharp tips by photo-crosslinking followed by solvent casting. The as-prepared MNs exhibit sufficient mechanical strength to disrupt *ex vivo* human abdominal skin, reaching the dermis. The intrinsic biocompatible nature of the crosslinked Gel coupled with their swelling ability, makes this system useful for fluid extraction and analysis. Therefore, it is demonstrated that the dry c-GelMA MNs insert a model agarose system and swell, being able to absorb up to 3.7 mg fluid *per* patch. As a proof-of-concept, urea was incorporated into a model agarose hydrogel system to mimic a normal and disease-state, and successfully extracted and quantified. The simple post-analysis step facilitates offline processing and goes in line with the recent trend of point of care diagnostics for healthcare monitoring. Once this methodology is proven in humans, this technology would be beneficial to patients with kidney disease, or high risk of developing kidney or heart disease, and also diabetes. The minimally invasive nature of this system is important to perform either periodic or continuous health status monitoring. In this vein, this approach could add significant clinical value as an accessible diagnostic system and revolutionize the way healthcare is delivered.

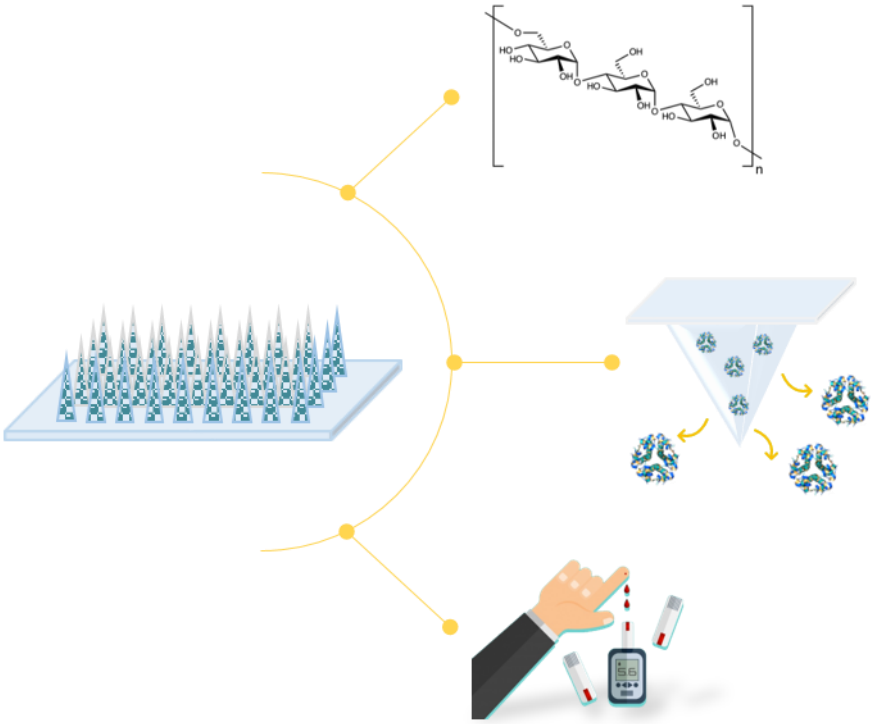

CHAPTER 3. PULLULAN MICRONEEDLE PATCHES FOR THE EFFICIENT TRANSDERMAL ADMINISTRATION OF INSULIN ENVISIONING DIABETES TREATMENT

This chapter is adapted from the published manuscript:
Daniela F. S. Fonseca, Paulo C. Costa, Isabel F. Almeida, Patrícia Dias-Pereira, Inês Correia-Sá, Verónica Bastos, Helena Oliveira, Margarida Duarte-Araújo, Manuela Morato, Carla Vilela, Armando J. D. Silvestre, Carmen S. R. Freire, Pullulan microneedle patches for the efficient transdermal administration of insulin envisioning diabetes treatment, Carbohydrate Polymers, 2020, 241, 116314.

3.1. Abstract

Dissolvable MNs patches using PL, a water-soluble polysaccharide with excellent film-forming ability, were fabricated for the transdermal administration of insulin, envisioning the non-invasive treatment of diabetes. PL MNs patches were successfully prepared by micromolding and revealed good thermal stability (Td_{max}=294 °C) and mechanical properties (> 0.15 N.needle^{-1}), penetrating skin up to 381 μm depth, as revealed by *in vitro* skin tests. After application into human abdominal skin *in vitro*, the MNs dissolved within 2 h releasing up to 87% of insulin. When stored at 4, 20 and 40 ºC for 4 weeks, insulin was able to retain its secondary structure, as shown by circular dichroism spectropolarimetry. The prepared PL MNs were non-cytotoxic towards human keratinocytes, being suitable for skin application. These findings suggest that PL MNs have potential to deliver insulin transdermally, thus avoiding its subcutaneous administration.

3.2. Introduction

Diabetes mellitus is a group of chronic metabolic disorders characterized by signs and symptoms of hyperglycemia, *viz.* high blood glucose levels [315]. Diabetes mellitus is currently recognized as one of the largest epidemics in the world and its incidence is rising. In 2015, it was estimated that 415 million people had diabetes and the latest reports predict that over 642 million people will be affected by 2040 [316]. Although there are different types of diabetes mellitus, type 1, type 2 and gestational diabetes are the most prevalent [315]. Type 2 diabetes is by far the most prevalent form of this disease, accounting for more than 90% of all cases and being responsible for the current global health problem [317].

The incidence of insulin-dependent type 1 diabetes is lower, but it is also raising, particularly in children younger than 5 years of age. The impairment of insulin secretion due to autoimmune destruction of pancreatic beta cells and/or peripheric insulin action resistance leads to chronic hyperglycemia and subsequent vascular and neuronal complications, that impact patients disease burden [318]. Therefore, insulin therapy is currently the most effective treatment to achieve normoglycemia in type 1 diabetes, minimizing related complications [315,317]. Insulin is usually administered subcutaneously due to its poor oral bioavailability [319], but subcutaneous injections are associated with increased inflammation and infection risk, as well as poor patient compliance [320]. In addition, repeated injections around the same spot may lead to skin thickening and poor glycemic control, resulting in suboptimal management of diabetes [321].

To overcome these drawbacks, minimally invasive alternative routes have been investigated, including oral, pulmonary, nasal, buccal, peritoneal and transdermal administration [322,323]. In particular, transdermal administration of insulin has gained a great momentum in the past few decades owing to its easy self-application coupled with improved patient adherence [322,324–326]. More recently, attention has been paid to the use of MNs as a simple and minimally invasive method for the self-administration of this pharmaceutical. MNs have the ability to accelerate insulin absorption, due to the richness in small vessels that the *stratum papillare* of the skin presents [139,327,328].

The first report concerning the use of MNs for insulin administration dates back to 2003, and showed that stainless steel devices provided therapeutic efficacy by reducing blood glucose levels in diabetic rats [329]. Since then, MNs for insulin administration have been sculped using several different materials, with polymers being the most extensively explored [9]. Nowadays, there is an increasing interest in the production of biopolymeric devices, including MNs [9], due to their intrinsic biocompatibility, safety, low

cost and sustainability. In this sense, literature reports the use of several biopolymers namely HA [170], starch and Gel [139], alginate [160], dextrin [330], poly-γ-glutamic acid [58] and chondroitin sulphate [182] in MNs for insulin administration [331].

PL is a non-ionic natural exopolysaccharide produced by yeasts and composed of α-(1→6) maltotriose residues. This biopolymer displays interesting properties regarding biomedical purposes, namely non-toxicity, water solubility, production of low viscosity solutions, excellent film forming ability, adhesiveness and good mechanical performance [261]. Furthermore, PL is emerging as an economic alternative to other natural gums of marine and plant origin [332,333]. During the past few years PL has been explored for the development of different materials for a panoply of applications [261,262], including functional packaging [334], tissue engineering [335,336] and also DD [337,338]. The demand for easy-to-use insulin administration justifies the need for more effective DD systems and the study of PL MNs for insulin administration will be offset by the benefit of those who suffer with diabetes. Our research team has been interested in the use of PL for the design of bio-based materials for different applications [334,339], and obtained promising preliminary results on the use of polysaccharides, including PL, for the fabrication of MNs [340]. So, in the current study, PL dissolvable MNs were prepared by micromolding and characterized in terms of morphology, mechanical properties, thermal stability, humidity stability and explored for incorporation and delivery of insulin. The DD efficiency was demonstrated *ex vivo* using human skin samples. In order to confirm their safety for skin applications the biocompatibility of PL MNs was tested *in vitro* in human keratinocytes.

3.3. Materials and methods

3.3.1. Chemicals and materials

PL powder (98%, MW 272 kDa) was purchased from B&K Technology Group (China). Insulin (from bovine pancreas, ≥ 25 $U.mg^{-1}$, MW approximately 5.8 kDa), sodium phosphate dibasic (≥99.0%), sodium phosphate monobasic (≥99.0%) were purchased from Sigma-Aldrich (Sintra, Portugal). Sodium chloride (≥99.0%) was acquired from Fluka (Sigma-Aldrich Chemie GmbH, Steinheim, Germany). Hydrochloric acid (37%) was purchased from Acros Organics (New Jersey, USA). Ultrapure water (Type 1, 18.2 MΩ cm at 25 °C) was obtained using a Milli-Q® Integral Water Purification System (Merck, Darmstadt, Germany). The HaCaT cell line was purchased from Cell Lines Services (Eppelheim, Germany) and Dulbecco's modified Eagle's medium, supplemented with 10% fetal bovine serum (FBS), 2 mM L-glutamine, 1% penicillin-

streptomycin (10,000 $U.mL^{-1}$), and 1% fungizone (250 $U.mL^{-1}$) from Gibco, Life Technologies (Grand Island, NY, USA).

3.3.2. Fabrication of PL MNs patches

Pyramidal PL MNs patches (size 8×8 mm^2, arrays 15×15, needle height 550 μm, needle base 200 μm, needle pitch 500 μm) were produced by solvent casting using female molds of polydimethylsiloxane (PDMS) (Micropoint Technologies Pte Ltd., Singapore). Firstly, different amounts of PL were dissolved in ultrapure water, under constant stirring overnight, to obtain solutions with distinct concentration, namely 6, 9, 12, 15, 18 and 24% (w/v). Density (ρ) and dynamic viscosity (η) measurements of PL solutions were carried out using an automated SVM3000 Anton Paar rotational Stabinger viscometer-densimeter in the 10 to 80 ºC temperature range and at atmospheric pressure (≈ 0.1 MPa). The density absolute uncertainty is ± 5×10^{-4} $g.cm^{-3}$, the dynamic viscosity relative uncertainty ± 1% and the temperature relative uncertainty is ± 0.02 ºC [341]. Then, approximately 40 μL of each PL solution was added to the PDMS mold and centrifuged (Hettich® Rotofix 32A) at 6000 rpm during 30 min to guarantee that the PL solution filled the pyramidal holes. Afterwards, approximately 60 μL of the same polymer solution were placed on the centrifuged layer and casted at 30 ºC overnight.

To prepare insulin-loaded MNs (each PL MNs patch incorporated 12.4 IU insulin), a two-step casting process was adopted, as described elsewhere [139]. First, insulin (2.7 mg) was dissolved into 0.3 mL of 0.01 M aqueous solution HCl and incorporated into the 24% (w/v) PL solution (0.5 mL). Approximately 40 μL of the drug-loaded PL was applied to the PDMS mold as the first layer and centrifuged. This step was repeated twice. A second layer of PL without insulin was then placed on the centrifuged first layer, followed by further centrifugation and solvent drying, according to the experimental conditions previously described to produce pure PL MNs. Finally, the PL 24% + Insulin MN patches were gently peeled off from the master molds and placed in a desiccator until further use.

3.3.3. Characterization of PL MNs patches

3.3.3.1. Morphological characterization

The obtained PL MNs were examined using a stereomicroscope (Nikon SMZ25, Tokyo, Japan) and microscope images were captured with a camera (SRH Plan Apo 2, Tokyo, Japan). Magnification power of the ocular lens was 5× and magnification of the objective lens was 5×, giving a total magnification of 25×. Image processing was performed using NIS Elements Imaging Software. The morphological analysis of MNs

was performed using scanning electron microscopy (SEM). Micrographs were obtained using a high voltage microscope (HITACHI SU 70) operated at 4.0 kV. Samples were previously coated with carbon using an EMITECH K950 coating system.

3.3.3.2. Mechanical characterization and preliminary insertion tests

Mechanical axial compressive tests were performed using a TA.XT2 Texture Analyser (Stable Micro Systems Ltd., Haslemere, UK). The MN patches were placed on the flat rigid surface of a stainless-steel base plate. An axial force was applied perpendicular to the axis of the array, at a constant speed of 0.01 $mm.s^{-1}$. The force was measured when the moving sensor touched the uppermost point of the needles. Then, the texture analyser recorded the force required to move the mount as a function of needle displacement [131].

For preliminary insertion studies, Parafilm® (Bemis Company Inc., Soignies, Belgium) was folded into eight layers to simulate the thickness of excised skin, following a simple method previously reported [144]. The MN arrays were then inserted into the Parafilm® layers using the texture analyser by applying a force of 40 N for 30 seconds. To measure the insertion ratio and depth, each layer of Parafilm® was examined under the microscope and the number of holes counted. The three samples providing the highest insertion rate (MNs prepared with 15, 18 and 24% PL) were selected for compression tests using different weights, from 450 to 1800 g per patch.

3.3.3.3. Thermogravimetric analysis

TGA of the selected samples, namely insulin, PL 24% and PL 24% + Insulin MNs, was carried out with a SETSYS Setaram TGA analyser (SETARAM Instrumentation, France) equipped with a platinum cell. Samples (5 mg) were heated from room temperature up to 800 ºC at a constant rate of 10 $ºC.min^{-1}$ under a nitrogen flow. Thermal decomposition was determined as the onset of significant weight loss (≥ 0.5%) after the initial moisture loss.

3.3.3.4. Fourier transform infrared- Attenuated total reflection spectroscopy

FTIR-ATR spectra of PL 24%, insulin and PL 24% + Insulin MNs were obtained on a Perkin-Elmer FT–IR System Spectrum BX spectrophotometer (Perkin-Elmer Inc., USA) equipped with a single horizontal Golden Gate ATR cell. To obtain each spectrum, 64 scans were acquired in the 4000–500 cm^{-1} range, with a resolution of 4 cm^{-1}.

3.3.3.5. Humidity stability testing

To study the stability of the PL-based MNs towards humidity, the PL 24% and PL 24% + Insulin MNs were stored at a high relative humidity (RH) environment, namely 75% RH. This condition was achieved by placing a saturated sodium chloride solution into a container. MNs were removed at pre-determined intervals, their weight was measured and the variation in MNs weight was determined and expressed in percentage.

3.3.3.6. Conformational stability of insulin under storage

PL 24% + Insulin MNs were stored at 4, 20 and 40 ºC for 1, 2, 3 and 4 weeks, and changes in the secondary structure of insulin were investigated by circular dichroism (CD) spectropolarimetry using a Jasco 1500 spectrophotometer, equipped with a Peltier system for temperature control. For that, stored MNs were dissolved in ultrapure water and the spectra were recorded at 20 ºC between 190 and 260 nm, at a 100 scans speed, time of 1s and 1 nm bandwidth. Each spectrum was obtained by subtracting the appropriate blank media from the experimental spectrum and was collected by averaging three spectra.

3.3.4. In vitro cell viability assays

The HaCaT cell line was purchased from Cell Lines Services (Eppelheim, Germany) and Dulbecco's modified Eagle's medium, supplemented with 10% fetal bovine serum (FBS), 2 mM L-glutamine, 1% penicillin-streptomycin (10,000 $U.mL^{-1}$), and 1% fungizone (250 $U.mL^{-1}$) from Gibco, Life Technologies (Grand Island, NY, USA). Cell viability was determined by the colorimetric 3-(4,5 dimethyl-2-thiazolyl)-2,5-diphenyl tetrazolium bromide (MTT) assay [302]. Cells were seeded in 96 wells plates at 9000 and 6000 cells *per* well for 2 and 24 h exposure, respectively. Cells were exposed to PL and insulin-loaded MNs dissolved into culture medium at 30 and 150 $\mu g.well^{-1}$ (defined previously by evaluation of 5-300 $\mu g.well^{-1}$, data not shown) and then further incubated for 2 and 24 h. HaCaT cells exposed to control medium were used as a negative control. At the end of the incubation time, 50 µL of MTT (at a concentration of 1 $g.L^{-1}$) were added to each well and incubated for 4 h at 37 °C in 5% CO_2 humidified atmosphere. After that, culture medium with MTT was removed and replaced by 150 µL of DMSO and the plate was placed in a shaker for 2 h in the dark to completely dissolve the formazan crystals. The

samples absorbance (*Abs*) was measured with a BioTek Synergy HT plate reader (Synergy HT Multi-Mode, BioTeK, Winooski, VT) at 570 nm with blank corrections.

3.3.5. Ex vivo skin insertion

Human abdominal skin tissue was obtained from female donors submitted to an abdominoplasty at *Centro Hospitalar de São João* (Porto, Portugal), after signing the respective informed consent. Approval of the Ethics Committee of *Hospital de São João* was obtained. Skin was obtained after cosmetic surgery, transported under refrigerated conditions and followed removal of the adipose tissue by blunt dissection using a scalpel (blade number 24). Then, the skin surface was washed, dried using a cotton swab, wrapped in aluminium foil and stored in a freezer at -20 °C until further use [342].

Prior to the insertion experiments, the skin was defrosted and cut into 25 mm diameter circles using a biopsy punch. Skin samples were then placed in a sealed Petri dish, on top of a cotton pad embedded in phosphate buffered saline for 1 hour to prevent dehydration. The skin samples were fixed into a rigid support using hypodermic needles and the MN arrays placed on their surface. The MNs were pressed against skin with a force of 40 N for 30 seconds using the TA.XT2 Texture Analyser (Stable Micro Systems, Ltd., Haslemere, UK). Then, the MN arrays were peeled off and the area of compression exposed to China ink for 1 min to identify the perforation sites. Residual ink was wiped from skin samples, which were then processed for histological examination. To prepare histological specimens, skin samples were embedded in Bouin's solution, fixed in 10% formalin, dehydrated and embedded in paraffin wax. Serial 7 μm thick sections were cut from each block using a pfm Rotary 3006 EM automated microtome. The skin sections were stained with haematoxylin and eosin and analysed using a Nikon Eclipse E600 microscope to determine the penetration depth [208].

3.3.6. In vitro insulin delivery

PL 24% + Insulin MNs were inserted into *ex vivo* human abdominal skin samples and secured using tape. The skin was subsequently placed in a sealed Petri dish on top of a cotton pad embedded in phosphate buffered saline for 2 h. At specified time intervals, the patches were removed from the skin samples. To determine the loading amount and residual amount of insulin in MNs, the patches were dissolved in DI water with stirring at 4 °C. The amount of insulin delivered into the skin was calculated by subtracting the amount of the peptide remaining in the MNs after insertion and on the

skin surface using tape (3 tape strips), from the amount originally introduced in the arrays at each sampling point [208].

To determine the amount of insulin in PL MNs, the absorbance of a stock solution was scanned between 250 and 310 nm using a UV-Vis Spectrophotometer Shimadzu UV-1800 and the absorption maximum was determined at 276 nm. The stock standard solution of insulin was prepared in 0.01 M HCl with a concentration of 468 µg mL^{-1}. Working standard solutions were prepared from the stock standard solution and a calibration curve (y=1.438x-0.045, r^2=0.996) was constructed in the range of 184, 221, 265, 318, 381, 395, 408, 423 and 452 µg mL^{-1} for insulin (n=3).

3.3.7. Statistical analysis

Statistical analyses were performed using GraphPad Prism Software (GraphPad Software Inc., San Diego, CA, USA). Data is presented as the mean values ± standard error. A Student's paired *t*-test was used for comparisons between data points and multiple data sets between groups were analysed with a one-way analysis of variance (ANOVA) followed by a Tukey's post hoc test, when necessary. For all comparisons, a difference of $p< 0.05$ was regarded as statistically significant. For the *in vitro* cell viability assays, data was analyzed by a one-way ANOVA followed by a Holm-Šídák test to evaluate the significance between the different MNs and cell viability was calculated with respect to control cells.

3.4. Results and discussion

The strategy followed in the present work involved the preparation of PL solutions with different concentrations, namely 6, 9, 12, 15, 18 and 24 % (w/v), followed by the fabrication of MNs by solvent casting, as illustrated in Figure 3.1 (a). The morphological characteristics, size and shape, and the mechanical performance of this set of MNs were assessed aiming to select the best MNs for the incorporation of insulin (Figure 3.1 (b)). Afterwards, the feasibility of using insulin-loaded MNs for the administration of this drug, was inferred via *in vitro* insertion tests and transdermal delivery in *ex vivo* human skin. Finally, the biocompatibility of these MNs was tested to evaluate their safety.

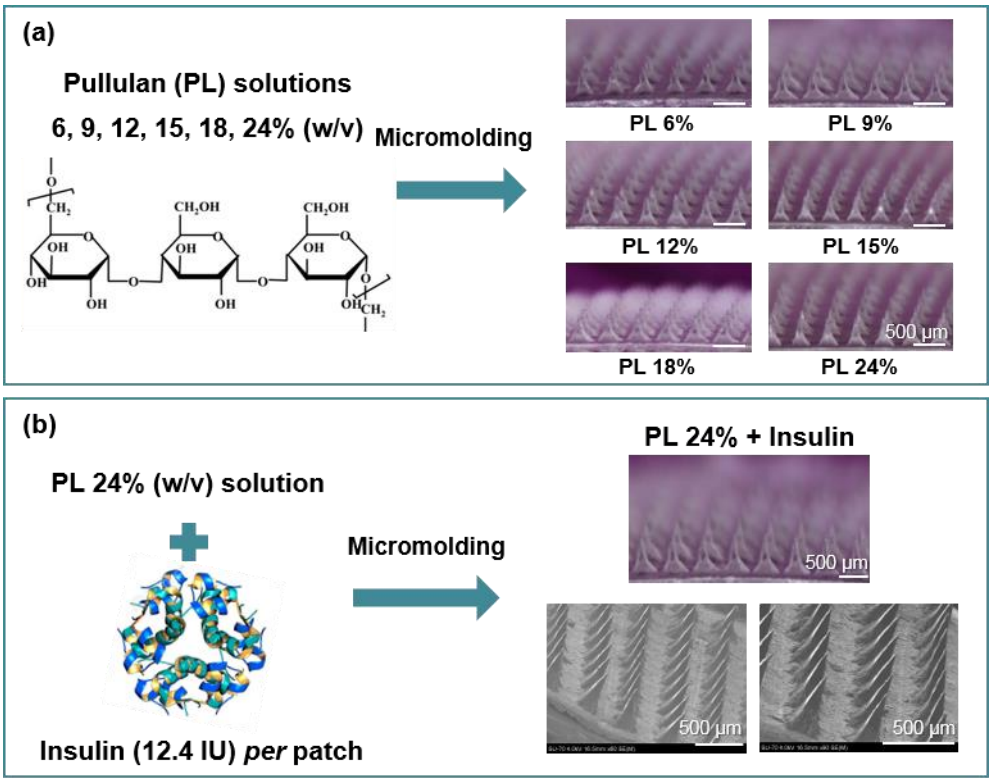

Figure 3. 1. (a) Schematic representation and Optic micrographs of PL MNs fabricated with 6, 9, 12, 15, 18 and 24% (w/v) PL solutions, and (b) schematic representation and Optic and scanning electron micrographs of PL 24% + Insulin MNs.

3.4.1. Preparation and characterization of the PL MNs patches

The preparation of MNs was carried out with pyramidal master molds (over conical ones) because they provide needles with higher mechanical strength, due to their larger cross-sectional area at the same base diameter [135]. In addition, micromolding by solvent casting was used to produce MNs owing to its simple processing coupled with low-cost and mass production potential at room temperature [9].

Firstly, PL solutions with 6, 9, 12, 15, 18 and 24% (w/v) were characterized in terms of density and viscosity (Figure 3.2), given that these two parameters play an important role in the polymer flowability and largely influence fabrication of micro-patterned polymeric devices [9]. At 20 ºC, the viscosity of the PL solutions ranged from 18 mPa s to 1148 mPa s, and the density varies between 1.01 g.cm^{-3} and 1.07 g.cm^{-3} for solutions of 6% (w/v) and 24% (w/v) respectively, confirming that these parameters increase with the polymer content. Therefore, all solutions proved to be suitable for MNs fabrication by micromolding considering the density and viscosity measurements [9].

PL MN arrays containing 225 needles (15×15) with pyramidal shape and sharp tips (≈ 3-15 µm) were successfully replicated for all PL solutions (Figure 3.1 (a)). The Optic micrographs (Figure 3.1 (a)) unveiled a homogeneous morphology, together with a

smooth and crack-free surface for all PL MNs. Therefore, the solvent-casting micromolding is indeed an attractive and scalable approach for MNs fabrication using PL solutions from 6 to 24% (w/v). Table 3.1 displays the detailed dimensions of the MNs fabricated with the different aqueous PL solutions.

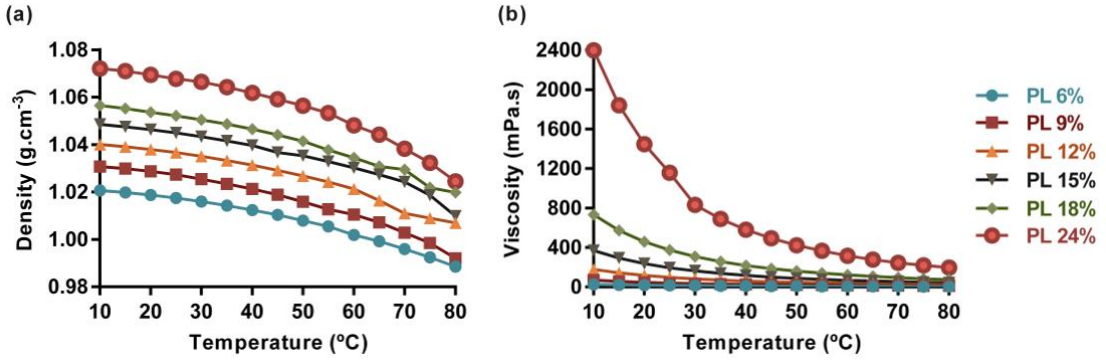

Figure 3. 2. Density (a) and viscosity (b) of PL aqueous solutions with concentration of 6, 9, 12, 15, 18 and 24 % (w/v).

Table 3. 1. Detailed dimensions of MNs fabricated using PL solutions with different concentrations (from 6 to 24 % w/v).

Dimensions of fabricated pullulan MNs						
Measurements (n=75)[a]	PL 6%	PL 9%	PL 12%	PL 15%	PL 18%	PL 24%
Height (µm)[1,ns]	445 ± 13	446 ± 18	478 ± 221	484 ± 24	490 ± 14	500 ± 14
Base width (µm)[ns]	201 ± 3	201 ± 2	202 ± 4	203 ± 6	202 ± 4	201 ± 3
Tip-to-tip distance (µm)[ns]	500 ± 1	500 ± 1	500 ±1	500 ± 1	500 ± 1	500 ± 1
Aspect ratio[ns]	2.23±0.07	2.23±0.09	2.39±0.11	2.42±0.12	2.45±0.07	2.50±0.07

[a] *n*=75, measurements performed on 15 random needles selected from 5 different arrays for each PL concentration. [1] Comparison between PL6-9%, PL12-15%, PL18-24% groups. [ns] No significant difference.

The base width of the MNs is around 200 µm and the needle pitch is around 500 µm, which reveals the successful replication of the master structure. The needle's height ranges from 445 ± 13 µm to 500 ± 14 µm and no statistical differences were found between PL 6% and 9%, 12% and 15%, 15% and 18%, and 18% and 24% (p>0.05). These data show that the increase in PL concentration leads to an increase in the average height of the corresponding MNs. The slight differences in MNs height, particularly for the MNs obtained from less concentrated solutions, when compared with the dimensions of the master mold, is certainly related with the solvent evaporation, ultimately leading to the decrease in needle's height. In this case height reduction is 17-

22%, 16-22%, 9-17%, 7-16%, 8-13% and 6-11% for MNs prepared with 6, 9, 12, 15, 18 and 24% (w/v) PL, respectively, which agrees with results reported for other biopolymeric MNs. For instance, MNs fabricated with alginate and modified with 3-aminophenylboronic acid and hyaluronic acid, using 700 µm depth master molds, reproduced microstructures of 650 µm height (7.1% reduction) [160]. Also, alginate/maltose MNs prepared using 800 µm depth master molds obtained structures with 730 µm height (8.8% reduction) [306]. The as-prepared PL MNs display similar aspect ratios, ranging between 2.23 ± 0.07 and 2.50 ± 0.07, which is in line with their comparable dimensions (Table 3.1). In the literature, it is reported that MNs with similar aspect ratio display similar mechanical properties, which allow us to expect no significant differences between the different MNs obtained in this study [9].

3.4.2. Mechanical evaluation and preliminary insertion studies of PL MNs patches

MNs should resist to skin insertion without bending or buckling, which will allow the delivery of drugs into the deepest skin layers and reach the bloodstream. In this study, the mechanical evaluation of the MNs arrays was performed by axial compression using a universal test machine. The profiles of force *versus* displacement after an axial force load are displayed in Figure 3.3 (a).

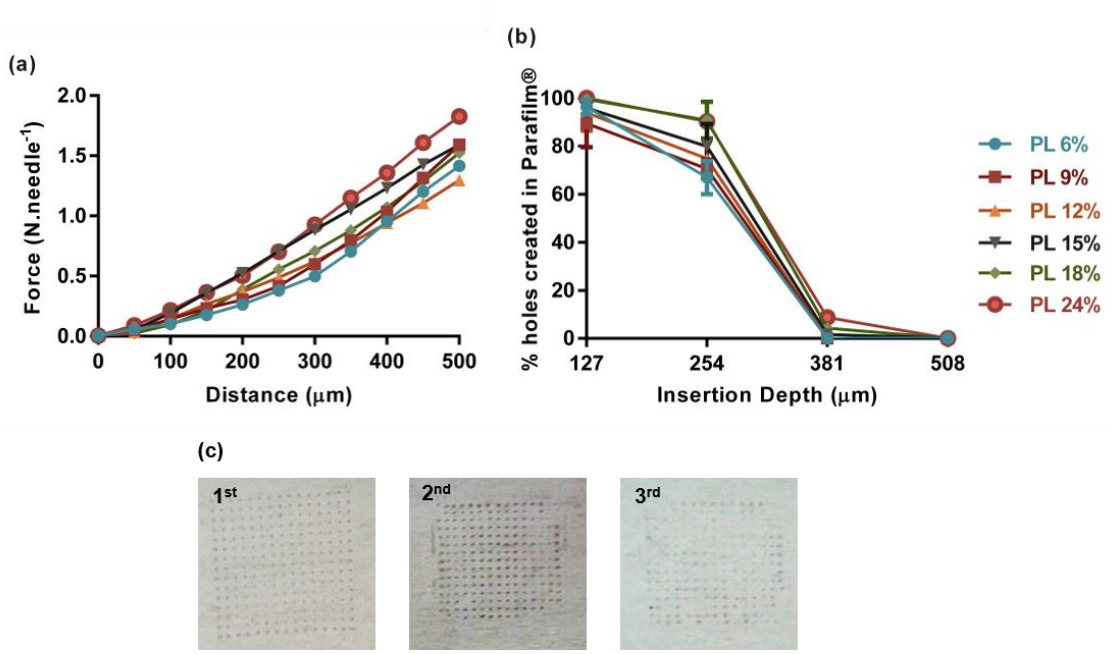

Figure 3. 3. (a) Force-displacement curves of MNs fabricated with 6, 9, 12, 15, 18 and 24% (w/v) PL solutions under an axial force load (*n*=9, measurements performed on 9 different regions of 5 arrays). (b) Insertion of PL MNs into a polymeric model membrane for skin insertion using Parafilm® (*n*=3). (c) Photos of the first, second and third Parafilm® layer after insertion using PL 24 % MNs.

The results show that all samples present the same mechanical behavior, with no abrupt discontinuity upon application of an axial force load. Instead, there is a continuous and gradual increase in force, which indicates a gradual deformation of the PL MNs, without their breaking as depicted in Figure 3.3 (a).

This mechanical profile is comparable to that reported in the literature for other MNs fabricated using other biopolymers, namely CS [208] or CMC [135]. Furthermore, the force *vs.* displacement values are on the same range of that registered for the last two biopolymers. Specifically, PL MNs produced in this study exhibited a force from 0.3-0.53 N/needle at 0.2 mm displacement, whereas CS and CMC MNs exhibited forces from 0.2 to 0.4 N/needle and up to 0.6 N/needle, respectively [135,208]. These values overcome the threshold value of 0.15 $N.needle^{-1}$ reported for skin insertion using other MNs [128] and confirm the suitability of PL MNs for skin insertion.

The skin insertion ability of these MN arrays was further investigated in a skin insertion setup composed of eight layers of Parafilm®, where an average force of 40 N was applied to each patch for 30 seconds. According to Figure 3.3 (b), all patches perforated the first and seconds layers of Parafilm®, but only the ones prepared with 15-24% of PL were able to reach the third layer. This third layer corresponds to a penetration depth of 381 μm, which is an indication that these PL MNs may reach the skin dermis (Figure 3.3 (c)). Afterwards, the MN patches that reach higher insertion depths in the skin model (PL 15, 18 and 24%) were selected to perform compression tests using different weights. In general, it was observed that a higher compression force and PL content originates higher reductions in the MNs height. The height reductions were all in the range of 5-25%. However, it was concluded that the results are not statistically significant among MN samples fabricated from 15 to 24% (w/v) PL. Based on these data, the MNs prepared with the PL solution of 24% (w/v) presented the highest insertion and, thus, were selected for the incorporation of insulin.

3.4.3. Preparation and characterization of insulin-loaded PL MNs patches

MNs prepared with a PL solution of 24% (w/v) and incorporating 12.4 IU insulin, *i.e*. 0.2 IU insulin *per* kg considering an individual of average body mass of 62 kg [343], produced arrays with a regular and homogeneous morphology (Figure 3.1 (b)). Similarly, the mechanical behaviour was comparable to that of the PL MNs without the polypeptide, showing that these needles bend and do not break under an axial force load (Figure 3.4 (a)).

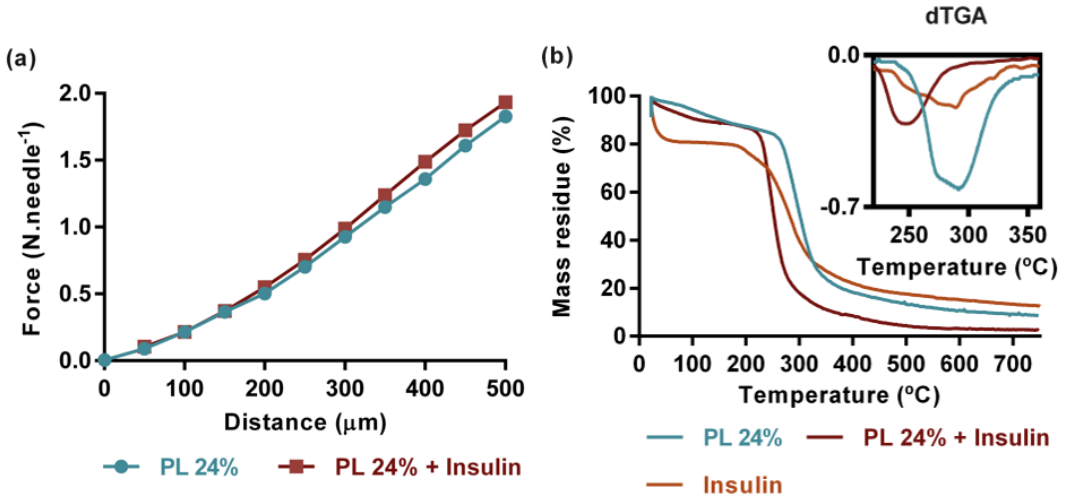

Figure 3. 4. (a) Force-displacement curves of PL 24% and PL 24% + Insulin (*n*=9, measurements performed on 9 different regions of 5 arrays). (b) Thermograms of insulin, and PL 24% and PL 24% + Insulin MNs. Inset displays the corresponding derivative plot of the thermogravimetric analysis of these samples.

The thermal stability and degradation profiles of the PL 24% and PL 24% + insulin MN, and pure insulin for comparison purposes, were assessed by TGA (Figure 3.4 (b)).The thermogram of the pure PL MNs exhibited a pattern of degradation typical of this polysaccharide, as previously reported for PL films [344,345]. A single-step weight-loss is observed with a maximum decomposition temperature (Td_{max}) of 294 ºC. At 800 ºC, a residue corresponding to 7% of the original mass of the sample is observed. Pure insulin displays an initial weight-loss due to water evaporation and the next weight loss, which starts at 230 ºC and reaches a Td_{max} at 286 ºC, is associated with insulin backbone decomposition [346].

The thermogram of PL 24% + Insulin also exhibits a single-step weight-loss, with a Td_{max} at 242 ºC. Herein, it is not possible to detect any significant weight-loss in insulin-loaded MNs related to insulin decomposition, which might be due to the low amount of insulin present in the MNs. These results show that the incorporation of insulin into the PL MNs promotes a slight decrease of the thermal stability of PL. However, considering sterilization methods for clinical application, these results show that all PL MNs studied are thermally stable and could resist autoclaving temperatures (*ca*. 121 ºC).

The hygroscopicity of PL 24% and PL 24% + Insulin MNs patches was evaluated by measuring their weight variation over one week when stored at a relative humidity of 75%. Figure 3.5 (a) shows the weight gain of these MNs patches, being observed that the weight of both PL MNs patches remained almost unaltered during the first two days and their increase after one week was less than 16%. Moreover, PL-based MNs patches

maintained their appearance, which suggests their stability in zones with high humidity storage conditions. These results are in line with the low hygroscopic nature of PL [347].

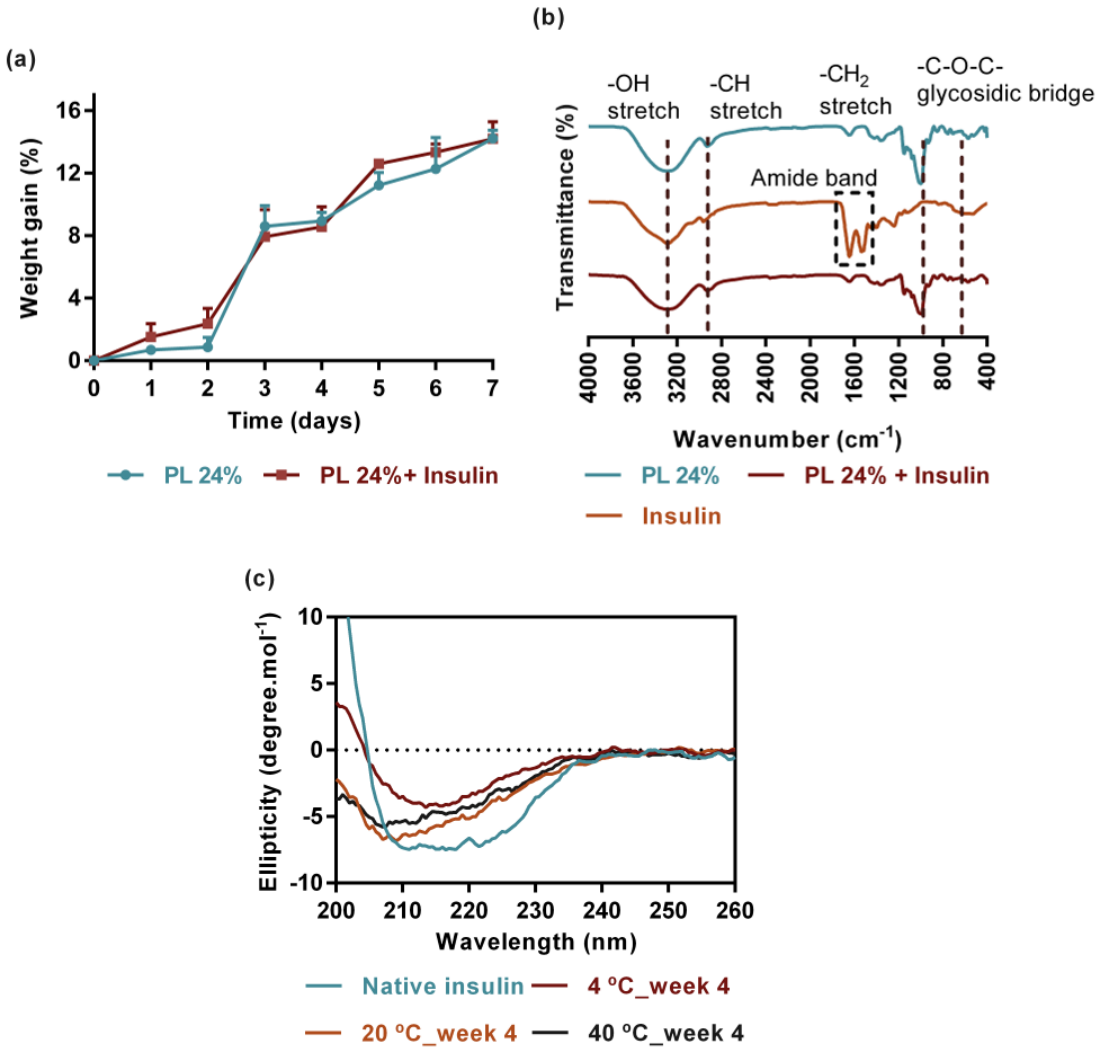

Figure 3. 5. (a) Weight gain (%) of PL 24% MNs and PL 24% + Insulin MNs when stored at 75% relative humidity for 7 days (*n*=5); (b) FTIR-ATR spectra of insulin, PL 24% and PL 24% + Insulin MNs. (c) Circular dichroism spectra of native insulin and insulin in PL 24% MNs after four weeks of storage at different temperature.

FTIR-ATR analysis was performed to assess possible interactions between the PL MNs and insulin that could affect the structural features of insulin. The FTIR-ATR spectrum of PL, as shown in Figure 3.5 (b) shows the typical bands of a polysaccharide backbone [348]. The vibrations around 3305 cm^{-1} are attributed to the OH stretching, whereas those at 2935 and 1250-1460 cm^{-1} are ascribed to CH and CH_2 stretching vibrations. The bending motion of adsorbed water (H–O–H) is evidenced at 1650 cm^{-1} and the glycosidic bridges (C–O–C), characteristic of polysaccharides, are observed at 1170-1050 cm^{-1} [348]. On the other hand, the FTIR-ATR spectrum of insulin displays a

peak at 1638 cm^{-1}, corresponding to the amide I vibration. The amide II band is usually observed at 1510-1580 cm^{-1}, representing the in-plane N–H bending and also C–N and C–C stretching vibrations [349]. After incorporation of insulin into the PL MNs, the spectrum unveils essentially the peaks of the PL matrix. This is certainly due to the low amount of insulin incorporated into the MNs. In addition, no shifts in peaks positions were observed, which indicates that there are no interactions between PL and insulin and that PL might be used as a matrix for the safe incorporation of this polypeptide, retaining its structural features. The stability of insulin loaded into the PL MNs was assessed by CD after storage at 4, 20 and 40 ºC for 4 weeks (Figure 3.5 (c)). The CD spectra of insulin displays a band at 208 nm and a slight increase at 223 nm, corresponding to the α-helix and β-structures of insulin [350]. After storage under different conditions, the CD pattern does not reflect changes in the secondary structure, suggesting that PL 24% + Insulin MNs are stable for at least one month under these storage conditions.

The qualitative measurement of the ratio of the bands showed that there is no conformational conversion of insulin [351]. Nevertheless, the shift in the wavelength might be associated with the presence of PL in solution. This result agrees with the FTIR-ATR data that suggested poor or no interactions between PL and insulin, and the integrity of the insulin structure. Overall, these results indicate that PL MNs allow the incorporation and transport of sensitive biologic drugs such as insulin, under dry conditions, enabling peptide stability without requiring cold chain distribution and storage.

3.4.4. Ex vivo skin insertion of insulin-loaded PL MNs patches

The skin insertion ratio and insertion depth of fabricated PL 24% (w/v) + Insulin MN arrays were assessed by placing the patches on top of *ex vivo* human abdominal skin and pressing with a small probe with a loading force of 40 N for 30 seconds. After applying the axial force load, removing the PL MN patches and applying a dye, the skin surface displayed black spots indicating that the dye was located within the skin (Figure 3.6 (a)).

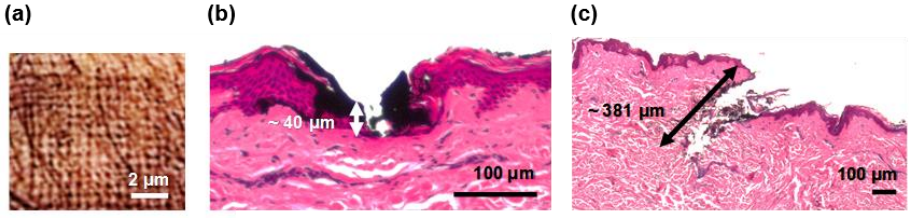

Figure 3. 6. (a) Photograph of top view of human abdominal skin after being pierced by PL MNs and stained using China ink. (b-c) Histological cross-section of human abdominal skin after being pierced by insulin-loaded PL MNs, hematoxylin and eosin staining.

Histological examination (Figure 3.6 (b-c)) successfully confirmed skin perforation, with the black dye selectively staining the sites of insertion. The PL 24% + Insulin MNs created puncture sites with an insertion depth between 40 and 381 μm. These results are comparable with published data, in which starch/gelatin MNs of 600 μm height (50 μm higher than these PL MNs), used also for insulin administration, created skin puncture sites of about 200 μm [139]. The differences in skin insertion depth may be due to natural skin elasticity [311]. Overall, these results reinforce the ability of MNs to cross the *SC* and epidermis and reach the dermis layer, using PL as the unique component of the MN arrays.

3.4.5. In vitro dissolution of PL MNs and insulin delivery

To evaluate the *in vitro* dissolution of the PL MNs, arrays of PL 24% + insulin were inserted into *ex vivo* human abdominal skin for 5, 15, 30, 50 and 120 min. After peeling off the MNs patches from the skin, it was observed that they gradually became smaller with increased insertion times. Furthermore, complete needle dissolution was attained 120 min after insertion due to contact with the extracellular matrix. PL 24% + Insulin MNs exhibited a slow initial insulin release within the first 30 min, followed by a quicker release over time (Figure 3.7).

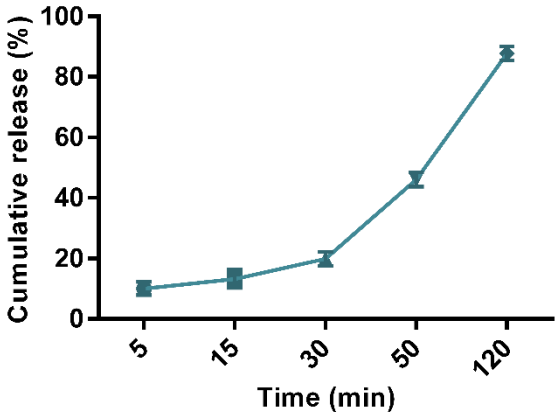

Figure 3. 7. *In vitro* dissolution of insulin to *ex vivo* human abdominal skin (*n*=3).

The PL dissolution in the first 30 min resulted into a release of 19% of the insulin located at the surface of the needles. Then, the gradual contact with the extracellular matrix provided a continuous insulin release with approximately 87% released 120 min after insertion.

3.4.6. In vitro cytotoxicity assay

Finally, to test the safety of these MNs, the cytotoxicity of pure PL and insulin-loaded PL MNs was evaluated towards human keratinocytes. The results showed that both PL and insulin-loaded polymeric mixtures were non-cytotoxic (Figure 3.8), considering that a material is cytotoxic if a reduction of 30% in cell viability is detected (ISO 10993-5:2009(E)).

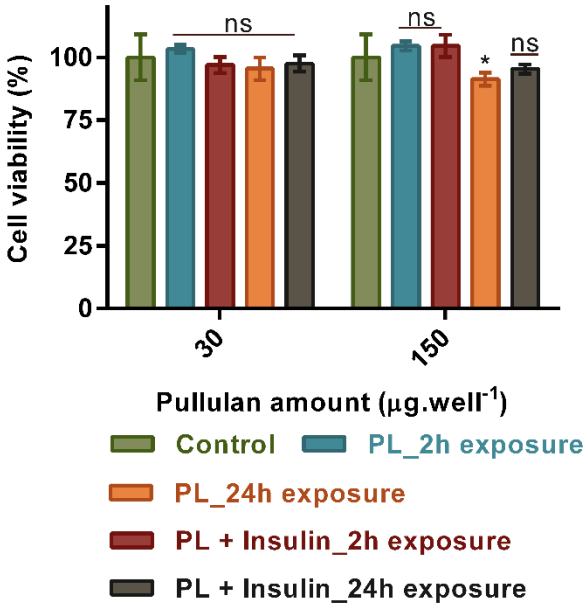

Figure 3. 8. Cell viability (%) of HaCaT cells upon exposure to 30 and 150µg pullulan *per* well with and without insulin (n=12, two independent experiments, ^{ns}: no significant difference and * statistically significant differences (p<0.05) relative to control).

After 2 h of exposure, the time previously determined for needle dissolution using human abdominal skin, all samples (with different amounts of PL MNs) provided normal cell growth values. After 24 h of exposure, a slight decrease in cell viability was achieved when using 150 µg PL *per* well, however, cell viability was still within the non-cytotoxic range. Overall, these results reinforce the safety of PL for biomedical applications, in particular for MN devices, which disrupt the upper layers of the skin and directly contact with the epidermal and dermal skin layers.

3.5. Conclusions

In this work, dissolvable MNs arrays fabricated using PL were prepared for the transdermal administration of insulin. The as-prepared PL MN arrays exhibited good mechanical properties, which enabled the perforation of human skin. In addition, insulin

can be incorporated into PL MNs with no changes in its secondary structure for at least one month of storage at 4, 20 and 40 ºC. PL MNs incorporating insulin were evaluated for transdermal delivery, showing that 87% of insulin was released to the skin in the first 120 min. The non-cytotoxic nature of these MNs support their safe use and hence, this work suggests that PL MNs incorporating insulin may in the future be a transdermal alternative to its administration, improving the quality of life of diabetic patients.

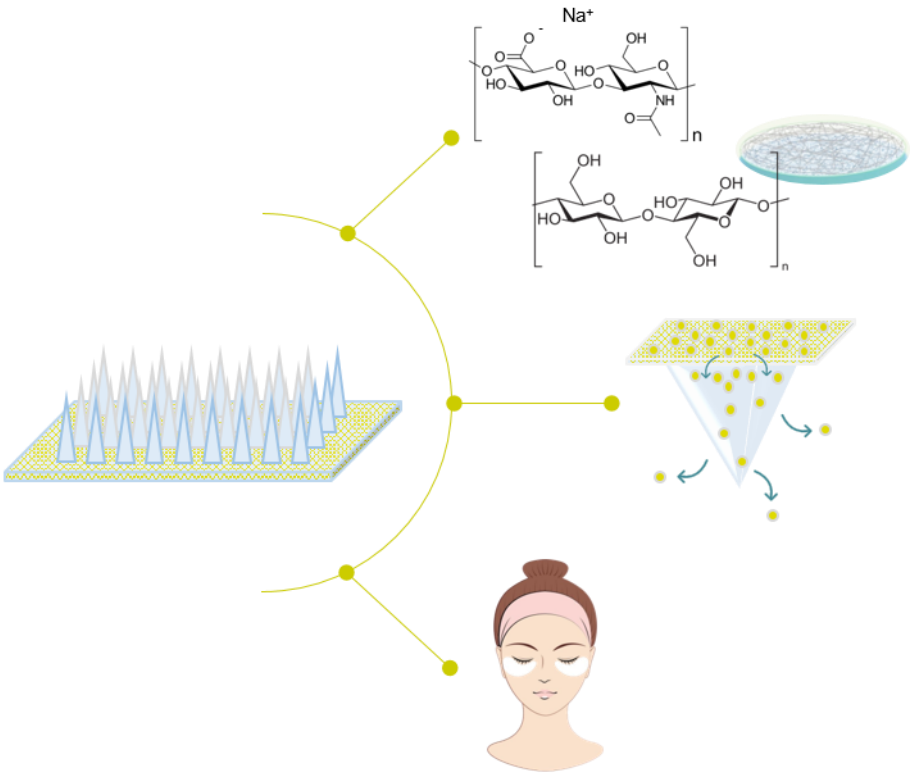

CHAPTER 4. BACTERIAL NANOCELLULOSE-HYALURONIC ACID MICRONEEDLE PATCHES FOR SKIN APPLICATIONS: *IN VITRO* AND *IN VIVO* EVALUATION

This chapter is adapted from the published manuscript:
Daniela F. S. Fonseca, Carla Vilela, Ricardo J. B. Pinto, Verónica Bastos, Helena Oliveira, José Catarino, Pedro Faísca, Catarina Rosado, Armando J. D. Silvestre, Carmen S. R. Freire, Bacterial nanocellulose-hyaluronic acid microneedles for skin applications: *In vitro* and *in vivo* evaluation, Materials Science and Engineering: C, (118) 2021.

4.1. Abstract

The aim of the present study was to develop innovative patches for dermo-cosmetic applications based on dissolvable HA MNs combined with BC as the back layer. HA was employed as an active biomacromolecule, with hydrating and regenerative properties and volumizing effect, whereas BC was used as support for the incorporation of an additional bioactive molecule. Rutin, a natural antioxidant, was selected as the model bioactive compound to demonstrate the effectiveness of the system. The obtained HA-MNs arrays present homogenous and regular arrays, with 200 μm in base width, 450 μm in height and 500 μm tip-to-tip distance, and with sufficient mechanical force to withstand skin insertion with a failure force higher than 0.15 N per needle. The antioxidant activity of rutin was neither affected by its incorporation in the MNs system nor by their storage at room temperature for 6 months. Preliminary *in vivo* studies in human volunteers unveiled their safety and cutaneous compatibility, as no significant changes in barrier function, *SC* hydration nor redness were detected. These results confirm the potentiality of this novel system for skin applications, *e.g.* cosmetics, taking advantage of the recognized properties of HA and the capacity of BC to control the release of bioactive molecules.

4.2. Introduction

Skin aging, as a process of chronological physiological changes induced by intrinsic and extrinsic factors, reflects a progressive loss of structural and functional cell integrity [352,353]. The clinical manifestation of skin aging is characterized by the loss of elasticity, wrinkles, rough-texture, and dry cutaneous appearance, in many aspects due to a decrease in the production of collagen, elastin and HA, the main constituents of the dermal extracellular matrix [352]. An effective and straightforward approach to counteract the effects of the aging process relies on the application of facial fillers and other cosmetic ingredients through skincare routine [354,355].

Anti-aging cosmetic products are mainly developed as semisolid formulations, such as creams or gels, for topical application. The topical administration of these cosmetics is easy, convenient, and safe. Nevertheless, the efficacy of these formulations is reduced due to the barrier function provided by skin, which limits the penetration of active compounds [354]. To overcome the skin penetration issues of the components of the dermal extracellular matrix, the injection of fillers was introduced as a therapeutic technology [355,356], providing superior rejuvenating effects when compared with conventional topical formulations. However, this is a costly, invasive and often painful approach that may cause systemic allergies [355,356], and that should only be performed by a trained healthcare professional. Taking in mind the drawbacks of these strategies, there is still a need for advanced technologies to increase the permeation of cosmetic ingredients while minimizing their losses.

In this vein, MNs have emerged as an alternative, non-invasive, and effective technology for cosmetic applications [9,357]. Conceptually, MNs are micron-scale needles placed on the underside of a patch, that enable a bypass of the *SC* and, thus, improve permeation of molecules into the skin [9]. The self-application and the minimally invasive nature of MNs are key attributes of these devices that have been studied as a platform for the delivery of a panoply of drugs and vaccines, as well as cosmetics [6].

HA has already been used in the production of MNs for cosmetic purposes, as the only active ingredient [358] or in combination with ascorbic acid or retinyl retinoate [177,359,360]. HA is a widely used cosmetic ingredient, being found in most of the formulations claimed as anti-aging or moisturizing [356,361]. This biomacromolecule is a glycosaminoglycan naturally found in the extracellular matrix of cells and human skin and as an endogenous component that creates a viscoelastic network that fills the spaces between collagen and elastin in the dermal extracellular matrix [355]. HA has a hydrophilic nature and strong water-binding ability, having an immediate plumping effect. Furthermore, HA stimulates fibroblasts and collagen production, exhibiting strong

aesthetic efficacy [356,361]. On the other hand, HA-based MNs have also been studied as minimally invasive devices for the delivery of different therapeutic agents, such as insulin [170] and doxorubicin [155]. Drug-loaded HA MNs systems are typically formulated by directly incorporating the active molecules as part of the polymeric mixture, before MNs production [156,170]. However, the addition of poorly water-soluble molecules usually requires their encapsulation [155,174], which is time-consuming and more expensive.

Another naturally occurring material with a well-known history in the cosmetics field is BC, a nanostructured biomaterial with an ultrafine fiber network, which allows its use as a macromolecular support for the incorporation of different biomolecules [362]. This biopolymer has been used for cosmetic purposes in the form of facial masks, enriched with active compounds (*e.g.*, plant extracts, phenolic compounds [363] or caffeine [364]), due to its peculiar porous structure, as well as water retention ability, moldability and good mechanical properties [365].

In this context, the purpose of this work is to combine the features of both biomaterials in a MN patch that employs HA as the needle matrix and BC as a back layer that mechanically support the MNs array and enables the incorporation of active ingredients. In this study, as a proof of concept, rutin was used as a model active ingredient to demonstrate the effectiveness of the system. Rutin is a natural flavonol glycoside, also referred to as quercetin-3-rutinoside, rutoside, sophorin, or vitamin P [366], with antioxidant properties and has shown anti-aging effects on human dermal fibroblasts [367]. It is hypothesized that the HA MNs will mechanically cause a temporary disruption in the *SC* barrier, enabling the permeation of the actives in the patch, and also improve the overall skin appearance, due to its plumping, smoothing and filling effect [368]. Then, BC will enable the release of bioactive molecules (rutin) through the microchannels created by the HA needles. Therefore, the innovative combination of the reinforcing ability and peculiar 3D porous structure of BC membranes with the features of HA, in the form of MNs patches, is expected to create a multifunctional tool for skin treatment, including skin aging applications. The obtained MNs patches were characterized in terms of their morphology, mechanical behavior, hygroscopicity, *in vitro* cytocompatibility, and rutin release profile. Furthermore, their tolerance was investigated *in vivo* using human volunteers.

4.3. Materials and methods

4.3.1. Chemicals and materials

HA sodium salt (MW 403.31 kDa) was purchased from Molekula Group (Darlington, UK). Rutin hydrate (≥ 95%) was purchased from Glentham Life Sciences (Wiltshire, UK). Sodium phosphate dibasic (≥99.0%), sodium phosphate monobasic (≥99.0%), 2,2-diphenyl-1-picrylhydrazyl (DPPH$^{\bullet}$, 95%), MTT (98%), DMSO (≥99.7%) were purchased from Sigma-Aldrich (St Louis, MO). HPLC-grade methanol and ethanol were supplied from Fisher Scientific Chemicals (Loures, Portugal), and ultrapure water was obtained using a Milli-Q® Integral Water Purification System. The HaCaT cell line was purchased from Cell Lines Services (Eppelheim, Germany) and Dulbecco's modified Eagle's medium, supplemented with 10% fetal bovine serum (FBS), 2 mM L-glutamine, 1% penicillin-streptomycin (10,000 U.mL^{-1}), and 1% fungizone (250 U.mL^{-1}) from Gibco, Life Technologies (Grand Island, NY, USA). BCwas biosynthesized in our laboratory in the form of wet membranes using the *Gluconacetobacter sacchari* bacterial strain and following established static culture procedures [369].

4.3.2. Preparation of rutin-loaded BC membranes (BC-R)

The rutin-loaded BC membranes (BC-R) were prepared as follow, wet BC membranes (7 cm diameter and 0.8 cm thickness) were compressed between two acrylic plates using absorbent paper to remove 50-60% of their water content. Then, the drained BC membranes were soaked in 8 mL of an aqueous phosphate buffered solution (pH 7.4) of rutin (69.87 μg.mL^{-1}) until complete absorption of the solution, resulting in membranes with 14.5 μg.cm^{-2} of rutin. Finally, the membranes were dried at 30 °C for 17 h (the time necessary to attain a constant weight) and then cut into squares of 7×7 mm^2.

4.3.3. Fabrication of BC-HA MNs patches

Pyramidal HA microneedle arrays (square array of 8 mm, 15 × 15 needles, needle height 550 μm, needle base 200 μm, needle pitch 500 μm) were produced using female molds of polydimethylsiloxane (PDMS) (Micropoint Technologies Pte Ltd., Singapore) by solvent casting. Firstly, a 5 % (w/v) HA solution was prepared by dissolving HA in Mili-Q water under constant stirring. Then, approximately 50 mg of HA solution was added to the PDMS mold and centrifuged (Hettich® Rotofix 32A) at 6000 rpm for 10 min to guarantee that the biopolymer solution filled the pyramidal holes. Afterward, approximately 50 mg of the same HA solution were placed on the centrifuged layer and

casted at 30 °C overnight. To prepare MNs with BC as a back layer, with and without rutin (HA-BC and HA-(BC-R), respectively), the HA MNs were prepared as aforementioned, but after 4-h of the casting step, the BC or BC-R membranes were placed on the top of the mold and left to dry at 30 °C overnight.

4.3.4. Characterization of HA MNs patches

4.3.4.1. Morphological characterization

The morphology of all HA-based MNs was firstly evaluated using a stereomicroscope (Nikon SMZ18, Tokyo, Japan) and microscope images were captured with a camera (SRH Plan Apo 2, Tokyo, Japan). The magnification power of the ocular lens was 5×, and magnification of the objective lens was 1.5, 5 and 8×, giving a total magnification of 7.5, 25, or 40×, respectively. Image processing was performed using NIS Elements Imaging Software (4.50.00 (Built 1117), 2017). Measurements were performed on 15 needles randomly selected from 5 different MNs arrays for each sample.

Morphological analysis of the as-prepared MNs was further performed using scanning electron microscopy (SEM). Micrographs were obtained using a high voltage microscope (HITACHI SU 70) operated at 15.0 kV. Samples were previously coated with carbon using an EMITECH K950 coating system.

4.3.4.2. Mechanical characterization and preliminary insertion tests using a model system

Mechanical axial compressive tests were performed on HA, HA-BC, and HA-(BC-R) MNs, using a TA.XT2 Texture Analyzer (Stable Micro Systems Ltd., Haslemere, UK). The MN patches were placed on the flat rigid surface of a stainless-steel base plate. An axial force was applied perpendicular to the axis of the array, at a constant speed of 0.01 $mm.s^{-1}$. The force was measured when the moving sensor touched the uppermost point of the needles. Then, the texture analyzer recorded the force required to move the mount as a function of needle displacement[131]. For preliminary insertion studies, Parafilm M® (Bemis Company Inc., Soignies, Belgium) was folded into eight layers to simulate the thickness of excised skin, following a simple method previously proposed [144]. The MN arrays were then inserted into the Parafilm M® film using the texture analyzer by applying a force of 40 N for 30 seconds. To measure the insertion ratio and depth, each layer of Parafilm M® was examined under the microscope and the number of holes counted.

4.3.4.3. Fourier transform Infrared-attenuated total reflection

FTIR-ATR spectra of HA, HA-BC, and HA-(BC-R) MNs, as well as BC and rutin, for comparison, were obtained on a Perkin-Elmer FT–IR System Spectrum BX spectrophotometer (Perkin-Elmer Inc., USA) equipped with a single horizontal Golden Gate ATR cell. To obtain each spectrum, 64 scans were acquired in the 4000–500 cm^{-1} range, with a resolution of 4 cm^{-1}.

4.3.4.4. Thermogravimetric analysis

TGA of HA, HA-BC, and HA-(BC-R) MNs, as well as BC and rutin, was carried out with a SETSYS Setaram TGA analyzer (SETARAM Instrumentation, Lyon, France) equipped with a platinum cell. Samples were heated from room temperature up to 800 °C at a constant rate of 10 $°C.min^{-1}$ under a nitrogen flow of 20 $mL.min^{-1}$.

4.3.4.5. Humidity stability testing

The as-prepared HA, HA-BC, and HA-(BC-R) MNs were placed in a dry desiccator for two days before the uptake measurements. Then, MNs were stored at room temperature in a chamber with high relative humidity (RH=98%) using a saturated potassium sulfate solution [370]. At pre-determined intervals, the samples were removed, the weight of MNs was measured and the increase in MNs weight was determined, following the equation below:

$$Moisture\ uptake(\%) = ((W_n - W_i)/W_i) \times 100$$

where W_i is the initial weight, and W_n is the weight of the MN array after moisture uptake at t=*n*.

4.3.4.6. Antioxidant activity

The antioxidant activity of rutin incorporated in the MNs was determined by the $DPPH^{\bullet}$ radical scavenging method [371]. To perform the experiments, the following samples were used: BC-R membranes immediately after preparation, HA-(BC-R) MNs immediately after fabrication, and HA-(BC-R) MNs after storage in a desiccator, covered with aluminum foil, at room temperature over 24 weeks. Rutin (0.005-0.01 % (w/v)) was dissolved in methanol, whereas the BC-R membranes and HA-(BC-R) MNs were suspended in methanol and left under agitation in the dark, up to 24 h, to solubilize and/or release rutin. For the study, rutin methanolic solutions prepared from BC-R and HA-(BC-

R) MNs were prepared to reach a concentration ranging from 5.8 to 50 μg.mL^{-1}. In this work, 100 μL of 0.1 mM DPPH$^{\bullet}$ methanolic solution were added to 50 μL of rutin methanolic solutions (from rutin, BC-R and HA-(BC-R) MNs) and diluted with 50 μL of methanol. After mixing, the samples were gently shaken and kept in the dark at room temperature for 30 min. The absorbance was measured at λ=517 nm using a 96-well microplate reader (Synergy-HT, Biotek Instruments, USA) against methanol as the blank. A calibration curve was obtained using rutin as standard, with concentrations between 5 and 50 μg.mL^{-1} ($y = 1.83x + 19.98$, r^2=0.996) for DPPH$^{\bullet}$ assay. The percentage of DPPH$^{\bullet}$ radical scavenging activity was calculated as follows:

$$Scavenging\ activity(\%) = \left[\left(Abs_{control} - Abs_{sample}\right)/Abs_{control}\right] \times 100$$

Then, the percentage of DPPH$^{\bullet}$ scavenging versus the concentration of samples was plotted. The concentration of the sample necessary to decrease the DPPH$^{\bullet}$ concentration by 50% was obtained by interpolation from linear regression analysis and denoted IC_{50} value (μg.mL^{-1}). Triplicate measurements were carried out for each sample, with three replicates.

4.3.4.7. In vitro cell viability assays

The manipulation and growth of the HaCaT cell line, a nontumorigenic immortalized human keratinocyte cell line, were performed and adapted to meet CLS recommendations. HaCaT cells were aseptically grown in Dulbecco's modified Eagle's medium, supplemented with 10% fetal bovine serum (FBS), 2 mM L-glutamine, 1% penicillin-streptomycin (10,000 U.mL^{-1}), and 1% fungizone (250 U.mL^{-1}), at 37 °C in a humidified atmosphere with 5% CO_2, as previously described [301]. Cells were daily observed for confluence and morphology using an inverted phase-contrast Eclipse TS100 microscope (Nikon, Tokyo, Japan).

Cell viability was determined by the colorimetric 3-(4,5 dimethyl-2-thiazolyl)-2,5-diphenyl tetrazolium bromide (MTT) assay. HaCaT cells were seeded in 96 wells plates at 6000 cells.well^{-1} for 24 h exposure. Extracts were prepared by placing the materials, namely HA and HA-(BC-R) MNs, a BC membrane, and rutin in contact with the culture medium for 24 h. Then, cells were exposed to 100 μL of the extracts and further incubated for 24 h. HaCaT cells exposed to control medium were used as a negative control. At the end of the incubation time, 50 μL of MTT (at a concentration of 1 g L^{-1}) were added to each well and incubated for 4 h at 37 °C in a 5% CO_2 humidified atmosphere. After that, the culture medium with MTT was removed and replaced by 150 μL of DMSO for formazan crystal solubilization. The samples absorbance (Abs) was

measured with a BioTek Synergy HT plate reader (Synergy HT Multi-Mode, BioTeK, Winooski, VT) at 570 nm.

4.3.5. Ex vivo skin insertion

In vitro skin insertion studies were performed using pig-ears skin immediately collected after animals were sacrificed at a local slaughterhouse (Raporal S.A, Lisbon) during the common procedure for processing of meat for human consumption. Skin samples were rinsed with cold water, and damaged skin was rejected. Full-thickness skin membranes were prepared by separating the whole skin carefully from the underlying cartilage and stored at -20 °C until required. Prior to the diffusion experiments, skin was defrosted and cut into squares of 2×2 cm^2. The skin samples were fixed into a rigid support using thumbtacks and the MN arrays placed on their surface. The MNs were manually pressed against the skin for 30 seconds, applying a force that could use to press a stamp into an envelope or to push an elevator button [27], and peeled off, followed by exposure of the area of compression to China ink for 1 min. Residual ink was wiped from skin samples, which were then processed for histological examination. To prepare histological specimens, skin samples were fixed in 10% formalin, dehydrated and embedded in paraffin. Serial 5 µm thick sections were cut from each block using a HM325 microtome (Microm). Skin sections were stained with hematoxylin and eosin and analyzed with a CX31 microscope (Olympus) to determine penetration depth. Images were acquired with the NanoZoomer-SQ Digital slide scanner (Hamamatsu Photonics).

4.3.6. In vitro rutin delivery

4.3.6.1. Dissolution assays

The HA-(BC-R) MNs were placed in 50 mL of ethanol: PBS (pH 7.4) (20:80), and rutin release was then carried out at 32 °C under magnetic stirring. At determined time intervals, 3 mL of solution was withdrawn and immediately replenished with an equal volume of fresh solution to maintain a constant volume. Rutin quantification in each aliquot was determined by UV-Vis spectrophotometry (Annexes 1.1 and 2.1) at λ=362 nm (n=3) using a UV-Vis Spectrophotometer Shimadzu UV-1800. Standard solutions in the range of 10-46 $\mu g.mL^{-1}$ were prepared and the absorption data was plotted against the concentration and examined for linearity. Linear regression was obtained from three independent calibration curves, over the range of 10-46 $\mu g.mL^{-1}$, with a regression line equation of $y = 0.0226x - 0.054$. The correlation coefficient shows a satisfying linear

regression, with a goodness-of-fit above 0.99 (r2 = 0.994). The rutin content at each time was plotted as a cumulated percentage release as follows:

$$C_{cumulative} = C_n + [(3 \times C_{n-1})/50]$$

where C_{n-1} and C_n are the rutin concentrations at time *n-1* and *n*).

4.3.6.2. In vitro skin permeation

Permeation studies were performed using pig-ears skin collected and prepared as previously described. Prior to the diffusion experiments, skin was defrosted and trimmed to fit the Franz diffusion cell apparatus. *In vitro* permeation experiments (*n*=5) were conducted on glass Franz type diffusion cells with a diffusional area of 0.95 cm^2 and a receptor compartment of 3.9 mL. The receptor phase contained ethanol: PBS (20:80) and the skin temperature was ≈ 32 °C. Full-thickness skin was fixed between the donor and the receptor phase with the *SC* facing upwards into the donor compartment. HA-(BC-R) arrays were perpendicularly pressed against the skin for 30 seconds, manually, whereas the rutin-loaded BC membranes were placed directly onto the skin. Samples from the receptor phase were withdrawn at 4, 6, 9 and 12 h and immediately replenished with an equal volume of fresh receptor phase. Rutin content in the samples was analyzed by UV spectrophotometry using a UV-Vis Spectrophotometer Evolution® 300 from Thermo Scientific (Hertfordshire, England) and detection was performed at its maximum absorption wavelength. Rutin concentration was determined from extrapolation of a calibration curve ($y = 0.0519x + 0.0071$, r^2=0.9974), prepared using solutions of 2-10 $\mu g.mL^{-1}$.

4.3.7. In vivo skin tolerance assays

In vivo skin tolerance tests were performed with 13 female and male volunteers, with no pre-existing skin conditions, with ages between 22 and 53 years old, after informed consent. The procedures were approved by the local responsible committee on human experimentation and performed in accordance with the Helsinki Declaration. Volunteers were provided with information on the study, the risks associated, and the confidentiality of all data upon recruitment. The information leaflet is available in the Annex 1.2.

BC-HA MNs patches were applied on the volar forearms of the volunteers for 24 h using an occlusive epicutaneous patch (Finn Chambers, Epitest, Finland). The MNs were inserted manually by the same person to guarantee repetitiveness of the application conditions. When pressing MNs against skin, volunteers felt an itching sensation and after application the MN arrays stayed in place, indicating a successful skin perforation.

A negative control (empty patch) was also used. Cutaneous compatibility was conducted by the non-invasive measurement of cutaneous biophysical properties in each tested site. *SC* hydration was determined with a Corneometer CM825 (CK Electronics GmbH, Germany), and skin barrier was probed with a Tewameter TM 300 (CK Electronics GmbH, Germany), accordingly to published guidelines [372]. To quantify the absence or grades of erythema, a colorimetry method was performed using a Minolta Chroma Meter CR-300 (Minolta Camera Co., Japan), in which the parameter a* reflects the red chromaticity. All measurements were performed in triplicate, using the CIE Lab system [373]. The basal values were determined before patch application with or without MNs, and further measurements were made at 24 h. Aiming to minimize the effect of inter-individual variability, the results were analyzed as the ratio between the value obtained after patch application and the basal values. At the end of the experiment, a structured questionnaire consisting of 5 questions was developed. The paper-based written questionnaires were provided to the volunteers to evaluate their feedback on the sensation and suitability of MNs application (scale-barely feeling it to strongly feeling it, from 0 to 5) (Annex 1.3).

4.3.8. Statistical analysis

Statistical analyses were performed using GraphPad Prism Software (GraphPad Software Inc., San Diego, CA, USA). Data is presented as the mean values ± standard error. A Student's paired t-test was used for comparisons between data points, and multiple data sets between groups were analyzed with a one-way analysis of variance (ANOVA) followed by a Tukey's post hoc test when necessary. For all comparisons, a difference of $p < 0.05$ was regarded as statistically significant. For the in vitro cell viability assays, data was analyzed by a one-way ANOVA followed by a Holm-Šídák test to evaluate the significance between the different MNs and cell viability was calculated with respect to control cells.

4.4. Results and discussion

The present work focused on the design of HA-based MNs patches that incorporate a BC membrane, loaded with a bioactive molecule (rutin), as a back layer of the MNs array (Figure 4.1 (a)).

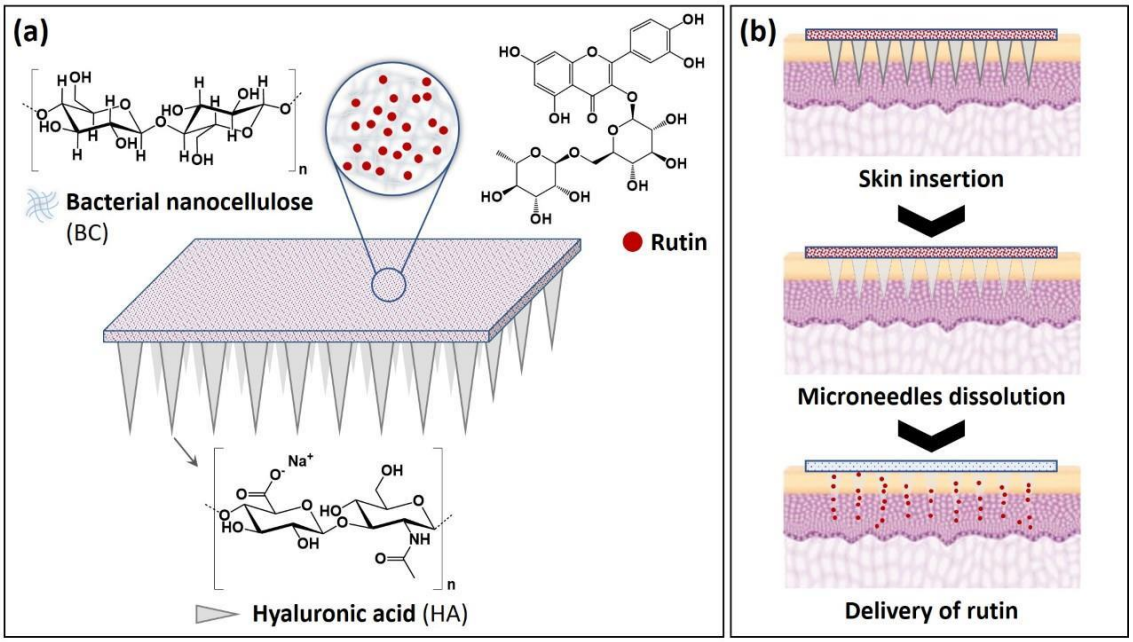

Figure 4. 1. (a) Schematic representation of the HA-(BC-R) MNs structure and (b) of the process of HA-(BC-R) MNs insertion and rutin release.

These MNs were designed to successfully insert into the skin and dissolve the HA matrix, releasing afterward the bioactive molecules from the BC membrane that supported the HA MNs (Figure 4.1 (b)). The obtained MNs patches were characterized in terms of their morphology, mechanical performance, ability to preserve the antioxidant properties of rutin, and rutin dissolution. The *in vitro* cytotoxicity of these MNs was also tested to infer about their safety for skin application. To prove the feasibility of this system, *ex vivo* porcine skin was used for tests and transdermal delivery. Finally, the cutaneous compatibility of these MNs patches was evaluated *in vivo* using human volunteers.

4.4.1. Morphological characterization

The fabricated HA MNs patches consisted of 225 needles (15×15) lined up, over a square array of 0.8 cm side (Figure 4.2 (a-c) (1)). The needles present a square-base and pyramidal shape, with a regular and uniform morphology and sharp tips (Figure 4.2 (a-c) (1)), which are fundamental for a good skin insertion ability [128]. No agglomerates or air bubbles were found along the needle's body, confirming the successful fabrication of HA MNs by solvent casting, even when the BC membrane was placed on the top of the micromolds. The optic micrographs of HA-(BC-R) MNs revealed the yellowish rutin-loaded BC back layer and clear HA needles, confirming that rutin was mainly kept in the BC membrane during the preparation procedure.

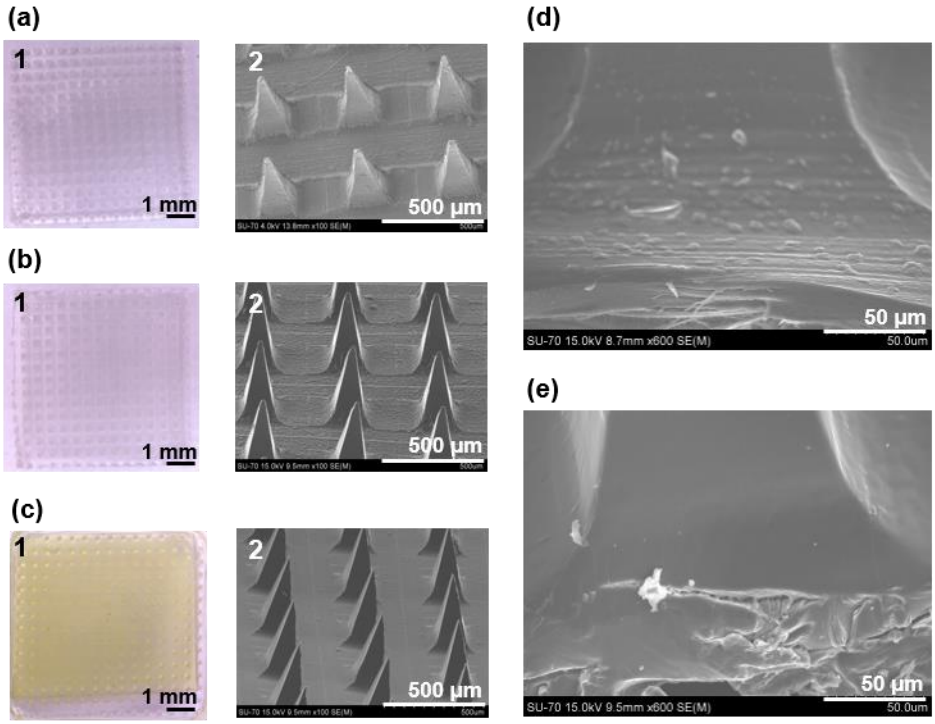

Figure 4. 2. (a) Top view of HA, (b) HA-BC and (c) HA-(BC-R) MNs. (1-2) Optic micrographs and (3) SEM of MNs. (d) Cross-section micrographs of HA-BC and (e) HA-(BC-R) MNs.

SEM analysis unveiled a smooth and regular morphology for all MN arrays (Figure 4.2 (a-c) (2)), similarly to that reported in the literature for other HA-based MNs [155,170]. Moreover, the presence of BC as a back layer is displayed in the cross-section micrographs, with the lamellar structure of BC membranes visible in the HA-BC MNs systems in Figure 4.2 (d). Regarding the HA-(BC-R) MNs, the BC membrane is also visible, but in this case, the lamellar structure is not perceived because it is filled with rutin molecules. Regarding dimensions, the resulting MNs measured 456, 472 and 460 µm in height for HA, HA-BC, and HA-(BC-R) MNs, respectively (Table 4.1). These height values allow these MNs to be able to disrupt the *SC* but not reach the nervous on skin and punch the blood vessels, confirming their non-invasive nature.

Table 4. 1. Detailed dimensions of MNs fabricated using HA, BC, and rutin.

Dimensions **of fabricated HA MNs**			
Measurements (n=75)[a]	HA	HA-BC	HA-(BC-R)
Height (µm)[ns]	456 ± 33	472 ± 18	460 ± 26
Base width (µm)[ns]	200 ± 2	200 ± 1	200 ± 2
Tip-to-tip distance (µm)[ns]	500 ± 2	500 ± 1	500 ± 2
Aspect ratio[ns]	2.26 ± 0.16	2.26 ± 0.14	2.28 ± 0.14

[a] n=75, measurements performed on 15 random needles selected from 5 different microneedle arrays for each composition. [ns]: no significant difference.

The base measured about 200 µm, and the space between two needles was 500 µm on average, as expected considering the dimensions of the PDMS master molds.

Comparing the different MNs, it is visible that the incorporation of BC as a back layer did not interfered in the solvent evaporation as no significant differences were detected in the needles' homogeneity and, and therefore, in their aspect ratio.

4.4.2. Mechanical evaluation and preliminary insertion tests

To assure successful application and DD, MNs must insert into skin without failure [128]. To evaluate the mechanical failure force of MNs, the axial force load *vs* displacement behaviour was determined using a texture analyzer. Figure 4.3 (a) unveils the profiles of the failure force against the distance travelled from contact onwards. When the needle tips contact with the probe, the force increases with the displacement, and no discontinuous points are detected, which indicates that HA-based MNs do not break but instead bend (Table 4.2).

The loading process is stopped when the probe reaches the baseplate. After 200 µm of displacement, the forces required to bend the HA-BC MNs (0.28-0.44 N.needle^{-1}) were higher than for HA (0.17-0.30 N.needle^{-1}) and HA-(BC-R) MNs (0.21-0.28 N.needle^{-1}). These results indicate that the use of BC as a back layer reinforces the MNs patch, but the incorporation of rutin results in MNs with similar mechanical properties as pure HA counterparts. However, above all, it is shown that all the as-prepared MNS did not break until compression reached 450 µm. Literature reports a maximum force of 0.15 N.needle^{-1} to insert human skin using MNs with 20 µm tip, and 0.058 N is determined as the average minimum force required for MNs to pierce throughout the top skin layer without breaking [71]. Therefore, considering the aforementioned data, the as-prepared MNs are expected to enable skin puncture and insertion. This mechanical behavior is analogous to those observed for other polymeric MNs, for example, prepared with CS [208] and CMC [135], which present similar axial force loads for the same displacement values. Furthermore, the mechanical performance of the as-prepared MNs are comparable to other HA-based MNs, which proved to have a minimum withstanding force higher than 0.05 N.needle^{-1} [154], and higher mechanical performance than ascorbic acid-loaded HA MNs, which presented fracture forces in the range of 0.059-0.161 N.needle^{-1} [93].

Regarding the preliminary insertion tests, the percentage of holes created in a Parafilm M® multilayer model system is shown in Figure 4.3 (b). Results showed that all MNs are able to fully pierce the first Parafilm M® layer and reach the third membrane layer. In fact, 72% and 19% of HA MNs pierced the second and the third Parafilm M® layer, respectively. The HA-BC and HA-(BC-R) MN patches fully pierced the first Parafilm M® layer, whereas 94% and 81% needles penetrated the second and third layers, as

illustrated in Figure 4.3 (c). These results confirm the reinforcing role of the BC membrane, however for these penetration depths; the negative effect of rutin is not reflected on the insertion ability of the MNs with rutin. In fact, the axial forces of the different MNs arrays for up to 250 um displacement is very similar (Figure 4.3 (a)). Since the average thickness of each Parafilm M® layer is 126 µm, the data suggest that HA-(BC-R) and HA-BC MNs might insert up to 378 µm depth that corresponds to 77% to 89 % of the needle height. Considering that the mean epidermis thickness ranges from 77± 26 µm to 267 ± 121 µm [374], and taking into account the estimated insertion depth, these systems might successfully disrupt the *SC* and bypass the epidermis, reaching the upper dermis.

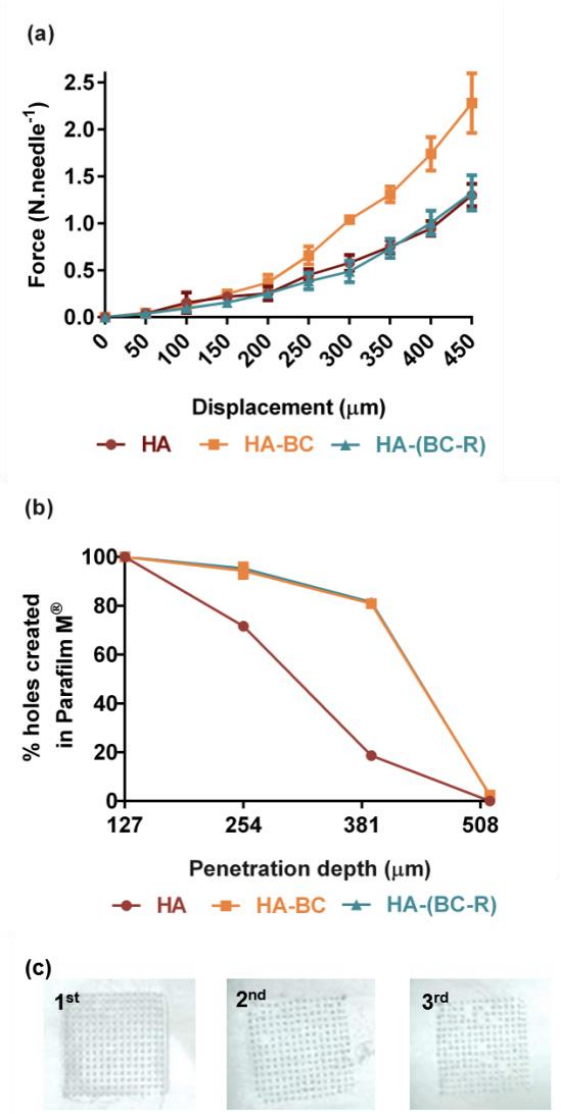

Figure 4. 3. (a) Force-displacement curves of HA, HA-BC, and HA-(BC-R) MNs under an axial force load (*n*=9, measurements performed on 9 different regions of 5 arrays). (b) Insertion of HA, HA-BC, and HA-(BC-R) MNs into a polymeric model membrane for skin insertion using Parafilm® (error bars are smaller than the data point (*n*=3). (c) Photos of the first, second, and third Parafilm® layer after insertion using HA-(BC-R) MNs.

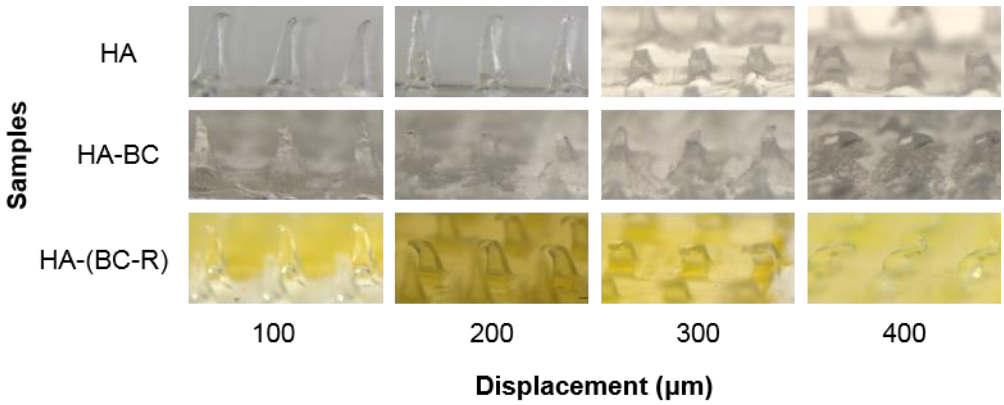

Figure 4. 4. Overview of morphological traits of microneedles after an axial force load.

4.4.3. Fourier transform infrared-Attenuated total reflection spectroscopy

The FTIR-ATR spectra of HA, BC, rutin, HA-BC and HA-(BC-R) are presented in Figure 4.5.

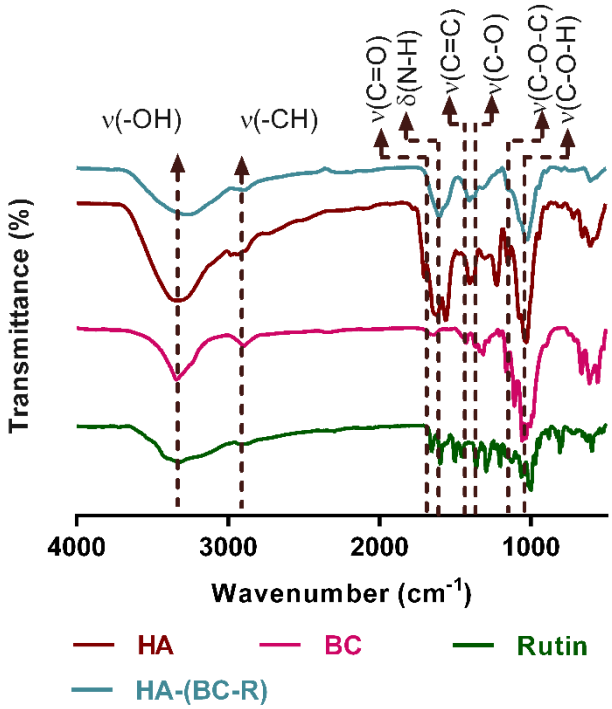

Figure 4. 5. FTIR-ATR spectra of HA, BC, rutin, and HA-(BC-R) MNs.

The spectrum of neat HA MNs (Figure 4.5) displays a prominent band at 3370 cm^{-1}, attributed to the ─OH and ─NH stretching vibrations. The band at 2927 cm^{-1} is ascribed to the stretching vibration of C-H and the band at 1620 cm^{-1} to the C=O stretching vibration of the amide carbonyl groups. The stretching vibration of the ─COO^- group, is

observed at 1402 cm^{-1} and the band at 1027 cm^{-1} is assigned to the C–OH stretching [375]. The spectrum of BC presents a fingerprint typical of cellulosic substrates [376], with the main bands at 3342 cm^{-1} (O–H stretching), 2886 cm^{-1} (C–H stretching) and 1056 cm^{-1} (C–O stretching). The spectrum of rutin displays absorption bands at 3306 cm^{-1}, assigned to the O–H stretching of the phenolic hydroxyl groups, at 2879 cm^{-1}, attributed to the C–H stretching, at 1654 cm^{-1} corresponding to the C=O stretching vibration and 1502 cm^{-1} to the asymmetric stretching of C=C. In addition, the peaks at 1057, 1121, and 1202 cm^{-1} are ascribed to the C–O–C stretching vibrations. Finally, the FTIR-ATR spectrum of HA-(BC-R) is an almost perfect sum of those of the pure components, showing no displacement peaks, which indicates weak interactions between rutin molecules and BC fibrils. Moreover, no evidence of the main peaks of rutin is observed, certainly due to the low loading of this phenolic in the BC membranes.

4.4.4. Thermogravimetric analysis

The thermal stability and degradation profiles of the HA-(BC-R) MNs and the corresponding individual components were assessed by thermogravimetric analysis under nitrogen flow, as shown in Figure 4.6.

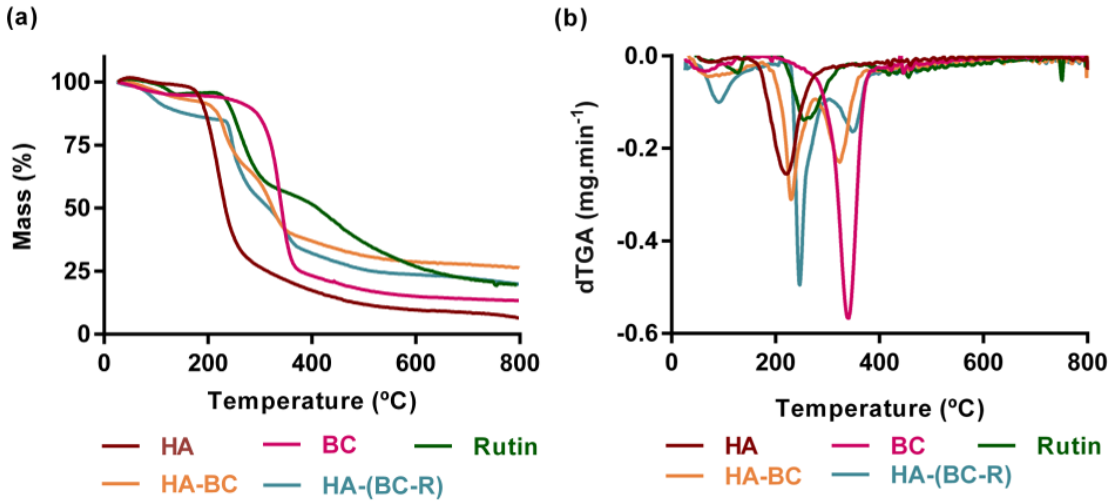

Figure 4. 6. (a) Thermograms and (b) corresponding derivative plot of HA, BC, rutin, and HA-BC and HA-(BC-R) MNs.

The thermal decomposition profile of HA exhibits a single weight-loss step degradation profile that starts at 150 °C and reaches a maximum decomposition temperature at about 222 °C, leaving a residue of ca. 6.4% at 800 °C. The TGA curve of BC also showed a single weight-loss feature, typical of cellulosic substrates, associated with the pyrolysis of the cellulose skeleton [377], with initial and maximum decomposition

temperatures at 215 and 338 °C, respectively [378]. On the other hand, the thermal decomposition profile of rutin displays two weight-loss events after water evaporation below 100 °C. The first decomposition stage, with a maximum decomposition temperature at 258 °C, corresponds to the phenolic moiety degradation, with a weight loss of *ca.* 43.4%. The second stage event, with a maximum at 458 °C, is assigned to the thermal decomposition of the sugar portion of rutin coupled with the carbonaceous residue formed before, leaving a residue corresponding to about 20% of the initial mass, at 800 °C [379]. The thermogravimetric profile of the HA-BC MNs indicates that thermal decomposition occurs in a double weight-loss step, with maximum decomposition temperatures at 231 and 325 °C due to HA and BC decomposition, respectively. Similarly, the HA-(BC-R) MNs patch displayed two-main degradation steps, after the water loss, with maximum decomposition temperatures at 232 and 336 °C. Overall, rutin incorporation into the BC back-layer membrane of the HA MN system does not significantly change the thermal stability of the system and all are thermally stable to support sterilization procedures (around 121 ºC) typically required in biomedical applications.

4.4.5. Humidity stability testing

To evaluate the stability of HA-based MNs towards humidity, their change in weight, when placed in a chamber with controlled humidity, *viz.* 98% RH at room temperature, was measured over a 28 -day period, as shown in Figure 4.7.

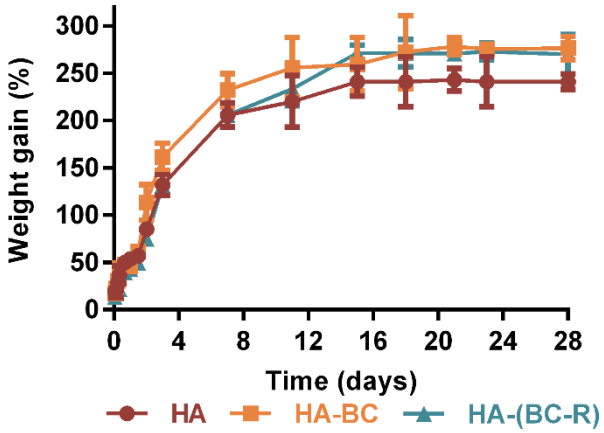

Figure 4. 7. Weight gain (%) of HA, HA-BC, and HA-(BC-R) MNs when stored at 98% relative humidity for 28 days (*n*=5).

Herein, the results indicate that all samples display a similar increment of mass during the experiment. Specifically, the weight of all MN patches increases rapidly and considerably in the first 7 days, reaching a plateau at day 11 and 15 for the HA, HA-BC, and HA-(BC-R) MNs, respectively. At this point, mass increments of 220 ± 20%, 256 ± 25%, and 233 ± 12% were detected for HA, HA-BC, and HA-(BC-R) MNs, respectively. Even though there are no significant differences between the different samples, a tendency for a higher humidity absorption for the samples incorporating BC was observed. Moisture absorption from the environment led to a softening of all MNs, with clear changes on the morphology being detected over a 7-days period (*i.e.*, the needle tips displayed a curvature). Therefore, these MNs patches must be packed and stored under low humidity conditions.

4.4.6. Antioxidant activity

The antioxidant activity, expressed as the IC_{50}, of the BC-R membrane and HA-(BC-R) MNs was determined immediately after their preparation (Figure 4.8 (a)), and after storage of the MN systems over 24 weeks (Figure 4.8 (b)). Pure rutin and BC were also evaluated for comparison

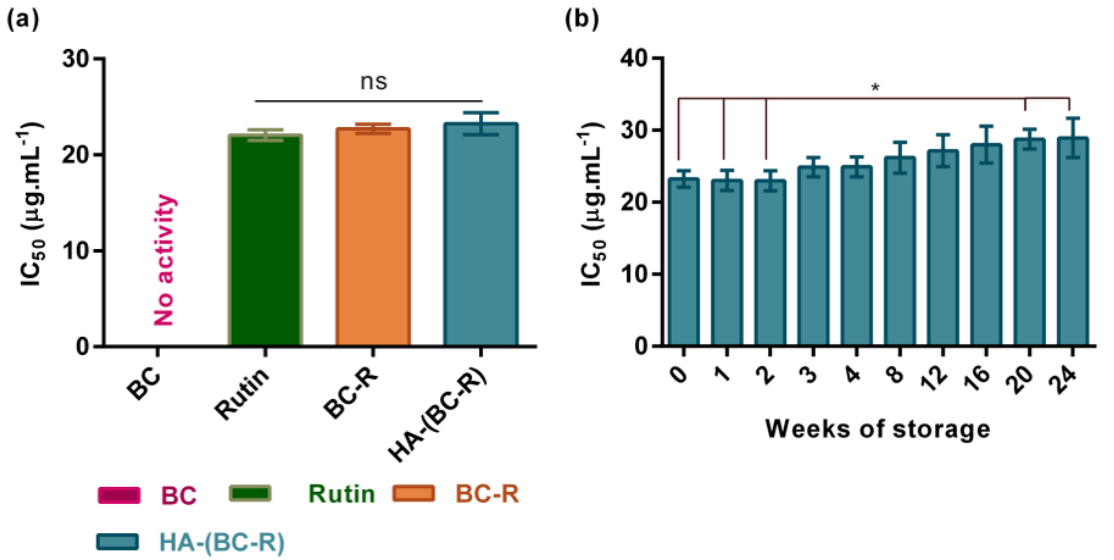

Figure 4. 8. Antioxidant activity expressed as the IC_{50} of (a) BC and rutin, and BC-R and HA-(BC-R) MNs immediately after preparation (n=3, ^{ns}: no significant differences in IC_{50} among these samples). (b) Antioxidant activity expressed as IC_{50} of HA-(BC-R) MNs over 24 weeks of storage (n=3, ^{ns}: no significant differences in IC_{50} among the samples prepared at 0, 1 and 2 and 20-24 weeks of storage).

Results have shown, as expected, that pure BC displays no antioxidant activity because cellulose lacks this functionality [380]. On the other hand, rutin presents an IC_{50}

of 22.04 ± 0.43 μg.mL^{-1}, comparable to that previously reported by Selvaraj *et al.*[381]. After impregnation into BC, and incorporation of this membrane as the back layer of the MNs array, the antioxidant activity is 22.70 ± 0.34 μg.mL^{-1} and 23.24 ± 0.77 μg.mL^{-1}, respectively. Furthermore, after 24 weeks of storage at room temperature, only a slight decrease in this parameter was observed (IC_{50} of 26.94 ± 2.97 μg.mL^{-1}). These results show that the fabrication process of MNs is sufficiently mild to preserve the activity of phenolic compounds, as rutin, and reinforce the suitability of storing these devices at room temperature, with no need for cold chain monitoring for at least 6 months.

4.4.7. In vitro cell viability assays

In order to guarantee the safety of the prepared MNs patches, the cytotoxicity of the HA-(BC-R) MNs system and of the individual components was evaluated against HaCaT cells (Figure 4.9).

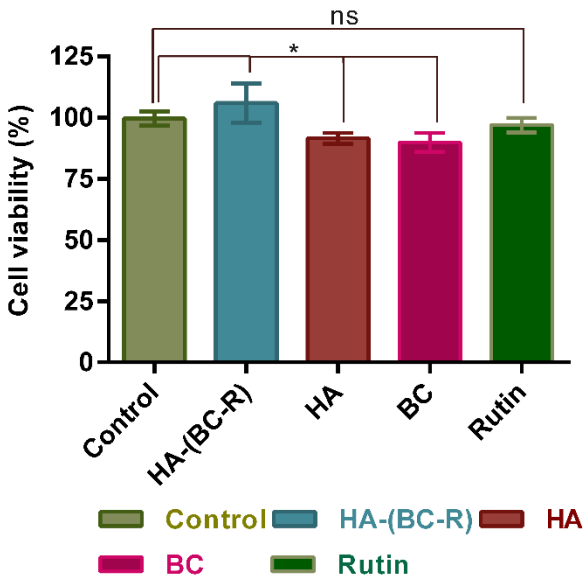

Figure 4. 9. Cell viability (%) of HaCaT cells upon exposure to HA, BC, Rutin, and HA-(BC-R) MNs for 24 h (n=12, two independent experiments, ^{ns}: no significant difference, * statistically significant differences (p<0.05) relative to control).

Our results confirmed that the components of these MNs patches, HA, BC, and rutin, are non-cytotoxic towards human keratinocytes cells, since the cell viabilities are all above 70%, *viz*. 91.5 ± 2.2, 89.8 ± 3.8 and 96.9 ± 2.9% for HA, BC, and rutin, respectively, confirming their suitability for clinical purposes [382]. When combined in a MNs device, the cell viability is preserved (105.9 ± 7.9%), indicating that the as-prepared

MNs appear as promising devices for skin applications and may be safely used, as demonstrated by this *in vitro* assay.

4.4.8. Ex vivo skin insertion

Ex vivo skin insertion was evaluated after manually inserting the HA-(BC-R) MNs patches into porcine ear skin, and upon removal, pores corresponding to the insertion site were observed (Figure 4.10).

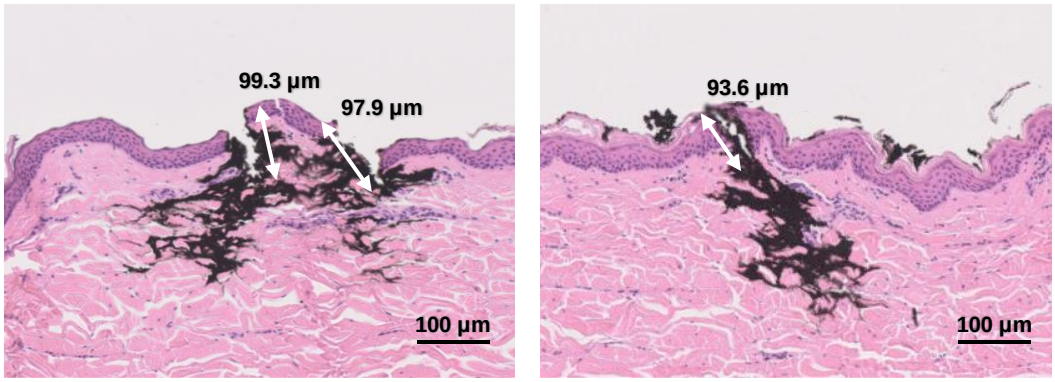

Figure 4. 10. Histological cross-sections of porcine ear skin after HA-(BC-R) MNs insertion, hematoxylin and eosin staining. The black staining corresponds to china ink which entered the MNs pores.

Histological examination demonstrated that HA-(BC-R) MNs created 47.3-99.3 µm depth cavities, which corresponds to about 22% of the needle height. Moreover, the *in vitro* skin samples analysis unveiled that MNs penetration corresponds to a needle insertion through the epidermis into the dermis (Figure 4.10). These results confirm the insertion capability of HA-(BC-R) MNs and the creation of pathways to enable drug/active molecules delivery successfully, overcoming the *SC* barrier and reaching the dermis.

4.4.9. In vitro rutin delivery

4.4.9.1. Dissolution assays

The *in vitro* dissolution assays were carried out in ethanol: PBS (20:80) solution over 16 h to investigate the release profile of rutin from the HA-BC MNs system and to have a first insight into its delivery ability. BC-rutin membranes were also investigated for comparison. Rutin was released in a time-dependent fashion, for both systems, as shown in Figure 4.11, with about 65 and 30% being released in the first hour for the BC-R membrane and HA-(BC-R) MNs, respectively.

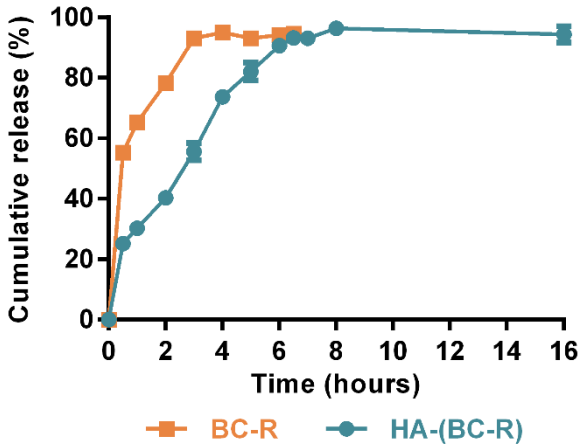

Figure 4. 11. *In vitro* dissolution of rutin from the HA-(BC-R) MNs and BC-R membrane (*n* = 3). In this figure, the standard deviation values are very small, and barely noticed.

A plateau at 94% of released rutin is reached for both BC-R membrane and HA-(BC-R) MNs, after 3 and 6.5 h, respectively. In this regard, it is possible to conclude that rutin is released more rapidly from the BC membrane system, due to the ease of access of the solvent medium to the BC membrane, which enables a faster solubilization of rutin when compared with the MNs where the HA needles cover one side of the BC membrane. To clarify the mechanism of rutin release from the MN system, the obtained release profile was adjusted to the Korsmeyer-Peppas model [383,384]. Wherein, results showed that the diffusional constant *n* is equal to 0.43 (r^2=0.952), suggesting that the release behavior may fit the Fickian diffusion considering a planar geometry (thin films). In literature, the Fickian diffusion is characterized by high solvent diffusion into the matrix, which leads to a gradient of solvent penetration and hence, drug release [385]. This suggests that in this study, the release of rutin might involve the absorption of water and desorption of rutin via diffusion. As water penetrates the BC matrix containing the dispersed phenolic, the polymer swells and the compound dissolves through the matrix and into the external releasing medium.

4.4.9.2. In vitro skin diffusion

The permeation of rutin from the HA-(BC-R) MNs, as well as from a BC membrane, through porcine skin, was also investigated (Figure 4.12).

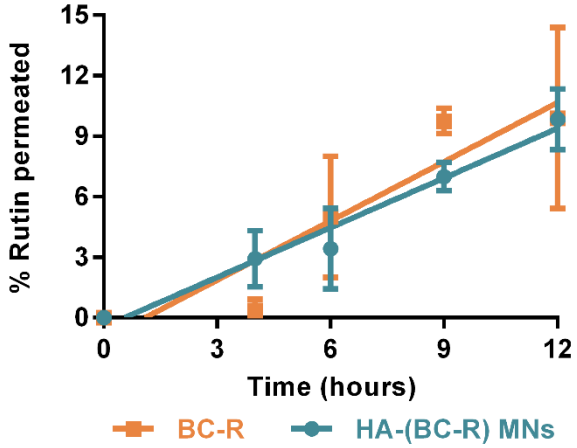

Figure 4. 12. Percentage of rutin permeated through time using a Franz cell apparatus (*n* = 5).

A slow rutin permeation was detected for both systems, with 9.8 ± 1.5% (1.39 ± 0.16 µg) and 9.9 ± 4.5% (1.08 ± 0.43 µg) of rutin being released, at the end of the experiment (12 h) from the HA-(BC-R) MNs and the BC membrane, respectively. As explained for the dissolution tests, the fact that the MN system is composed by a BC membrane over a HA-based MNs array is probably linked to the low permeation rates observed. In order for rutin to be released from the MNs system into the skin, HA needs to solubilize after insertion, facilitating the hydration of BC and enabling the solubilization of rutin. Only then, rutin will be able to permeate through the skin. In the other system, owing to the fact that the BC-R membrane is contacting directly with the skin, rutin is solubilized more rapidly, and therefore, there is a faster permeation process. However, since an overnight application (*ca.* 8 h) is envisioned for this type of system and taking into account that the amount of permeated rutin in this timeframe is similar for both devices, the feasibility of the MNs patch for administration of HA and bioactive molecules into skin is foreseen.

4.4.10. In vivo skin tolerance assays

Finally, to infer about the safety, suitability, and practicality of the system, the *in vivo* skin tolerance of HA-BC MNs was investigated by applying this patch in the volar forearms of human volunteers for 24 h (Figure 4.13 (a)).

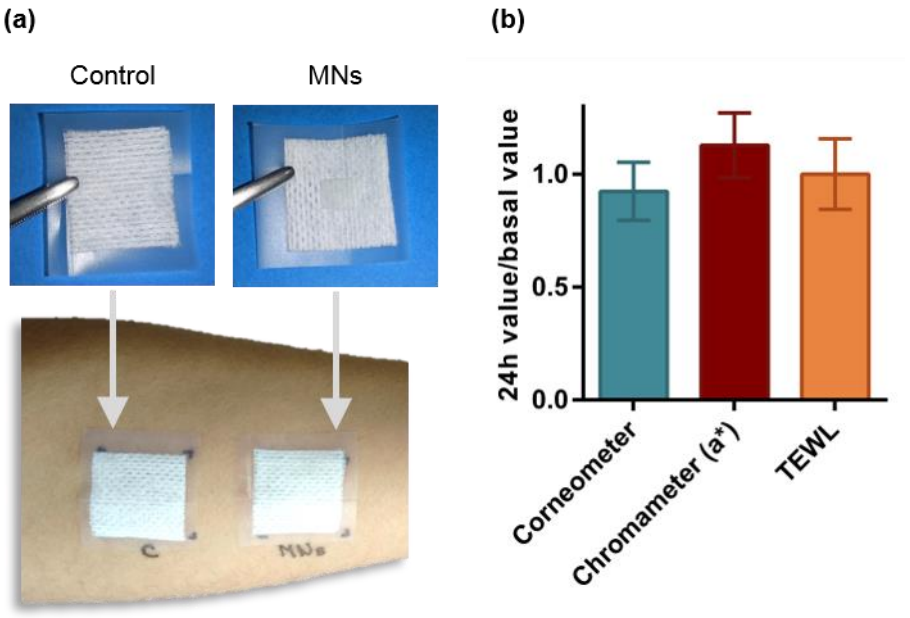

Figure 4. 13. (a) Representation of the application of MNs into the volar forearm of a volunteer and (b) variation in skin hydration, redness, and barrier function after MNs application (*n*=13 volunteers).

For the purpose of this study, no active compound was incorporated, aiming to infer about the safety of the model system. At the end of the application period, volunteers only had the BC layer attached to the occlusion/adhesion membrane, confirming that the HA needles dissolved when applied in the skin. Figure 4.13 (b) summarizes the results concerning the most representative skin tolerance parameters, namely skin redness, hydration, and TEWL. The *SC* hydration, assessed by the corneometer, was slightly lower than the control (Figure 4.13 (b)), nevertheless, no statistical differences were detected. Moreover, no significant increase in skin redness was noticed, indicating that these were well tolerated and did not cause erythema. Regarding the skin barrier function, the TEWL (Figure 4.13 (b)) was also not significantly affected, indicating that the MNs had no negative impact in the barrier function of the skin. In this case, higher inter-subject variability was detected. Overall, these results reflect the innocuous nature of the device and reinforce its biocompatible nature. Moreover, it may be reasonably postulated that BC provides skin occlusion and protection, decreasing TEWL [386]. Regarding the volunteer's feedback (Figure 4.14), it was possible to conclude that the application of MNs is easy and practical.

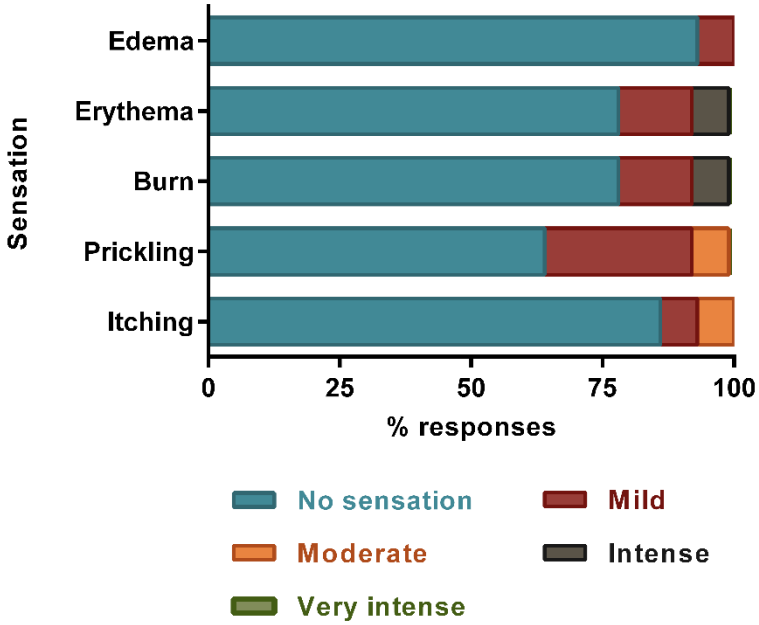

Figure 4. 14. Post-insertion questionnaire results concerning the MNs application (*n*=13 volunteers).

Most of the volunteers experienced no sensation concerning the feeling of edema, erythema, burn, prickling or itching. Some volunteers reported a mild to intense erythema and burn sensation in the tested site, but this discomfort was caused by the adhesive used to maintain the MNs in contact with the skin.

4.5. Conclusions

The present study demonstrates for the first time the successful preparation of a versatile and dual behaviour MN patch prepared with two biopolymers, HA as a cosmetic ingredient and BC as macromolecular support for the incorporation of active compounds, namely rutin. The obtained HA-BC MNs display suitable morphology, mechanical properties and cytocompatibility. In addition, these arrays successfully penetrated through the skin, delivering rutin. The *in vivo* safety and suitability of application of these devices, using human volunteers, reinforces their effectiveness and safe use as a dermo-cosmetic system and opens new avenues for the incorporation of different active ingredients, which will enable tailoring the delivery system and broad their field of application.

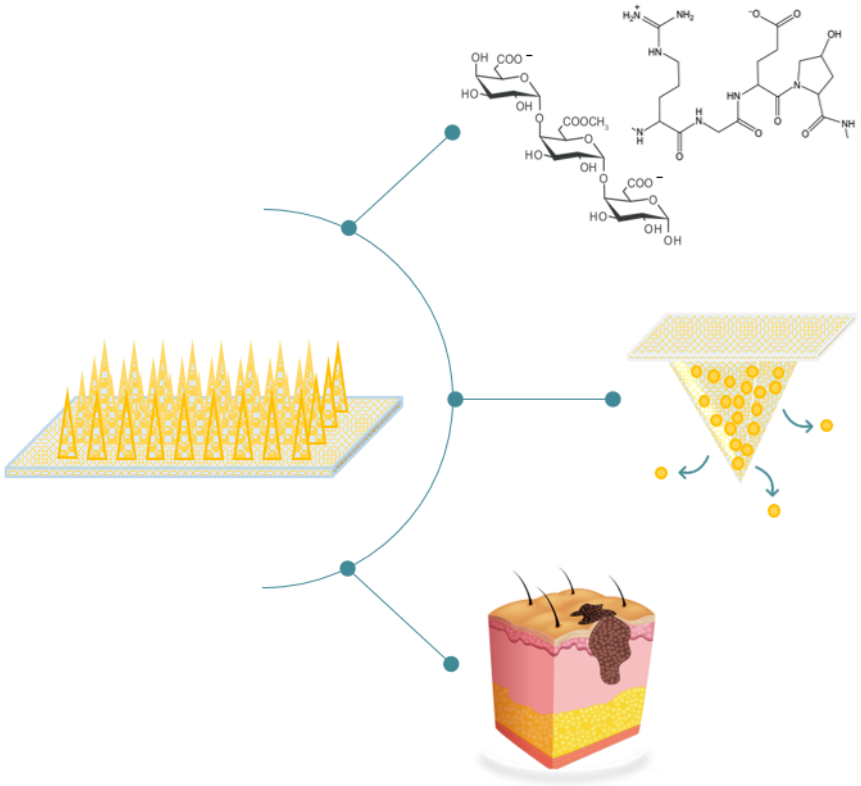

CHAPTER 5. GELATIN-PECTIN MICRONEEDLES FOR INTRADERMAL DELIVERY OF CURCUMIN TOWARDS MELANOMA TREATMENT: PRELIMINARY RESULTS

5.1. Abstract

Melanoma, which arises from malfunctioning of normal melanocytes in the epidermis, is amidst the most lethal types of skin cancers. From the panoply of bioactive natural compounds that has been studied for melanoma treatment, Cur arises as a promising candidate. Apart from its potential therapeutic effects, major limitations such as poor aqueous solubility and bioavailability, limit its application. Considering the targeted administration of drugs achieved using MNs and the valorization of research using biopolymers, the purpose of this study is to prepare and characterize Gel-Pec MNs loaded with Cur, to improve the bioavailability of this bioactive molecule, envisioning their applicability in melanoma treatment. Firstly, dose-response curves were generated, testing eight Cur concentrations on three melanoma cell lines. This evaluation was performed for 24 and 48 hours to define the IC_{50}. Then, several Gel-Pec solutions were prepared aiming to select the most suitable polymers concentrations and proportions. Subsequently, Cur, in the free form or as a nanogel was introduced into the MNs, taking in consideration the IC_{50} values previously determined. Then, their morphology and mechanical performance were evaluated, and it was found that the micromolding process was suitable for Gel-Pec MNs preparation. MNs composed of 75/25% (v/v) Gel-Pec provided the highest mechanical strength and the incorporation of Cur does not affect their performance. These preliminary results clearly outline the potentialities of Gel-Pec MNs for loading of Cur envisioning the non-invasive treatment of melanoma.

5.2. Introduction

Melanoma, the deadliest form of skin cancer, is a global public health problem, with more than 100 000 new cases estimated in 2020, and about 7 000 deaths [387]. The cutaneous melanoma arises when melanocytes escape the tight regulation of keratinocytes [388] and start proliferating, leading to the formation of a naevus or common mole. This proliferation can be restricted to the epidermis or dermis, being called junctional or dermal naevus, or involve components of both layers, being denominated compound naevus [389]. Even though naevi are generally benign, they can progress to stages in which the cells have metastatic potential. At this stage, it is extremely aggressive with a notorious high resistance to common cytotoxic agents [389,390].

The pathogenesis of melanoma is multifactorial with a complex combination of genetic and environmental factors [391,392]. Indeed, skin is prone to injuries caused by sun overexposure and ultraviolet radiation which are the most important risk factors [393]. Currently, most common cancer treatments, such as surgery, chemo or radiotherapy, are associated with several unintended side effects, compromising patient's quality of life and well-being [394,395]. Therefore, the search for safer and target therapies is warranted [389].

Amongst innovative therapeutic strategies, many have been focused on the use of nutraceuticals or natural substances isolated form food and plants owing to their role in the prevention and protection against cancer [396]. Among the panoply of natural compounds, Cur has shown outstanding potential in the treatment of melanoma [397]. This yellow pigment is a natural phenolic compound extracted from the rhizomes of turmeric, *Curcuma longa* L., a member of the ginger family [398,399]. Cur has been explored as a potential therapeutic agent against melanoma due to its antioxidant and anti-inflammatory properties [397–400], which are responsible for the attenuation of the mediators in the inflammatory response, regulating tumour suppressor pathways and inhibiting proliferation of cancer cells by induction of apoptosis [397]. Evidence shows that Cur inhibits vital processes of cancerous cells, namely adhesion, migration, invasion, and spreading [397].

Despite the large body of information about the health effects of Cur, its low solubility and lack of systemic bioavailability are regarded as major problems [397–400]. In this vein, many attempts have been made to overcome the poor bioavailability of this bioactive compound, calling upon diverse delivery strategies, namely by encapsulation in liposomal formulations [401], polymeric micelles [402], inclusion complexes with

cyclodextrin [403], nanoemulsions [404] and development of polymer-Cur conjugates [405,406], either in the form of nanocapsules or nanogels.

More recently, MNs have emerged as efficient systems for transdermal administration of different drugs [9]. These minimally invasive DDS bypass the *SC*, creating micron-size pores, enabling delivery of the therapeutic agents directly to the epidermis or upper dermis. This form of DD has become a hot topic in recent years due to their advantageous characteristics. As a hybrid of hypodermic needles and transdermal patches, this system enables enhanced DD of therapeutics, while overcoming the drawbacks of traditional oral and parenteral administration [5]. In this sense, aiming to improve Cur solubility and stability, HA MNs containing Cur-loaded micelles were produced and proved to deliver 74.7% Cur after 360 min using a Franz cell apparatus [164]. Furthermore, PVA-based MNs containing Cur nanosuspensions were fabricated by Abdelghany *et al*. [407], showing a complete dissolution using *ex vivo* neonatal porcine skin after 60 min. In addition, Cur from the MNs arrays reached deeper skin layers, when compared with the delivery of Cur nanosuspension or free Cur. The aforementioned polymeric MNs have been studied to enhance Cur administration, aiming the intradermal or systemic delivery of this compound, with good prospects in the treatment of a panoply of diseases and cancers.

Considering the recognised biocompatibility and biodegradability of natural biopolymers, the purpose of this work is to prepare and characterize novel biopolymeric MNs using Gel and Pec for Cur delivery, targeting the treatment of melanoma. Gel and Pec were selected for MNs fabrication as they are considered valuable matrices to prepare structural complexes that coacervate, being previously exploited for films and coating-forming purposes [408].

First, Cur cytotoxic effect was explored by evaluating the viability of melanoma cells using three melanoma cell lines. Then, Gel:Pec ratios were optimized to achieve the nest to MNs' morphology, and the effect of crosslinking addition was also tested. Finally, Gel:Pec MNs incorporating free Cur and a nanogel-loaded formulation (CurNg) were prepared and studied. This preliminary evaluation was essential to understand the potential of these systems and infer about their performance and applicability.

5.3. Materials and methods

5.3.1. Chemicals and materials

Pec (67-71% degree of esterification) was purchased from Acros Organics (Fisher Scientific, Leicestershire, England) and Gel (tested according to Ph Eur, bloom 164) from Fluka (Sigma-Aldrich Chemie GmbH, Steinheim, Germany). Calcium chloride

(anhydrous, analytical grade) was purchased from Carlo Erba Reagents S.A.S (Chaussée du Vexin, France). Cur (≥95% purity) was purchased from ChemCruz (Dallas, Texas, USA) and Cur-loaded hyaluronan-based nanohydrogels (CurNg) were kindly provided by Professor Matricardi (Sapienza University of Rome) and prepared as previously reported [406]. Sodium phosphate dibasic (≥99.0% purity), sodium phosphate monobasic (≥99.0% purity), MTT (98%) and DMSO (≥99.7%) where purchased from Sigma-Aldrich (St Louis, MO). Sodium chloride (≥99% purity) was purchased from Fluka (Sigma-Aldrich Chemie GmbH, Steinheim, Germany. Ultrapure water was obtained using a Milli-Q® Integral Water Purification System. The MNT-1, SK-MEL-28 and A375 cell lines were kindly provided from Cell Line Services (Eppelheim, Germany) and Dulbecco's modified Eagle's medium, fetal bovine serum (FBS), L-glutamine, penicillin-streptomycin (10,000 $U.mL^{-1}$), and fungizone (250 $U.mL^{-1}$) were purchased from Gibco®, Life Technologies (Grand Island, NY, USA).

5.3.2. In vitro cell viability assays

The manipulation and growth of the cell lines were performed and adapted to meet Cell Line Services (CLS) recommendations. MNT-1 and A375 were aseptically grown in Dulbecco's modified Eagle's medium, supplemented with 10% fetal bovine serum (FBS), 2 mM L-glutamine, 1% penicillin-streptomycin (10,000 $U.mL^{-1}$), and 1% fungizone (250 $U.mL^{-1}$). SK-MEL-28 were cultured in Minimum essential Medium Eagle (MEM) supplemented with 10% FBS and 1% L-glutamine, non-essential aminoacids (NEAA), sodium pyruvate and 1% penicillin-streptomycin (10,000 $U.mL^{-1}$), and 1% fungizone (250 $U.mL^{-1}$). Cells were incubated at 37 °C in a humidified atmosphere with 5% CO_2, as previously described [409]. Cells were daily observed for confluence and morphology using an inverted phase-contrast Eclipse TS100 microscope (Nikon, Tokyo, Japan).

Cell viability was determined by the colorimetric MTT assay [302]. MNT-1 and A375 cells were seeded in 96 wells plates at 35,000 and 25,000 cells per well for 24 and 48 h exposure. On the other hand, SK-MEL-28 cells were seeded in 96 wells plates at 50,000 and 25,000 cells per well for 24 and 48h exposure respectively. Upon reaching confluency, cells were exposed to various concentrations of Cur in DMSO (1-50 $\mu g.mL^{-1}$) [410]. Untreated cells were kept as control. At the end of the incubation time, 50 µL of MTT (at a concentration of 1 $g.L^{-1}$) were added to each well and incubated for 4 h at 37 ºC in 5% CO_2 humidified atmosphere. After that, culture medium with MTT was removed and replaced by 150 µL of DMSO and the plate was placed in a shaker for 2 h in the dark to completely dissolve the formazan crystals. The absorbance of the samples was measured with a BioTek Synergy HT plate reader (Synergy HT Multi-Mode, BioTeK,

Winooski, VT) at 570 nm with blank corrections. The cytotoxicity (IC_{50}) was calculated based on the absorbance of treated cell aqueous media, which is proportional to the number of metabolically active cells and indirectly approximates cell viability. IC_{50} is defined as the drug concentration required to inhibit the growth of cells by 50% relative to control.

5.3.3. Fabrication of Gel-Pec MNs patches

The detailed composition of the MNs prepared in this study is described in Table 5.1.

Table 5. 1. Detailed composition of the aqueous polymeric mixture for MNs fabrication.

Microneedles	Composition			
	Gel/Pec[1]	$CaCl_2$[2]	Cur[3]	CurNg[3]
100 Gel	100/0	-	-	-
75/25 Gel-Pec	75/25	-	-	-
50/50 Gel-Pec	50/50	-	-	--
25/75 Gel-Pec	25/75	-	-	-
100 Pec	0/100	-	-	-
1c-Pec	0/100	1	-	-
5c-Pec	0/100	5	-	-
1c-75/25 Gel-Pec	75/25	1	-	-
5c-75/25 Gel-Pec	75/25	5	-	-
75/25 Gel-Pec-Cur	75/25	-	10	-
75/25 Gel-Pec-CurNg	75/25	-	-	10

[1]Composition in ratio of Gel/Pec v/v(%). [2]Composition in w/w in relation to Pec. [3]Curcumin amount per patch (ug).

In brief, Gel solution (5% (w/v), pH=5.19) was prepared by dissolving Gel in Mili-Q water under constant stirring at 45 ºC and then cooling to 35 ºC. Pec solution (5% (w/v)) was prepared by dissolving Pec powder in Mili-Q water under stirring at 35 ºC. To prepare 100 Gel and 100 Pec MNs, Gel and Pec solutions were employed. To prepare Gel-Pec MNs (from 25 to 75% (v/v)), aliquots of Gel and Pec solutions were combined, and the hydrogels were left under stirring for 3 hours. After complete mixing of the solutions, the temperature was decreased to 30 ºC.

To prepare crosslinked matrices (Table 5.1), $CaCl_2$ (1% or 5% (w/w) in relation to Pec) was added to Pec or 75/25 Gel-Pec mixtures. Non-crosslinked 75/25 Gel-Pec MNs loaded with Cur were prepared by incorporation of Cur powder or nanogel (10 µg Cur *per* patch) on the biopolymeric mixtures.

To prepare pyramidal-shape MNs, female molds of PDMS (Micropoint Technologies Pte Ltd., Singapore), size 8 mm × 8 mm, arrays of 15 × 15 needles with 550 µm height,

200 µm base and needle pitch 500 µm, were used. The solutions were degassed and 100 µL were spread over the MNs master molds and centrifuged (Hettich® Rotofix 32A) at 6000 rpm (4025 *g*) during 10 min. Afterwards, the MN molds were left to dry at 30 ºC overnight and then removed from the master mold.

5.3.4. Preliminary characterization of Gel-Pec MNs patches

5.3.4.1. Morphological characterization

The obtained Gel-Pec MNs were characterized using a stereomicroscope (Nikon SMZ18, Tokyo, Japan) and images were captured with a digital camera (SRH Plan Apo 2, Tokyo, Japan). Magnification power of the ocular lens was 5× and magnification of the objective lens was 1.5, 5 and 8×, corresponding to a total magnification of 7.5, 25 or 40×, respectively. Image acquisition was performed using NIS Elements Imaging Software (4.50.00 (Built 1117), 2017).

5.3.4.2. Mechanical characterization and preliminary insertion tests

Mechanical axial compressive tests were performed on the Gel-Pec MNs, using a TA.XT2 Texture Analyser (Stable Micro Systems Ltd., Haslemere, UK). The MNs patches were placed on the flat rigid surface of a stainless-steel base plate. An axial force was applied perpendicular to the axis of the MN array, at a constant speed of 0.01 $mm.s^{-1}$. The force was measured when the moving sensor touched the uppermost point of the needles. Then, the texture analyser recorded the force required to move the mount as a function of needle displacement [131].

For preliminary insertion studies, a simple method previously described [144] was performed. First, Parafilm M® (Bemis Company Inc., Soignies, Belgium) was folded into eight layers to simulate the thickness of excised skin, and the MN arrays were then inserted into the Parafilm M® using the texture analyser and applying a force of 40 N for 30 seconds. Then, to measure the insertion ratio and depth, each layer of Parafilm M® was examined under the microscope and the number of holes in each layer was counted.

5.3.5. Statistical analysis

Statistical analyses were performed using GraphPad Prism Software (GraphPad Software Inc., San Diego, CA, USA). Data is presented as the mean values ± standard error. A Student's paired *t*-test was used for comparisons between data points and multiple data sets between groups were analysed with a one-way analysis of variance

(ANOVA) followed by a Tukey's post hoc test, when necessary. For all comparisons, a difference of $p < 0.05$ was regarded as statistically significant. For the *in vitro* cell viability assays, data was analysed by a one-way ANOVA followed by a Holm-Šídák test to evaluate the significance between the different MNs and cell viability was calculated with respect to control cells.

5.4. Results and discussion

The aim of this study was the preparation and preliminary characterization of MNs based on Gel and Pec and loaded with Cur envisioning their application as non-invasive micron sized systems for Cur delivery towards melanoma treatment (Figure 5.1).

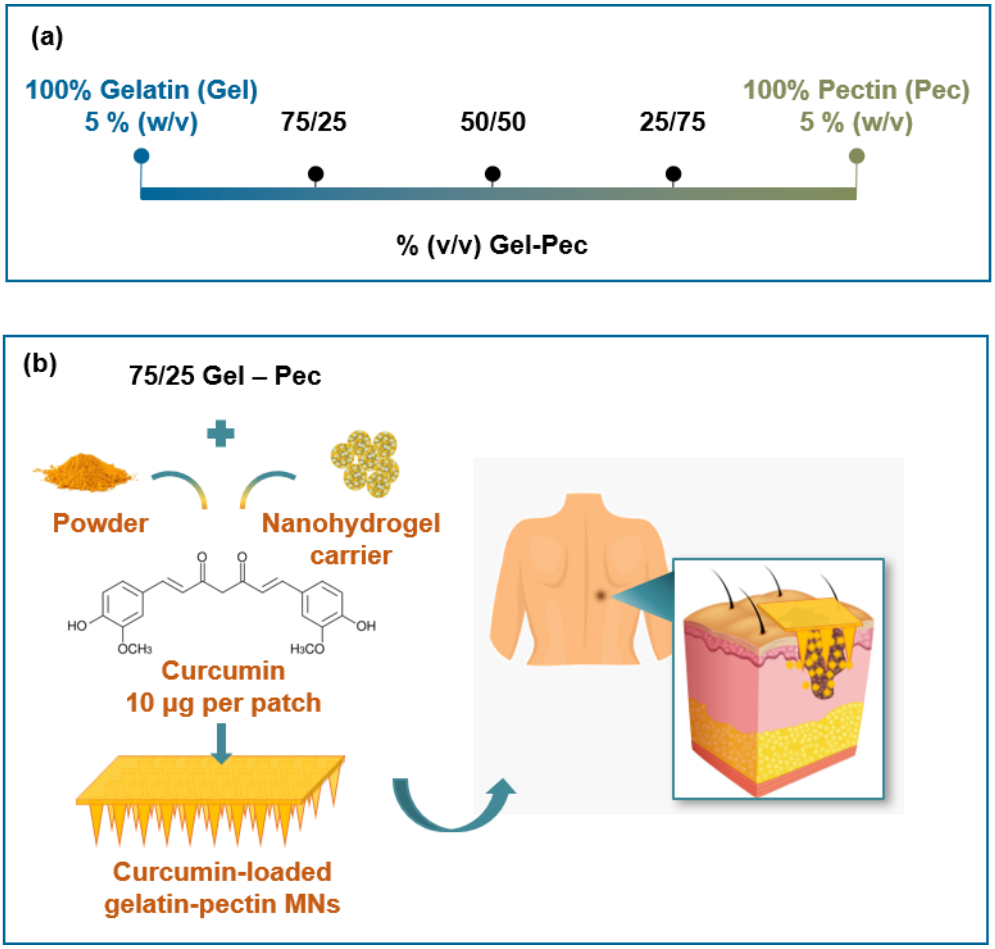

Figure 5. 1. Schematic representation of (a) polymeric composition of MNs under study and (b) Cur MNs preparation and target application.

First and foremost, the evaluation of dose-response cell viability curves upon exposure of different melanoma cell lines to Cur enabled the determination of IC_{50}. This allowed selecting the amount of Cur to incorporate into each MNs patch (Figure 5.1). Then, the fabrication of Gel-Pec MNs was optimized by testing Gel (5% w/v) and Pec

(5% (w/v)) in different proportions, *i.e.* 100 Gel, 75/25 Gel-Pec, 50/50 Gel-Pec, 25/75 Gel-Pec and 100 Pec. To determine the effect of crosslinking on the mechanical reinforcement of MNs, 100 Pec and 75/25 Gel-Pec were reticulated with 1 and 5% $CaCl_2$ (1c-Pec, 1c-75/25 Gel/Pec, 5c-Pec and 5c-75/25 Gel-Pec) and evaluated. Finally, free Cur and CurNg were incorporated into 75/25 Gel-Pec MNs due to their superior mechanical performance, and their morphology and mechanical characteristics were determined. To infer about the insertion ability of Cur-loaded MNs, preliminary insertion tests were performed using a model system based on Parafilm®.

5.4.1. In vitro cell viability assays

The effect of Cur powder on the *in vitro* cell viability was investigated using three different melanoma cell lines (Figure 5.2), *viz.* MNT-1, SK-MEL-28 and A375, being MNT-A cells highly pigmented and SK-MEL-28 and A375 amelanotic.

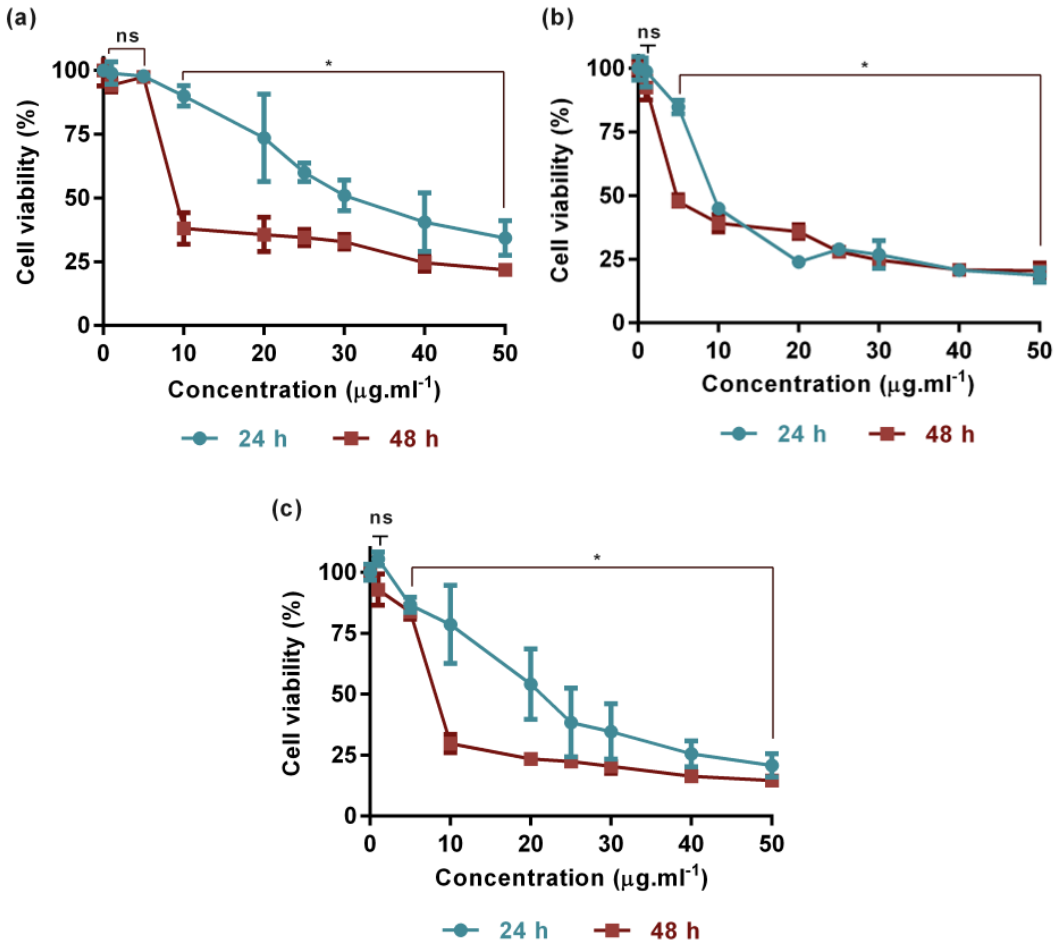

Figure 5. 2. Dose response curves with different concentrations of Cur on (a) MNT-1, (b) SK-MEL-28 and (c) A375 cells upon exposure for 24 and 48h exposure (*n*=12, two independent

experiments, ^{ns}: no significant difference, * statistically significant differences (p<0.05) relative to control which is concentration =0).

For all cell lines, Cur was found to exhibit concentration and time-dependent cytotoxic effects, as previously reported [410,411] and shown in Figure 5.2. In general, treatment of all cell lines with 1 and 5 μg. mL^{-1} Cur displayed no cytotoxic effects, except for SK-MEL-28 after 48 h of exposure. Herein, the results indicate that for low Cur concentrations, viability of the melanoma cell lines is virtually not affected and may not be useful for melanoma treatment purposes.

In particular, regarding MNT-1 and A375 cell lines (Figure 5.2. (a and c)), cell viability was not affected by exposure at 10 μg. mL^{-1} for 24 h. However, exposure to Cur concentrations higher than 10 μg. mL^{-1} induced cytotoxicity in a dose- and time-dependent manner, as cell viability was maintained below 70%. On the other hand, when evaluating the cell viability of SK-MEL-28, it is possible to conclude that cells viability decreases to less than 50% after exposure at ≥ 10 μg. mL^{-1}. Also, for concentrations higher than 25 μg. mL^{-1}, cell viability is not dependent of the exposure time, with similar cell viability reductions obtained for 24 and 48 h of Cur exposure.

The IC_{50} for Cur was found to be around 10 and 30, 5 and 10, and 10 and 20 μg.mL^{-1} for 24 and 48 h exposure regarding MNT-1, SK-MEL-28 and A375 cell lines, respectively. This could be due to slight differences in uptake profile and Cur metabolism by the different melanoma cells [411,412]. Previous results indicate an IC_{50} value of 17.25 μg.mL^{-1} for Cur towards ovarian cancer cells after 48 h exposure, that is comparable to that observed for A375 cell line [410].

Overall, the different cell lines exposed to Cur displayed cell viability reduction, indicating the potential of using this bioactive compound in the treatment of melanoma. Considering the present data, the amount of 10 μg Cur *per* patch was considered for the next steps.

5.4.2. Morphological characterization and mechanical evaluation of Gel-Pec MNs

5.4.2.1. Optimization of Gel and Pec concentration in MNs

A range of polymeric formulations (100 Gel, 75/25, 50/50 and 25/75% (v/v) Gel-Pec, 100% Pec)) were investigated for their potential in MNs fabrication. The prepared MNs arrays provided structurally intact needles (Figure 5.3), allowing us to conclude that all polymeric formulations displayed good film-forming ability, as previously reported for films of Gel-Pec [408].

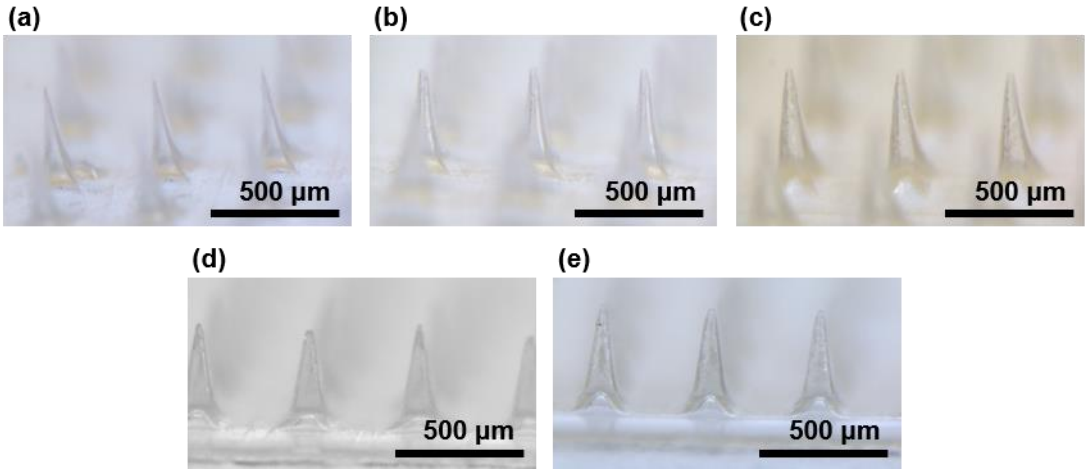

Figure 5. 3. Optic micrographs of MNs arrays fabricated using (a) 100% Gel, (b) 75/25% (v/v) Gel-Pec, (c) 50/50% (v/v) Gel-Pec, (d) 25/75% (v/v) Gel-Pec and (e) 100% Pec.

Moreover, all MNs arrays displayed uniform needles, with no air bubbles entrapped into the needle's body. In general, regarding MN's dimensions (Table 5.2), there are no statistical differences between the different patches, either considering the needle height, base, or interspacing between needles. The MNs measured from 432 ± 23 to 472 ± 18 µm in height, representing a decrease of *ca.* 11-26% when compared with the depth of the master mold. This decrease is due to solvent evaporation and well described in literature for other biopolymeric MNs prepared by solvent casting [160,306].

Table 5. 2. Detailed dimensions of MNs fabricated using different polymeric Gel and Pec formulations

Dimensions of fabricated Gel-Pec MNs					
Measurements (n=75)[a]	100 Gel	75/25 Gel-Pec	50/50 Gel-Pec	25/75 Gel-Pec	100 Pec
Height (µm)[ns]	440 ± 19	459 ± 8	472 ± 18	452 ± 16	460 ± 8
Base width (µm)[ns]	199 ± 1	200 ± 1	200 ± 1	200 ± 1	200 ± 1
Tip-to-tip distance (µm)[ns]	496 ± 5	494 ± 5	497 ± 5	496 ± 4	498 ± 2

[a] *n*=75, measurements performed on 15 random needles selected from 5 different microneedle arrays for each composition. [ns]: no significant difference.

Since the morphological features of all MNs arrays are similar, an evaluation of the mechanical performance of MNs was required to select the array that exhibits stronger mechanical properties. This is imperative to assure successful insertion into the skin without failure. In this regard, to evaluate the mechanical failure force of the as-prepared MNs, the axial force load *vs* displacement was obtained using a texture analyzer (Figure 5.4).

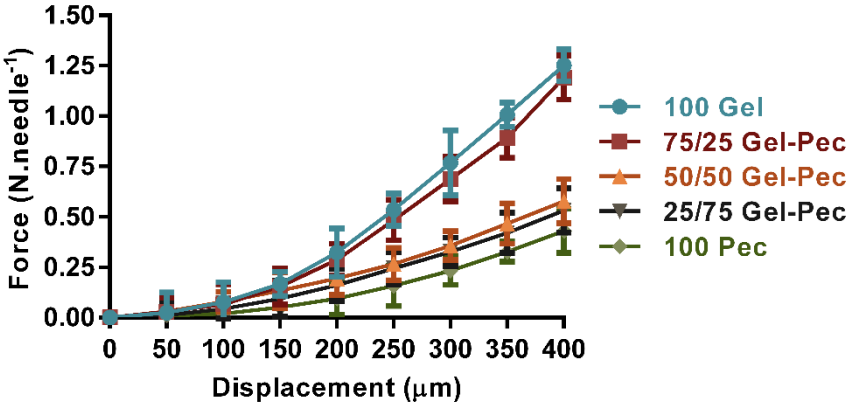

Figure 5. 4. Force displacement curves of 100 Gel, 75/25, 50/50 and 25/75 Gel-Pec, and 100 Pec MNs under an axial force load (*n*=9, measurements performed on 9 different regions of 5 arrays).

The force displacement curves of all MNs arrays display no discontinuity points after compression, suggesting that these MNs did not fractured, but instead bended. This progressive deformation without breaking is comparable to other biopolymeric MNs which shown not to break under an axial force load [208,210]. Therefore, it is not possible to determine the failure force. In this vein, a comparison was made between the forces that Gel-Pec MNs and other biopolymeric MNs (which proved to successfully penetrate skin) were able to withstand. For example, PL MNs exhibited a force of 0.3-0.53 N.needle^{-1} at 0.2 mm displacement whereas CS and CMC MNs exhibited forces from 0.2 to 0.4 N.needle^{-1} and 0.6 N.needle^{-1}, respectively, at the same displacement. Herein, Gel and 75/25 Gel-Pec withstand about 0.28-0.32 N. needle^{-1} which may confirm the suitability of the as-prepared MNs for skin insertion.

Aiming to infer about the impact of crosslinking into the morphology and mechanical properties of 100 Pec and 75/25 Gel-Pec MNs, the hydrogels were crosslinked with 1 and 5% $CaCl_2$ (w/w in relation to Pec). Pec MNs incorporating 100% Pec were selected due to its low mechanical performance as shown in Figure 5.4, in an attempt to reinforce these devices. Similarly, 75/25 Gel-Pec MNs were also chosen to understand if crosslinking could improve the mechanical behaviour.

The first step, consisting on the preparation and morphological evaluation of the crosslinked matrices, unveiled the successful preparation of 1c-Pec, 1c-75/25 Gel-Pec and 5c-75/25 Gel-Pec as shown in Table 5.3 and Figure 5.5 (a-c). On the other hand, the brittle and fragile structure of 5c-Pec MNs resulted into the non-successful fabrication of MNs arrays.

Table 5. 3. Detailed dimensions of MNs fabricated using crosslinked polymeric Gel-Pec MNs

Dimensions of fabricated crosslinked Gel-Pec MNs			
Measurements (n=75)[a]	1c- Pec	1c- 75/25 Gel-Pec	5c- 75/25 Gel-Pec
Height (µm)[ns]	432 ± 23	462 ± 46	459 ± 39
Base width (µm)[ns]	200 ± 1	199 ± 2	200 ± 1
Tip-to-tip distance (µm)[ns]	494 ± 6	497 ± 5	498 ± 6

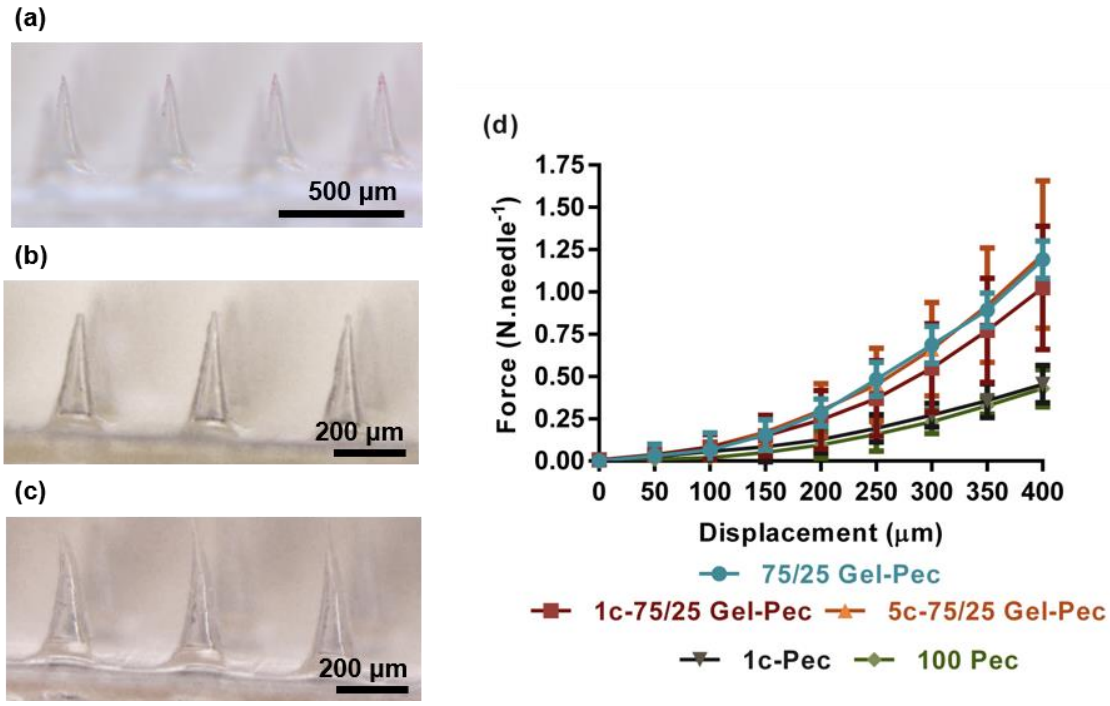

Figure 5. 5. Optic micrographs of (a) 1c-Pec, (b) 1c-75/25 Gel-Pec and (c) 5c-75/25 Gel-Pec MNs. (d) Force displacement curves obtained for 1c-Pec, 1c-75/25 Gel-Pec and 5c-75/25 Gel-Pec MNs under an axial force load, and comparison with non-crosslinked MNs (*n*=9, measurements performed on 9 different regions of 5 arrays).

The as-prepared 1c-Pec, 1c-75/25 Gel-Pec and 5c-75/25 Gel-Pec arrays displayed MNs of uniform pyramidal shape but the topography of the base features' irregular regions (data not shown). The evident heterogeneity in the microstructure of these MNs may be due to the presence of aggregates formed during crosslinking of Pec by $CaCl_2$ [408]. In the Gel-Pec MNs, an entangled phase of $CaCl_2$-crosslinked pectin connects and encases the secondary component, Gel.

Regarding the mechanical behaviour under an axial force load (Figure 5.5 (d)), crosslinked MNs display a similar profile to the uncrosslinked MNs arrays and do not provide superior strength. Therefore, for the purpose of this study, 75/25 Gel-Pec MNs were chosen to incorporate Cur (free powder) or the Cu nanogel carrier.

5.4.2.2. Preparation and evaluation of curcumin-loaded Gel-Pec MNs

The fabrication of Cur-loaded 75/25 Gel-Pec MNs was successfully achieved as shown in Figure 5.6.

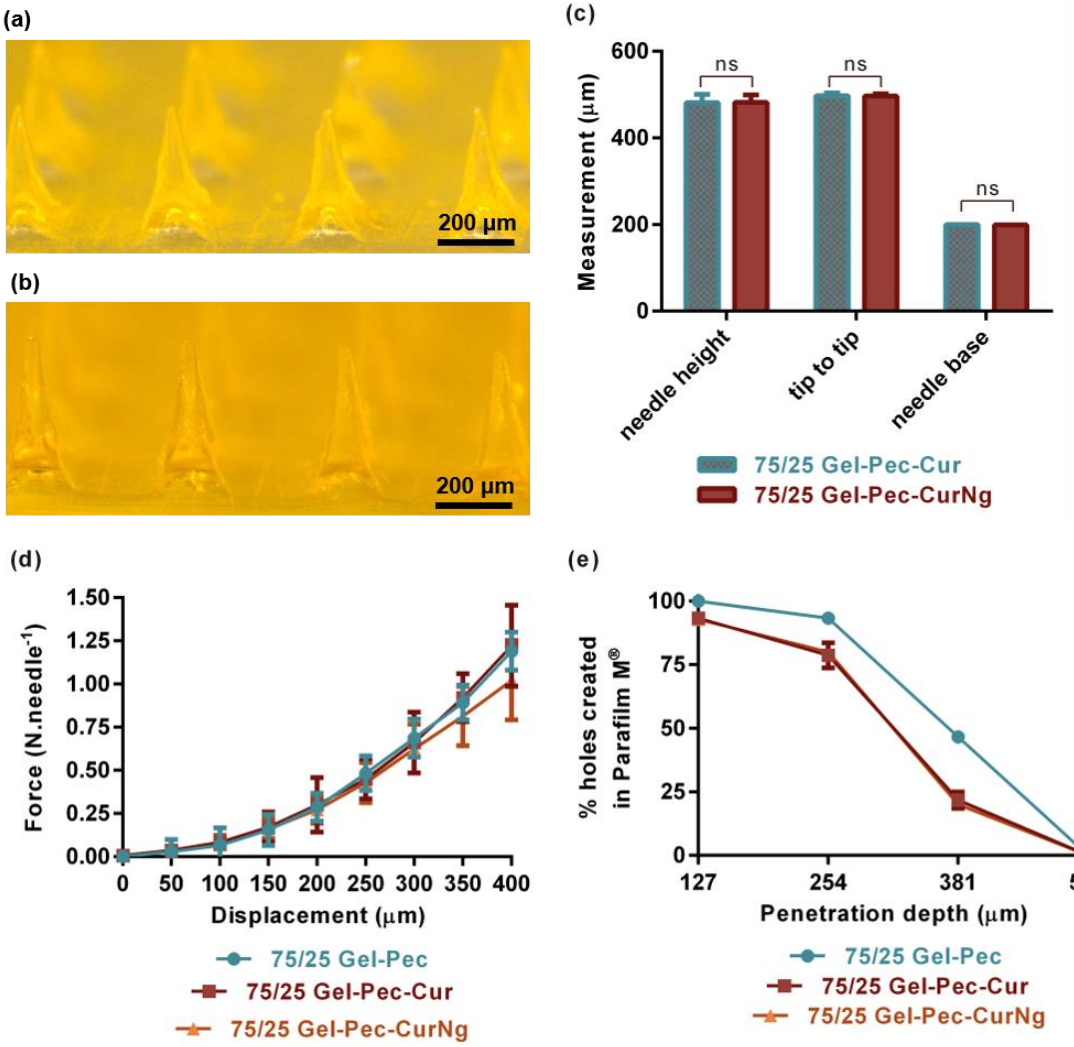

Figure 5. 6. Optic micrographs of (a) 75/25 Gel-Pec-Cur and (b) 75/25 Gel-Pec-CurNg MNs. (c) Dimensions of Cur-loaded MNs (*n*=75, measurements performed on 15 random needles selected from 5 different arrays). (d) Force displacement curves of crosslinked and non-crosslinked 75/25 Gel-Pec MNs after an axial force load (*n*=9, measurements performed on 9 different regions of 5 arrays). (e) Insertion of 75/25 Gel-Pec-Cur, 75/25 Gel-Pec-CurNg and 75/25 Gel-Pec MNs into a polymeric model membrane for skin insertion using Parafilm® (*n*=3, error bars are smaller than the data point).

Full MNs arrays, with a square-base and pyramidal shape were prepared (Figure 5.6 (a-b)), indicating that both Cur formulations were suitable for MNs fabrication using these two biopolymers. Cur and CurNg are well distributed along the needles, with no evidence of agglomerates or clusters, originating MNs with a homogeneous and smooth appearance. MNs size is very similar between samples (Figure 5.6 (c)), suggesting that

there is no significant difference in solutions fluidity. Moreover, the incorporation of Cur and CurNg did not impact the mechanical strength of the MNs, as previously reported for other biopolymeric MNs loaded with Cur (Figure 5.6 (d)) [164]. Literature reports that the incorporation of Cur into HA MNs does not have a significant effect on the MN mechanics, with the blank and Cur-loaded samples withstanding 9.80 N [164]. Finally, the preliminary insertion test using the Parafilm® skin model, allows to infer that Cur and CurNg-loaded MNs are able to penetrate up to 381 μm in depth. This data indicates that the as-prepared MNs might be able to successfully penetrate skin, disrupting the *SC*, reaching the epidermis and the top of the dermis.

5.5. Conclusions

In this study, we demonstrated for the first time, the potential of Gel-Pec MNs for Cur incorporation envisioning melanoma treatment. *In vitro* cytotoxicity studies unveiled that Cur could effectively decrease cell viability of three different melanoma cell lines, which indicates Cur as a promising therapeutic for DD in anti-tumor applications. It was shown that 75/25 Gel-Pec MNs presented good mechanical strength and might insert skin properly. Incorporation of two Cur forms into 75/25 Gel-Pec MNs was successfully achieved, as MNs presented regular and homogeneous structures. The addition of Cur does not affect the good mechanical properties to the MNs, enabling the disruption of the Parafilm® skin model. Overall, Gel-Pec MNs loaded with Cur have potential to be an effective DDS for melanoma treatment.

Future evaluations are of foremost importance to confirm the potential of Gel-Pec MNs loaded with Cur, namely the evaluation of Cur bioactivity after incorporation into the MNs, the stability over storage, and skin insertion and delivery, both *in vitro* and *in vivo*.

CHAPTER 6. CONCLUDING REMARKS AND FUTURE WORK

6.1. Concluding remarks

The fabrication of biopolymeric MNs has gained increasing attention in the last decade. Recent literature highlights that these innovative systems have been employed both for DD and ISF extraction. Dozens of biopolymers have been reported in the preparation of MNs, with polysaccharides being the most widely studied. These natural polymers have been extensively exploited to support applications in the field of healthcare, while meeting the demand of environmentally sustainable technologies to support our future needs.

During this thesis, the preparation and characterization of MNs by using polysaccharides and a protein, through simple and greener fabrication methodologies was accomplished. Specifically, four innovative biopolymer-based MNs systems, for ISF and DD, were successfully developed and characterized. In the first part of this thesis, c-GelMA, was employed in the fabrication of swellable MNs, by micromolding combined with photo-crosslinking, for potential application in the extraction of ISF towards quantification of urea. The ability of c-GelMA MNs to reach the upper dermis region, coupled with its swelling ability, is imperative to enable ISF absorption and recover >98% of the metabolite when inserted into an *in vitro* model system.

Afterwards, dissolvable PL MNs were prepared envisioning the minimally invasive transdermal administration of insulin. The good thermal stability and non-hygroscopic behaviour are useful for the incorporation and storage of the peptide for up to 4 weeks at 4, 20 or 40 ºC. Furthermore, the application of insulin-loaded PL MNs into human abdominal skin *ex vivo* demonstrated that the polysaccharide dissolves within 2 hours, releasing about 87% of insulin. The next work described the preparation of MN patches for dermo-cosmetic applications, combining HA as a cosmetic ingredient, and BC as a macromolecular support for the incorporation of an additional bioactive molecule, in this case rutin, a natural antioxidant. The rutin molecules incorporated in the MNs retained their antioxidant properties over six months of storage at room temperature suggesting the stability of the systems during storage. An *in vivo* study unveiled the safety and cutaneous compatibility of the system which was found to be easy, practical and minimally invasive. The last research chapter of this thesis deals with the preparation of Gel-Pec MNs for administration of Cur envisioning the treatment of melanoma. A preliminary evaluation showed that Cur decreases the viability of three melanoma cell lines, which supports its use in melanoma treatment. In this perspective, Cur and a nanogel-loaded Cur were incorporated into Gel-Pec MNs which maintained their morphology and mechanical features, highlighting the potential of using these MNs systems in real applications.

The acquired scientific knowledge demonstrated that different biopolymers can be potentially exploited as a source of unique materials for DD and fluid extraction applications.

In particular, the biopolymers herein studied can be employed in micromolding fabrication procedures by solvent casting using water solutions, reinforcing the sustainable character of the devices. Furthermore, the use of biopolymers such as PL, HA, Gel and Pec, will not only be useful for functional purposes, but also of great help in protecting the environment from pollution by contributing to improve sustainability of waste management. In conclusion, this thesis opens new perspectives regarding biopolymeric matrices and DD, which will endorse innovation in the pharmaceutical market in the future.

6.2. Future work

Following the main objective of this PhD Thesis and considering the main results and conclusions, some interesting research topics, which are worth of further investigation, are here suggested:

- To complement the DD profiles of the different bioactive compounds with *in vivo* permeation studies and assessment of pharmacokinetics profile;
- To evaluate the diffusion and partitioning of biomolecules between MNs and the different skin layers;
- To determine the dissolution and degradation profile of the different biopolymers in skin and establish a relation with drug permeation;
- To probe the long-term stability of MNs and bioactive compounds, by exploring a more extensive range of storage conditions, to fully characterize the optimal storage conditions and maintenance of MNs morphology and stability of the active ingredients;
- To investigate the ISF extraction using *in vivo* models and also to study the simultaneous uptake of multiple target molecules, to infer about the potential of using these devices in the field of multiple molecular diagnostics and also liquid biopsies;
- To design systems capable of extracting and analysing metabolites, through the incorporation of adequate sensing/responsive systems, as a vital aspect of point-of-care diagnostics, revolutionizing the practice of emergency medicine and personalized health.

REFERENCES

[1] K.K. Jain, Drug delivery systems - An overview, Methods Mol. Biol. 437 (2008) 1–50. doi:10.1007/978-1-59745-210-6_1.

[2] O. Gassmann, G. Reepmeyer, M. von Zedtwitz, Leading pharmaceutical innovation: Trends and drivers for growth in the pharmaceutical industry, Springer Science & Business Media, 2013.

[3] A.C. Watkinson, M.-C. Kearney, H.L. Quinn, A.J. Courtenay, R.F. Donnelly, Future of the transdermal drug delivery market – have we barely touched the surface?, Expert Opin. Drug Deliv. 13 (2016) 523–532. doi:10.1517/17425247.2016.1130034.

[4] K.B. Ita, Transdermal drug delivery: Progress and challenges, J. Drug Deliv. Sci. Technol. 24 (2014) 245–250. doi:10.1016/S1773-2247(14)50041-X.

[5] E. Larrañeta, R.E.M. Lutton, A.D. Woolfson, R.F. Donnelly, Microneedle arrays as transdermal and intradermal drug delivery systems: Materials science, manufacture and commercial development, Mater. Sci. Eng. R Reports. 104 (2016) 1–32. doi:10.1016/j.mser.2016.03.001.

[6] E. Larrañeta, M.T.C. McCrudden, A.J. Courtenay, R.F. Donnelly, Microneedles: A New Frontier in Nanomedicine Delivery, Pharm. Res. 33 (2016) 1055–1073. doi:10.1007/s11095-016-1885-5.

[7] Y.-C.C. Kim, J.-H.H. Park, M.R. Prausnitz, Microneedles for drug and vaccine delivery, Adv. Drug Deliv. Rev. 64 (2012) 1547–1568. doi:10.1016/j.addr.2012.04.005.

[8] M. Wang, L. Hu, C. Xu, Recent advances in the design of polymeric microneedles for transdermal drug delivery and biosensing, Lab Chip. 17 (2017) 1373–1387. doi:10.1039/C7LC00016B.

[9] D.F.S. Fonseca, C. Vilela, A.J.D. Silvestre, C.S.R. Freire, A compendium of current developments on polysaccharide and protein-based microneedles, Int. J. Biol. Macromol. 136 (2019) 704–728. doi:10.1016/j.ijbiomac.2019.04.163.

[10] N.B. Shelke, R. James, C.T. Laurencin, S.G. Kumbar, Polysaccharide biomaterials for drug delivery and regenerative engineering, Polym. Adv. Technol. 25 (2014) 448–460. doi:10.1002/pat.3266.

[11] E. Markovsky, H. Baabur-Cohen, A. Eldar-Boock, L. Omer, G. Tiram, S. Ferber, P. Ofek, D. Polyak, A. Scomparin, R. Satchi-Fainaro, Administration, distribution, metabolism and elimination of polymer therapeutics, J. Control. Release. 161 (2012) 446–460. doi:10.1016/j.jconrel.2011.12.021.

[12] B.D. Ulery, L.S. Nair, C.T. Laurencin, Biomedical applications of biodegradable polymers, J. Polym. Sci. Part B Polym. Phys. 49 (2011) 832–864. doi:10.1002/polb.22259.

[13] S. Grund, M. Bauer, D. Fischer, Polymers in Drug Delivery-State of the Art and Future Trends, Adv. Eng. Mater. 13 (2011) B61–B87. doi:10.1002/adem.201080088.

[14] S.G. Kumbar, C.T. Laurencin, M. Deng, Natural and Synthetic Biomedical Polymers, Elsevier Science, 2014. doi:10.1016/C2011-0-07330-1.

[15] S.U. Org, Transforming Our World: The 2030 Agenda for Sustainable Development, in: A New Era Glob. Heal., 2018. doi:10.1891/9780826190123.ap02.

[16] A.C. Anselmo, S. Mitragotri, An overview of clinical and commercial impact of drug delivery systems, J. Control. Release. 190 (2014) 15–28. doi:10.1016/j.jconrel.2014.03.053.

[17] Y. Zhang, H.F. Chan, K.W. Leong, Advanced materials and processing for drug delivery: The past and the future, Adv. Drug Deliv. Rev. 65 (2013) 104–120. doi:10.1016/j.addr.2012.10.003.

[18] B. Wang, L. Hu, T.J. Siahaan, Drug delivery: principles and applications, Second, John Wiley & Sons, Hoboken, New Jersey, 2016. doi:10.1002/9781118833322.

[19] L.S. Goodman, L.L. Brunton, B. Chabner, B.C. Knollmann, Goodman & Gilman's The Pharmacological Basis of Therapeutics, 12th Editi, McGraw-Hill, New York, 2011.

[20] S. Wiedersberg, R.H. Guy, Transdermal drug delivery: 30 + years of war and still fighting!, J. Control. Release. 190 (2014) 150–156. doi:10.1016/j.jconrel.2014.05.022.

[21] W.K. Raja, S. MacCorkle, I.M. Diwan, A. Abdurrob, J. Lu, F.G. Omenetto, D.L. Kaplan, Transdermal delivery devices: Fabrication, mechanics and drug release from silk, Small. 9 (2013) 3704–3713. doi:10.1002/smll.201202075.

[22] B. Das Kurmi, P. Tekchandani, R. Paliwal, S.R. Paliwal, Transdermal Drug Delivery: Opportunities and Challenges for Controlled Delivery of Therapeutic Agents Using Nanocarriers, Curr. Drug Metab. 18 (2017) 481–495. doi:10.2174/1389200218666170222150555.

[23] K. Park, Drug delivery of the future: Chasing the invisible gorilla, J. Control. Release. 240 (2016) 2–8. doi:10.1016/j.jconrel.2015.10.048.

[24] D. Brambilla, P. Luciani, J.-C. Leroux, Breakthrough discoveries in drug delivery technologies: The next 30 years, J. Control. Release. 190 (2014) 9–14. doi:10.1016/j.jconrel.2014.03.056.

[25] R.F. Donnelly, T.R.R. Singh, D.I.J. Morrow, A.D. Woolfson, Transdermal Drug Delivery, in: Microneedle-Mediated Transdermal Intradermal Drug Deliv., John Wiley & Sons, Ltd, Chichester, UK, 2012: pp. 1–19. doi:10.1002/9781119959687.ch1.

[26] Global Transdermal Drug Delivery Market Analysis & Opportunity Outlook 2021, (2017). http://www.researchnester.com/reports/global-transdermal-drug-delivery-market-analysis-opportunity-outlook-2021/111 (accessed July 20, 2017).

[27] J.W. Wiechers, The barrier function of the skin in relation to percutaneous absorption of drugs, Pharm. Weekbl. 11 (1989) 185–198. doi:10.1007/BF01959410.

[28] C.A. Lipinski, F. Lombardo, B.W. Dominy, P.J. Feeney, Experimental and

computational approaches to estimate solubility and permeability in drug discovery and development settings, Adv. Drug Deliv. Rev. 23 (1997) 3–25. doi:10.1016/S0169-409X(00)00129-0.

[29] T.-M. Tuan-Mahmood, M.T.C. McCrudden, B.M. Torrisi, E. McAlister, M.J. Garland, T.R.R. Singh, R.F. Donnelly, Microneedles for intradermal and transdermal drug delivery, Eur. J. Pharm. Sci. 50 (2013) 623–637. doi:10.1016/j.ejps.2013.05.005.

[30] K. Ita, Ceramic microneedles and hollow microneedles for transdermal drug delivery: Two decades of research, J. Drug Deliv. Sci. Technol. 44 (2018) 314–322. doi:10.1016/j.jddst.2018.01.004.

[31] K. Ita, Transdermal delivery of drugs with microneedles: Strategies and outcomes, J. Drug Deliv. Sci. Technol. 29 (2015) 16–23. doi:10.1016/j.jddst.2015.05.001.

[32] N.S. Rejinold, J.-H. Shin, H.Y. Seok, Y.-C. Kim, Biomedical applications of microneedles in therapeutics: recent advancements and implications in drug delivery, Expert Opin. Drug Deliv. 13 (2016) 109–31. doi:10.1517/17425247.2016.1115835.

[33] E.M. Cahill, E.D. O'cearbhaill, Toward Biofunctional Microneedles for Stimulus Responsive Drug Delivery, Bioconjug. Chem. 26 (2015) 1289–1296. doi:10.1021/acs.bioconjchem.5b00211.

[34] Y. Ye, J. Yu, D. Wen, A.R. Kahkoska, Z. Gu, Polymeric microneedles for transdermal protein delivery, Adv. Drug Deliv. Rev. 127 (2018) 106–118. doi:10.1016/j.addr.2018.01.015.

[35] L. Wei-Ze, H. Mei-Rong, Z. Jian-Ping, Z. Yong-Qiang, H. Bao-Hua, L. Ting, Z. Yong, Super-short solid silicon microneedles for transdermal drug delivery applications, Int. J. Pharm. 389 (2010) 122–129. doi:10.1016/j.ijpharm.2010.01.024.

[36] P. Khanna, K. Luongo, J.A. Strom, S. Bhansali, Sharpening of hollow silicon microneedles to reduce skin penetration force, J. Micromechanics Microengineering. 20 (2010) 045011. doi:10.1088/0960-1317/20/4/045011.

[37] K.B. Vinayakumar, G.M. Hegde, M.M. Nayak, N.S. Dinesh, K. Rajanna, Fabrication and characterization of gold coated hollow silicon microneedle array for drug delivery, Microelectron. Eng. 128 (2014) 12–18. doi:10.1016/j.mee.2014.05.039.

[38] J. Li, B. Liu, Y. Zhou, Z. Chen, L. Jiang, W. Yuan, L. Liang, Fabrication of a Ti porous microneedle array by metal injection molding for transdermal drug delivery, PLoS One. 12 (2017) 0172043. doi:10.1371/journal.pone.0172043.

[39] M.T. Hoang, K.B. Ita, D.A. Bair, Solid Microneedles for Transdermal Delivery of Amantadine Hydrochloride and Pramipexole Dihydrochloride, Pharmaceutics. 7 (2015) 379–396. doi:10.3390/pharmaceutics7040379.

[40] S.M. Olhero, E. Lopes, J.M.F. Ferreira, Fabrication of ceramic microneedles – The role of specific interactions between processing additives and the surface of oxide particles

in Epoxy Gel Casting, J. Eur. Ceram. Soc. 36 (2016) 4131–4140. doi:10.1016/j.jeurceramsoc.2016.06.035.

[41] P.M. Wang, M. Cornwell, J. Hill, M.R. Prausnitz, Precise Microinjection into Skin Using Hollow Microneedles, J. Invest. Dermatol. 126 (2006) 1080–1087. doi:10.1038/sj.jid.5700150.

[42] M.W. Tibbitt, C.B. Rodell, J.A. Burdick, K.S. Anseth, Progress in material design for biomedical applications, Proc. Natl. Acad. Sci. 112 (2015) 14444–14451. doi:10.1073/pnas.1516247112.

[43] Q. Wei, R. Haag, Universal polymer coatings and their representative biomedical applications, Mater. Horizons. 2 (2015) 567–577. doi:10.1039/c5mh00089k.

[44] M. Niaounakis, Biopolymers : applications and trends, Elsevier, 2015. doi:10.1016/C2014-0-00936-7.

[45] M. Thanou, J.. Verhoef, H.. Junginger, Chitosan and its derivatives as intestinal absorption enhancers, Adv. Drug Deliv. Rev. 50 (2001) S91–S101. doi:10.1016/S0169-409X(01)00180-6.

[46] M.S. Gerstel, V.A. Place, Drug delivery device, US3964482A, 1976.

[47] S. Henry, D. V. McAllister, M.G. Allen, M.R. Prausnitz, Microfabricated Microneedles: A Novel Approach to Transdermal Drug Delivery, J. Pharm. Sci. 87 (1998) 922–925. doi:10.1021/js980042+.

[48] F. Ikeno, J. Lyons, H. Kaneda, M. Baluom, L.Z. Benet, M. Rezaee, Novel percutaneous adventitial drug delivery system for regional vascular treatment, Catheter. Cardiovasc. Interv. 63 (2004) 222–230. doi:10.1002/ccd.20167.

[49] M.L. Reed, C. Wu, J. Kneller, S. Watkins, D.A. Vorp, A. Nadeem, L.E. Weiss, K. Rebello, M. Mescher, A.J. Conrad Smith, W. Rosenblum, M.D. Feldman, Micromechanical devices for intravascular drug delivery, J. Pharm. Sci. 87 (1998) 1387–1394. doi:10.1021/js980085q.

[50] R.F. Donnelly, T.R.R. Singh, A.D. Woolfson, Microneedle-based drug delivery systems: Microfabrication, drug delivery, and safety, Drug Deliv. 17 (2010) 187–207. doi:10.3109/10717541003667798.

[51] J.C. Birchall, R. Clemo, A. Anstey, D.N. John, Microneedles in Clinical Practice-An Exploratory Study Into the Opinions of Healthcare professionals and the Public, Pharm. Res. 28 (2011) 95–106. doi:10.1007/s11095-010-0101-2.

[52] M.W. Ashraf, S. Tayyaba, N. Afzulpurkar, Micro Electromechanical Systems (MEMS) Based Microfluidic Devices for Biomedical Applications, Int. J. Mol. Sci. 12 (2011) 3648–3704. doi:10.3390/ijms12063648.

[53] P.G. Jung, T.W. Lee, D.J. Oh, S.J. Hwang, I.D. Jung, S.M. Lee, J.S. Ko, Nickel microneedles fabricated by sequential copper and nickel electroless plating and copper

chemical wet etching, Sensors Mater. 20 (2008) 45–53. doi:10.18494/sam.2008.507.

[54] S. Chandrasekaran, A.B. Frazier, Characterization of surface micromachined metallic microneedles, J. Microelectromechanical Syst. 12 (2003) 289–295. doi:10.1109/JMEMS.2003.811731.

[55] J.-H. Park, Y.-K. Yoon, S.-O. Choi, M.R. Prausnitz, M.G. Allen, Tapered Conical Polymer Microneedles Fabricated Using an Integrated Lens Technique for Transdermal Drug Delivery, IEEE Trans. Biomed. Eng. 54 (2007) 903–913. doi:10.1109/TBME.2006.889173.

[56] I.-C. Lee, J.-S. He, M.-T. Tsai, K.-C. Lin, Fabrication of a novel partially dissolving polymer microneedle patch for transdermal drug delivery, J. Mater. Chem. B. 3 (2015) 276–285. doi:10.1039/C4TB01555J.

[57] G. Cole, J. McCaffrey, A.A. Ali, J.W. McBride, C.M. McCrudden, E.M. Vincente-Perez, R.F. Donnelly, H.O. McCarthy, Dissolving microneedles for DNA vaccination: Improving functionality via polymer characterization and RALA complexation, Hum. Vaccines Immunother. 13 (2017) 50–62. doi:10.1080/21645515.2016.1248008.

[58] M.-C. Chen, M.-H. Ling, S.J. Kusuma, Poly-γ-glutamic acid microneedles with a supporting structure design as a potential tool for transdermal delivery of insulin, Acta Biomater. 24 (2015) 106–116. doi:10.1016/j.actbio.2015.06.021.

[59] Y. Hiraishi, T. Nakagawa, Y.S. Quan, F. Kamiyama, S. Hirobe, N. Okada, S. Nakagawa, Performance and characteristics evaluation of a sodium hyaluronate-based microneedle patch for a transcutaneous drug delivery system, Int. J. Pharm. 441 (2013) 570–579. doi:10.1016/j.ijpharm.2012.10.042.

[60] Y.-S. Tsai, M.-Y. Chen, S.-K. Lan, H.-T. Tsai, M.-C. Chen, T.-S. Tzai, Transdermal delivery of leuprolide acetate with chitosan microneedles: A promising tool for androgen deprivation therapy, Eur. Urol. Suppl. 16 (2017) e1304. doi:10.1016/s1569-9056(17)30808-4.

[61] I.-C. Lee, W. Lin, J. Shu, S. Tsai, C. Chen, M. Tsai, Formulation of two-layer dissolving polymeric microneedle patches for insulin transdermal delivery in diabetic mice, J. Biomed. Mater. Res. - Part A. 105 (2017) 84–93. doi:10.1002/jbm.a.35869.

[62] Y.-H. Park, S.K. Ha, I. Choi, K.S. Kim, J. Park, N. Choi, B. Kim, J.H. Sung, Fabrication of degradable carboxymethyl cellulose (CMC) microneedle with laser writing and replica molding process for enhancement of transdermal drug delivery, Biotechnol. Bioprocess Eng. 21 (2016) 110–118. doi:10.1007/s12257-015-0634-7.

[63] W. Yu, G. Jiang, D. Liu, L. Li, Z. Tong, J. Yao, X. Kong, Transdermal delivery of insulin with bioceramic composite microneedles fabricated by gelatin and hydroxyapatite, Mater. Sci. Eng. C. 73 (2017) 425–428. doi:10.1016/j.msec.2016.12.111.

[64] S.-M. An, K.-Y. Seong, S.-G. Yim, Y.J. Hwang, S.H. Bae, S.Y. Yang, B.-S. An,

Intracutaneous delivery of gelatins induces lipolysis and suppresses lipogenesis of adipocytes, Acta Biomater. 67 (2018) 238–247. doi:10.1016/j.actbio.2017.11.050.

[65] S. Bhatnagar, S.R. Chawla, O.P. Kulkarni, V.V.K. Venuganti, Zein Microneedles for Transcutaneous Vaccine Delivery: Fabrication, Characterization, and in Vivo Evaluation Using Ovalbumin as the Model Antigen, ACS Omega. 2 (2017) 1321–1332. doi:10.1021/acsomega.7b00343.

[66] D. Ding, J. Pan, S.H. Lim, S. Amini, L. Kang, A. Miserez, Squid suckerin microneedle arrays for tunable drug release, J. Mater. Chem. B. 5 (2017) 8467–8478. doi:10.1039/c7tb01507k.

[67] H.X. Nguyen, A.K. Banga, Fabrication, characterization and application of sugar microneedles for transdermal drug delivery, Ther. Deliv. 8 (2017) 249–264. doi:10.4155/tde-2016-0096.

[68] E.Z. Loizidou, N.A. Williams, D.A. Barrow, M.J. Eaton, J. McCrory, S.L. Evans, C.J. Allender, Structural characterisation and transdermal delivery studies on sugar microneedles: Experimental and finite element modelling analyses, Eur. J. Pharm. Biopharm. 89 (2015) 224–231. doi:10.1016/j.ejpb.2014.11.023.

[69] K. Lee, C.Y. Lee, H. Jung, Dissolving microneedles for transdermal drug administration prepared by stepwise controlled drawing of maltose, Biomaterials. 32 (2011) 3134–3140. doi:10.1016/j.biomaterials.2011.01.014.

[70] L.Y. Chu, S.O. Choi, M.R. Prausnitz, Fabrication of dissolving polymer microneedles for controlled drug encapsulation and delivery: Bubble and pedestal microneedle designs, J. Pharm. Sci. 99 (2010) 4228–4238. doi:10.1002/jps.22140.

[71] M.R. Prausnitz, Microneedles for transdermal drug delivery, Adv. Drug Deliv. Rev. 56 (2004) 581–587. doi:10.1016/j.addr.2003.10.023.

[72] K. van der Maaden, E. Sekerdag, W. Jiskoot, J. Bouwstra, Impact-Insertion Applicator Improves Reliability of Skin Penetration by Solid Microneedle Arrays, AAPS J. 16 (2014) 681–684. doi:10.1208/s12248-014-9606-7.

[73] M. Witting, K. Obst, M. Pietzsch, W. Friess, S. Hedtrich, Feasibility study for intraepidermal delivery of proteins using a solid microneedle array, Int. J. Pharm. 486 (2015) 52–58. doi:10.1016/j.ijpharm.2015.03.046.

[74] Y. Chen, B.Z. Chen, Q.L. Wang, X. Jin, X.D. Guo, Fabrication of coated polymer microneedles for transdermal drug delivery, J. Control. Release. 265 (2017) 14–21. doi:10.1016/j.jconrel.2017.03.383.

[75] H.S. Gill, M.R. Prausnitz, Coated microneedles for transdermal delivery, J. Control. Release. 117 (2007) 227–237. doi:10.1016/j.jconrel.2006.10.017.

[76] P.C. Demuth, J.J. Moon, H. Suh, P.T. Hammond, D.J. Irvine, Releasable Layer-by-Layer Assembly of Stabilized Lipid Nanocapsules on Microneedles for Enhanced

Transcutaneous Vaccine Delivery, ACS Nano. 6 (2012) 8041–8051. doi:10.1021/nn302639r.

[77] K. van der Maaden, E. Sekerdag, P. Schipper, G. Kersten, W. Jiskoot, J. Bouwstra, Layer-by-Layer Assembly of Inactivated Poliovirus and N-Trimethyl Chitosan on pH-Sensitive Microneedles for Dermal Vaccination, Langmuir. 31 (2015) 8654–8660. doi:10.1021/acs.langmuir.5b01262.

[78] C. Wang, Y. Ye, G.M. Hochu, H. Sadeghifar, Z. Gu, Enhanced Cancer Immunotherapy by Microneedle Patch-Assisted Delivery of Anti-PD1 Antibody, Nano Lett. 16 (2016) 2334–2340. doi:10.1021/acs.nanolett.5b05030.

[79] R.F. Donnelly, M.T.C. McCrudden, A.Z. Alkilani, E. Larrañeta, E. McAlister, A.J. Courtenay, M.C. Kearney, T.R. Raj Singh, H.O. McCarthy, V.L. Kett, E. Caffarel-Salvador, S. Al-Zahrani, A.D. Woolfson, Hydrogel-forming microneedles prepared from “super swelling” polymers combined with lyophilised wafers for transdermal drug delivery, PLoS One. 9 (2014) e111547. doi:10.1371/journal.pone.0111547.

[80] S. Khumpuang, M. Horade, K. Fujioka, S. Sugiyama, Geometrical strengthening and tip-sharpening of a microneedle array fabricated by X-ray lithography, Microsyst. Technol. 13 (2007) 209–214. doi:10.1007/s00542-006-0173-4.

[81] S.R. Patel, A.S.P. Lin, H.F. Edelhauser, M.R. Prausnitz, Suprachoroidal drug delivery to the back of the eye using hollow microneedles, Pharm. Res. 28 (2011) 166–176. doi:10.1007/s11095-010-0271-y.

[82] N. Roxhed, B. Samel, L. Nordquist, P. Griss, G. Stemme, Painless drug delivery through microneedle-based transdermal patches featuring active infusion, IEEE Trans. Biomed. Eng. 55 (2008) 1063–1071. doi:10.1109/TBME.2007.906492.

[83] S.P. Davis, W. Martanto, M.G. Allen, M.R. Prausnitz, Hollow metal microneedles for insulin delivery to diabetic rats, IEEE Trans. Biomed. Eng. 52 (2005) 909–915. doi:10.1109/TBME.2005.845240.

[84] H.J.G.E. Gardeniers, R. Luttge, E.J.W. Berenschot, M.J. De Boer, S.Y. Yeshurun, M. Hefetz, R. Van’t Oever, A. Van Den Berg, Silicon micromachined hollow microneedles for transdermal liquid transport, J. Microelectromechanical Syst. 12 (2003) 855–862. doi:10.1109/JMEMS.2003.820293.

[85] P. Griss, G. Stemme, Side-opened out-of-plane microneedles for microfluidic transdermal liquid transfer, J. Microelectromechanical Syst. 12 (2003) 296–301. doi:10.1109/JMEMS.2003.809959.

[86] W. Martanto, J.S. Moore, T. Couse, M.R. Prausnitz, Mechanism of fluid infusion during microneedle insertion and retraction, J. Control. Release. 112 (2006) 357–361. doi:10.1016/j.jconrel.2006.02.017.

[87] M.J. Akers, Excipient-drug interactions in parenteral formulations, J. Pharm. Sci. 91

(2002) 2283–2300. doi:10.1002/jps.10154.

[88] R. Donnelly, P. McCarron, D. Morrow, A. Morrissey, D. Woolfson, Microneedles/Delivery Device and Method, (2007).

[89] R.F. Donnelly, T.R.R. Singh, M.J. Garland, K. Migalska, R. Majithiya, C.M. McCrudden, P.L. Kole, T.M.T. Mahmood, H.O. McCarthy, A.D. Woolfson, Hydrogel-forming microneedle arrays for enhanced transdermal drug delivery, Adv. Funct. Mater. 22 (2012) 4879–4890. doi:10.1002/adfm.201200864.

[90] S. Yang, Y. Feng, L. Zhang, N. Chen, W. Yuan, T. Jin, A scalable fabrication process of polymer microneedles, Int. J. Nanomedicine. 7 (2012) 1415–1422. doi:10.2147/IJN.S28511.

[91] B. Koch, I. Rubino, F.-S. Quan, B. Yoo, H.-J. Choi, Microfabrication for Drug Delivery, Materials (Basel). 9 (2016) 646. doi:10.3390/ma9080646.

[92] M. Rajabi, N. Roxhed, R.Z. Shafagh, T. Haraldson, A.C. Fischer, W. Van Der Wijngaart, G. Stemme, F. Niklaus, Flexible and stretchable microneedle patches with integrated rigid stainless steel microneedles for transdermal biointerfacing, PLoS One. 11 (2016) e0166330. doi:10.1371/journal.pone.0166330.

[93] I. Huh, S. Kim, H. Yang, M. Jang, G. Kang, H. Jung, Effects of two droplet-based dissolving microneedle manufacturing methods on the activity of encapsulated epidermal growth factor and ascorbic acid, Eur. J. Pharm. Sci. 114 (2018) 285–292. doi:10.1016/j.ejps.2017.12.025.

[94] F. Sammoura, J. Kang, Y.-M. Heo, T. Jung, L. Lin, Polymeric microneedle fabrication using a microinjection molding technique, Microsyst. Technol. 13 (2007) 517–522. doi:10.1007/s00542-006-0204-1.

[95] D. Banks, Microengineering, MEMS, and Interfacing: A practical Guide, in: Microengineering, MEMS, Interfacing A Pract. Guid., CRC Press, 2006: pp. 1–10. doi:10.1201/9781420015416.

[96] M.J. Madou, Fundamentals of Microfabrication: The Science of Miniaturization, Second Edition, Second Edi, CRC Press, 2002. doi:10.1037/023990.

[97] F.J. Verbaan, S.M. Bal, D.J. van den Berg, W.H.H. Groenink, H. Verpoorten, R. Lüttge, J.A. Bouwstra, Assembled microneedle arrays enhance the transport of compounds varying over a large range of molecular weight across human dermatomed skin, J. Control. Release. 117 (2007) 238–245. doi:10.1016/j.jconrel.2006.11.009.

[98] W. Martanto, S.P. Davis, N.R. Holiday, J. Wang, H.S. Gill, M.R. Prausnitz, Transdermal delivery of insulin using microneedles in vivo, Pharm. Res. 21 (2004) 947–952. doi:10.1023/B:PHAM.0000029282.44140.2e.

[99] K. Lee, H.C. Lee, D.S. Lee, H. Jung, Drawing lithography: Three-dimensional fabrication of an ultrahigh-aspect-ratio microneedle, Adv. Mater. 22 (2010) 483–486.

doi:10.1002/adma.200902418.

[100] S. Bystrova, R. Luttge, Micromolding for ceramic microneedle arrays, Microelectron. Eng. 88 (2011) 1681–1684. doi:10.1016/j.mee.2010.12.067.

[101] I. Papautsky, E.T.K. Peterson, Micromolding, in: Encycl. Microfluid. Nanofluidics, Springer US, Boston, MA, 2014: pp. 1–17. doi:10.1007/978-3-642-27758-0_986-2.

[102] M.T.C. McCrudden, A.Z. Alkilani, A.J. Courtenay, C.M. McCrudden, B. McCloskey, C. Walker, N. Alshraiedeh, R.E.M. Lutton, B.F. Gilmore, A.D. Woolfson, R.F. Donnelly, Considerations in the sterile manufacture of polymeric microneedle arrays, Drug Deliv. Transl. Res. 5 (2014) 3–14. doi:10.1007/s13346-014-0211-1.

[103] Y.-H. Lin, I.-C. Lee, W.-C. Hsu, C.-H. Hsu, K.-P. Chang, S.-S. Gao, Rapid fabrication method of a microneedle mold with controllable needle height and width, Biomed. Microdevices. 18 (2016) 85. doi:10.1007/s10544-016-0113-8.

[104] C.Y. Jin, M.H. Han, S.S. Lee, Y.H. Choi, Mass producible and biocompatible microneedle patch and functional verification of its usefulness for transdermal drug delivery, Biomed. Microdevices. 11 (2009) 1195–1203. doi:10.1007/s10544-009-9337-1.

[105] J.M. Lippmann, E.J. Geiger, A.P. Pisano, Polymer investment molding: Method for fabricating hollow, microscale parts, Sensors Actuators, A Phys. 134 (2007) 2–10. doi:10.1016/j.sna.2006.05.009.

[106] M.C. Chen, S.F. Huang, K.Y. Lai, M.H. Ling, Fully embeddable chitosan microneedles as a sustained release depot for intradermal vaccination, Biomaterials. 34 (2013) 3077–3086. doi:10.1016/j.biomaterials.2012.12.041.

[107] E. Esposito, F. Ruggiero, R. Vecchione, P.A. Netti, Room temperature consolidation of a porous poly(lactic-co-glycolic acid) matrix by the addition of maltose to the water-in-oil emulsion, Materials (Basel). 9 (2016). doi:10.3390/ma9060420.

[108] R. Vecchione, S. Coppola, E. Esposito, C. Casale, V. Vespini, S. Grilli, P. Ferraro, P.A. Netti, Electro-Drawn Drug-Loaded Biodegradable Polymer Microneedles as a Viable Route to Hypodermic Injection, Adv. Funct. Mater. 24 (2014) 3515–3523. doi:10.1002/adfm.201303679.

[109] J.D. Kim, M. Kim, H. Yang, K. Lee, H. Jung, Droplet-born air blowing: Novel dissolving microneedle fabrication, J. Control. Release. 170 (2013) 430–436. doi:http://dx.doi.org/10.1016/j.jconrel.2013.05.026.

[110] A. Caliò, P. Dardano, V. Di Palma, M.F. Bevilacqua, A. Di Matteo, H. Iuele, L. De Stefano, Polymeric microneedles based enzymatic electrodes for electrochemical biosensing of glucose and lactic acid, Sensors Actuators B Chem. 236 (2016) 343–349. doi:http://dx.doi.org/10.1016/j.snb.2016.05.156.

[111] P. Dardano, A. Caliò, V. Di Palma, M.F. Bevilacqua, A. Di Matteo, L. De Stefano, A

Photolithographic Approach to Polymeric Microneedles Array Fabrication, Materials (Basel). 8 (2015) 8661–8673. doi:10.3390/ma8125484.

[112] A.R. Johnson, C.L. Caudill, J.R. Tumbleston, C.J. Bloomquist, K.A. Moga, A. Ermoshkin, D. Shirvanyants, S.J. Mecham, J.C. Luft, J.M. DeSimone, Single-Step Fabrication of Computationally Designed Microneedles by Continuous Liquid Interface Production, PLoS One. 11 (2016) e0162518. doi:10.1371/journal.pone.0162518.

[113] G.A. Appuhamillage, J.C. Reagan, S. Khorsandi, J.R. Davidson, W. Voit, R.A. Smaldone, 3D printed remendable polylactic acid blends with uniform mechanical strength enabled by a dynamic Diels-Alder reaction, Polym. Chem. 8 (2017) 2087–2092. doi:10.1039/c7py00310b.

[114] A. Döpp, E. Guillaume, C. Thaury, J. Gautier, K. Ta Phuoc, V. Malka, 3D printing of gas jet nozzles for laser-plasma accelerators, Rev. Sci. Instrum. 87 (2016) 073505. doi:10.1063/1.4958649.

[115] M. Matteucci, M. Fanetti, M. Casella, F. Gramatica, L. Gavioli, M. Tormen, G. Grenci, F. De Angelis, E. Di Fabrizio, Poly vinyl alcohol re-usable masters for microneedle replication, Microelectron. Eng. 86 (2009) 752–756. doi:10.1016/j.mee.2009.01.068.

[116] S. Lau, J. Fei, H. Liu, W. Chen, R. Liu, Multilayered pyramidal dissolving microneedle patches with flexible pedestals for improving effective drug delivery, J. Control. Release. 265 (2017) 113–119. doi:10.1016/j.jconrel.2016.08.031.

[117] K.J. Cha, T. Kim, S.J. Park, D.S. Kim, Simple and cost-effective fabrication of solid biodegradable polymer microneedle arrays with adjustable aspect ratio for transdermal drug delivery using acupuncture microneedles, J. Micromechanics Microengineering. 24 (2014) 115015. doi:10.1088/0960-1317/24/11/115015.

[118] S.J. Moon, S.S. Lee, H.S. Lee, T.H. Kwon, Fabrication of microneedle array using LIGA and hot embossing process, in: Microsyst. Technol., Springer-Verlag, 2005: pp. 311–318. doi:10.1007/s00542-004-0446-8.

[119] M. Han, D.K. Kim, S.H. Kang, H.-R. Yoon, B.-Y. Kim, S.S. Lee, K.D. Kim, H.G. Lee, Improvement in antigen-delivery using fabrication of a grooves-embedded microneedle array, Sensors Actuators, B Chem. 137 (2009) 274–280. doi:10.1016/j.snb.2008.11.017.

[120] Q.L. Wang, X.P. Zhang, B.Z. Chen, X.D. Guo, Dissolvable layered microneedles with core-shell structures for transdermal drug delivery, Mater. Sci. Eng. C. 83 (2018) 143–147. doi:10.1016/j.msec.2017.11.009.

[121] V. Latza, P.A. Guerette, D. Ding, S. Amini, A. Kumar, I. Schmidt, S. Keating, N. Oxman, J.C. Weaver, P. Fratzl, A. Miserez, A. Masic, Multi-scale thermal stability of a hard thermoplastic protein-based material, Nat. Commun. 6 (2015) 8313. doi:10.1038/ncomms9313.

[122] S.P. Sullivan, N. Murthy, M.R. Prausnitz, Minimally invasive protein delivery with rapidly dissolving polymer microneedles, Adv. Mater. 20 (2008) 933–938. doi:10.1002/adma.200701205.

[123] H. Yang, S. Kim, G. Kang, S.F. Lahiji, M. Jang, Y.M. Kim, J.-M.M. Kim, S.-N.N. Cho, H. Jung, Centrifugal Lithography: Self-Shaping of Polymer Microstructures Encapsulating Biopharmaceutics by Centrifuging Polymer Drops, Adv. Healthc. Mater. 6 (2017) 1700326. doi:10.1002/adhm.201700326.

[124] N. Guo, M.C. Leu, Additive manufacturing: Technology, applications and research needs, Front. Mech. Eng. 8 (2013) 215–243. doi:10.1007/s11465-013-0248-8.

[125] M.A. Luzuriaga, D.R. Berry, J.C. Reagan, R.A. Smaldone, J.J. Gassensmith, Biodegradable 3D printed polymer microneedles for transdermal drug delivery, Lab Chip. 18 (2018) 1223–1230. doi:10.1039/c8lc00098k.

[126] P. Jung-Hwan, P. Mark, Analysis of mechanical failure of polymer microneedles by axial force, J. Korean Phys. Soc. 56 (2010) 1223. doi:10.3938/jkps.56.1223.

[127] Q.L. Wang, J.W. Ren, B.Z. Chen, X. Jin, C.Y. Zhang, X.D. Guo, Effect of humidity on mechanical properties of dissolving microneedles for transdermal drug delivery, J. Ind. Eng. Chem. 59 (2018) 251–258. doi:10.1016/j.jiec.2017.10.030.

[128] S.P. Davis, B.J. Landis, Z.H. Adams, M.G. Allen, M.R. Prausnitz, Insertion of microneedles into skin: Measurement and prediction of insertion force and needle fracture force, J. Biomech. 37 (2004) 1155–1163. doi:10.1016/j.jbiomech.2003.12.010.

[129] J. Zahn, N. Talbot, D. Liepmann, A. Pisano, Microfabricated polysilicon microneedles for minimally invasive biomedical devices, Biomed. Microdevices. 2 (2000) 295–303. doi:10.1023/A:1009907306184.

[130] Y.K. Demir, Z. Akan, O. Kerimoglu, Characterization of Polymeric Microneedle Arrays for Transdermal Drug Delivery, PLoS One. 8 (2013) e77289. doi:10.1371/journal.pone.0077289.

[131] J.-H.H. Park, M.G. Allen, M.R. Prausnitz, Biodegradable polymer microneedles: Fabrication, mechanics and transdermal drug delivery, J. Control. Release. 104 (2005) 51–66. doi:10.1016/j.jconrel.2005.02.002.

[132] S.D. Gittard, B. Chen, H. Xu, A. Ovsianikov, B.N. Chichkov, N.A. Monteiro-Riviere, R.J. Narayan, The Effects of Geometry on Skin Penetration and Failure of Polymer Microneedles., J. Adhes. Sci. Technol. 27 (2013) 227–243. doi:10.1080/01694243.2012.705101.

[133] R.F. Donnelly, R. Majithiya, T.R.R. Singh, D.I.J.J. Morrow, M.J. Garland, Y.K. Demir, K. Migalska, E. Ryan, D. Gillen, C.J. Scott, A.D. Woolfson, Design, optimization and characterisation of polymeric microneedle arrays prepared by a novel laser-based micromoulding technique, Pharm. Res. 28 (2011) 41–57. doi:10.1007/s11095-010-

0169-8.

[134] W.G.G. Smith, Analytic solutions for tapered column buckling, Comput. Struct. 28 (1988) 677–681. doi:https://doi.org/10.1016/0045-7949(88)90011-9.

[135] J.W. Lee, J.-H.H. Park, M.R. Prausnitz, Dissolving microneedles for transdermal drug delivery, Biomaterials. 29 (2008) 2113–2124. doi:10.1016/j.biomaterials.2007.12.048.

[136] N. Roxhed, T.C. Gasser, P. Griss, G.A. Holzapfel, Gö. Stemme, Penetration-enhanced ultrasharp microneedles and prediction on skin interaction for efficient transdermal drug delivery, J. Microelectromechanical Syst. 16 (2007) 1429–1440. doi:10.1109/JMEMS.2007.907461.

[137] M.S. Lhernould, C. Gobillon, P. Lambert, Microneedle array penetration tests: Understanding the “bed of nails” phenomenon, ONdrugDelivery. 40 (2013) 29–32.

[138] S.M. Bal, J. Caussin, S. Pavel, J.A. Bouwstra, In vivo assessment of safety of microneedle arrays in human skin, Eur. J. Pharm. Sci. 35 (2008) 193–202. doi:10.1016/j.ejps.2008.06.016.

[139] M.-H.H. Ling, M.-C.C. Chen, Dissolving polymer microneedle patches for rapid and efficient transdermal delivery of insulin to diabetic rats, Acta Biomater. 9 (2013) 8952–8961. doi:10.1016/j.actbio.2013.06.029.

[140] R.F. Donnelly, M.J. Garland, D.I.J. Morrow, K. Migalska, T.R.R. Singh, R. Majithiya, A.D. Woolfson, Optical coherence tomography is a valuable tool in the study of the effects of microneedle geometry on skin penetration characteristics and in-skin dissolution, J. Control. Release. 147 (2010) 333–341. doi:10.1016/j.jconrel.2010.08.008.

[141] Y.A. Gomaa, M.J. Garland, F. McInnes, L.K. El-Khordagui, C. Wilson, R.F. Donnelly, Laser-engineered dissolving microneedles for active transdermal delivery of nadroparin calcium, Eur. J. Pharm. Biopharm. 82 (2012) 299–307. doi:10.1016/j.ejpb.2012.07.008.

[142] K. Takada, N. Yoshimoto, N. Hamasaki, Y. Ueda, T. Nakahigashi, Y. Ito, T. Nakahigashi, N. Yoshimoto, Y. Ueda, N. Hamasaki, K. Takada, Transdermal Insulin Application System with Dissolving Microneedles, Diabetes Technol. Ther. 14 (2012) 891–899. doi:10.1089/dia.2012.0096.

[143] E. Abd, S.A. Yousef, M.N. Pastore, K. Telaprolu, Y.H. Mohammed, S. Namjoshi, J.E. Grice, M.S. Roberts, Skin models for the testing of transdermal drugs, Clin. Pharmacol. Adv. Appl. 8 (2016) 163–176. doi:10.2147/CPAA.S64788.

[144] E. Larrañeta, J. Moore, E.M. Vicente-Pérez, P. González-Vázquez, R. Lutton, A.D. Woolfson, R.F. Donnelly, A proposed model membrane and test method for microneedle insertion studies, Int. J. Pharm. 472 (2014) 65–73. doi:10.1016/j.ijpharm.2014.05.042.

[145] J.Y. Hong, E.J. Ko, S.Y. Choi, K. Li, A.R. Kim, J.O. Park, B.J. Kim, Efficacy and safety

of a novel, soluble microneedle patch for the improvement of facial wrinkle, J. Cosmet. Dermatol. 17 (2018) 235–241. doi:10.1111/jocd.12426.

[146] Y. Lee, S. Kumar, S.H. Kim, K.Y. Seong, H. Lee, C. Kim, Y.S. Jung, S.Y. Yang, Odorless glutathione microneedle patches for skin whitening, Pharmaceutics. 12 (2020) 100. doi:10.3390/pharmaceutics12020100.

[147] M. Wang, Y. Han, X. Yu, L. Liang, H. Chang, D.C. Yeo, C. Wiraja, M.L. Wee, L. Liu, X. Liu, C. Xu, Upconversion Nanoparticle Powered Microneedle Patches for Transdermal Delivery of siRNA, Adv. Healthc. Mater. 9 (2020) 1900635. doi:10.1002/adhm.201900635.

[148] M. Bok, Z.J. Zhao, S. Jeon, J.H. Jeong, E. Lim, Ultrasonically and Iontophoretically Enhanced Drug-Delivery System Based on Dissolving Microneedle Patches, Sci. Rep. 10 (2020). doi:10.1038/s41598-020-58822-w.

[149] L. Dong, Y. Li, Z. Li, N. Xu, P. Liu, H. Du, Y. Zhang, Y. Huang, J. Zhu, G. Ren, J. Xie, K. Wang, Y. Zhou, C. Shen, J. Zhu, J. Tao, Au Nanocage-Strengthened Dissolving Microneedles for Chemo-Photothermal Combined Therapy of Superficial Skin Tumors, ACS Appl. Mater. Interfaces. 10 (2018) 9247–9256. doi:10.1021/acsami.7b18293.

[150] H. Yang, X. Wu, Z. Zhou, X. Chen, M. Kong, Enhanced transdermal lymphatic delivery of doxorubicin via hyaluronic acid based transfersomes/microneedle complex for tumor metastasis therapy, Int. J. Biol. Macromol. 125 (2019) 9–16. doi:10.1016/j.ijbiomac.2018.11.230.

[151] J.H. Kim, J.U. Shin, S.H. Kim, J.Y. Noh, H.R. Kim, J. Lee, H. Chu, K.Y. Jeong, K.H. Park, J.D. Kim, H.K. Kim, D.H. Jeong, T.S. Yong, J.W. Park, K.H. Lee, Successful transdermal allergen delivery and allergen-specific immunotherapy using biodegradable microneedle patches, Biomaterials. 150 (2018) 38–48. doi:10.1016/j.biomaterials.2017.10.013.

[152] F. Chen, Q. Yan, Y. Yu, M.X. Wu, BCG vaccine powder-laden and dissolvable microneedle arrays for lesion-free vaccination, J. Control. Release. 255 (2017) 36–44. doi:10.1016/j.jconrel.2017.03.397.

[153] M. Avcil, G. Akman, J. Klokkers, D. Jeong, A. Çelik, Efficacy of bioactive peptides loaded on hyaluronic acid microneedle patches: A monocentric clinical study, J. Cosmet. Dermatol. 19 (2020) 328–337. doi:10.1111/jocd.13009.

[154] A. Than, K. Liang, S. Xu, L. Sun, H. Duan, F. Xi, C. Xu, P. Chen, Transdermal Delivery of Anti-Obesity Compounds to Subcutaneous Adipose Tissue with Polymeric Microneedle Patches, Small Methods. 1 (2017) 1700269. doi:10.1002/smtd.201700269.

[155] Y. Hao, Y. Chen, M. Lei, T. Zhang, Y. Cao, J. Peng, L. Chen, Z. Qian, Near-Infrared Responsive PEGylated Gold Nanorod and Doxorubicin Loaded Dissolvable Hyaluronic

Acid Microneedles for Human Epidermoid Cancer Therapy, Adv. Ther. 1 (2018) 1800008. doi:10.1002/adtp.201800008.

[156] S.S. Kim, J. Lee, F.L. Shayan, S.S. Kim, I. Huh, Y. Ma, H. Yang, G. Kang, H. Jung, Physicochemical study of ascorbic acid 2-glucoside loaded hyaluronic acid dissolving microneedles irradiated by electron beam and gamma ray, Carbohydr. Polym. 180 (2018) 297–303. doi:10.1016/j.carbpol.2017.10.044.

[157] H. Du, P. Liu, J. Zhu, J. Lan, Y. Li, L. Zhang, J. Zhu, J. Tao, Hyaluronic Acid-Based Dissolving Microneedle Patch Loaded with Methotrexate for Improved Treatment of Psoriasis, ACS Appl. Mater. Interfaces. 11 (2019) 43588–43598. doi:10.1021/acsami.9b15668.

[158] Y.Y. Li, Y. Xie, H. Wang, J. Mao, Y.Y. Li, M. Hussain, J.J. Zhu, L. Zhang, J. Tao, J.J. Zhu, Enhanced: In vitro efficacy for inhibiting hypertrophic scar by bleomycin-loaded dissolving hyaluronic acid microneedles, J. Mater. Chem. B. 7 (2019) 6604–6611. doi:10.1039/c9tb01449g.

[159] Y. Park, B. Kim, Skin permeability of compounds loaded within dissolving microneedles dependent on composition of sodium hyaluronate and carboxymethyl cellulose, Korean J. Chem. Eng. 34 (2017) 133–138. doi:10.1007/s11814-016-0240-1.

[160] W. Yu, G. Jiang, Y. Zhang, D. Liu, B. Xu, J. Zhou, Polymer microneedles fabricated from alginate and hyaluronate for transdermal delivery of insulin, Mater. Sci. Eng. C. 80 (2017) 187–196. doi:10.1016/j.msec.2017.05.143.

[161] S.W.T. Chew, A.H. Shah, M. Zheng, H. Chang, C. Wiraja, T.W.J. Steele, C. Xu, A Self-adhesive Microneedle Patch with Drug loading Capability through Swelling Effect, Bioeng. Transl. Med. (2020). doi:10.1002/btm2.10157.

[162] J.-T.T. Choi, S.-J.J. Park, J.-H.H. Park, Microneedles containing cross-linked hyaluronic acid particulates for control of degradation and swelling behaviour after administration into skin, J. Drug Target. 26 (2018) 884–894. doi:10.1080/1061186X.2018.1435664.

[163] D.S. Kim, J.T. Choi, C.B. Kim, Y.R. Shin, P. gu Park, H. Kim, J.M. Lee, J.H. Park, Microneedle Array Patch (MAP) Consisting of Crosslinked Hyaluronic Acid Nanoparticles for Processability and Sustained Release, Pharm. Res. 37 (2020) 1–11. doi:10.1007/s11095-020-2768-3.

[164] Z. Cheng, H. Lin, Z. Wang, X. Yang, M. Zhang, X. Liu, B. Wang, Z. Wu, D. Chen, Preparation and characterization of dissolving hyaluronic acid composite microneedles loaded micelles for delivery of curcumin, Drug Deliv. Transl. Res. (2020). doi:10.1007/s13346-020-00735-2.

[165] J. Zhu, L. Dong, H. Du, J. Mao, Y. Xie, H. Wang, J. Lan, Y. Lou, Y. Fu, J. Wen, B. Jiang, Y. Li, J. Zhu, J. Tao, 5-Aminolevulinic Acid-Loaded Hyaluronic Acid Dissolving Microneedles for Effective Photodynamic Therapy of Superficial Tumors with Enhanced

Long-Term Stability, Adv. Healthc. Mater. 8 (2019) 1900896. doi:10.1002/adhm.201900896.

[166] S.Y. Park, H.U. Lee, Y.C. Lee, G.H. Kim, E.C. Park, S.H. Han, J.G. Lee, S. Choi, N.S. Heo, D.L. Kim, Y.S. Huh, J. Lee, Wound healing potential of antibacterial microneedles loaded with green tea extracts, Mater. Sci. Eng. C. 42 (2014) 757–762. doi:10.1016/j.msec.2014.06.021.

[167] J.N. Zhang, B.Z. Chen, M. Ashfaq, X.P. Zhang, X.D. Guo, Development of a BDDE-crosslinked hyaluronic acid based microneedles patch as a dermal filler for anti-ageing treatment, J. Ind. Eng. Chem. 65 (2018) 363–369. doi:10.1016/j.jiec.2018.05.007.

[168] K. Matsuo, Y. Yokota, Y. Zhai, Y.S. Quan, F. Kamiyama, Y. Mukai, N. Okada, S. Nakagawa, A low-invasive and effective transcutaneous immunization system using a novel dissolving microneedle array for soluble and particulate antigens, J. Control. Release. 161 (2012) 10–17. doi:10.1016/j.jconrel.2012.01.033.

[169] S. Liu, M.N. Jin, Y.S. Quan, F. Kamiyama, K. Kusamori, H. Katsumi, T. Sakane, A. Yamamoto, Transdermal delivery of relatively high molecular weight drugs using novel self-dissolving microneedle arrays fabricated from hyaluronic acid and their characteristics and safety after application to the skin, Eur. J. Pharm. Biopharm. 86 (2014) 267–276. doi:10.1016/j.ejpb.2013.10.001.

[170] S. Liu, M.N. Jin, Y.S. Quan, F. Kamiyama, H. Katsumi, T. Sakane, A. Yamamoto, The development and characteristics of novel microneedle arrays fabricated from hyaluronic acid, and their application in the transdermal delivery of insulin, J. Control. Release. 161 (2012) 933–941. doi:10.1016/j.jconrel.2012.05.030.

[171] Y. Kim, S.A. Bhattaccharjee, M. Beck-Broichsitter, A.K. Banga, Fabrication and characterization of hyaluronic acid microneedles to enhance delivery of magnesium ascorbyl phosphate into skin, Biomed. Microdevices. 21 (2019). doi:10.1007/s10544-019-0455-0.

[172] M. Dangol, S. Kim, C.G. Li, S. Fakhraei Lahiji, M. Jang, Y. Ma, I. Huh, H. Jung, Anti-obesity effect of a novel caffeine-loaded dissolving microneedle patch in high-fat diet-induced obese C57BL/6J mice, J. Control. Release. 265 (2017) 41–47. doi:10.1016/j.jconrel.2017.03.400.

[173] Z. Zhu, X. Ye, Z. Ku, Q. Liu, C. Shen, H. Luo, H. Luan, C. Zhang, S. Tian, C.Y. Lim, Z. Huang, H. Wang, Transcutaneous immunization via rapidly dissolvable microneedles protects against hand-foot-and-mouth disease caused by enterovirus 71, J. Control. Release. 243 (2016) 291–302. doi:10.1016/j.jconrel.2016.10.019.

[174] S.G. Lee, J.H. Jeong, K.M. Lee, K.H. Jeong, H. Yang, M. Kim, H. Jung, S. Lee, Y.W. Choi, Nanostructured lipid carrier-loaded hyaluronic acid microneedles for controlled dermal delivery of a lipophilic molecule, Int. J. Nanomedicine. 9 (2013) 289–299.

doi:10.2147/IJN.S54529.

[175] J. Mönkäre, M. Reza Nejadnik, K. Baccouche, S. Romeijn, W. Jiskoot, J.A. Bouwstra, IgG-loaded hyaluronan-based dissolving microneedles for intradermal protein delivery, J. Control. Release. 218 (2015) 53–62. doi:10.1016/j.jconrel.2015.10.002.

[176] Y. Park, K.S. Kim, M. Chung, J.H. Sung, B. Kim, Fabrication and characterization of dissolving microneedle arrays for improving skin permeability of cosmetic ingredients, J. Ind. Eng. Chem. 39 (2016) 121–126. doi:10.1016/j.jiec.2016.05.022.

[177] G. Kang, T.N.T. Tu, S. Kim, H. Yang, M. Jang, D. Jo, J. Ryu, J. Baek, H. Jung, Adenosine-loaded dissolving microneedle patches to improve skin wrinkles, dermal density, elasticity and hydration, Int. J. Cosmet. Sci. 40 (2018) 199–206. doi:10.1111/ics.12453.

[178] Z. Gui, X. Wu, S. Wang, Y. Cao, J. Wan, Q. Shan, Z. Yang, J. Zhang, S. Gui, Dissolving Microneedles Integrated With Liquid Crystals Facilitate Transdermal Delivery of Sinomenine Hydrochloride, J. Pharm. Sci. 106 (2017) 3548–3555. doi:10.1016/j.xphs.2017.07.027.

[179] W. Yao, C. Tao, J. Zou, H. Zheng, J. Zhu, Z. Zhu, J. Zhu, L. Liu, F. Li, X. Song, Flexible two-layer dissolving and safing microneedle transdermal of neurotoxin: A biocomfortable attempt to treat Rheumatoid Arthritis, Int. J. Pharm. 563 (2019) 91–100. doi:10.1016/j.ijpharm.2019.03.033.

[180] S. Liu, S. Zhang, Y. Duan, Y. Niu, H. Gu, Z. Zhao, S. Zhang, Y. Yang, X. Wang, Y. Gao, P. Yang, Transcutaneous immunization of recombinant Staphylococcal enterotoxin B protein using a dissolving microneedle provides potent protection against lethal enterotoxin challenge, Vaccine. 37 (2019) 3810–3819. doi:10.1016/j.vaccine.2019.05.055.

[181] Y. Ito, S. Kobuchi, G. Inoue, E. Kakumu, M. Aoki, T. Sakaeda, K. Takada, Dissolving microneedles for enhanced local delivery of capsaicin to rat skin tissue, J. Drug Target. 25 (2017) 420–424. doi:10.1080/1061186X.2016.1266650.

[182] Y. Ito, T. Yamazaki, N. Sugioka, K. Takada, Self-dissolving micropile array tips for percutaneous administration of insulin, J. Mater. Sci. Mater. Med. 21 (2010) 835–841. doi:10.1007/s10856-009-3923-x.

[183] D. Poirier, F. Renaud, V. Dewar, L. Strodiot, F. Wauters, J. Janimak, T. Shimada, T. Nomura, K. Kabata, K. Kuruma, T. Kusano, M. Sakai, H. Nagasaki, T. Oyamada, Hepatitis B surface antigen incorporated in dissolvable microneedle array patch is antigenic and thermostable, Biomaterials. 145 (2017) 256–265. doi:10.1016/j.biomaterials.2017.08.038.

[184] M. Zaric, P.D. Becker, C. Hervouet, P. Kalcheva, B. Ibarzo Yus, C. Cocita, L.A. O'Neill, S.Y. Kwon, L.S. Klavinskis, Long-lived tissue resident HIV-1 specific memory CD8+T

cells are generated by skin immunization with live virus vectored microneedle arrays, J. Control. Release. 268 (2017) 166–175. doi:10.1016/j.jconrel.2017.10.026.

[185] H. Zhan, F. Ma, Y. Huang, J. Zhang, X. Jiang, Y. Qian, Application of composite dissolving microneedles with high drug loading ratio for rapid local anesthesia, Eur. J. Pharm. Sci. 121 (2018) 330–337. doi:10.1016/j.ejps.2018.06.014.

[186] N.N. Aung, T. Ngawhirunpat, T. Rojanarata, P. Patrojanasophon, P. Opanasopit, B. Pamornpathomkul, HPMC/PVP Dissolving Microneedles: a Promising Delivery Platform to Promote Trans-Epidermal Delivery of Alpha-Arbutin for Skin Lightening, AAPS PharmSciTech. 21 (2020) 1–13. doi:10.1208/s12249-019-1599-1.

[187] Z. Chen, B. Han, L. Liao, X. Hu, Q. Hu, Y. Gao, Y. Qiu, Enhanced transdermal delivery of polydatin via a combination of inclusion complexes and dissolving microneedles for treatment of acute gout arthritis, J. Drug Deliv. Sci. Technol. 55 (2020) 101487. doi:10.1016/j.jddst.2019.101487.

[188] R.P. Gala, R. Uz Zaman, M.J. D'souza, S.M. Zughaier, Novel whole-cell inactivated Neisseria gonorrhoeae microparticles as vaccine formulation in microneedle-based transdermal immunization, Vaccines. 6 (2018) 60. doi:10.3390/vaccines6030060.

[189] H.S. Seon-Woo, H.J. Kim, J.Y. Roh, J.H. Park, Dissolving Microneedle Systems for the Oral Mucosal Delivery of Triamcinolone Acetonide to Treat Aphthous Stomatitis, Macromol. Res. 27 (2019) 282–289. doi:10.1007/s13233-019-7031-6.

[190] E. Kim, G. Erdos, S. Huang, T.W. Kenniston, S.C. Balmert, C. Donahue Carey, V. Stalin Raj, M.W. Epperly, W.B. Klimstra, B.L. Haagmans, E. Korkmaz, L.D. Falo, A. Gambotto, Microneedle array delivered recombinant coronavirus vaccines: Immunogenicity and rapid translational development, EBioMedicine. (2020) 102743. doi:10.1016/j.ebiom.2020.102743.

[191] S. Fakhraei Lahiji, S.H. Seo, S. Kim, M. Dangol, J. Shim, C.G. Li, Y. Ma, C. Lee, G. Kang, H. Yang, K.Y. Choi, H. Jung, Transcutaneous implantation of valproic acid-encapsulated dissolving microneedles induces hair regrowth, Biomaterials. 167 (2018) 69–79. doi:10.1016/j.biomaterials.2018.03.019.

[192] E. Korkmaz, E.E. Friedrich, M.H. Ramadan, G. Erdos, A.R. Mathers, O.B. Ozdoganlar, N.R. Washburn, L.D. Falo, Tip-Loaded Dissolvable Microneedle Arrays Effectively Deliver Polymer-Conjugated Antibody Inhibitors of Tumor-Necrosis-Factor-Alpha Into Human Skin, J. Pharm. Sci. 105 (2016) 3453–3457. doi:10.1016/j.xphs.2016.07.008.

[193] S. Kim, H. Yang, J. Eum, Y. Ma, S. Fakhraei Lahiji, H. Jung, Implantable powder-carrying microneedles for transdermal delivery of high-dose insulin with enhanced activity, Biomaterials. 232 (2020) 119733. doi:10.1016/j.biomaterials.2019.119733.

[194] K.Y. Hwa, V.H.S. Chang, Y.Y. Cheng, Y. Da Wang, P.S. Jan, B. Subramani, M.J. Wu, B.K. Wang, Analyzing polymeric matrix for fabrication of a biodegradable microneedle

array to enhance transdermal delivery, Biomed. Microdevices. 19 (2017). doi:10.1007/s10544-017-0224-x.

[195] L. Yan, A.P. Raphael, X. Zhu, B. Wang, W. Chen, T. Tang, Y. Deng, H.J. Sant, G. Zhu, K.W. Choy, B.K. Gale, T.W. Prow, X. Chen, Nanocomposite-strengthened dissolving microneedles for improved transdermal delivery to human skin, Adv. Healthc. Mater. 3 (2014) 555–564. doi:10.1002/adhm.201300312.

[196] H.-J. Chen, D. Lin, F. Liu, L. Zhou, D. Liu, Z. Lin, C. Yang, Q. Jin, T. Hang, G. He, X. Xie, Transdermal Delivery of Living and Biofunctional Probiotics through Dissolvable Microneedle Patches, ACS Appl. Bio Mater. 1 (2018) 374–381. doi:10.1021/acsabm.8b00102.

[197] J.-Y.Y. Kim, M.-R.R. Han, Y.-H.H. Kim, S.-W.W. Shin, S.-Y.Y. Nam, J.-H.H. Park, Tip-loaded dissolving microneedles for transdermal delivery of donepezil hydrochloride for treatment of Alzheimer's disease, Eur. J. Pharm. Biopharm. 105 (2016) 148–155. doi:10.1016/j.ejpb.2016.06.006.

[198] M. He, G. Yang, S. Zhang, X. Zhao, Y. Gao, Dissolving Microneedles Loaded With Etonogestrel Microcrystal Particles for Intradermal Sustained Delivery, J. Pharm. Sci. 107 (2018) 1037–1045. doi:10.1016/j.xphs.2017.11.013.

[199] J. Jin, V. Reese, R. Coler, D. Carter, M. Rolandi, Chitin Microneedles for an Easy-to-Use Tuberculosis Skin Test, Adv. Healthc. Mater. 3 (2014) 349–353. doi:10.1002/adhm.201300185.

[200] M.-Y.M.-C. Chen, Y.-Y. Chen, H.-T. Tsai, T.-S. Tzai, M.-Y.M.-C. Chen, Y.-S. Tsai, Transdermal Delivery of Luteinizing Hormone-releasing Hormone with Chitosan Microneedles: A Promising Tool for Androgen Deprivation Therapy, Anticancer Res. 37 (2017) 6791–6797. doi:10.21873/anticanres.12139.

[201] G. Yao, G. Quan, S. Lin, T. Peng, Q. Wang, H. Ran, H. Chen, Q. Zhang, L. Wang, X. Pan, C. Wu, Novel dissolving microneedles for enhanced transdermal delivery of levonorgestrel: In vitro and in vivo characterization, Int. J. Pharm. 534 (2017) 378–386. doi:10.1016/j.ijpharm.2017.10.035.

[202] M.C. Chen, K.Y. Lai, M.H. Ling, C.W. Lin, Enhancing immunogenicity of antigens through sustained intradermal delivery using chitosan microneedles with a patch-dissolvable design, Acta Biomater. 65 (2018) 66–75. doi:10.1016/j.actbio.2017.11.004.

[203] Y.H. Chen, K.Y. Lai, Y.H. Chiu, Y.W. Wu, A.L. Shiau, M.C. Chen, Implantable microneedles with an immune-boosting function for effective intradermal influenza vaccination, Acta Biomater. 97 (2019) 230–238. doi:10.1016/j.actbio.2019.07.048.

[204] A. Chandrasekharan, Y.J. Hwang, K.Y. Seong, S. Park, S. Kim, S.Y. Yang, Acid-treated water-soluble chitosan suitable for microneedle-assisted intracutaneous drug delivery, Pharmaceutics. 11 (2019) 209. doi:10.3390/pharmaceutics11050209.

[205] J. Chi, X. Zhang, C. Chen, C. Shao, Y. Zhao, Y. Wang, Antibacterial and angiogenic chitosan microneedle array patch for promoting wound healing, Bioact. Mater. 5 (2020) 253–259. doi:10.1016/j.bioactmat.2020.02.004.

[206] Y.H. Chiu, M.C. Chen, S.W. Wan, Sodium Hyaluronate/Chitosan Composite Microneedles as a Single-Dose Intradermal Immunization System, Biomacromolecules. 19 (2018) 2278–2285. doi:10.1021/acs.biomac.8b00441.

[207] R. Justin, B. Chen, Multifunctional chitosan–magnetic graphene quantum dot nanocomposites for the release of therapeutics from detachable and non-detachable biodegradable microneedle arrays, Interface Focus. 8 (2018) 20170055. doi:10.1098/rsfs.2017.0055.

[208] M.-C. Chen, M.-H. Ling, K.-Y. Lai, E. Pramudityo, Chitosan microneedle patches for sustained transdermal delivery of macromolecules, Biomacromolecules. 13 (2012) 4022–4031. doi:10.1021/bm301293d.

[209] Y. Ito, K. Matsumoto, N. Osakama, R. Yoshioka, S. Kobuchi, T. Sakaeda, K. Takada, Dissolving Microneedles as Skin Allergy Test Device, Biol. Pharm. Bull. 40 (2017) 531–534. doi:10.1248/bpb.b16-00768.

[210] L.K. Vora, A.J. Courtenay, I.A. Tekko, E. Larrañeta, R.F. Donnelly, Pullulan-based dissolving microneedle arrays for enhanced transdermal delivery of small and large biomolecules, Int. J. Biol. Macromol. (2019). doi:10.1016/j.ijbiomac.2019.12.184.

[211] W. Yu, G. Jiang, D. Liu, L. Li, H. Chen, Y. Liu, Q. Huang, Z. Tong, J. Yao, X. Kong, Fabrication of biodegradable composite microneedles based on calcium sulfate and gelatin for transdermal delivery of insulin, Mater. Sci. Eng. C. 71 (2017) 725–734. doi:10.1016/j.msec.2016.10.063.

[212] A. Nayak, H. Babla, T. Han, D.B. Das, Lidocaine carboxymethylcellulose with gelatine co-polymer hydrogel delivery by combined microneedle and ultrasound, Drug Deliv. 23 (2016) 668–679. doi:10.3109/10717544.2014.935985.

[213] C.H. Chen, V.B.H. Shyu, C.T. Chen, Dissolving microneedle patches for transdermal insulin delivery in diabetic mice: Potential for clinical applications, Materials (Basel). 11 (2018) 1625. doi:10.3390/ma11091625.

[214] C. Edens, N.C. Dybdahl-Sissoko, W.C. Weldon, M.S. Oberste, M.R. Prausnitz, Inactivated polio vaccination using a microneedle patch is immunogenic in the rhesus macaque, Vaccine. 33 (2015) 4683–4690. doi:10.1016/j.vaccine.2015.01.089.

[215] B. Cai, W. Xia, S. Bredenberg, H. Li, H. Engqvist, Bioceramic microneedles with flexible and self-swelling substrate, Eur. J. Pharm. Biopharm. 94 (2015) 404–410. doi:10.1016/j.ejpb.2015.06.016.

[216] B.Z. Chen, M. Ashfaq, D.D. Zhu, X.P. Zhang, X.D. Guo, Controlled Delivery of Insulin Using Rapidly Separating Microneedles Fabricated from Genipin-Crosslinked Gelatin,

Macromol. Rapid Commun. 39 (2018) 1800075. doi:10.1002/marc.201800075.

[217] Z. Luo, W. Sun, J. Fang, K.J. Lee, S. Li, Z. Gu, M.R. Dokmeci, A. Khademhosseini, Biodegradable Gelatin Methacryloyl Microneedles for Transdermal Drug Delivery, Adv. Healthc. Mater. 8 (2019) 1801054. doi:10.1002/adhm.201801054.

[218] J.Y. Lee, S.H. Park, I.H. Seo, K.J. Lee, W.H. Ryu, Rapid and repeatable fabrication of high A/R silk fibroin microneedles using thermally-drawn micromolds, Eur. J. Pharm. Biopharm. 94 (2015) 11–19. doi:10.1016/j.ejpb.2015.04.024.

[219] J.A. Stinson, W.K. Raja, S. Lee, H.B. Kim, I. Diwan, S. Tutunjian, B. Panilaitis, F.G. Omenetto, S. Tzipori, D.L. Kaplan, Silk Fibroin Microneedles for Transdermal Vaccine Delivery, ACS Biomater. Sci. Eng. 3 (2017) acsbiomaterials.6b00515. doi:10.1021/acsbiomaterials.6b00515.

[220] S. Wang, M. Zhu, L. Zhao, D. Kuang, S.C. Kundu, S. Lu, Insulin-Loaded Silk Fibroin Microneedles as Sustained Release System, ACS Biomater. Sci. Eng. 5 (2019) 1887–1894. doi:10.1021/acsbiomaterials.9b00229.

[221] S. Chen, H. Matsumoto, Y. Moro-Oka, M. Tanaka, Y. Miyahara, T. Suganami, A. Matsumoto, Smart Microneedle Fabricated with Silk Fibroin Combined Semi-interpenetrating Network Hydrogel for Glucose-Responsive Insulin Delivery, ACS Biomater. Sci. Eng. 5 (2019) 5781–5789. doi:10.1021/acsbiomaterials.9b00532.

[222] Y. Gao, M. Hou, R. Yang, L. Zhang, Z. Xu, Y. Kang, P. Xue, Highly Porous Silk Fibroin Scaffold Packed in PEGDA/Sucrose Microneedles for Controllable Transdermal Drug Delivery, Biomacromolecules. 20 (2019) 1334–1345. doi:10.1021/acs.biomac.8b01715.

[223] J. Lee, S.H. Park, E.H. Jang, J.H. Kim, Y.N. Youn, W. Ryu, Fabrication and characterization of silk fibroin microneedle meshes for perivascular drug delivery, in: Trans. Annu. Meet. Soc. Biomater. Annu. Int. Biomater. Symp., Society for Biomaterials, 2019: p. 68.

[224] Z. Yin, D. Kuang, S. Wang, Z. Zheng, V.K. Yadavalli, S. Lu, Swellable silk fibroin microneedles for transdermal drug delivery, Int. J. Biol. Macromol. 106 (2018) 48–56. doi:10.1016/j.ijbiomac.2017.07.178.

[225] K. Tsioris, W.K. Raja, E.M. Pritchard, B. Panilaitis, D.L. Kaplan, F.G. Omenetto, Fabrication of silk microneedles for controlled-release drug delivery, Adv. Funct. Mater. 22 (2012) 330–335. doi:10.1002/adfm.201102012.

[226] P. Medhi, O. Olatunji, A. Nayak, C.T. Uppuluri, R.T. Olsson, B.N. Nalluri, D.B. Das, Lidocaine-loaded fish scale-nanocellulose biopolymer composite microneedles, AAPS PharmSciTech. 18 (2017) 1488–1494. doi:10.1208/s12249-017-0758-5.

[227] A. Aditya, B. Kim, R.D. Koyani, B. Oropeza, M. Furth, J. Kim, N.P. Kim, Kinetics of collagen microneedle drug delivery system, J. Drug Deliv. Sci. Technol. 52 (2019) 618–

623. doi:10.1016/j.jddst.2019.03.007.

[228] S. Bhatnagar, P. Kumari, S.P. Pattarabhiran, V.V.K. Venuganti, Zein Microneedles for Localized Delivery of Chemotherapeutic Agents to Treat Breast Cancer: Drug Loading, Release Behavior, and Skin Permeation Studies, AAPS PharmSciTech. 19 (2018) 1818–1826. doi:10.1208/s12249-018-1004-5.

[229] Y. Lee, S.R. Dugansani, S.H. Jeon, S.H. Hwang, J.H. Kim, S.H. Park, J.H. Jeong, Drug-Delivery System Based on Salmon DNA Nano- and Micro-Scale Structures, Sci. Rep. 7 (2017). doi:10.1038/s41598-017-09904-9.

[230] H. Chang, M. Zheng, X. Yu, A. Than, R.Z. Seeni, R. Kang, J. Tian, D.P. Khanh, L. Liu, P. Chen, C. Xu, A Swellable Microneedle Patch to Rapidly Extract Skin Interstitial Fluid for Timely Metabolic Analysis, Adv. Mater. 29 (2017) 1702243. doi:10.1002/adma.201702243.

[231] H.M. Mansour, M.J. Sohn, A. Al-Ghananeem, P.P. DeLuca, Materials for pharmaceutical dosage forms: Molecular pharmaceutics and controlled release drug delivery aspects, Int. J. Mol. Sci. 11 (2010) 3298–3322. doi:10.3390/ijms11093298.

[232] M.T. Alam, N. Parvez, P.K. Sharma, FDA-Approved Natural Polymers for Fast Dissolving Tablets, J. Pharm. 2014 (2014) 1–6. doi:10.1155/2014/952970.

[233] H.L. Quinn, L. Bonham, C.M. Hughes, R.F. Donnelly, Design of a Dissolving Microneedle Platform for Transdermal Delivery of a Fixed-Dose Combination of Cardiovascular Drugs, J. Pharm. Sci. 104 (2015) 3490–3500. doi:10.1002/jps.24563.

[234] K. Fukushima, A. Ise, H. Morita, R. Hasegawa, Y. Ito, N. Sugioka, K. Takada, Two-layered dissolving microneedles for percutaneous delivery of peptide/protein drugs in rats, Pharm. Res. 28 (2011) 7–21. doi:10.1007/s11095-010-0097-7.

[235] Z. Tang, C. He, H. Tian, J. Ding, B.S. Hsiao, B. Chu, X. Chen, Polymeric nanostructured materials for biomedical applications, Prog. Polym. Sci. 60 (2016) 86–128. doi:10.1016/j.progpolymsci.2016.05.005.

[236] Y. Ito, S. Kashiwara, K. Fukushima, K. Takada, Two-layered dissolving microneedles for percutaneous delivery of sumatriptan in rats, Drug Dev. Ind. Pharm. 37 (2011) 1387–1393. doi:10.3109/03639045.2011.576426.

[237] O. Olatunji, R.T. Olsson, Microneedles from Fishscale-Nanocellulose Blends Using Low Temperature Mechanical Press Method, Pharmaceutics. 7 (2015) 363–378. doi:10.3390/pharmaceutics7040363.

[238] O. Olatunji, C.C. Igwe, A.S. Ahmed, D.O.A.A. Alhassan, Gg.O. Asieba, B. Das Diganta, Microneedles from fish scale biopolymer, J. Appl. Polym. Sci. 131 (2014) n/a-n/a. doi:10.1002/app.40377.

[239] E. Marin, M.I. Briceño, C. Caballero-George, Critical evaluation of biodegradable polymers used in nanodrugs, Int. J. Nanomedicine. 8 (2013) 3071–3091.

doi:10.2147/IJN.S47186.

[240] N.R. Nair, V.C. Sekhar, K.M. Nampoothiri, A. Pandey, Biodegradation of Biopolymers, in: Curr. Dev. Biotechnol. Bioeng. Prod. Isol. Purif. Ind. Prod., Elsevier, 2016: pp. 739–755. doi:10.1016/B978-0-444-63662-1.00032-4.

[241] R. Justin, S. Román, D. Chen, K. Tao, X. Geng, R.T. Grant, S. MacNeil, K. Sun, B. Chen, Biodegradable and conductive chitosan-graphene quantum dot nanocomposite microneedles for delivery of both small and large molecular weight therapeutics, RSC Adv. 5 (2015) 51934–51946. doi:10.1039/c5ra04340a.

[242] E. Eltayib, A.J. Brady, E. Caffarel-Salvador, P. Gonzalez-Vazquez, A. Zaid Alkilani, H.O. McCarthy, J.C. McElnay, R.F. Donnelly, Hydrogel-forming microneedle arrays: Potential for use in minimally-invasive lithium monitoring, Eur. J. Pharm. Biopharm. 102 (2016) 123–131. doi:10.1016/j.ejpb.2016.03.009.

[243] J. Zhu, X. Zhou, H.J. Kim, M. Qu, X. Jiang, K.J. Lee, L. Ren, Q. Wu, C. Wang, X. Zhu, P. Tebon, S. Zhang, J. Lee, N. Ashammakhi, S. Ahadian, M.R. Dokmeci, Z. Gu, W. Sun, A. Khademhosseini, Gelatin Methacryloyl Microneedle Patches for Minimally Invasive Extraction of Skin Interstitial Fluid, Small. (2020) 1905910. doi:10.1002/smll.201905910.

[244] S. Yang, F. Wu, J. Liu, G. Fan, W. Welsh, H. Zhu, T. Jin, Phase-Transition Microneedle Patches for Efficient and Accurate Transdermal Delivery of Insulin, Adv. Funct. Mater. 25 (2015) 4633–4641. doi:10.1002/adfm.201500554.

[245] K.Y. Lee, J.A. Rowley, P. Eiselt, E.M. Moy, K.H. Bouhadir, D.J. Mooney, Controlling mechanical and swelling properties of alginate hydrogels independently by cross-linker type and cross-linking density, Macromolecules. 33 (2000) 4291–4294. doi:10.1021/ma9921347.

[246] C. Vilela, R.J.B. Pinto, S. Pinto, P.A.A.P. Marques, A.J.D. Silvestre, C.S.R. Freire, Polysaccharide based hybrid materials, Springer International Publishing, Cham, 2018. doi:10.1007/978-3-030-00347-0.

[247] A. Nayak, D.B. Das, G.T. Vladisavljević, Microneedle-Assisted Permeation of Lidocaine Carboxymethylcellulose with Gelatine Co-polymer Hydrogel, Pharm. Res. 31 (2014) 1170–1184. doi:10.1007/s11095-013-1240-z.

[248] S. Liu, D. Wu, Y.S. Quan, F. Kamiyama, K. Kusamori, H. Katsumi, T. Sakane, A. Yamamoto, Improvement of Transdermal Delivery of Exendin-4 Using Novel Tip-Loaded Microneedle Arrays Fabricated from Hyaluronic Acid, Mol. Pharm. 13 (2016) 272–279. doi:10.1021/acs.molpharmaceut.5b00765.

[249] World Health Organization, Recommendations to assure the quality , safety and efficacy of BCG vaccines, 2011. http://www.who.int/biologicals/areas/vaccines/TRS_979_Annex_3.pdf (accessed

August 20, 2018).

[250] X. Yan, Y. Lin, Y. Jiang, Y. Xu, Q. Tan, Adipose-derived SVFs with hyaluronic acid accelerate diabetic wound healing in diabetic porcine model, Int. J. Clin. Exp. Med. 11 (2018) 735–740.

[251] E. Larrañeta, M. Henry, N.J. Irwin, J. Trotter, A.A. Perminova, R.F. Donnelly, Synthesis and characterization of hyaluronic acid hydrogels crosslinked using a solvent-free process for potential biomedical applications, Carbohydr. Polym. 181 (2018) 1194–1205. doi:10.1016/j.carbpol.2017.12.015.

[252] S. Bayarri, L. González-Tomás, E. Costell, Viscoelastic properties of aqueous and milk systems with carboxymethyl cellulose, Food Hydrocoll. 23 (2009) 441–450. doi:10.1016/j.foodhyd.2008.02.002.

[253] N. Dhar, S.P. Akhlaghi, K.C. Tam, Biodegradable and biocompatible polyampholyte microgels derived from chitosan, carboxymethyl cellulose and modified methyl cellulose, Carbohydr. Polym. 87 (2012) 101–109. doi:10.1016/j.carbpol.2011.07.022.

[254] A.R.C. Duarte, V.M. Correlo, J.M. Oliveira, R.L. Reis, Recent Developments on Chitosan Applications in Regenerative Medicine, in: Biomater. from Nat. Adv. Devices Ther., John Wiley & Sons, Inc., Hoboken, New Jersey, 2016: pp. 221–243. doi:10.1002/9781119126218.ch14.

[255] P. Baldrick, The safety of chitosan as a pharmaceutical excipient, Regul. Toxicol. Pharmacol. 56 (2010) 290–299. doi:10.1016/j.yrtph.2009.09.015.

[256] Q.X. Wu, D.Q. Lin, S.J. Yao, Design of chitosan and its water soluble derivatives-based drug carriers with polyelectrolyte complexes, Mar. Drugs. 12 (2014) 6236–6253. doi:10.3390/md12126236.

[257] B. Bellich, I. D'Agostino, S. Semeraro, A. Gamini, A. Cesàro, "The good, the bad and the ugly" of chitosans, Mar. Drugs. 14 (2016). doi:10.3390/md14050099.

[258] A. Rodrigues, M. Emeje, Recent applications of starch derivatives in nanodrug delivery, Carbohydr. Polym. 87 (2012) 987–994. doi:10.1016/j.carbpol.2011.09.044.

[259] F. Torres, D. Arce, Starch-Based Nanocomposites for Biomedical Applications, in: Biodegrad. Polym. Nanocomposites, CRC Press, 2015: pp. 73–94. doi:10.1201/b19314-5.

[260] R. Wang, P.J. Dijkstra, M. Karperien, Dextran, in: Biomater. from Nat. Adv. Devices Ther., John Wiley & Sons, Inc., Hoboken, New Jersey, 2016: pp. 307–319. doi:10.1002/9781119126218.ch18.

[261] R.S. Singh, G.K. Saini, J.F. Kennedy, Pullulan: Microbial sources, production and applications, Carbohydr. Polym. 73 (2008) 515–531. doi:10.1016/j.carbpol.2008.01.003.

[262] R.S. Singh, N. Kaur, V. Rana, J.F. Kennedy, Pullulan: A novel molecule for biomedical

applications, Carbohydr. Polym. 171 (2017) 102–121. doi:10.1016/j.carbpol.2017.04.089.

[263] S. Van Vlierberghe, G.J. Graulus, S.K. Samal, I. Van Nieuwenhove, P. Dubruel, Porous hydrogel biomedical foam scaffolds for tissue repair, in: Biomed. Foam. Tissue Eng. Appl., Woodhead Publishing, 2014: pp. 335–390. doi:10.1533/9780857097033.2.335.

[264] H.J. Jin, D.L. Kaplan, Mechanism of silk processing in insects and spiders, Nature. 424 (2003) 1057–1061. doi:10.1038/nature01809.

[265] J. Brown, C.L. Lu, J. Coburn, D.L. Kaplan, Impact of silk biomaterial structure on proteolysis, Acta Biomater. 11 (2015) 212–221. doi:10.1016/j.actbio.2014.09.013.

[266] Y. Cao, B. Wang, Biodegradation of silk biomaterials, Int. J. Mol. Sci. 10 (2009) 1514–1524. doi:10.3390/ijms10041514.

[267] X. You, J.H. Chang, B.K. Ju, J.J. Pak, Rapidly dissolving fibroin microneedles for transdermal drug delivery, Mater. Sci. Eng. C. 31 (2011) 1632–1636. doi:10.1016/j.msec.2011.06.010.

[268] P.C. Demuth, Y. Min, D.J. Irvine, P.T. Hammond, Implantable silk composite microneedles for programmable vaccine release kinetics and enhanced immunogenicity in transcutaneous immunization, Adv. Healthc. Mater. 3 (2014) 47–58. doi:10.1002/adhm.201300139.

[269] C. Rieu, L. Bertinetti, R. Schuetz, C.C. Salinas-Zavala, J.C. Weaver, P. Fratzl, A. Miserez, A. Masic, The role of water on the structure and mechanical properties of a thermoplastic natural block co-polymer from squid sucker ring teeth, Bioinspiration and Biomimetics. 11 (2016) 055003. doi:10.1088/1748-3190/11/5/055003.

[270] P.A. Guerette, S. Hoon, Y. Seow, M. Raida, A. Masic, F.T. Wong, V.H.B. Ho, K.W. Kong, M.C. Demirel, A. Pena-Francesch, S. Amini, G.Z. Tay, D. Ding, A. Miserez, Accelerating the design of biomimetic materials by integrating RNA-seq with proteomics and materials science, Nat. Biotechnol. 31 (2013) 908–915. doi:10.1038/nbt.2671.

[271] M. Demir, L. Ramos-Rivera, R. Silva, S.N. Nazhat, A.R. Boccaccini, Zein-based composites in biomedical applications, J. Biomed. Mater. Res. - Part A. 105 (2017) 1656–1665. doi:10.1002/jbm.a.36040.

[272] S. Fakhraei Lahiji, Y. Jang, Y. Ma, M. Dangol, H. Yang, M. Jang, H. Jung, Effects of dissolving microneedle fabrication parameters on the activity of encapsulated lysozyme, Eur. J. Pharm. Sci. 117 (2018) 290–296. doi:10.1016/j.ejps.2018.03.003.

[273] A. Levin, M. Tonelli, J. Bonventre, J. Coresh, J.A. Donner, A.B. Fogo, C.S. Fox, R.T. Gansevoort, H.J.L. Heerspink, M. Jardine, B. Kasiske, A. Köttgen, M. Kretzler, A.S. Levey, V.A. Luyckx, R. Mehta, O. Moe, G. Obrador, N. Pannu, C.R. Parikh, V. Perkovic, C. Pollock, P. Stenvinkel, K.R. Tuttle, D.C. Wheeler, K.U. Eckardt, D. Adu, S.K. Agarwal, M. Alrukhaimi, H.J. Anders, G. Ashuntantang, S. Basnet, A.K. Bello, W.

Chailimpamontree, R. Correa-Rotter, J. Craig, W.G. Douthat, H.I. Feldman, M.R. Ganji, G. Garcia-Garcia, M.B. Gharbi, D.C. Harris, V. Jha, D.W. Johnson, R. Kazancioglu, R. Langham, Z.H. Liu, Z.A. Massy, M. Nangaku, R.G. Nelson, D. O'Donoghue, I. Okpechi, R. Pecoits-Filho, N.R. Powe, G. Remuzzi, C. Roberts, J. Rossert, L. Sola, B. Stengel, E.K.S. M, Y. Suzuki, T. Tanaka, S. Tatiyanupanwong, B. Thomas, K. Uhlig, R. Walker, S.L. White, A. Wiecek, C.W. Yang, Global kidney health 2017 and beyond: a roadmap for closing gaps in care, research, and policy, Lancet. 390 (2017) 1888–1917. doi:10.1016/S0140-6736(17)30788-2.

[274] V.A. Luyckx, M. Tonelli, J.W. Stanifer, The global burden of kidney disease and the sustainable development goals, Bull. World Health Organ. 96 (2018) 414-422C. doi:10.2471/BLT.17.206441.

[275] M. Baker, In biomarkers we trust?, Nat. Biotechnol. 23 (2005) 297–304. doi:10.1038/nbt0305-297.

[276] N. Fogh-Andersen, B.M. Altura, B.T. Altura, O. Siggaard-Andersen, Composition of interstitial fluid, Clin. Chem. 41 (1995) 1522–1525. doi:10.1093/clinchem/41.10.1522.

[277] E. Cengiz, W. V. Tamborlane, A tale of two compartments: Interstitial versus blood glucose monitoring, Diabetes Technol. Ther. 11 (2009). doi:10.1089/dia.2009.0002.

[278] W.F. Brechue, H.T. Hammel, Osmotic effects of ions diffusing in capillary plasma can explain Starling's osmotic force in plasma–ISF exchange, Comp. Exerc. Physiol. 7 (2010) 153–171. doi:10.1017/S1755254011000092.

[279] H. Wiig, M.A. Swartz, Interstitial fluid and lymph formation and transport: Physiological regulation and roles in inflammation and cancer, Physiol. Rev. 92 (2012) 1005–1060. doi:10.1152/physrev.00037.2011.

[280] P.M. Wang, M. Cornwell, M.R. Prausnitz, Minimally invasive extraction of dermal interstitial fluid for glucose monitoring using microneedles, Diabetes Technol. Ther. 7 (2005) 131–141. doi:10.1089/dia.2005.7.131.

[281] V. Gubala, L.F. Harris, A.J. Ricco, M.X. Tan, D.E. Williams, Point of care diagnostics: Status and future, Anal. Chem. 84 (2012) 487–515. doi:10.1021/ac2030199.

[282] P.R. Miller, R.M. Taylor, B.Q. Tran, G. Boyd, T. Glaros, V.H. Chavez, R. Krishnakumar, A. Sinha, K. Poorey, K.P. Williams, S.S. Branda, J.T. Baca, R. Polsky, Extraction and biomolecular analysis of dermal interstitial fluid collected with hollow microneedles, Commun. Biol. 1 (2018). doi:10.1038/s42003-018-0170-z.

[283] E. Caffarel-Salvador, A.J. Brady, E. Eltayib, T. Meng, A. Alonso-Vicente, P. Gonzalez-Vazquez, B.M. Torrisi, E.M. Vicente-Perez, K. Mooney, D.S. Jones, S.E.J. Bell, C.P. McCoy, H.O. McCarthy, J.C. McElnay, R.F. Donnelly, Hydrogel-forming microneedle arrays allow detection of drugs and glucose in vivo: Potential for use in diagnosis and therapeutic drug monitoring, PLoS One. 10 (2015) e0145644.

doi:10.1371/journal.pone.0145644.

[284] B.Q. Tran, P.R. Miller, R.M. Taylor, G. Boyd, P.M. Mach, C.N. Rosenzweig, J.T. Baca, R. Polsky, T. Glaros, Proteomic Characterization of Dermal Interstitial Fluid Extracted Using a Novel Microneedle-Assisted Technique, J. Proteome Res. 17 (2018) 479–485. doi:10.1021/acs.jproteome.7b00642.

[285] T. Kiang, S. Ranamukhaarachchi, M. Ensom, Revolutionizing Therapeutic Drug Monitoring with the Use of Interstitial Fluid and Microneedles Technology, Pharmaceutics. 9 (2017) 43. doi:10.3390/pharmaceutics9040043.

[286] J. Chen, M. Wang, Y. Ye, Z. Yang, Z. Ruan, N. Jin, Fabrication of sponge-forming microneedle patch for rapidly sampling interstitial fluid for analysis, Biomed. Microdevices. 21 (2019). doi:10.1007/s10544-019-0413-x.

[287] C. Kolluru, R. Gupta, Q. Jiang, M. Williams, H. Gholami Derami, S. Cao, R.K. Noel, S. Singamaneni, M.R. Prausnitz, Plasmonic Paper Microneedle Patch for On-Patch Detection of Molecules in Dermal Interstitial Fluid, ACS Sensors. 4 (2019) 1569–1576. doi:10.1021/acssensors.9b00258.

[288] P.P. Samant, M.R. Prausnitz, Mechanisms of sampling interstitial fluid from skin using a microneedle patch, Proc. Natl. Acad. Sci. U. S. A. 115 (2018) 4583–4588. doi:10.1073/pnas.1716772115.

[289] R.K. Sivamani, D. Liepmann, H.I. Maibach, Microneedles and transdermal applications, Expert Opin. Drug Deliv. 4 (2007) 19–25. doi:10.1517/17425247.4.1.19.

[290] M.Y. Kim, B. Jung, J.-H.H. Park, Hydrogel swelling as a trigger to release biodegradable polymer microneedles in skin, Biomaterials. 33 (2012) 668–678. doi:10.1016/j.biomaterials.2011.09.074.

[291] D. Al Sulaiman, J.Y.H. Chang, N.R. Bennett, H. Topouzi, C.A. Higgins, D.J. Irvine, S. Ladame, Hydrogel-Coated Microneedle Arrays for Minimally Invasive Sampling and Sensing of Specific Circulating Nucleic Acids from Skin Interstitial Fluid, ACS Nano. 13 (2019) 9620–9628. doi:10.1021/acsnano.9b04783.

[292] A. Mandal, A. V. Boopathy, L.K.W. Lam, K.D. Moynihan, M.E. Welch, N.R. Bennett, M.E. Turvey, N. Thai, V.H. Jenny, J.C. Love, P.T. Hammond, D.J. Irvine, Cell and fluid sampling microneedle patches for monitoring skin-resident immunity, Sci. Transl. Med. 10 (2018). doi:10.1126/scitranslmed.aar2227.

[293] R. He, Y. Niu, Z. Li, A. Li, H. Yang, F. Xu, F. Li, A Hydrogel Microneedle Patch for Point-of-Care Testing Based on Skin Interstitial Fluid, Adv. Healthc. Mater. 9 (2020) 1901201. doi:10.1002/adhm.201901201.

[294] T. Liu, G. Luo, M. Xing, Biomedical Applications of Polymeric Microneedles for Transdermal Therapeutic Delivery and Diagnosis: Current Status and Future Perspectives, Adv. Ther. (2020) 1900140. doi:10.1002/adtp.201900140.

[295] K. Yue, G. Trujillo-de Santiago, M.M. Alvarez, A. Tamayol, N. Annabi, A. Khademhosseini, Synthesis, properties, and biomedical applications of gelatin methacryloyl (GelMA) hydrogels, Biomaterials. 73 (2015) 254–271. doi:10.1016/j.biomaterials.2015.08.045.

[296] M. Amer, R.K. Chen, Self-Adhesive Microneedles with Interlocking Features for Sustained Ocular Drug Delivery, Macromol. Biosci. 20 (2020) 2000089. doi:10.1002/mabi.202000089.

[297] K.S. Lim, B.J. Klotz, G.C.J. Lindberg, F.P.W. Melchels, G.J. Hooper, J. Malda, D. Gawlitta, T.B.F. Woodfield, Visible Light Cross-Linking of Gelatin Hydrogels Offers an Enhanced Cell Microenvironment with Improved Light Penetration Depth, Macromol. Biosci. 19 (2019) 1900098. doi:10.1002/mabi.201900098.

[298] A. Lavrentieva, T. Fleischhammer, A. Enders, H. Pirmahboub, J. Bahnemann, I. Pepelanova, Fabrication of Stiffness Gradients of GelMA Hydrogels Using a 3D Printed Micromixer, Macromol. Biosci. (2020) 2000107. doi:10.1002/mabi.202000107.

[299] A.K. Dąbrowska, G.-M.M. Rotaru, S. Derler, F. Spano, M. Camenzind, S. Annaheim, R. Stämpfli, M. Schmid, R.M. Rossi, A.K. Dabrowska, G.-M.M. Rotaru, S. Derler, F. Spano, M. Camenzind, S. Annaheim, R. Stämpfli, M. Schmid, R.M. Rossi, Materials used to simulate physical properties of human skin, Ski. Res. Technol. 22 (2016) 3–14. doi:10.1111/srt.12235.

[300] P.C. Parvathy, A.N. Jyothi, Water sorption kinetics of superabsorbent hydrogels of saponified cassava starch-graft-poly(acrylamide), Starch/Staerke. 64 (2012) 803–812. doi:10.1002/star.201200001.

[301] A. Ascenso, T. Pedrosa, S. Pinho, F. Pinho, J.M.P.F. De Oliveira, H.C. Marques, H. Oliveira, S. Simões, C. Santos, The Effect of Lycopene Preexposure on UV-B-Irradiated Human Keratinocytes, Oxid. Med. Cell. Longev. 2016 (2016) 8214631. doi:10.1155/2016/8214631.

[302] T. Mosmann, Rapid colorimetric assay for cellular growth and survival: Application to proliferation and cytotoxicity assays, J. Immunol. Methods. 65 (1983) 55–63. doi:10.1016/0022-1759(83)90303-4.

[303] C.T.S. Ching, T.R. Chou, T.P. Sun, S.Y. Huang, H.L. Shieh, Simultaneous, noninvasive, and transdermal extraction of urea and homocysteine by reverse iontophoresis., Int. J. Nanomedicine. 6 (2011) 417–423. doi:10.2147/ijn.s16418.

[304] Y. Ito, M.F. Hsu, A. Bettaieb, S. Koike, A. Mello, M. Calvo-Rubio, J.M. Villalba, F.G. Haj, Protein tyrosine phosphatase 1B deficiency in podocytes mitigates hyperglycemia-induced renal injury, Metabolism. 76 (2017) 56–69. doi:10.1016/j.metabol.2017.07.009.

[305] B. Li, J.F. Kennedy, Q.G. Jiang, B.J. Xie, Quick dissolvable, edible and heatsealable blend films based on konjac glucomannan - Gelatin, Food Res. Int. 39 (2006) 544–549.

doi:10.1016/j.foodres.2005.10.015.

[306] Y. Zhang, G. Jiang, W. Yu, D. Liu, B. Xu, Microneedles fabricated from alginate and maltose for transdermal delivery of insulin on diabetic rats, Mater. Sci. Eng. C. 85 (2018) 18–26. doi:10.1016/j.msec.2017.12.006.

[307] P. Erkoc, F. Seker, T. Bagci-Onder, S. Kizilel, Gelatin Methacryloyl Hydrogels in the Absence of a Crosslinker as 3D Glioblastoma Multiforme (GBM)-Mimetic Microenvironment, Macromol. Biosci. 18 (2018) 1700369. doi:10.1002/mabi.201700369.

[308] H.R. Kavousi, M. Fathi, S.A.H. Goli, Stability enhancement of fish oil by its encapsulation using a novel hydrogel of cress seed mucilage/chitosan, Int. J. Food Prop. 20 (2017) 1890–1900. doi:10.1080/10942912.2017.1357042.

[309] E. V. Hackl, V. V. Khutoryanskiy, G.M.B. Tiguman, I. Ermolina, Evaluation of water properties in HEA-HEMA hydrogels swollen in aqueous-PEG solutions using thermoanalytical techniques, J. Therm. Anal. Calorim. 121 (2015) 335–345. doi:10.1007/s10973-015-4446-y.

[310] X. Zhao, Q. Lang, L. Yildirimer, Z.Y. Lin, W. Cui, N. Annabi, K.W. Ng, M.R. Dokmeci, A.M. Ghaemmaghami, A. Khademhosseini, Photocrosslinkable Gelatin Hydrogel for Epidermal Tissue Engineering, Adv. Healthc. Mater. 5 (2016) 108–118. doi:10.1002/adhm.201500005.

[311] Y.A. Gomaa, D.I.J. Morrow, M.J. Garland, R.F. Donnelly, L.K. El-Khordagui, V.M. Meidan, Effects of microneedle length, density, insertion time and multiple applications on human skin barrier function: Assessments by transepidermal water loss, Toxicol. Vitr. 24 (2010) 1971–1978. doi:10.1016/j.tiv.2010.08.012.

[312] M. Senel, M. Dervisevic, N.H. Voelcker, Gold microneedles fabricated by casting of gold ink used for urea sensing, Mater. Lett. 243 (2019) 50–53. doi:10.1016/j.matlet.2019.02.014.

[313] S. Farnebo, E.K. Zettersten, A. Samuelsson, E. Tesselaar, F. Sjöberg, Assessment of Blood Flow Changes in Human Skin by Microdialysis Urea Clearance, Microcirculation. 18 (2011) 198–204. doi:10.1111/j.1549-8719.2010.00077.x.

[314] R. Chaudhari, A. Joshi, R. Srivastava, PH and Urea Estimation in Urine Samples using Single Fluorophore and Ratiometric Fluorescent Biosensors, Sci. Rep. 7 (2017). doi:10.1038/s41598-017-06060-y.

[315] T. Tuomi, N. Santoro, S. Caprio, M. Cai, J. Weng, L. Groop, The many faces of diabetes: A disease with increasing heterogeneity, Lancet. 383 (2014) 1084–1094. doi:10.1016/S0140-6736(13)62219-9.

[316] K. Ogurtsova, J.D. da Rocha Fernandes, Y. Huang, U. Linnenkamp, L. Guariguata, N.H. Cho, D. Cavan, J.E. Shaw, L.E. Makaroff, IDF Diabetes Atlas: Global estimates

for the prevalence of diabetes for 2015 and 2040, Diabetes Res. Clin. Pract. 128 (2017) 40–50. doi:10.1016/j.diabres.2017.03.024.

[317] R.A. DeFronzo, E. Ferrannini, L. Groop, R.R. Henry, W.H. Herman, J.J. Holst, F.B. Hu, C.R. Kahn, I. Raz, G.I. Shulman, D.C. Simonson, M.A. Testa, R. Weiss, Type 2 diabetes mellitus, Nat. Rev. Dis. Prim. 1 (2015) 15019. doi:10.1038/nrdp.2015.19.

[318] A. Rydén, E.S. Rstadius, K. Bergenheim, A. Romanovschi, F. Thorén, E.A. Witt, C. Sternhufvud, The humanistic burden of Type 1 Diabetes Mellitus in Europe: Examining health outcomes and the role of complications, PLoS One. 11 (2016). doi:10.1371/journal.pone.0164977.

[319] M. Saffran, B. Pansky, G.C. Budd, F.E. Williams, Insulin and the gastrointestinal tract, J. Control. Release. 46 (1997) 89–98. doi:10.1016/S0168-3659(96)01578-7.

[320] C. V. Asche, L. Shane-McWhorter, S. Raparla, Health Economics and Compliance of Vials/Syringes Versus Pen Devices: A Review of the Evidence, Diabetes Technol. Ther. 12 (2010) S-101-S-108. doi:10.1089/dia.2009.0180.

[321] J.G. Derraik, M. Rademaker, W.S. Cutfield, J.M. Peart, C. Jefferies, P.L. Hofman, Poorer glycaemic control is associated with increased skin thickness at injection sites in children with type 1 diabetes, Int J Pediatr Endocrinol. 2014 (2014) 2. doi:10.1186/1687-9856-2014-2.

[322] R. Shah, M. Patel, D. Maahs, V. Shah, Insulin delivery methods: Past, present and future, Int. J. Pharm. Investig. 6 (2016) 1. doi:10.4103/2230-973x.176456.

[323] F. Carmo, P. Sathler, P. Zancan, C. Rodrigues, H. Castro, V. de Sousa, M. Sola-Penna, L. Cabral, Therapeutic Nanosystems for Oral Administration of Insulin, Curr. Pharm. Biotechnol. 15 (2014) 620–628. doi:10.2174/1389201015666140915150826.

[324] E. Matteucci, O. Giampietro, V. Covolan, D. Giustarini, P. Fanti, R. Rossi, Insulin administration: Present strategies and future directions for a noninvasive (possibly more physiological) delivery, Drug Des. Devel. Ther. 9 (2015) 3109–3118. doi:10.2147/DDDT.S79322.

[325] S.N. Economidou, D.A. Lamprou, D. Douroumis, 3D printing applications for transdermal drug delivery, Int. J. Pharm. 544 (2018) 415–424. doi:10.1016/j.ijpharm.2018.01.031.

[326] X. Jin, D.D. Zhu, B.Z. Chen, M. Ashfaq, X.D. Guo, Insulin delivery systems combined with microneedle technology, Adv. Drug Deliv. Rev. 127 (2018) 119–137. doi:10.1016/j.addr.2018.03.011.

[327] S. Ross, N. Scoutaris, D. Lamprou, D. Mallinson, D. Douroumis, Inkjet printing of insulin microneedles for transdermal delivery, Drug Deliv. Transl. Res. 5 (2015) 451–461. doi:10.1007/s13346-015-0251-1.

[328] X. Chen, L. Wang, H. Yu, C. Li, J. Feng, F. Haq, A. Khan, R.U. Khan, Preparation,

properties and challenges of the microneedles-based insulin delivery system, J. Control. Release. 288 (2018) 173–188. doi:10.1016/j.jconrel.2018.08.042.

[329] D. V McAllister, P.M. Wang, S.P. Davis, J.-H.J.-H. Park, P.J. Canatella, M.G. Allen, M.R. Prausnitz, Microfabricated needles for transdermal delivery of macromolecules and nanoparticles: fabrication methods and transport studies, Proc. Natl. Acad. Sci. 100 (2003) 13755–13760. doi:10.1073/pnas.2331316100.

[330] Y. Ito, E. Hagiwara, A. Saeki, N. Sugioka, K. Takada, Feasibility of microneedles for percutaneous absorption of insulin, Eur. J. Pharm. Sci. 29 (2006) 82–88. doi:10.1016/j.ejps.2006.05.011.

[331] R.J. Narayan, Transdermal delivery of insulin via microneedles, J. Biomed. Nanotechnol. 10 (2014) 2244–2260. doi:10.1166/jbn.2014.1976.

[332] B. Mishra, V. Suneetha, K. Rath, The role of microbial pullulan, a biopolymer in pharmaceutical approaches: A review, J. Appl. Pharm. Sci. 1 (2011) 45–50.

[333] V. Suneetha, K. V Sindhuja, S.K. Singh, Screening and characterization of pullulan producing microorganism from plant leaves in Chittoor district, Asian J. Microbiol. Biotechnol. Environ. Sci. 12 (2010) 149–155. https://www.researchgate.net/publication/281233626 (accessed November 15, 2019).

[334] N.H.C.S. Silva, C. Vilela, A. Almeida, I.M. Marrucho, C.S.R. Freire, Pullulan-based nanocomposite films for functional food packaging: Exploiting lysozyme nanofibers as antibacterial and antioxidant reinforcing additives, Food Hydrocoll. 77 (2017) 921–930. doi:10.1016/j.foodhyd.2017.11.039.

[335] Amrita, A. Arora, P. Sharma, D.S. Katti, Pullulan-based composite scaffolds for bone tissue engineering: Improved osteoconductivity by pore wall mineralization, Carbohydr. Polym. 123 (2015) 180–189. doi:10.1016/j.carbpol.2015.01.038.

[336] R.S. Singh, N. Kaur, V. Rana, J.F. Kennedy, Recent insights on applications of pullulan in tissue engineering, Carbohydr. Polym. 153 (2016) 455–462. doi:10.1016/j.carbpol.2016.07.118.

[337] X. Tao, T. Tao, Y. Wen, J. Yi, L. He, Z. Huang, Y. Nie, X. Yao, Y. Wang, C. He, X. Yang, Novel Delivery of Mitoxantrone with Hydrophobically Modified Pullulan Nanoparticles to Inhibit Bladder Cancer Cell and the Effect of Nano-drug Size on Inhibition Efficiency, Nanoscale Res. Lett. 13 (2018) 345. doi:10.1186/s11671-018-2769-x.

[338] L. Huang, B. Chaurasiya, D. Wu, H. Wang, Y. Du, J. Tu, T.J. Webster, C. Sun, Versatile redox-sensitive pullulan nanoparticles for enhanced liver targeting and efficient cancer therapy, Nanomedicine Nanotechnology, Biol. Med. 14 (2018) 1005–1017. doi:10.1016/j.nano.2018.01.015.

[339] S.C.M. Fernandes, P. Sadocco, J. Causio, A.J.D. Silvestre, I. Mondragon, C.S.R. Freire, Antimicrobial pullulan derivative prepared by grafting with 3-

aminopropyltrimethoxysilane: Characterization and ability toformtransparent films, Food Hydrocoll. 35 (2014) 247–252. doi:10.1016/j.foodhyd.2013.05.014.

[340] C. Freire, D. Fonseca, C. Vilela, P. Costa, I. Almeida, P. Pereira, A. Silvestre, Polysaccharide-based microneedles for transdermal delivery of insulin, in: Abstr. Pap. Am. Chem. Soc., American Chemical Society (ACS), Washington, DC, 2019.

[341] A. Bhattacharjee, J.A. Lopes-da-Silva, M.G. Freire, J.A.P. Coutinho, P.J. Carvalho, Thermophysical properties of phosphonium-based ionic liquids, Fluid Phase Equilib. 400 (2015) 103–113. doi:10.1016/j.fluid.2015.05.009.

[342] E. Trovatti, N.H.C.S. Silva, I.F. Duarte, C.F. Rosado, I.F. Almeida, P. Costa, C.S.R. Freire, A.J.D. Silvestre, C.P. Neto, Biocellulose membranes as supports for dermal release of lidocaine, Biomacromolecules. 12 (2011) 4162–4168. doi:10.1021/bm201303r.

[343] S.C. Walpole, D. Prieto-Merino, P. Edwards, J. Cleland, G. Stevens, I. Roberts, The weight of nations: An estimation of adult human biomass, BMC Public Health. 12 (2012) 439. doi:10.1186/1471-2458-12-439.

[344] E. Trovatti, S.C.M. Fernandes, L. Rubatat, C.S.R. Freire, A.J.D. Silvestre, C.P. Neto, Sustainable nanocomposite films based on bacterial cellulose and pullulan, Cellulose. 19 (2012) 729–737. doi:10.1007/s10570-012-9673-9.

[345] E. Trovatti, S.C.M.M. Fernandes, L. Rubatat, D. da S. Perez, C.S.R.R. Freire, A.J.D.D. Silvestre, C.P. Neto, Pullulan-nanofibrillated cellulose composite films with improved thermal and mechanical properties, Compos. Sci. Technol. 72 (2012) 1556–1561. doi:10.1016/j.compscitech.2012.06.003.

[346] B.V. Farahani, H. Ghasemzaheh, S. Afraz, Intelligent semi-IPN chitosan-PEG-PAAm hydrogel for closed-loop insulin delivery and kinetic modeling, RSC Adv. 6 (2016) 26590–26598. doi:10.1039/c5ra28188a.

[347] M.R. Rekha, C.P. Sharma, Pullulan as a promising biomaterial for biomedical applications: A perspective, Trends Biomater. Artif. Organs. 20 (2007) 111–116.

[348] M. Kacuráková, P. Capek, V. Sasinková, N. Wellner, A. Ebringerová, FT-IR study of plant cell wall model compounds: Pectic polysaccharides and hemicelluloses, Carbohydr. Polym. 43 (2000) 195–203. doi:10.1016/S0144-8617(00)00151-X.

[349] J.L.R. Arrondo, A. Muga, J. Castresana, F.M. Goñi, Quantitative studies of the structure of proteins in solution by Fourier-transform infrared spectroscopy, Prog. Biophys. Mol. Biol. 59 (1993) 23–56. doi:10.1016/0079-6107(93)90006-6.

[350] Y. Pocker, S.B. Biswas, Conformational Dynamics of Insulin in Solution. Circular Dichroic Studies, Biochemistry. 19 (1980) 5043–5049. doi:10.1021/bi00563a017.

[351] L. Sun, X. Zhang, Z. Wu, C. Zheng, C. Li, Oral glucose- and pH-sensitive nanocarriers for simulating insulin release in vivo, Polym. Chem. 5 (2014) 1999–2009.

doi:10.1039/c3py01416a.

[352] L. Partridge, J. Deelen, P.E. Slagboom, Facing up to the global challenges of ageing, Nature. 561 (2018) 45–56. doi:10.1038/s41586-018-0457-8.

[353] S. Zhang, E. Duan, Fighting against Skin Aging: The Way from Bench to Bedside, Cell Transplant. 27 (2018) 729–738. doi:10.1177/0963689717725755.

[354] K. Sakamoto, R.Y. Lochhead, H.I. Maibach, Y. Yamashita, Cosmetic Science and Technology: Theoretical Principles and Applications, 2017.

[355] S.H. Bentkover, The biology of facial fillers, Facial Plast. Surg. 25 (2009) 73–85. doi:10.1055/s-0029-1220646.

[356] V. Nobile, D. Buonocore, A. Michelotti, F. Marzatico, Anti-aging and filling efficacy of six types hyaluronic acid based dermo-cosmetic treatment: Double blind, randomized clinical trial of efficacy and safety, J. Cosmet. Dermatol. 13 (2014) 277–287. doi:10.1111/jocd.12120.

[357] F. Tasca, C. Tortolini, P. Bollella, R. Antiochia, Microneedle-based electrochemical devices for transdermal biosensing: a review, Curr. Opin. Electrochem. 16 (2019) 42–49. doi:10.1016/j.coelec.2019.04.003.

[358] S.Y. Choi, H.J. Kwon, G.R. Ahn, E.J. Ko, K.H. Yoo, B.J. Kim, C. Lee, D. Kim, Hyaluronic acid microneedle patch for the improvement of crow's feet wrinkles, Dermatol. Ther. 30 (2017) e12546. doi:10.1111/dth.12546.

[359] M. Kim, H. Yang, H. Kim, H. Jung, H. Jung, Novel cosmetic patches for wrinkle improvement: Retinyl retinoate- and ascorbic acid-loaded dissolving microneedles, Int. J. Cosmet. Sci. 36 (2014) 207–212. doi:10.1111/ics.12115.

[360] J.H. An, H.J. Lee, M.S. Yoon, D.H. Kim, Anti-Wrinkle Efficacy of Cross-Linked Hyaluronic Acid-Based Microneedle Patch with Acetyl Hexapeptide-8 and Epidermal Growth Factor on Korean Skin, Ann. Dermatol. 31 (2019) 263. doi:10.5021/ad.2019.31.3.263.

[361] S.N.A. Bukhari, N.L. Roswandi, M. Waqas, H. Habib, F. Hussain, S. Khan, M. Sohail, N.A. Ramli, H.E. Thu, Z. Hussain, Hyaluronic acid, a promising skin rejuvenating biomedicine: A review of recent updates and pre-clinical and clinical investigations on cosmetic and nutricosmetic effects, Int. J. Biol. Macromol. 120 (2018) 1682–1695. doi:10.1016/j.ijbiomac.2018.09.188.

[362] A.J.D. Silvestre, C.S.R. Freire, C.P. Neto, Do bacterial cellulose membranes have potential in drug-delivery systems?, Expert Opin. Drug Deliv. 11 (2014) 1113–1124. doi:10.1517/17425247.2014.920819.

[363] E.S. Morais, N.H.C.S. Silva, T.E. Sintra, S.A.O. Santos, B.M. Neves, I.F. Almeida, P.C. Costa, I. Correia-Sá, S.P.M. Ventura, A.J.D. Silvestre, M.G. Freire, C.S.R. Freire, Anti-inflammatory and antioxidant nanostructured cellulose membranes loaded with

phenolic-based ionic liquids for cutaneous application, Carbohydr. Polym. 206 (2019) 187–197. doi:10.1016/j.carbpol.2018.10.051.

[364] N.H.C.S. Silva, I. Drumond, I.F. Almeida, P. Costa, C.F. Rosado, C.P. Neto, C.S.R. Freire, A.J.D. Silvestre, Topical caffeine delivery using biocellulose membranes: A potential innovative system for cellulite treatment, Cellulose. 21 (2014) 665–674. doi:10.1007/s10570-013-0114-1.

[365] G. Pacheco, C.V. de Mello, B.G. Chiari-Andréo, V.L.B. Isaac, S.J.L. Ribeiro, É. Pecoraro, E. Trovatti, Bacterial cellulose skin masks—Properties and sensory tests, J. Cosmet. Dermatol. 17 (2018) 840–847. doi:10.1111/jocd.12441.

[366] B. Gullón, T.A. Lú-Chau, M.T. Moreira, J.M. Lema, G. Eibes, Rutin: A review on extraction, identification and purification methods, biological activities and approaches to enhance its bioavailability, Trends Food Sci. Technol. 67 (2017) 220–235. doi:10.1016/j.tifs.2017.07.008.

[367] S.J. Choi, S.N. Lee, K. Kim, D.H. Joo, S. Shin, J. Lee, H.K. Lee, J. Kim, S. Bin Kwon, M.J. Kim, K.J. Ahn, I.S. An, S. An, H.J. Cha, Biological effects of rutin on skin aging, Int. J. Mol. Med. 38 (2016) 357–363. doi:10.3892/ijmm.2016.2604.

[368] R. Stern, H.I. Maibach, Hyaluronan in skin: aspects of aging and its pharmacologic modulation, Clin. Dermatol. 26 (2008) 106–122. doi:10.1016/j.clindermatol.2007.09.013.

[369] E. Trovatti, L.S. Serafim, C.S.R. Freire, A.J.D. Silvestre, C.P. Neto, Gluconacetobacter sacchari: An efficient bacterial cellulose cell-factory, Carbohydr. Polym. 86 (2011) 1417–1420. doi:10.1016/j.carbpol.2011.06.046.

[370] L. Greenspan, Humidity fixed points of binary saturated aqueous solutions, J. Res. Natl. Bur. Stand. A Phys. Chem. 81 A (1977) 89–96. doi:10.6028/jres.081A.011.

[371] O.P. Sharma, T.K. Bhat, DPPH antioxidant assay revisited, Food Chem. 113 (2009) 1202–1205. doi:10.1016/j.foodchem.2008.08.008.

[372] J. Pinnagoda, R.A. Tupkek, T. Agner, J. Serup, Guidelines for transepidermal water loss (TEWL) measurement: A Report from the Standardization Group of the European Society of Contact Dermatitis, Contact Dermatitis. 22 (1990) 164–178. doi:10.1111/j.1600-0536.1990.tb01553.x.

[373] G.E. Piérard, EEMCO guidance for the assessment of skin colour, J. Eur. Acad. Dermatology Venereol. 10 (1998) 1–11. doi:10.1016/S0926-9959(97)00183-9.

[374] P. Oltulu, B. Ince, N. Kökbudak, S. Findik, F. Kiliç, Measurement of epidermis, dermis, and total skin thicknesses from six different body regions with a new ethical histometric technique, Turk Plast. Rekonstruktif ve Estet. Cerrahi Derg. 26 (2018) 56–61. doi:10.4103/tjps.tjps_2_17.

[375] S.A. de Oliveira, B.C. da Silva, I.C. Riegel-Vidotti, A. Urbano, P.C. de Sousa Faria-

Tischer, C.A. Tischer, Production and characterization of bacterial cellulose membranes with hyaluronic acid from chicken comb, Int. J. Biol. Macromol. 97 (2017) 642–653. doi:10.1016/j.ijbiomac.2017.01.077.

[376] E.J. Foster, R.J. Moon, U.P. Agarwal, M.J. Bortner, J. Bras, S. Camarero-Espinosa, K.J. Chan, M.J.D. Clift, E.D. Cranston, S.J. Eichhorn, D.M. Fox, W.Y. Hamad, L. Heux, B. Jean, M. Korey, W. Nieh, K.J. Ong, M.S. Reid, S. Renneckar, R. Roberts, J.A. Shatkin, J. Simonsen, K. Stinson-Bagby, N. Wanasekara, J. Youngblood, Current characterization methods for cellulose nanomaterials, Chem. Soc. Rev. 47 (2018) 2609–2679. doi:10.1039/c6cs00895j.

[377] S. Wang, Q. Liu, Z. Luo, L. Wen, K. Cen, Mechanism study on cellulose pyrolysis using thermogravimetric analysis coupled with infrared spectroscopy, Front. Energy Power Eng. China. 1 (2007) 413–419. doi:10.1007/s11708-007-0060-8.

[378] A.R.P. Figueiredo, A.G.P.R. Figueiredo, N.H.C.S. Silva, A. Barros-Timmons, A. Almeida, A.J.D. Silvestre, C.S.R. Freire, Antimicrobial bacterial cellulose nanocomposites prepared by in situ polymerization of 2-aminoethyl methacrylate, Carbohydr. Polym. 123 (2015) 443–453. doi:10.1016/j.carbpol.2015.01.063.

[379] C.A. de Oliveira, D.D. Peres, F. Graziola, N.A.B. Chacra, G.L.B. de Araújo, A.C. Flórido, J. Mota, C. Rosado, M.V.R. Velasco, L.M. Rodrigues, A.S. Fernandes, A.R. Baby, Cutaneous biocompatible rutin-loaded gelatin-based nanoparticles increase the SPF of the association of UVA and UVB filters, Eur. J. Pharm. Sci. 81 (2016) 1–9. doi:10.1016/j.ejps.2015.09.016.

[380] Y.H. Tsai, Y.N. Yang, Y.C. Ho, M.L. Tsai, F.L. Mi, Drug release and antioxidant/antibacterial activities of silymarin-zein nanoparticle/bacterial cellulose nanofiber composite films, Carbohydr. Polym. 180 (2018) 286–296. doi:10.1016/j.carbpol.2017.09.100.

[381] K. Selvaraj, R. Chowdhury, C. Bhattacharjee, Isolation and structural elucidation of flavonoids from aquatic fern Azolla microphylla and evaluation of free radical scavenging activity, Int. J. Pharm. Pharm. Sci. 5 (2013) 743–749.

[382] I. 10993-5:2009 - Biological evaluation of medical devices - Part 5: Tests for in vitro cytotoxicity, ISO 10993-5:2009 - Biological evaluation of medical devices - Part 5: Tests for in vitro cytotoxicity, (2009).

[383] M. Pandey, M.C.I.M. Amin, N. Mohamad, N. Ahmad, S. Muda, Structure and Characteristics of Bacterial Cellulose-Based Hydrogels Prepared by Cryotropic Gelation and Irradiation Methods, Polym. - Plast. Technol. Eng. 52 (2013) 1510–1518. doi:10.1080/03602559.2013.820755.

[384] S. Ye, L. Jiang, C. Su, Z. Zhu, Y. Wen, W. Shao, Development of gelatin/bacterial cellulose composite sponges as potential natural wound dressings, Int. J. Biol.

Macromol. 133 (2019) 148–155. doi:10.1016/j.ijbiomac.2019.04.095.

[385] P. Costa, J.M. Sousa Lobo, Modeling and comparison of dissolution profiles, Eur. J. Pharm. Sci. 13 (2001) 123–133. doi:10.1016/S0928-0987(01)00095-1.

[386] I.F. Almeida, T. Pereira, N.H.C.S. Silva, F.P. Gomes, A.J.D. Silvestre, C.S.R. Freire, J.M. Sousa Lobo, P.C. Costa, Bacterial cellulose membranes as drug delivery systems: An in vivo skin compatibility study, Eur. J. Pharm. Biopharm. 86 (2014) 332–336. doi:10.1016/j.ejpb.2013.08.008.

[387] SEER, Melanoma of the Skin - Cancer Stat Facts, Natl. Cancer Inst. (2019). https://seer.cancer.gov/statfacts/html/melan.html (accessed April 21, 2020).

[388] N.K. Haass, K.S.M. Smalley, M. Herlyn, The role of altered cell-cell communication in melanoma progression, J. Mol. Histol. 35 (2004) 309–318. doi:10.1023/B:HIJO.0000032362.35354.bb.

[389] V. Gray-Schopfer, C. Wellbrock, R. Marais, Melanoma biology and new targeted therapy, Nature. 445 (2007) 851–857. doi:10.1038/nature05661.

[390] M.S. Soengas, S.W. Lowe, Apoptosis and melanoma chemoresistance, Oncogene. 22 (2003) 3138–3151. doi:10.1038/sj.onc.1206454.

[391] Z. Ali, N. Yousaf, J. Larkin, Melanoma epidemiology, biology and prognosis, in: Eur. J. Cancer, Suppl., Elsevier, 2013: pp. 81–91. doi:10.1016/j.ejcsup.2013.07.012.

[392] E. Erdei, S.M. Torres, A new understanding in the epidemiology of melanoma, Expert Rev. Anticancer Ther. 10 (2010) 1811–1823. doi:10.1586/era.10.170.

[393] R. Gordon, Skin cancer: An overview of epidemiology and risk factors, Semin. Oncol. Nurs. 29 (2013) 160–169. doi:10.1016/j.soncn.2013.06.002.

[394] M.U.R. Naidu, G.V. Ramana, P.U. Rani, I.K. Mohan, A. Suman, P. Roy, Chemotherapy-induced and/or radiation therapy-induced oral mucositis - Complicating the treatment of cancer, Neoplasia. 6 (2004) 423–431. doi:10.1593/neo.04169.

[395] M. Hofman, J.L. Ryan, C.D. Figueroa-Moseley, P. Jean-Pierre, G.R. Morrow, Cancer-Related Fatigue: The Scale of the Problem, Oncologist. 12 (2007) 4–10. doi:10.1634/theoncologist.12-s1-4.

[396] A. Sreedhar, J. Li, Y. Zhao, Next-Gen Therapeutics for Skin Cancer: Nutraceuticals, Nutr. Cancer. 70 (2018) 697–709. doi:10.1080/01635581.2018.1470651.

[397] H. Mirzaei, G. Naseri, R. Rezaee, M. Mohammadi, Z. Banikazemi, H.R. Mirzaei, H. Salehi, M. Peyvandi, J.M. Pawelek, A. Sahebkar, Curcumin: A new candidate for melanoma therapy?, Int. J. Cancer. 139 (2016) 1683–1695. doi:10.1002/ijc.30224.

[398] H. Mirzaei, A. Shakeri, B. Rashidi, A. Jalili, Z. Banikazemi, A. Sahebkar, Phytosomal curcumin: A review of pharmacokinetic, experimental and clinical studies, Biomed. Pharmacother. 85 (2017) 102–112. doi:10.1016/j.biopha.2016.11.098.

[399] B. Salehi, Z. Stojanović-Radić, J. Matejić, M. Sharifi-Rad, N. V. Anil Kumar, N. Martins,

J. Sharifi-Rad, The therapeutic potential of curcumin: A review of clinical trials, Eur. J. Med. Chem. 163 (2019) 527–545. doi:10.1016/j.ejmech.2018.12.016.

[400] S.M. Nabavi, G.L. Russo, I. Tedesco, M. Daglia, I.E. Orhan, S.F. Nabavi, A. Bishayee, K.C. Nagulapalli Venkata, M. Abdollahi, Z. Hajheydari, Curcumin and Melanoma: From Chemistry to Medicine, Nutr. Cancer. 70 (2018) 164–175. doi:10.1080/01635581.2018.1412485.

[401] T. Feng, Y. Wei, R.J. Lee, L. Zhao, Liposomal curcumin and its application in cancer, Int. J. Nanomedicine. 12 (2017) 6027–6044. doi:10.2147/IJN.S132434.

[402] M. Chopra, R. Jain, A.K. Dewangan, S. Varkey, S. Mazumder, Design of curcumin loaded polymeric nanoparticles-optimization, formulation and characterization, J. Nanosci. Nanotechnol. 16 (2016) 9432–9442. doi:10.1166/jnn.2016.12363.

[403] F. Ye, D. Lei, S. Wang, G. Zhao, Polymeric micelles of octenylsuccinated corn dextrin as vehicles to solubilize curcumin, LWT. 75 (2017) 187–194. doi:10.1016/j.lwt.2016.08.054.

[404] S. Guerrero, M. Inostroza-Riquelme, P. Contreras-Orellana, V. Diaz-Garcia, P. Lara, A. Vivanco-Palma, A. Cárdenas, V. Miranda, P. Robert, L. Leyton, M.J. Kogan, A.F.G. Quest, F. Oyarzun-Ampuero, Curcumin-loaded nanoemulsion: A new safe and effective formulation to prevent tumor reincidence and metastasis, Nanoscale. 10 (2018) 22612–22622. doi:10.1039/c8nr06173d.

[405] G. Ganesh, M.K. Singh, S. Datri, V. Venkata, S. Reddy, Design and Development of Curcumin Nanogel for Squamous Cell Carcinoma, J. Pharm. Sci. Res. 11 (2019) 1638–1645.

[406] E. Montanari, C. Di Meo, T. Coviello, V. Gueguen, G. Pavon-Djavid, P. Matricardi, Intracellular delivery of natural antioxidants via hyaluronan nanohydrogels, Pharmaceutics. 11 (2019) 532. doi:10.3390/pharmaceutics11100532.

[407] S. Abdelghany, I.A. Tekko, L. Vora, E. Larrañeta, A.D. Permana, R.F. Donnelly, Nanosuspension-based dissolving microneedle arrays for intradermal delivery of curcumin, Pharmaceutics. 11 (2019). doi:10.3390/pharmaceutics11070308.

[408] S. Farris, K.M. Schaich, L.S. Liu, P.H. Cooke, L. Piergiovanni, K.L. Yam, Gelatin-pectin composite films from polyion-complex hydrogels, Food Hydrocoll. 25 (2011) 61–70. doi:10.1016/j.foodhyd.2010.05.006.

[409] A.C. Menezes, M. Carvalheiro, J.M.P. Ferreira de Oliveira, A. Ascenso, H. Oliveira, Cytotoxic effect of the serotonergic drug 1-(1-Naphthyl)piperazine against melanoma cells, Toxicol. Vitr. 47 (2018) 72–78. doi:10.1016/j.tiv.2017.11.011.

[410] S.S.D. Kumar, M. Surianarayanan, R. Vijayaraghavan, A.B. Mandal, D.R. Macfarlane, Curcumin loaded poly(2-hydroxyethyl methacrylate) nanoparticles from gelled ionic liquid - In vitro cytotoxicity and anti-cancer activity in SKOV-3 cells, Eur. J. Pharm. Sci.

51 (2014) 34–44. doi:10.1016/j.ejps.2013.08.036.

[411] C. Lu, E. Song, D.N. Hu, M. Chen, C. Xue, R. Rosen, S.A. McCormick, Curcumin induces cell death in human uveal melanoma cells through mitochondrial pathway, Curr. Eye Res. 35 (2010) 352–360. doi:10.3109/02713680903521944.

[412] J. Odot, P. Albert, A. Carlier, M. Tarpin, J. Devy, C. Madoulet, In vitro and in vivo anti-tumoral effect of curcumin against melanoma cells, Int. J. Cancer. 111 (2004) 381–387. doi:10.1002/ijc.20160.

[413] I.C.H.H.T. Guideline, Validation of analytical procedures: text and methodology Q2 (R1), in: Int. Conf. Harmon. Geneva, Switz., 2005: pp. 11–12.

ANNEXES

Annex from Chapter 4

1. Materials and methods

1.1. *In vitro* rutin delivery

1.1.1. *Analytical method development*

To determine the wavelength of maximum absorption of rutin, rutin (25 μg.mL^{-1}) was dissolved in ethanol and the UV-Vis spectrum was recorded in the range of 200-700 nm using a UV-Vis Spectrophotometer Shimadzu UV-1800.

1.1.2. *Analytical method validation*

Validation was performed following the ICH guidelines,[413] considering the parameters linearity, accuracy, precision, selectivity, detection limit and quantitation limit.

Linearity was checked with standard solutions of rutin in the concentration range of 10-46 μg.mL^{-1}. The standard curve was analyzed by linear regression of absorbance versus rutin concentration.

Precision was expressed as relative standard deviation (RSD %) and was determined by evaluating repeatability (intra-day) and intermediate precision (inter-day). Repeatability was determined by analysis of six replicates in the same day under the same experimental conditions, whereas intermediate precision was evaluated by assaying six replicates on three different days.

In the accuracy experiments, the standard addition method was applied. For that, 6 HA-(BC-R) MNs were placed into 2 mL of PBS for 24 h. This extract (2 mL) was spiked with three different volumes (44.8, 738 and 988 μL) of rutin standard solution (60 μg.mL^{-1}), and adjusting the final volume to 3 mL, obtaining theoretical final concentrations of 23.2, 29 and 34 μg.mL^{-1}. Accuracy was expressed as percent of recovery, estimated as the relation between the experimental (C_e) and the theoretical (C_t) concentrations following the equation: $100 \times (C_e/C_t)$.

Selectivity was determined by scanning the spectrum of each component of the matrix (HA-(BC-R)) alone as well as in combination with rutin, from 200-800 nm. The interfering effect of the components in the matrix was evaluated by comparing the maximum absorption (λ_{max}) of 362 nm.

The detection limit (LD) and quantitation limit (QL) were determined based on the standard deviation of the response (σ) and the slope (S) of the constructed calibration curve. The LD was expressed as $(3.3 \times \sigma)/S$ and LQ was calculated by $(10 \times \sigma)/S$.

1.2. Information leaflet concerning the characteristics of the MN patch and the general application mode

MicroSkinCare
Microneedle patch for cosmetic purposes

PATIENT INFORMATION LEAFLET

This leaflet contains important information for you. Read it carefully before you apply the patch.

- Keep this leaflet. You may need to read it again
- Ask the researcher if you need more information or advice.
- Only use this patch for the person directed, do not pass it onto others. It may harm them.

IN THIS LEAFLET

1. What Microneedle patches are and what they are used for

Microneedles are patches consisting of extremely small needles used to administer active pharmaceutical ingredients, without penetrating the skin and underlying tissue as deeply as traditional hypodermic needles. When used for cosmetic purposes, rows of several microneedles are put onto tiny patches that are then applied to the skin (225 microneedles or 15x15 in this case of this study). The microneedles make microscopic holes in the surface of the skin to deliver rutin through a process called transdermal drug delivery. They cause minimal pain and trauma compared to hypodermic needles (Figure 1 (A) and (B)). They are a relatively new medical technology and are the subject of extensive research and study.

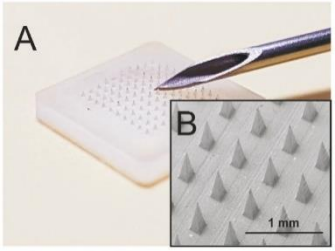

Figure1. (A) Picture showing the size comparison of the microneedle patches to a hypodermic needle and (B) Picture showing the size of microneedles in the patch.

Microneedles are virtually painless because they do not go deep enough to touch any nerves, penetrating only the surface of the skin, which consequently does not cause bleeding. The limited breakage of the skin also means that there is less chance of infection and injury. Additionally, these patches make it easier to deliver exactly the right amount of a medicine, making it possible to use lower doses.
The size of a microneedle is measured in microns. One micron is one thousandth of a millimetre, and the microneedles used are between about 450 microns in height.

2. Where to apply the patch

Apply the patch to your forearm.

3. How to apply the Microneedle patch

Step 1. Prepare the skin

- Wash your hands before application, preferably with an antibacterial soap, and then dry.
- Choose an area of non-irritated, intact skin on your forearm.
- Avoid skin which is red, irritated or has any other blemishes, for instance large scars
- Ensure the area of skin where the patch is to be applied is hairless or nearly hairless.
- Make sure the area of skin chosen is completely dry, clean and cool.
- If necessary, wash it with water and dry. Do not use soap, alcohol, oil

lotions or other detergents on the area of skin.

- After a hot bath or shower, wait until your skin is completely dry and cool.

Step 2. Opening the pouch

- Each patch is sealed in its own pouch.
- Take the patch out and apply it immediately; do not remove the patch from the pouch until needed.
- Do not use if the pouch is open, the patch is damaged or has been dropped.
- Retain the empty pouch in order to dispose of the patch later.

Step 3. Application

- Some may find it easier to rest their arm on a flat surface for application purposes.
- Ensure that the patch is being held so that the microneedles are pointed towards the skin.
- Try not to touch the microneedles on the patch with your hand.
- Carefully place the patch onto an area of hairless skin, ideally on the forearm or upper arm. (Figure2.)
- Press the patch firmly into the skin.
- Apply firm pressure on the back of the patch to ensure insertion of the patch in the skin. Ensure that pressure is applied in the direction of the skin
- The pressure required may be described as “pressing a button on an elevator” or “putting a stamp on a postcard”
- Do not to apply too much pressure, as this may cause pain or possibly break the patch
- Hold the patch in place for at least 30 seconds and then release pressure. Make sure it sticks to your arm.

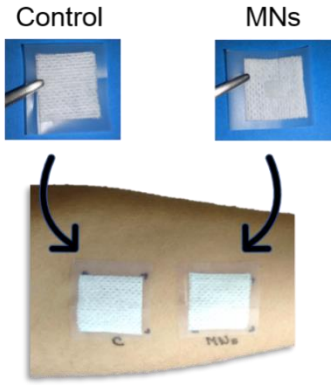

Figure2. Picture showing the site of application of a microneedle patch to the forearm.

Step 4. Disposing the patch

- Remove the patch from the skin. This should not cause any pain.
- Return the patch to the pouch and dispose of the used patch as per household waste.
- The skin may appear red or itchy, but this will subside within a short time and is of no concern.
- As with all medications, ensure the patch is kept out of reach and site of children.

Step 5. Wash

- Wash your hands afterwards with clean water

4. Further information

What do Microneedle patches contain?
There is an active ingredient in the patches used for experimental purposes.
The needle size is about 450 microns in height; each patch contains 15x15 microneedles. The patch is prepared from a water based gel containing hyaluronic acid sodium salt, a well-known biopolymer, with non-toxic and non-irritant nature. Hyaluronic acid is in fact, used for a number of applications in particular for skincare application.

1.3. Questionnaire for post-insertion in human volunteers

In vivo experimental insertion of hyaluronic acid microneedles

Structured Questionnaire

The questionnaire consists of 5 questions which should take no longer than 5 minutes. All responses will be kept anonymous and no one will be identifiable in the research. The following items describe the sensations or the visible side effects of microneedles application. I kindly ask you to answer to the following parameters (circle the number) accordingly to the sensation degree ranging from 1, which means don't feel anything, to 5 which is classified as very intense.

Age: _____ Gender: _____ Date: ____/10/2019

1. Sensation of itching

1	2	3	4	5
Not at all		Mild		Very intense

2. Sensation of prickling/tingling

1	2	3	4	5
Not at all		Mild		Very intense

3. Sensation of burn

1	2	3	4	5
Not at all		Mild		Very intense

4. Sensation of erythema

1	2	3	4	5
Not at all		Mild		Very intense

5. Sensation of edema

1	2	3	4	5
Not at all		Mild		Very intense

2. Results and discussion

2.1. *In vitro* rutin delivery

2.1.1. *Analytical method validation results*

In the present work, UV-Vis spectrophotometry was adopted as a suitable method for the quantitative determination of rutin in the HA MNs. The spectrum of rutin in the 200-700 nm unveiled two absorption maxima, at λ=258 and 362 nm (Figure S1).

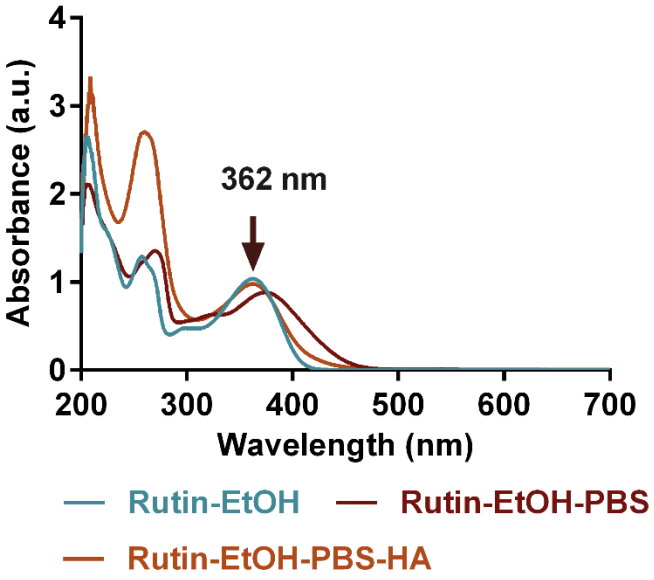

Figure S1. UV-Vis spectra of rutin dissolved in ethanol (Rutin-EtOH), rutin dissolved in ethanol:phosphate buffer (20:80) (Rutin-EtOH-PBS) and after adding hyaluronic acid (Rutin-EtOH-PBS-HA), in the range of 200-700 nm.

The components of the polymeric matrix interfere in the measurement of the absorption maxima at 258 nm but the absorbance of HA and PBS at 362 nm is negligible relative to rutin absorption at this wavelength. Hence, 362 nm was adopted as a measuring wavelength to avoid any absorption from the other components. Standard solutions in the concentration range of 10-46 μg.mL^{-1} were prepared and the absorption data was plotted against the concentration and examined for linearity. Linear regression was obtained from three independent calibration curves, over the range of 10-46 μg.mL^{-1}, with a regression line equation of $y = 0.0226x - 0.054$. The correlation coefficient shows a satisfying linear regression, with a goodness-of-fit above 0.99 (r^2 = 0.994) and the detection and quantitation limits determined for rutin are 2.49 and 7.56 μg.mL^{-1}, respectively.

Precision and accuracy were establish based on the results of three concentrations

around the value test of rutin (80, 100 and 120%). The intra-day precision (Table S1) displays a mean relative standard deviation (RSD) value of 1.04, 2.08 and 1.71% for 80, 100 and 120% rutin concentrations. In the interday analysis, RSD varies from 1.20, 0.78 and 0.26% for the defined 80, 100 and 120% rutin concentrations, confirming the precision of the methodology and good repeatability. Regarding the percentage analytical recovery of rutin, results indicate that the mean values range from 97.7 to 98.4%, indicating that the conditions under study are reliable to quantify this phenolic.

Table S1

Precision and accuracy of UV-Vis spectroscopy method for rutin determination

Parameters	Concentration (%)	Concentration ($\mu g.mL^{-1}$)		RSD (%)
Intraday precision	80	22.58 ± 0.24		1.04
	100	27.47 ± 0.57		2.08
	120	32.42 ± 0.55		1.71
Interday precision	80	22.72 ± 0.27		1.20
	100	27.01 ± 0.22		0.78
	120	33.27 ± 0.09		0.26
		Theoretical concentration ($\mu g.mL^{-1}$)	Experimental concentration ($\mu g.mL^{-1}$)	Recovery (%)
Accuracy	80	23.87 ±0.49	22.45 ± 0.04	97.77 ± 0.17
	100	28.9 ± 0.48	27.77 ± 0.02	98.15 ± 0.08
	120	34.67 ± 0.50	33.45 ± 0.76	98.38 ± 2.12